Methods Towards Asymmetric Functionalization in Porous Systems

Rath, Nicole

(2020)

Methods Towards Asymmetric Functionalization in Porous Systems

TECHNISCHE UNIVERSITÄT DARMSTADT

vom Fachbereich Chemie

der Technischen Universität Darmstadt

zur Erlangung des Grades

Doctor rerum naturalium

(Dr. rer. nat.)

Dissertation

von

Nicole Rath

aus Jena

Erstgutachterin: Prof. Dr. Annette Andrieu-Brunsen

Zweitgutachter: Prof. Dr. Markus Biesalski

Darmstadt 2020

Tag der Einreichung: 08.09.2020

Tag der mündlichen Prüfung: 22.10.2020

„It's hard to make a living on the main roads.“

Geralt von Riva in The Witcher

Die vorliegende Arbeit wurde am Ernst-Berl-Institut für Technische Chemie und Makromolekulare Chemie der Technischen Universität unter der Leitung von Frau Prof. Dr. Annette Andrieu-Brunsen in der Zeit vom 01.09.2015 bis 14.05.2019 durchgeführt.

Teile dieser Arbeit wurden bereits veröffentlicht oder auf Tagungen präsentiert:

Veröffentlichungen

N. Herzog, R. Brilmayer, M. Stanzel, A. Kalyta, D. Spiehl, E. Dörsam, C. Hess, A. Andrieu-Brunsen: „Gravure printing for mesoporous film preparation“, *RSC Adv.*, **2019**, 9, 23570-23578.

N. Herzog and M. Nau, J. Schmidt, T. Meckel, M. Biesalski and A. Andrieu-Brunsen: „Janus-Type Hybrid Paper Membranes“, *Adv. Mater. Interfaces*, **2019**, 6, 1900892.

C. Dubois, N. Herzog, C. Rüttiger, A. Geißler, E. Grange, U. Kunz, H.-J. Kleebe, M. Biesalski, T. Meckel, T. Gutmann, M. Gallei, A. Andrieu-Brunsen: „Fluid Flow Programming in Paper-Derived Silica–Polymer Hybrids“, *Langmuir*, **2017**, 33 (1), 332-339.

Vorarbeiten: N. Herzog, J. Kind, C. Hess, A. Andrieu-Brunsen: „Surface plasmon & visible light for polymer functionalization of mesopores and manipulation of ionic permselectivity“, *Chem. Commun.*, **2015**, 51, 11697-11700.

Patent: M. Nau, N. Herzog, A. Andrieu-Brunsen, M. Biesalski: "Verfahren zur Erzeugung von chemischen anisotropen Papierbeschichtungen" Patent DE 102018124255.7 (01.10.2018).

Tagungsbeiträge

Poster: N. Herzog, J. Kind, A. Andrieu-Brunsen: “Surface plasmon & visible light induced polymer functionalization of mesopores and ionic permselectivity modulation”, *Makromolekulares Kolloquium*, **24.–26. Februar 2016**, Freiburg, Deutschland.

Poster: N. Herzog, J. Kind, A. Andrieu-Brunsen: “Surface plasmon & visible light for polymer functionalization of mesoporous films and manipulation of ionic permselectivity”, *25. Lecture Conference on Photochemistry*, **26.–28. September 2016**, Jena, Deutschland.

Poster: N. Herzog, J. Kind, A. Andrieu-Brunsen: „Surface plasmon & visible light for polymer functionalization of mesoporous films”, *5th International Conference on Multifunctional, Hybrid and Nanomaterials*, **6.-10. März 2017**, Lissabon, Portugal.

Poster: N. Herzog, M. Gallei, T. Meckel, M. Biesalski, A. Andrieu-Brunsen, “Fluid Flow in Paper-Derived Silica-Polymer Hybrids”, *255st American Chemical Society National Meeting and Exposition (ACS 2018)*, **18.–22. März 2018**, New Orleans, USA.

Poster: N. Herzog, M. Gallei, T. Meckel, M. Biesalski, A. Andrieu-Brunsen, “Fluid Flow in Paper-Derived Silica-Polymer Hybrids”, *Leipziger Symposium on Dynamic Sorption*, **17. April 2018**, Leipzig, Deutschland.

Poster: N. Herzog, D. John, A. Andrieu-Brunsen: „Surface plasmon & visible light initiated polymer functionalization of mesoporous silica films“, *6th International Symposium Frontiers in Polymer Science*, **5.-8. Mai 2019**, Budapest, Ungarn.

Vortrag: N. Herzog, A. Andrieu-Brunsen: “Surface plasmon & visible light for polymer functionalization of mesoporous silica films”, *255st American Chemical Society National Meeting and Exposition (ACS 2018)*, **18.–22. März 2018**, New Orleans, USA.

Acknowledgements

Mein herzlicher Dank gilt Frau Prof. Dr. Annette Andrieu-Brunsen für das entgegengebrachte Vertrauen, die fachliche Unterstützung und für die Ermöglichung meiner Promotion in ihrer Arbeitsgruppe.

Zudem möchte ich mich bei Herrn Prof. Dr. Biesalski für die Übernahme des Korreferats, die Bereitstellung der Infrastruktur und die fachlichen Diskussionen gemeinsam mit seiner Arbeitsgruppe bedanken.

Vielen Dank an die Fachprüfer Prof. Dr. Marcus Rose und Prof. Dr. Christian Hess, sowie dem Prüfungsvorsitzenden Dr. Stefan Immel für die unkomplizierte Zusage.

Ein großer Dank geht an alle Kollegen des Arbeitskreises Andrieu-Brunsen sowie Biesalski für die gute Zusammenarbeit, Hilfsbereitschaft und die schöne Zeit auch mal gerne abseits der Uni. Dabei geht ein besonderer Dank an meine beiden Kollegen Mathias Stanzel und Robert Brilmayer für die freundschaftliche, schöne und schwitzige Arbeitsatmosphäre im *Labüro*.

Des Weiteren gilt mein Dank Petra Krause, Bärbel Webert, Vanessa Schmidt, Conny Golla, Heike Herbert und Martina Ewald zum einen für die Unterstützung bei all dem bürokratischen Dingen sowie für die netten Unterhaltungen abseits des Unialltags.

Auch möchte ich meinen Praktikanten Niels Postulka, Marco Schöpp, Dominik Richter, Monika Labecka und Anastasia Kalyta für eine hervorragende Arbeit danken. Es hat sehr viel Spaß gemacht und mich bei meiner eigenen Arbeit unterstützt.

Zusätzlich danke ich der NMR- und MS-Abteilung der TU Darmstadt für die schnelle und zuverlässige Messung vieler Proben. Ein weiterer Dank geht an Ulrike Kunz, Karl Kopp, Dr. Andreas Geißler, Dr. Torsten Gutmann und Johannes Schmidt für die freundliche Unterstützung bei diversen TEM, XPS, REM, Festkörper-NMR und BET-Messungen. Dr. Tobias Meckel möchte ich für die Einführung in die Welt der Mikroskopie, Dr. Dieter Spiehl als zuverlässiger Ansprechpartner rund um Druckprozesse und Prof. Dr.-Ing. Markus Gallei für die Zusammenarbeit und den Austausch in Bezug auf ferrocenhaltige Polymere danken.

Ein weiterer Dank geht an meine ehemaligen Komillitonen Mareike Zieglowski, Christian Stadtmüller, Svenja Wesp und Marcel Krauße für die gegenseitige Unterstützung während des Studiums, die vielen gemeinsamen Mittagessen und die entstandene Freundschaft. Ein besonderer Dank geht auch an Christian Rüttiger für unsere wöchentlichen Frühstückstreffen, der ständige Austausch und das stets offene Ohr.

Natürlich möchte ich mich auch bei Mathias Stanzel, Christian Rüttiger und meiner Familie für das akribische Korrekturlesen meiner Arbeit bedanken.

Ein abschließender Dank geht an meine ganze Familie und meinen Freund für die bedingungslose Unterstützung, andauernde Motivation und den nötigen Ausgleich. Danke das ich mich immer auf euch verlassen kann.

Table of Content

1. Abstract - Zusammenfassung

Die Miniaturisierung von technischen Geräten ist nach wie vor ein wichtiger Trend. Dies macht sich besonders in der Elektronikindustrie bemerkbar. In den vergangenen zwei Jahrzehnten wurden große Anstrengungen bei der Herstellung von miniaturisierten Komponenten und dem Aufbau von Nanostrukturen unternommen.[1] Nicht nur die Forschung und Entwicklung bestehender Materialien mit Strukturen auf der Nanometerskala sind wichtig, sondern auch das Design neuer Materialien in dieser Größenordnung und neue Anwendungen in Abhängigkeit von nanostrukturierten Materialien. In diesem Zusammenhang haben hybride mesoporöse Materialien, die die Eigenschaften nanoskaliger Poren und organischer makromolekularer Komponenten vereinen, in den letzten zwei Jahrzehnten großes Interesse in der Natur- und Ingenieurwissenschaft geweckt.[2]

Diese Arbeit ist in drei Abschnitte unterteilt. Im ersten Kapitel wird die Automatisierung der Herstellung von mesoporösen Silica Filmen mittels Tiefdruck erfolgreich durchgeführt. Die so hergestellten Filme werden mit Filmen verglichen, die durch konventionelle Tauchbeschichtungsverfahren hergestellt werden. In beiden Verfahren wird das EISA-Verfahren (*evaporation-induced self-assembly*) als Mechanismus für die Nanoporenbildung durch Templat-Anordnung und die Silicabildung durch Hydrolyse und Kondensation von Silanen verwendet. Durch die Optimierung von Prozessparameter werden mesoporöse Silicafilme mit unterschiedlichen Schichtdicken erzeugt. Im Allgemeinen erzeugt der Gravurdruck, als automatisierter Prozess, sehr homogene mesoporöse Silicafilme über große Bereiche ohne Randeffekte. Durch die Verwendung eines Co-Kondensats kann der Gravurdruck als schnelles und einfaches Verfahren zur Herstellung multifunktionaler Schichten eingesetzt werden, was neuartige Architekturen ermöglicht. Darüber hinaus wird die Anbindung eines Coinitiators auf der Silicaoberfläche für unterschiedliche Schichtdicken untersucht und optimiert. Im Ausblick konnte eine weitere vielversprechende Methode zur automatisierten Herstellung mesoporöser Silicafilme vorgestellt werden. In ersten Versuchen erweist sich ein 3D-Druckverfahren, das auf Silicabildung durch photoinitiierte Vernetzung basiert, als vielversprechend.

Die Ergebnisse bezüglich der mit Coinitator funktionalisierten mesoporösen Silica werden im zweiten Kapitel für die gezielte Polymerfunktionalisierung unter Verwendung von sichtbarem Licht und Nahfeldmoden verwendet. Die Farbstoff-sensitisierte Polymerisation von DMAEMA mit Methylenblau und einem sekundären Amin mit rotem Licht als Initiator konnte erfolgreich durchgeführt werden. Wenn das Amin an die Oberfläche gebunden wird, erfolgt die Polymerbildung auf der mesoporösen Silicaoberfläche. In verschiedenen Experimenten konnte eine zeit-, konzentrations- und energieabhängige Bildung der Polymermenge gezeigt werden.

Sowohl positiv als auch negativ geladene Monomere konnten erfolgreich polymerisiert werden. Durch die Verwendung eines Lasers als induzierende Lichtquelle konnte mit den entsprechenden Reaktionsparametern eine ortsaufgelöste Polymerfunktionalisierung in x-y-Richtung realisiert werden. Die Farbstoff-sensitisierte Polymerisation wird mit Nah-Feld Moden wie Oberflächenplasmonen (SP) oder transversalen Wellenleitermoden (TM) kombiniert. Die SP-induzierte Polymerisation in mesoporösen Silicafilmen kann in Bezug auf die erzeugte Polymermenge durch Variation der Polymerisationszeit und der Energie gesteuert werden. Bei der Energie müssen nicht nur die einstellbare Laserleistung, sondern auch die Kopplungseffizienz und die Form der SP und TM berücksichtigt werden. Dies hängt stark von der optischen Qualität des Films ab und ist innerhalb der angewandten Präparationsmethoden nur sehr schwer zu reproduzieren und zu optimieren. Durch den Vergleich der erzeugten C=O-Schwingungsbandenintensität und damit der erzeugten Polymermenge zwischen SP-induzierten und lichtinduzierten Polymerisationen wird der energieverstärkende Faktor (*enhancement facor*) der SP demonstriert. Es ist auch möglich, die TM zur Initiierung der Polymerfunktionalisierung zu verwenden. Es kann gezeigt werden, dass die SP-induzierte Polymerisation in x-y-Richtung lokal begrenzt ist, während die TM-induzierte Polymerisation in der Fläche stärker verteilt ist. In dem Fall, dass sowohl die SP- als auch die TM-induzierte Polymerisation im gleichen mesoporösen Silicafilm stattfindet, wird für die SP-induzierte Polymerisation weniger Polymer nachgewiesen als für die TM-induzierte Polymerisation, obwohl die SP einen Verstärkungsfaktor aufweist. Dieses weist eindeutig darauf hin, dass das Polymer im Falle der TM-induzierten Polymerisation auch an der äußeren Oberfläche gebildet wird. Um die Probleme der Reporduktion der mesoporösem Silica beschichteten Gold-Substrate zu vermeiden, wird im Ausblick auf eine Polymerisation mittels eines durch TIRF erzeugten evanescenten Feldes vorgestellt. In ersten Experimenten konnte eine erfolgreiche Polymerisation unter Verwendung eines evaneszenten Feldes gezeigt werden.

Im dritten Teil dieser Arbeit wird die lokale Funktionalisierung mit Silica auf hierarchisch porösem Papier gezeigt. Der Fokus liegt dabei auf der Einführung neuer Strukturen, mesoporöses Silica oder dichtes Silica, in Labor-Papier. Dabei wurde die Menge an Silica auf den Papieren variiert. Dabei kann eine Fluid-Stop-Barriere für die Wasseraufnahme ausschließliche durch Verwendung von Silica zur Papierfunktionalisierung gezeigt werden. Zudem kann gezeigt werden, dass das Flächengewicht des mit Silica funktionalisierten Papiers eine entscheidende Rolle spielt. Der wahrscheinlichste Mechanismus beruht auf einem *Pinning* an der Dreiphasen-Kontaktlinie auf dem rauen strukturierten Papier, das dadurch ermöglicht wird, dass die beschichteten Fasern eine Quellung des Cellulosematerials nicht zulassen. Diese Hypothese wird durch eine eher geringe Abnahme der freien Oberflächenenergie von Cellulose

zu Silica an Modelloberflächen unterstützt werden. Durch die Anwendung eines einfachen Tauchbeschichtungsverfahrens und Einstellung der anfänglichen TEOS-Konzentration (Silica-Precursor) in der Beschichtungslösung und des Trocknungsprozesses werden die Benetzungseigenschaften durch einen Gradienten im Papierquerschnitt eingestellt. Dabei sind Benetzungseigenschaften von hydrophil zum Janus-Typ und zur Hydrophob möglich. Durch die Kontrolle der Silicaverteilung ist eine maßgeschneiderte Benetzung entlang des Papierquerschnitts realisierbar. In ersten Versuchen wird die Anwendung als Membran zur Öl-Wasser-Trennung erfolgreich demonstriert. Durch eine anschließende Funktionalisierung der mesoporösen silica beschichteten Papier mit dem redoxreaktiven Polymer PFcMA kann eine Schaltung der Papiere in Bezug auf die Benetzung bewirken werden. In ersten Versuche konnte eine initiale Silica-Funktionalisierung der Faser und die anschließende Papierbildung erfolgreich durchgeführt werden. Dieses System könnte in Zukunft eine multifunktionelle Funktionalisierung in Papieren ermöglichen und so neue maßgeschneiderte Papiere produzieren.

2. Introduction

Miniaturization of technical devices is still an important trend. In applications devices are supposed to show improved quality, get faster and introduce more functions per device. This is especially noticeable in the electronics industry. The electronic components used to date consist of individual structures in the order of less than 100 nanometers. In the past two decades great efforts have been made in the production of miniaturized components and the construction of nanostructures.[1] Not only the research and development of existing materials with structures on the nanometer scale are important, but also the design of new materials at this scale and new applications depending on nanostructured materials. In this context, hybrid mesoporous materials, which combine the properties of nanoscale pores and organic macromolecular components, have attracted considerable interest from natural and engineering science over the last two decades.[2]

Mesoporous materials are characterized by an adjustable, stable and rigid structure with pores adjustable in the range of less than hundred nanometers to Ångströms. Their surface chemistry can be adjusted by the composition of the starting material or post-synthetic functionalization. Furthermore, thin mesoporous films can be applied to a variety of substrates at low temperatures and, due to their optical transparency in the visible region, can be used for applications in microelectronics and optoelectronics.[3] For example, nanostructured materials with a well-defined ordered mesopore structure and a defined and adjustable chemical functionalization can be prepared in a sol-gel process.[4, 5]

In addition, incorporation of polymers into mesopores provides access to a broad variety of functional hybrid materials. Polymers inherit a wealth of characteristics, which can be controlled by the choice of monomer(s) and degree of polymerization. For example, polymers with stimuli-responsive properties are of great importance for materials research and bio-materials. Thereby, light, pH, temperature, solvent, or voltage can be used as stimuli.[6-8] Applying a stimuli, induces a change in properties such as ionic transport or wettability. Such materials are used in pharmaceutics for drug release, other applications are found in sensors or permeable membranes.[8]

The polymer-functionalized mesoporous hybrid materials represent a relatively new class of functional materials in controlled release, heterogeneous catalysis or solar cells.[4, 9, 10] By using polyelectrolytes for mesoporous material functionalization, it is for example possible to produce charge-regulated transport and membranes that mimic transport control in nature. Such membranes and pores represent a promising basis for nanofluidics.[11]

In general, surface modification with polymers can be achieved by physical adsorption (physisorption) or by the covalent attachment of polymers. Covalent binding can be achieved using grafting onto, grafting from or grafting through techniques. During the grafting from approach, the polymers are synthesized directly at the surface initiated by an initiator prior covalently attached to the surface. Due to the limited diffusion of large (polymer) molecules in small pores, grafting from is the preferred approach for modifying mesoporous materials with polymers. In addition to a large number of surface-initiated polymerizations[12-16], light-initiation and photolithography continues to be of great interest because locally resolved functionalization and polymer amount control is required in x-y-z direction.[1]

Controlling local resolution in polymer functionalization and thus potentially miniaturizing functionalization control could open new material properties of such mesoporous hybrid materials for example in the context of transport control. The most established approach for localized polymer functionalization is photolithography. The local resolution in the application of classical photolithography is limited by the Abbe limit due to diffraction.[1] Exceeding this limit using a STED (stimulated emission depletion) microscope is honored with Nobel Prize to Stefan Hell in 2014. In this case, resolution down to 2.4 ± 0.3 nm could be achieved.[17] This technique is transferred to nano-/photolithography in the last years. [18-20] An alternative overcoming this limit could be the use of near-field electromagnetic modes such as surface plasmons which have a definite penetration depth into the surrounding medium outgoing from the metallic medium they arise. This could be an alternative to the local control of photolithographic processes on the nanometer scale.[21, 22] However, the use of surface plasmons has only a few studies since initial work of Soppera and coworkers have addressed this topic – but not addressing porous film.[23-25] Aim to combine such surface plasmons with radical polymerization of stimuli-responsive monomer in mesoporous silica because organic-inorganic mesoporous materials with local functionalization are highly interesting for nanofluidics, filtration-sensing elements, sensor arrays.[2]

From a general perspective, radical polymerization requires disruption of a C=C double bond. To achieve this a photoinitiator requires an energy of 6.3 eV which corresponds to a wavelength of 196.8 nm.[26] In addition to the technical complexity of generating those high-frequency electromagnetic radiation, the adsorption of potentially present oxygen, which can thereby react to toxic ozone, is problematic. Another disadvantage of such low wavelength light is its low penetration depth. Consequently, it would be advantageous to use visible light ideally in grafting from polymerizations to functionalize mesoporous materials. In the last few years some studies of visible light induced polymerization for different polymerization mechanism like ROMP[27, 28], RAFT[29], ATRP[30] and dye sensitized polymerization[31] have been published. Most of

these polymerizations are initiated with energy rich blue light below 500 nm. The dye sensitized polymerization on the other hand is sensitive to the total visible light spectrum (400-700 nm) and polymerization initiation at wavelength above 500 nm is possible as extensively demonstrated by the group of Lalevée.[32, 33] This visible light induced radical polymerization requires a two-component initiator based on dyes and a coinitiator. The advantage of using dyes is that their absorption spectra are within visible light and therefore there are a variety of commercially available lasers compatible with these initiators.

Besides mesoporous films, paper can be classified as a porous matrix. Paper provides a much higher complexity with respect to structure and the resulting function such as fluid imbibition or mechanical stability. These paper characteristics, among others, depend on porosity which again is determined by the fibre type, fibre density and fibre interstices. Especially, the role of nanoscale pores in paper on its function is not well understood. Introducing tailor-made mesoporosity into paper is expected to allow insights into the role of mesopores and functionalized mesopores on material functionality of such a hierarchical and structurally complex material. With respect to application cellulose fiber-derived hierarchically porous sheets with ordered mesoporosity are highly interesting for filtration, sensing, catalysis, cell growth, drug delivery, or fluidic applications.[34] In this context important parameters to control and even to change with time are transport and flow characteristics which are highly controlled by porosity and surface functionalization influencing charge density and wettability.

In addition to porosity and functionalization the material architecture has to be considered. For example, directed transport can be observed in asymmetrically designed, Janus-type membranes. Janus membranes or -materials in general are named after the two-faced Roman god Janus and inherit orthogonal properties on their top and bottom side such as hydrophobicity/hydrophilicity or positively/negatively charge.[35-39] The behavior of the two different sides of such membranes, particles, rods or micelles are promising in different applications like oil/water separation, droplet manipulation, fog collection, unidirectional water flow, bubble aeration, ion gating and energy harvesting.[40-46]

Regarding paper, membranes and the aim to tune fluid movement in such membranes especially the control of wettability is of interest. Thereby, usually perfluorinated molecules are used to achieve hydrophobic surface properties. In case of silica materials, a broad library of perfluorinated silanes for functionalization is commercially available. But the use of perfluorinated compounds has to raise concerns with regards to the environmental impact, especially if these coatings would be implemented on an industrial scale. [47] Alternative coating

procedures allowing adjustment of wettability and with this fluid movement in cellulose fiber webs, i.e. paper is of great importance.

3. State of the Art / Theory

3.1. Shaping Mesoporous Silica

Mesoporous silica is characterized by a defined porous structure with silanol groups on the surface. Mesoporous silica has a high thermal stability[48] and also the advantage of a very high accessible surface area. However, the chemical resistance at extreme pH values (strongly basic (pH> 9) and strongly acid (pH< 2)) can be a disadvantage.[49, 50] According to IUPAC, mesopores are defined to exhibit pore diameters of 2 - 50 nm.[51] Mesoporous silica films or coatings are generated using evaporation self-assembly (EISA) usually in a dip- or spin-coating process (**Figure 1**).[5] Two processes for nanoscale organization of inorganic structures are discussed in literature. The liquid crystal templating mechanism (LCT) in which an inorganic phase condenses to a stabilized surfactant mesophase, and the co-operative self-assembly mechanism (CSA) in which the surfactant molecules and inorganic species hybrid form intermediates that form surfactant species as independent blocks of hybrid structures.[52-54]

When the sol/precursor solution (solvent, silica-precursor, template, water and catalysator) is deposited on the supporting substrate, the volatile components evaporate at the air / film interface. This leads to the enrichment of the template and silica oligomers. When the template reaches a concentration equal to the critical micellar concentration (CMC), micelles are formed and the self-assembly process starts.[55] After the evaporation of the solvent, the final formation of mesostructures takes place. This is called a module steady state (MSS), the hybrid intermediate behaves like a liquid crystal phase depending on the composition of the MSS.[56] It is adjustable from one to three dimensions in the range of relative humidity from 20-70 %.[57] With subsequently temperature treatment such as 60 °C and 120 °C the precursor molecule hydrolyses and condensates forming the ceramic silica structure around the template micelles. The template removal is described in literature either by thermal treatment in which the template is burned out, or by chemical extraction of the template using suitable solvents.[58, 59] The former can't be performed with co-condensed silica films bearing organic groups without losing them. For this EISA process, a variety of precursor materials can be used which results in titania, zircona, niobia, silica, etc..[5, 60-63]

For example the group of K. Kuroda presented numerus studies on the functionalization during the synthesis by co-condensation of inorganic-organic nanocomposites: One example is the investigation of controlled synthesis of nanostructured silica-based materials from tailored alkoxysilanes.[64] Kuroda and co-workers also show a thickness control of mesoporous silica film by etching via drop casting method.[65]

The obtained mesoporous structure in mesoporous silica films or coatings can be adjusted during the film preparation process, by varying process parameters such as relative humidity, withdrawal speed or the ratio of the inorganic precursor- and template molecules. The functional pore network is characterized by the pore topology, pore filling, and the nature of the pore walls and interface.[4]

Besides the silane component the template strongly influences the generated mesoporous structure. The most researched templates are a range of low molecular weight surfactants such as CTAB and commercially available amphiphilic triblock copolymers such as Pluronic®.[5, 66] In most cases accessible pore sizes of less than 10 nm can be achieved. For example Wiesner and his group systematically developed and investigated block-copolymer templates and their structure formation using different blockcopolymers.[67, 68] For example poly(isoprene-block-ethylene oxide) (PI-*b*-PEO) can be used as template, integrating the hydrophilic phase of the polymer into the ceramic phase, allowing a more rational hybrid morphology.[48, 69, 70] By using block copolymers like PI-b-PEO with higher molecular weight instead of conventional low molecular weight surfactants, the production of mesopores and their accessible length scale can be extended by about one order of magnitude.[71]

The investigation of the liquid deposition processes and environmental surroundings of the mesopores is mainly done in the research groups of D. Grosso and C. Sanchez.[57, 72-76] Finally, EISA process parameters strongly influence mesoporous film formation. The EISA process is often referred to dip or spin coating. Dip coating is the simplest and least expensive method. The speed of coating is a decisive factor influencing the layer thickness of the desired film. In addition, homogeneous wetting of the substrate is critical, especially when high surface tension solvents, such as water, are used. As observed by Grosso *et al.*, the film thickness does not increase with the withdrawal speed as observed for classical dip coating but a decrease of film thickness for speed between 0.01 and 0.5 mm/s .[77] After reaching a minimum at 0.5 mm/s an increase of film thickness with increasing withdrawal speeds. As discussed by Grosso *et al.*, Faustini *et al.* and Hwang *et al.*, this is attributed to an additional regime of deposition taking place at ultra-low withdrawal speed, where evaporation and capillary convective effects govern the deposition rate.[77-79] The critical thickness for which crack formation occurs can be considerably increased if the capillary regime of deposition is selected.[77] The draining regime is described by Landau-Levich-model. Here the film thickness is increasing with the withdrawal speed for high speeds of dip-coating process whereas the capillary regimes behaves in exactly the opposite way and is valid for low withdrawal speeds. At medium speeds it is described as a mixed regime, where the thickness is perfectly described by the sum of the contribution of the two previous regimes.[73] Another factor that plays a role in the formation of the layer thickness

is the filling quantity of the dip-coating reservoir, which does not influence the formation of the two regimes just mentioned, but only the absolute values of film thickness.[80] This is important in terms of reproducibility for later applications.

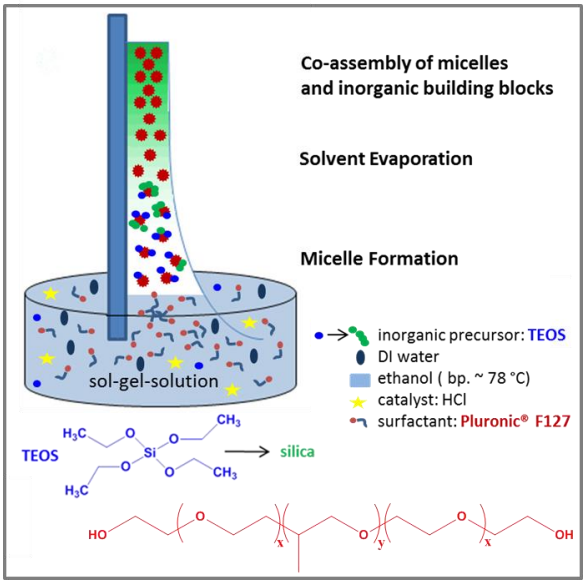

Figure 1. Forming a mesoporous thin film by dip-coating. In the first step, a sol solution is manufactured, in which the condensation to silica oligomers takes place slowly. In the second step, the CMC is achieved by evaporation of the solvents and the formation of the micelles starts. In the third step, the final mesostructure is formed depending on the ambient equilibrium. In the fourth step, the inorganic network is condensed and stabilizes the hybrid structure. Figure adapted from N. Herzog *et al.* in RSC Adv. 2019, 9, 23570-23578 used by CC BY.

To broaden mesoporous silica film functionality film architecture and material structural has to be considered. Only a few examples demonstrate hierarchical mesoporous film design for example with functional density variation in z-direction (along film thickness), although this results in fascinating material properties like tailor made vapor sorption, optical reflectance, or ionic permselectiviy.[81-84]

The research groups of Ozin, Soler-Illia, and Miguez reported the synthesis of multilayer mesoporous films consisting of different mesoporous materials, silica and titania, on top of each other, resulting in photonic structures due to refractive index differences between individual layers.[82, 85, 86] The differences in refractive indices, adjusted by the different materials and porosities, lead to Bragg stack formation, reflectors or mirrors.[82] These layered systems also lead to different vapor sorption properties and can differ in pore sizes, pore structures and chemical composition.[81, 84]

In summary evaporation-induced-self-assembly (EISA) in combination with dip coating is a well-established way to obtain silica films with tailored mesostructures and functionality. With respect to coating processes, the EISA process is suitable for industrial applications, for example

by combination with spray coating.[87] Beyond spray-coating, single step processes are investigated. A prominent example is printing such mesoporous materials and thus provide a good possibility for automation.[88]

Besides dip coating, spin coating or spray coating as deposition methods for the precursor solution, printing is a very versatile alternative concerning process automatization.

Printing is a powerful tool for the manufacturing of thin films and coatings. Especially, mesoporous coatings provide an ordered porous framework able to include a variety of functional molecules, resulting in hybrid materials with organized and specific features such as their large surface area and functionalized mesopore walls enabling even further tuning of material characteristics such as e.g. control of ionic permselectivity.[4, 49, 89] Although a few examples of ink-jet printed, structured mesoporous coatings are reported[90-96], a technology allowing the construction of highly defined multiple layer and step gradient coatings with the potential for scale up is still missing. Nevertheless, porous structures with well controlled composition along the film thickness are of special interest in advanced molecular transport control and porous material compartmentalization, and thus in technologies such as sensors, separation or energy conversion. To date composition control along the film thickness is achieved by multistep coatings with intermediate temperature-stabilization steps to avoid dissolution of bottom layers upon subsequent layer dip coating. Despite being very time consuming, this procedure also affects film homogeneity along the film thickness. In addition, substrate rims induce film inhomogeneity's, too, limiting the fabrication of small patterns, for example desired in microelectronic devices. Consequently, a technology is required that allows 1) homogeneous large area coatings, 2) structured deposition, while being scalable to an industrial size, 3) generation of well-defined multilayer at the nanoscale 4) reproducibility at an efficient time scale.

With respect to production of complex mesoporous film architectures, gravure printing bares the potential to generate more homogeneous films in much shorter production time compared to established EISA using dip- or spin-coating and ink-jet printing. In addition, standardization and automation of the film preparation process as well as complex film architecture fabrication should be relatively easy. Combining structuring by gravure printing with different sol inks and co-condensation approaches, known from classical sol-gel chemistry, and subsequent post-functionalization strategies as well supports complex film architecture design. In general, gravure printing allows nanoscale adjustment of film thickness and film homogeneity based on the applied substrate, ink viscosity, cell volume, printing speed and printing force. Consequently, smart process design is expected to not only allow the deposition of

homogeneous, and structured mesoporous film architectures on the nanometer scale in an automated fashion but as well layer selective functional placement.

These criteria are fulfilled by printing technologies. With respect to mesoporous materials, printing is mainly based on paste printing, usually fabricating net-like macroscopic architectures consisting of mesoporous silica mostly intended to be used for cell growth.[97, 98] Thereby, ordered mesoporous structures such as hexagonally arranged mesopores have been demonstrated.[97] Only a few studies focus on printing with higher local resolution. For example, Kotz *et al.* demonstrated printing of fused silica 3D structures by using stereolithography.[99] Instead of a sol that is used for EISA based dip-coating, SiO_2 particles within a UV-curable polymer are applied. Thereby, the polymer matrix stabilizes the 3D structure upon hardening with UV-light followed by sintering resulting in a silica structure. This approach allows the design of transparent 3D silica structures but does not allow to print mesoporous 3D materials. Other experiments to create a 3D ceramic structure are based on ink-jet printing using layer-by-layer deposition of ceramic suspension micro droplets ejected via nozzles.[91-93] As well, Brinker demonstrated silica nanostructures prepared by the printing procedures pen lithography and ink-jet printing. Printing also works with functional organosilanes for patterning self-assembled monolayers which leads to functional, hierarchically organized structures.[90] Unfortunately, ink-jet printing of microdot arrays of mesoporous silica is limited to the homogeneity of the dots. For optimized results, this technique is limited to hydrophobic organosilanes as co-condensates.[94] The hydrophobic organosilanes are required to avoid clogging of the nozzle aperture.[95] Currently, gravure printing is explored as an alternative fabrication process to be combined with sol-gel chemistry. A recent study published in 2018 demonstrates gravure printing of silica nanoparticles for metal oxides thin film formation.[100] But, to the best of our knowledge, gravure printing has not been used to generate ordered mesoporous silica coatings besides the work presented in this thesis. Thereby, gravure printing of mesoporous architectures bares a strong potential for automated thin film production with highly defined composition.

In addition to the aforementioned EISA process, the mechanism of light-induced self-assembly (LISA) is the subject of current research. In this process, sols are prepared from a precursor, a polymer template, and a photoacid generator (PAG) based on diphenylioidonium salts (Ph2I+X-), and exposed as a thin film in an exposure chamber with UV radiation. Solvent is not absolutely necessary.[88] The UV radiation, on the one hand, evaporates the solvent, if present, and on the other hand, in combination with the photoacid, generates a Brönsted acid which catalyzes the hydrolysis and condensation of the silicate network. When using visible light as irradiation source, the photosensitized acid generation proceeds by electron transfer between a photosensitizer (PS) and PAG. The role of a photosensitizer is to absorb light energy

and to generate excited species PS* that transfer an electron to the Ph2I+X- resulting in radical cations PS+•. The radical cations are responsible for acid generation (H+X-), either by deprotonation of hydrogen donors or by interaction with other radical species. The photo-acid catalysis the hydrolysis and condensation of silica precursors, which leads to film formation. Besides simplicity, a remarkable advantage of this method is the possibility to use visible light with a suitable PS. Curcumin is an example of such photosensitizer and can be applied with blue light (λ = 405 nm).[88, 101, 102]

Blue light is a typical laser wavelength used in 3D printing technology such as stereolithography apparatus (SLA) or digital light processing (DLP). These two technologies are very similar, with SLA using two motors to quickly move a laser beam across the print area, curing the resin. In contrast, DLP uses a digital canvas to project a single image of each layer over the entire surface at once. The objects are made the same in either process, either pulled out of the resin so as to make room for the uncured resin at the bottom of the container to form the next layer, or printed at the bottom of the container next layer above. These two techniques have great potential to print mesoporous silica structures in 3D objects in an automated fashion. For example, Steldinger *et al.* recently show the successful printing of porous carbon structures with SLA 3D printing technique.

For the functionalization of such mesoporous materials, various strategies are known in the literature: post-grafting, co-condensation and the use of periodic mesoporous organosilicas (PMO).[4] A disadvantage of post-grafting methods is that inhomogeneities of the bound molecules are reported.[103] For example, the pore entrance might have higher degrees of functionalization than areas that are located further inside the pore, which is also difficult to detect by conventional analytical methods. One advantage of the post-functionalization method is that the structures of the original silica membrane are not significantly changed upon functionalization. Only the silica wall is functionalized, which usually reduces the materials porosity.[103]

In co-condensation approaches, it has been demonstrated that small hydrophilic molecules, e.g. APTES can successfully be used to generate mesoporous aminosilica thin films.[50] The introduction of hydrophobic precursor molecules is more difficult.[104] Based on a gradual adjustment of the polymer density, the direct co-condensation of polymerization initiators would be of particular interest, since such a homogeneous distribution of initiators should be ensured and pore blocking is prohibited. However, a major disadvantage, is that the admixing of an organosilane influences the structure formation. In literature, ratios of up to 40 mol% of organic silanes in relation to TEOS are described because the degree of mesoscopic order of the

products decreases with increasing concentration of co-condensate. However, non-polar silane functionalizations often cannot be incorporated in such large proportions as structural preservation. One criterion which the functionalization component must have is an alkoxy group for incorporation in the inorganic framework via condensation.

Another method for the functionalization of silica membranes is the use of bridged organosilane precursors. However, these precursors usually have to be elaborately synthesized. The organic species are homogeneously bound in the three-dimensional silica matrix via two covalent bonds. One disadvantage is that the pores are disordered and show a broad distribution of pore size. By adding structuring surfactants, periodically ordered pore systems with a small pore radius distribution can also be synthesized.

The following open research questions have been identified:

- Is mesoporous silica printable in an automated fashion and how do printed films compare to dip-coated mesoporous films?
- Can functionally hierarchical (multilayer) films be generated by printing using different inks using co-condensation?

3.2. Local Functionalization of Interfaces

In the past two decades, great efforts have been made in the production of miniaturized components and the construction of nanostructures.[105] Not only the research and development of existing materials with structures on the nanometer scale are in focus, but also the design of new materials and the resulting applications. For the preparation of structured materials, a distinction can in principle be made between two general strategies. One strategy is the bottom-up approach. This describes self-assembly at the molecular or nanoobject level into structures. In this case, structures down to a few nanometers can be achieved. The second strategy is based on top down techniques. Top down techniques for (nanoscale) structure fabrication are lithographic techniques, such as electron beam lithography, or dip pen lithography (**Figure 2**).[1, 106-109] Electron beam lithography is most widely used to produce mesoscopic structures with high resolution and high accuracy in alignment and high flexibility in pattern replication.[110] Nowadays, a resolving power down to below 10 nm has been reported for common resists containing poly methyl methacrylate or hydrogen silsequioxane.[111] For example the dip-pen nanolithography can directly transfer a variety of inks like small molecules, polymers, proteins,

peptides, colloidal nanoparticles, metal ions and sols with different patterns to various substrates at a length scale of under 50 nm.[112] All these methods focus on structuring a surface in x-y direction without considering the direction perpendicular to the surface. Structuring for example functionalization of a porous film along the pore length going beyond multilayer formation is still an open question especially with respect to polymer functionalization. But especially polymer functionalization has been demonstrated to equip nanoscale pores with interesting transport properties such as gated pore accessibility.[40, 113-116] The simplest type of localized functionalization as well with polymers of surfaces is photolithography. In this case, the image of a photomask is transferred to a photosensitive photoresist.[117] Within unprotected areas of the surface (no photomask), the photoresist is chemically modified and can be developed. This is called a positive resist because polymer in the areas that have been exposed to radiation can be destroyed and removed. If the irradiated areas are cross-linked by radiation, it is called a negative resist, since the unirradiated and thus not cross-linked areas are subsequently removed.[118] The lateral resolution is essentially determined by the applied wavelength of light. The light used for optical lithography is usually monochromatic with wavelengths of $\lambda = 436$ nm and 365 nm in ultra-violet (UV) and 248 nm and 193 nm in deep UV. Extreme Ultra Violet lithography represents the photolithography process that has the most potential in terms of structure reduction.[119] The highest resolution could be achieved when light with λ in the range of 13.5 nm (equivalent to about 92 eV) is used, which is generated in the formation of plasmas. The reduction of the wavelength requires technological changes though. Due to the very small λ, the light is already strongly absorbed by the atmosphere and by most materials, and therefore requires usage of high vacuum. The masks must also have highly reflective surfaces ($\sim$70 %) and thus also differ from conventional exposure masks. Furthermore, the EUV technology places much higher demands on the surface roughness ($\pm$ 0.25 nm) as well as on the dimensional accuracy of the masks and the materials to be exposed.[120]

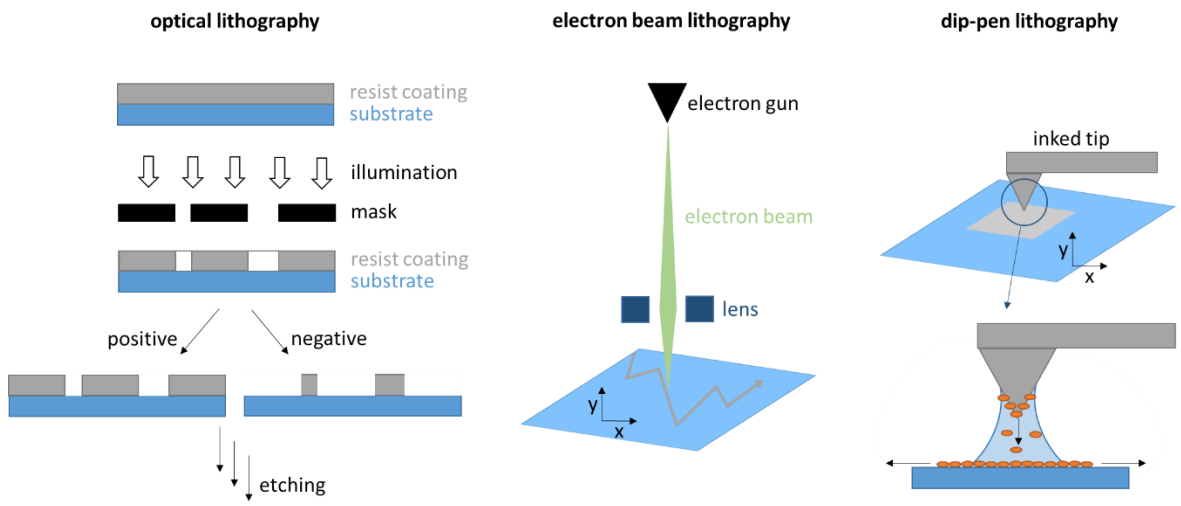

Figure 2. Schematic image of photolithography, electron beam lithography and dip-pen lithography.

Miniaturization is crucial to design complex patterned or compartmentalized functional material architectures, for example in the development of smart membranes, which are of interest for example in "Lab-on-Chip" devices or μ-electronic sensors. Structuring of polymers at interfaces is usually achieved by reducing the size of the surface presenting component or by lithographical approaches. Due to Abbe's diffraction limit, these are usually limited to micrometer dimensions.[1]

3.2.1. Mesoporous Silica as Interface

With respect to functionalization of mesoporous thin films and transport control especially local control along the pore length (transport direction) ideally at the nanoscale is of interest in the field of local functionalization. This is still an unsolved challenge. As polymerization can be initiated with light and light irradiation in general allows patterning at the microscale, overcoming this size limitation is a current research question which is as well addressed in this thesis. Overcoming the Abbe's diffraction limit would need nanoscopically limited light. This is in principle provided by near-field modes such as surface plasmons (**Figure 3**). But the wavelength of surface plasmons in case of planar metal electrode surfaces is usually located in the visible light range (460 to 650 nm). Thus polymerization reaction at this wavelength range are required.

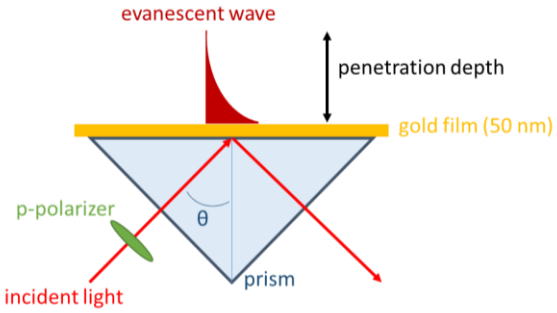

Figure 3. Schematic image of surface plasmon resonance.

The electromagnetic field of nearfield modes is characterized by local nanometer dimensions and tunable wavelength in the visible light range. Surprisingly, surface plasmons are mainly used for sensing[121, 122] and only few studies on surface plasmon induced polymerization are reported.[23, 24] Polymerization initiated by visible light can for example be achieved with multicomponent initiating systems, such as the combination of dyes as photosensitizer and amines as radical initiating molecules (Mechanism dicussed in chapter 5.1).[32] Examples are cyanine dyes,[123, 124] methylene blue[125] or alexa dyes that can be excited with visible light. Initially, the research group of Soppera, as well as the group of Kreiter demonstrated the possibility to initiate a solution photopolymerization with the surface plasmon of metallic nanoparticles by using near-field modes.[23, 126] In 2011, the research group of M. Kreiter demonstrated the possibility of using near-field irradiation to perform chemical reactions and assembly at the nanoscale.[127] Laser irradiation to generate surface plasmons on nanoparticles and guide a colloidal assembly located on the areas of surface plasmon dependent on the light doses has been used. The nanoparticle in the shape of crescents with plasmon hot-spots on the tips and the middle of crescent when the particles are separated.[128] Soppera and coworkers demonstrate the nanoscale photopolymerization using enhanced near-field modes of Ag-nanoparticles.[129] The local and not homogenous functionalization around the spherical nanoparticle corresponds to the incident polarization angle of light.[126] Taking a deeper look into mechanism governed by photochemical parameters, the reduction of functionalization size to a few nanometers has been demonstrated.[24] Félidj and coworkers showed the covalent grafting of an aryl film derived from diazonium salts on regular array of gold nanostripes in the region of maximum field enhancement.[130] The film thickness can be varied by localized surface plasmon (LSP) wavelength as well as incident light energy. This approach has also been demonstrated for gold nanorods showing the functionalization preferred on so-called surface plasmon induced hot-spots depended on light polarization,[131] followed by a study of multi-functionalization of gold nanodisks by two different types of functional poly(aryl) layers.[25] The strategy in this approach is based on varying the polarization of the incident light leading to

site-selective hot-spots. LSP induced grafting of an organic layer on Au-triangle (size of 100 nm) through visible light irradiation is shown in a study of Lacroix and coworkers in 2017.[132] The selective grafting is strongly depending on the polarization of the incident light. Therefore, the functionalization takes place either between adjacent particles or at the corners of triangles.

All these studies are based on metallic nanoparticles of different sizes and shapes leading to the localized functionalization using surface plasmons.[275] However, investigations on plane gold surfaces resulting in surface plasmon resonance mainly deal with the investigation of kinetics of (bio-)molecules binding to the surface for determination of association and dissociation rate constants. Here, SPR is used as a sensor and not as an initiating system for (photo-)chemical reaction like shown for nanoparticles. Last year, the plasmon-induced reversible addition-fragmentation chain-transfer (RAFT) polymerization on a surface was reported for the first time by Erzina *et al.*[133] The RAFT initiator is bound to the gold grating surface, then a solution with monomer and AIBN as radical starter is in the film surroundings. When generating the surface plasmon with the suitable wavelengths of light, the polymerization starts. Grafting from approaches are suitable for functionalization in mesoporous silica.[134, 135] Nonetheless, the confinement of mesopores can lead to steric hindrance of a polymer chain using the grafting-to approach, but this suits perfect for binding molecules which can be used as initiating reactants later on.

Generally, combining visible-light photo-initiation concepts with (surface) functionalization of mesopores, visible light-induced, localized near-field functionalization in water becomes accessible. The combination of mesoporous silica films and the polymerization within the pores with near-field modes such as surface plasmons was published the first time by our research group as a proof of concept in 2015.[136] Further investigation in this field resulted in the following research questions.

The following open research questions have been identified:

- Can near field (surface plasmon) induced polymerizations at planar surfaces (visible light > 500 nm) been developed to functionalize mesoporous silica films? If yes, which parameters (time, energy) influence the near field induced polymerization in mesoporous silica?
- Can the visible light induced polymerization be carried out with transversal modes as well as with surface plasmons and does this result in differences in polymer functionalization?

3.2.2. Paper as porous matrix

Paper is a nonwoven made of fibers of natural origin, which is produced by the dewatering of a pulp suspension. Paper was produced already as an information carrier and means of communication in China about 2,000 years ago. The pulps for papermaking are mainly obtained by mechanical or chemical pulping of natural wood. They contain cellulose as a constituent, polymeric building block. Depending on the type of digestion, the fibers on the surface may contain lignins and hemicelluloses in addition to the cellulose. Furthermore, the fibers carry negative charges on the surface, which arise in a natural process (cellular respiration) by oxidation of the hydroxyl groups of the cellulose to carboxyl groups. The cellulose polymers form partially crystalline microfibrils via hydrogen bonds. These continue to connect to macrofibrils and eventually to fibers (**Figure 4**). This hierarchical structure gives the fibers extraordinary properties, such as high tensile strength and high chemical resistance to water and other solvents.

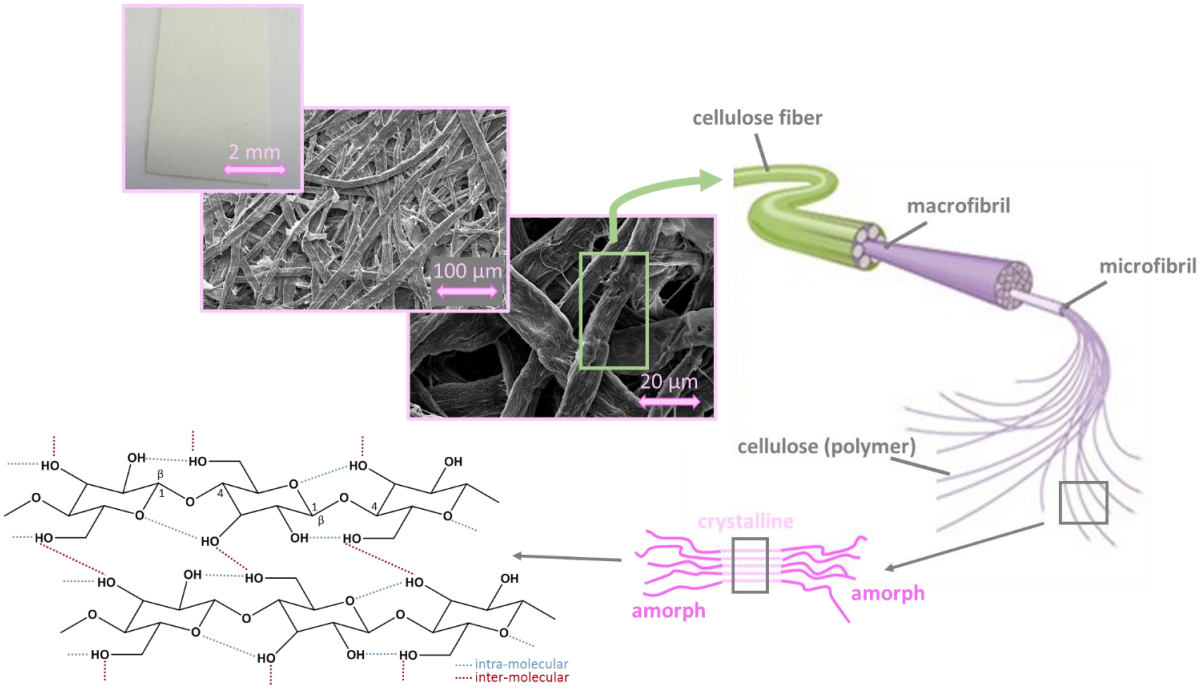

Figure 4. Schematic structure of paper. Paper is a weave of cellulose fibers. The fibers consist of macrofibrils, which are composed of microfibrils. These are composed of the individual cellulose polymers. The cellulose forms crystalline and amorphous areas. In the crystalline areas intramolecular and intermolecular hydrogen bonds are formed.

The standard papermaking process is technically very well developed today. Paper is produced worldwide in large quantities (approx. 411 million tons in 2016), with Germany being the fourth largest producing country of paper with 22.6 million tons of production.[137] Paper is usually produced as a flat and inexpensive product. Paper production is a very large volume business with more than 3,000 different types of paper in the main markets of print media

(share in Germany: 38 %), packaging products (49 %), hygiene products (6 %) and specialty technical papers (6 %).[137, 138] While print media are losing more and more importance, as a result of the digital revolution, particular attention has been paid to papers that have a functional character and are included in the group of specialty technical papers. Examples of these functional papers range from filter and sealant materials, to thermal or decorative paper and carrier webs for adhesives (adhesive tapes) or security papers.[139] In this context, analytics or medical diagnostics play an increasingly important role for functional papers. There are known applications like chromatography paper, analysis paper for pH and urine or as pregnancy tests. These applications take advantage of the unique properties of paper. Due to the above mentioned structure, paper is porous and can transport liquids without external pumps. Papers are chemically and thermally more stable compared to porous plastics or textiles and show almost no thermal expansion. They are also very tear-resistant and can be recycled after use or even energetically recycled. These aspects make paper ideal as a bio-compatible substrate and attractive for further functionalization.

These characteristics have ensured that new applications, in addition to the established applications mentioned above, have become the focus of current research. Examples are microfluidic papers for paper based diagnostics,[140-144] papers as bioanalytical devices in medical research,[145, 146] ceramic papers for catalytic applications[147] or papers for quantitative gas sensing.[148] With respect to its macroscopic properties such as color, roughness or tensile strength, paper has been very well studied. Generally, the relationship between properties that are relevant for the use of paper in conventional applications (print media or packaging papers) and the raw material or process parameters are also well known. Contrary to this, processes that allow production of highly oriented nonwoven papers, and thus papers with sophisticated structural control beyond grammage adjustment, are less studied.

Macropores in paper of the order of 10^{-6} m can be adjusted, for example in the standard process of paper production by the selection of fibers, the pretreatment of fibers, and the density of fibers in the laid nonwoven. In contrast, the control of pores on the nanometer scale poses a great challenge. Paper fibers that are moist after being extracted from wood and thus kept in a swollen state have a very high specific surface and a large number of very small nanoscale pores. However, these fibers are neither trivial in handling nor for further processing into functional papers. The fiber structure can change dramatically upon drying, hindering the setting of a reproducible pore structure.[149] However, in the production of functional papers, which form intrinsically small pores, nanoscale pores can be transferred to paper fibers in a controlled manner. This has been achieved, for example by embedding block copolymers in the macroporous paper matrix.[150] Likewise, mesoporous structures of inorganic silica can be

deposited in-situ on the fibers.[151] Silica as well as paper are bio-based materials. The amount of silica does not have to be very high in relation to the paper to introduce nanoporosity in addition to the natural pores of the paper. One example besides silica to generate nanoporosity in paper is “never-dried-cellulose”.[149] Here the swollen fibers have very small pores. These highly porous pulps are also not very mechanically stable and it is not trivial to stabilize the highly porous structure. Different porosities can vary the material properties in relation to the fluid imbibition.[152]

The definition of microfluidics is given by Whiteside as a science and technology of systems that process or manipulate small amounts of fluids, using channels with dimensions of ten to hundreds of micrometers.[153] Nevertheless, the classical microfluidic systems of the first and second generation based on silicon, glass or polydimethylsiloxane (PDMS) are hardly used commercially because of high production costs as well as the additionally required pumps for regulated transport of fluids in the system.[154, 155] As inexpensive solution fiber-fleece-like materials, such as nitrocellulose membranes or paper, in which the fluid transport is driven by capillary force, came into focus. These materials promise a simple handling due to intrinsic fluid transport.[155] Research related to this topic has gained increasing interest for the development of low-cost point-of-care diagnostic tools.

It was demonstrated that fluid flow can be modulated by changing channel dimensions or by engineering the paper cellulose fiber structures or surface chemistry.[156, 157] Up to now, fluid flow in paper is mainly adjusted by changing fiber density and thus macroporosity and fluid penetration is prevented by hydrophobizing certain areas (patches), e.g. by wax printing.[158, 159] In a recent work by Vlessidis and co-workers, flow velocity was manipulated by adding channels parallel to the flow direction to accelerate flow and to slow down fluid flow perpendicular to the flow direction.[160] Engineering of paper-based devices even shows the potential for upscaling, because it can be combined with printing techniques allowing to print μ-fluidic channels as well as reagents such as bio molecular recognition units into reactive patches.[161] All these studies share the common approach of adjusting fluid flow by material design. Although the fluid flow can be adjusted, external as well as on-line acceleration or deceleration of fluid flow during operation and thus the design of dynamic devices and flow control have not been investigated.

Besides paper-based materials for fluid flow and transport control, ordered mesoporous ceramic structures prepared by sol-gel chemistry and evaporation induced self-assembly[5] are very interesting regarding transport modulation at the nanoscale, especially after functionalization as described in chapter 3.2.1, too.[162-164] Mesopores with pore diameters below 10 nm for

example allow to gate ionic permselectivity. In the last years an increasing amount of research was dedicated to the investigation and generation of bioinspired switchable mesopores. Combining responsive functional groups with mesopores, transport could be gated upon temperature[165], pH[166, 167], specific molecules[113, 168], voltage[169-171] and light.[172-174] Cellulose fiber-derived hierarchically porous sheets with ordered mesoporosity are highly interesting for filtration, sensing, catalysis, cell growth, drug delivery, or fluidic applications.[34] In this context important parameters to control and even to change with time are transport and flow characteristics. In a given porous matrix surface chemistry allows to modulate surface characteristics such as wetting or charge.

The motivation for combining both materials, paper and mesopores, is to obtain stable nanopores in paper and to combine fluid flow and transport control of small molecules or ions. Combining sol-gel chemistry and EISA with rationally designed paper may result in new possibilities in fluid flow and molecular transport control as well as in further understanding of fluid flow modulation on a micro- to nanoscale. This hypothesis is based on the multitude of publication, in which the fluid flow is correlated to Lucas-Washburn relation or Darcy's law.[156, 175, 176] To externally manipulate fluid flow on-line the paper sheet porosity or hydrophobicity has to be modulated. In terms of external hydrophobicity modulation on planar surfaces or in mesopores, ferrocene-containing polymers show great potential. [177, 178] One important property is the setting of surface wettability, which has been used, e.g. for the preparation of self-cleaning surfaces, tunable optical lenses, lab on chip systems, microfluidic devices, textile applications, thin film sensors, and smart membranes.[177, 179-186]

Regarding molecular transport control, functionalized mesoporous ceramic structures[5] show very interesting properties[4, 187, 188] and may be combined with macroscopically designed paper-templated ceramics.[189] The paper-templated ceramic is produced in this example by sintering fillers that are introduced into the paper during the paper manufacturing process. Here macroscopic structures are produced. It is also known that sol-gel chemistry can be used to produce paper-tempered ceramics. Here only very few examples for the production of nanostructures in combination with cellulose fibers are known and these have not yet been used for reintegration into functional papers/materials.[190]

Nowadays, the combination of silica and paper has attracted great interest because both materials are biobased and attempts to mimic properties found in plants and animals are followed. Besides the combination of materials inheriting complementary properties such as paper and ceramic (mesoporous) coatings material symmetry (or asymmetry) and thus local distribution of structural or functional components has a strong influence on material

performance. Natural cactus, spider silk, lotus leafs and desert beetles are some of the fascinating examples, because of their asymmetrical physical structure or chemical properties called Janus materials.[35-39] The definition of Janus materials in general is broadly diversified and includes all materials with asymmetrical surfaces as well as composites. Janus materials are well known since the Nobel Prize lecture of de Gennes in 1991, but first mentioned in 1898 by the group of Veyssié.[191, 192] In 2016, the group of Xu refined the definition to materials having opposing properties at the two respective interfaces and proposed three configurations of Janus membranes.[39] One is the "A to B"-type material, which shows a physical and/or chemical gradient across a membrane cross-section. Whereas A-to-B or A- and B-type Janus membranes are defined as having a clear interface between the layers. Jiang and coworkers developed a coating followed by peeling strategy for the facile preparation of multifunctional Janus membranes.[35] This Janus-type membrane is based on fully synthetic polymers, i.e. polyethylene terephthalate (PET)/polytetrafluoroethylene (PTFE). The membrane is modified by tannic acid and diethylenetriamine to form a hydrophilic coating on the surface while the membrane stays hydrophilic. Peeling off the top PTFE layer from the hydrophilic membrane results in a Janus membrane with unidirectional water permeation properties at the oil/water interface. Most recently, the group of Ikkala presented a membrane consisting of cotton modified with an perfluorooctyltrichlorosilane through chemical vapor deposition (CVD) of one side to generate a Janus material in one step.[42] Those composite materials exhibit a directional gating of water droplets in air-water as well as oil-water systems with integrated selectivity to oil or water inspired by the passive transport across cell membranes based on transmembrane hydrophilic/hydrophobic interactions of the regulating membrane permeability.[193, 194]

Fluid flow as can be deduced from Lucas-Washburn or Darcy's Law in paper strongly depends on wettability. Wettability again depends on the hydrophobicity of the substrate and the surface tensions. Thus hydrophobization is supposed to allow the control of wetting. One way to create hydrophobic interfaces is the use of silanes. There are two general factors to consider enabling these coating systems derived from silanes, (without regard of the specific silanes utilized), namely structure and surface chemistry. Structured silane based coatings feature a plethora of particle-based systems, i.e. nano-, micro- or "raspberry"-particles, that combine surface chemistry and structure to achieve all kinds of interface properties like super hydrophobic/philic, oleophobic/philic or amphiphobic coatings.[195, 196] Compositions to generate hydrophobic interfaces feature typically the synthesis and modification of silica particles using precursors like tetraethoxysilane (TEOS) for the particle formation, i.e. generation of structure, and hydrophobic perfluorinated - or alkyl- silanes to implement the desired surface chemistry.[197-200] Additionally, the utilization of poly(dimethylsilane) (PDMS) in combination

with silica-particles has yielded to promising results with regard of mechanical stable coatings, something that has always been challenging with regard to micro/nano-structured surfaces. [201, 202] While these strategies evidently have demonstrated great improvement in such material design, the production of the material is rather laborious, including delicate sol/gel processes and necessity for several steps to produce the interface. [203, 204] In addition, the use of perfluorinated compounds in surface modification has to raise concerns with regards to the environmental impact, if these coatings would be implemented on an industrial scale.[47] Comparably, when silanes are implemented without the generation of a micro- or nano structure, for example on cellulosic substrate, the wettability of surfaces can only be modulated by alteration of the silane derivatives used and thus the final surface energy.[205, 206] However, all these techniques implement a range of organo- and perfluorinated compounds.[207] Interestingly, coating of cellulose fiber webs, i.e. paper with TEOS, without further modification, resulted in a slightly increase of the hydrophobicity, when silica-amount between 14 and 58 g/m² are deposited. Due to the excessive amount of silica deposited, the fibers micro-structure was consequently masked and contact angle (CA) analysis effectively sampled a slightly structured silica surface.[208]

The following open research questions have been identified:

- How does fiber architecture (nanoscale porosity) influence water flow in paper sheets?
- Can nanoporosity in paper be adjusted by (mesoporous) silica coatings and how do process parameters allow variation of coating content.
- Is a stimuli-responsive switching from hydrophobic to hydrophilic possible on silica coated paper in analogy to silica free papers?
- Is it possible to locally control coating amount and does the silica coating distribution influence transport (fluid flow) in paper?

4. Aim and Strategy

Based on the mentioned open research questions (chapter 3) this work has been divided into three sub-projects. The first part involves the fabrication of mesoporous silica films via the evaporation induced self-assembly (EISA) process using gravure printing and the comparison to dip-coated films. Different precursor solutions or inks are used. Thereby gravure printing bares the potential for automated and fast mesoporous film preparation (chapter 6.1). The second sub-project focuses on the polymer functionalization of mesoporous silica films being compatible with surface plasmon initiations on planar gold films and thus being initiated using visible light and especially red light with a wavelengths of 633 nm. As polymerization methods the free radical dye-sensitized polymerization as a two-component initiating system is explored and a transfer to a near field mode induced polymerization is discussed (Chapter 6.2). The third sub-project investigates the effect of silica coating on lab made paper sheets. Two different fiber types are explored. The wetting behavior of silica coated paper and redox responsive polymer functionalized silica coatings in paper is investigated with contact angle measurements and water imbibition tests giving new insights into the role of mesoporosity and wettability on fluid imbibition in paper (Chapter 6.3). In the following, the aim of the projects is explained and the individual strategies are presented in more detail.

4.1. Strategies for Mesoporous Silica Film Preparation

To enable automated and fast printing of mesoporous silica films on large scale and keeping the option of multilayer formation using different inks gravure printing is a potentially suitable method. In general, gravure printing is a powerful tool for thin film preparation with the opportunity to print well-defined multiple layers. In gravure printing, the sol-gel solution is serving as ink and is transferred by a gravure cylinder with definite cell volume to the supporting substrate.

The influence of process parameters such as cell volume of gravure cylinder or printing force on film characteristics such as layer thicknesses has to be investigated and compared to classical film preparation via dip coating. A comparison of the films produced using different coating processes is discussed regarding pore accessibility based on ionic permselectivity and film morphology. Furthermore, multi-functional architectures should be generated by means of multiple subsequent coating steps. To induce functional hierarchy, the in-situ functionalization using a co-condensate in the sol-gel solution is used. 3-[Bis(2-hydroxyethyl)amino]propyl-triethoxysilane is used as co-condensate, since it can be used as a coinitiator for the dye-sensitized polymerization described in the chapter 5.1. Furthermore, the post-grafting

functionalization with the coinitiator is examined and a comparison is sought. The functionalization is characterized by means of cyclic voltammetry, ellipsometry and XPS. An overview of the strategy is depicted in **Figure 5**.

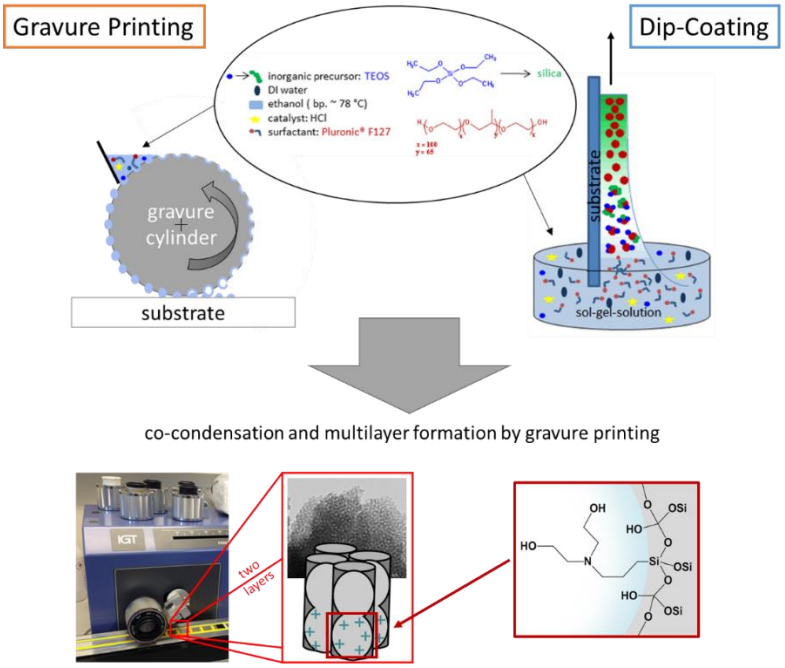

Figure 5. Strategy for film preparation of mesoporous silica films and a molecular functionalization of these. Figure adapted from N. Herzog *et al.* in RSC Adv. 2019, 9, 23570-23578 used by CC BY.

The optimized and fully characterized films are used as a basis for the next main part of this work (chapter 6.2).

4.2. Strategies for Polymerfunctionalization of Mesoporous Silica Films with Visible Light or Near-field Modes

To allow surface-plasmon initiated polymer functionalization of mesoporous silica films on planar gold layers a suitable polymer functionalization strategy based on visible light and surface plasmons with a wavelength around 633 nm has to be identified (**Figure 6**) and systematically investigated with respect to its potential of polymer amount and location control.

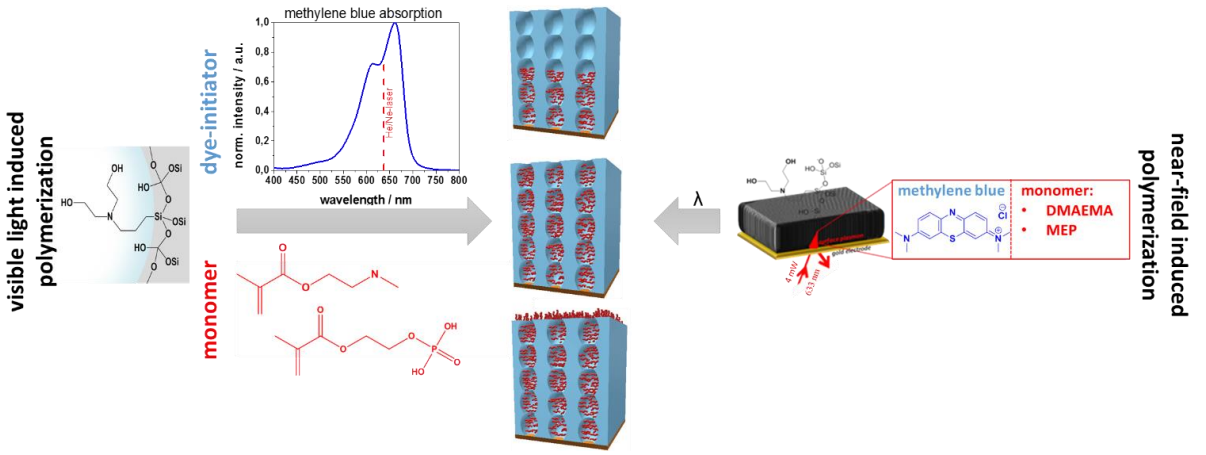

Figure 6. Polymer-functionalization of mesoporous silica films with dye-sensitized polymerization induced by visible light (red light) and near-field modes.

Dye-sensitized polymerizations at a wavelengths of 663 nm (red light) is used and applied to the polymer functionalization of different mesoporous silica films with 2-(Dimethylamino)ethylmethacrylat (DMAEMA) and 2-(methacryloyloxy)ethyl phosphate (MEP) as monomers. To gain a basic understanding of the dye-sensitized polymerization the polymerization is investigated in solution. The reaction parameters are subsequently transferred to the polymerization in the mesoporous silica films. Two different light sources are used. Firstly, a LED light, which can be used for a comprehensive polymer functionalization in mesoporous silica films is used. Secondly, a He/Ne laser which is suitable for surface plasmon generation at planar gold surfaces in the Kretschmann configuration is used (**Figure 10**). With both light sources different parameters like polymerization time, light intensity, monomer concentration can be investigated. In addition, the difference between the polymerization in the pores and outside on the planar mesoporous film surface can be observed. This is realized by CO_2 plasma treatment of the coinitiator functionalized mesoporous silica before polymerization resulting in destruction of the coinitiator at the outer silica surface. Finally, surface plasmon- and transversal optical waveguide mode initiation of the polymerization is investigated. As the surface plasmon has a limited penetration depth the potential for a control of functionalization in z-direction is given. Parameters favoring potential nanoscale local limitation of polymer grafting from initiated by surface plasmons such as polymerization time and laser beam power are investigated.

4.3. Silica-Paper Hybrid Materials

To get insights into and to control the role of the fiber nanoporosity on fluid transport in paper mesoporous and nonporous (dense) silica coatings are used. Therefore, paper sheets are dip-

coated with a sol-gel solution containing with a mesopore forming template to generate mesoporous silica functionalization or using a sol-gel solution without template to get a dense silica coating (**Figure 7**).

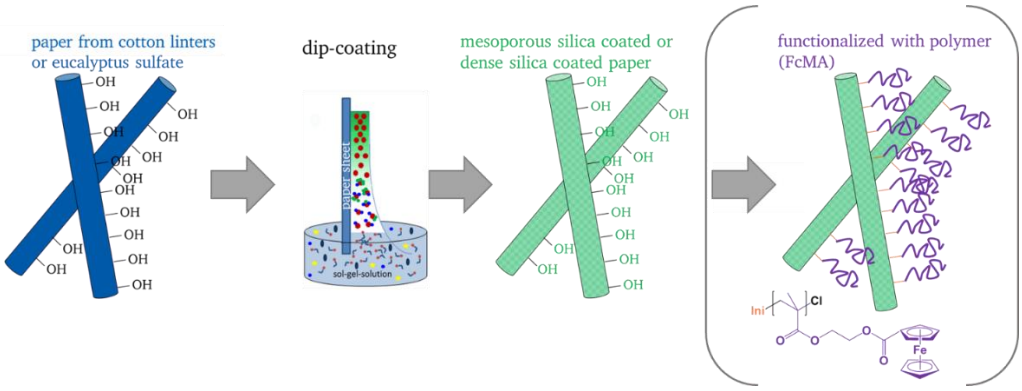

Figure 7. Functionalization of paper sheets from cotton linters or eucalyptus sulfate by dip-coating with sol-gel solution with mesoporous or dense silica. Silica coated paper sheets from cotton linters are further functionalized with a redox-active polymer FcMA.

In a first study cotton linters fibers are coated. To not only understand the effect of mesoporous versus nonporous coatings but as well the possibility of switching wettability and thus fluid imbibition further functionalization using a redox-responsive polymer (cooperation with Prof. Gallei (Universität des Saarlandes). The redox switchable polymer is grafted from the surface using surface-initiated atom transfer radical polymerization (SI-ATRP). In SI-ATRP, a controlled radical polymerization according to the grafting from principle is carried out from a surface previously modified with initiator. The functionalized papers are analyzed concerning wetting behaviors, water sorption tests and morphology. In addition, the coating process using dense silica is transferred to eucalyptus sulfate fibers varying TEOS concentration and drying conditions to vary silica material distributions along the paper cross section. Therefore, vacuum and atmospheric pressure during drying is used. Material distribution is shown with imaging procedures, by name fluorescence microscopy. A first application example in the form of an oil/water separation membrane for silica-coated papers is to be realized. This part is done in close collaboration with Dr. M. Nau.

5. Methods

The following chapter describe the type of polymerization and measurement methods as well as data evaluation procedures used in this thesis are briefly introduced.

5.1. Dye-Sensitized Polymerization

Many different initiators for the photoinitiation of polymerizations have been developed. They mainly differ in the number of components required for initiation, and their absorption wavelength. Most photoinitiated polymerizations are radical polymerizations and they can be classified into one-component initiators and multi-component initiators. Dye sensitized polymerizations, applied in this work, are multi-component free-radical photopolymerizations. They require a dye and a coinitiator, e.g. methylene blue and 3-[Bis(2-hydroxyethyl)amino]propyl-triethoxysilane.

In case of one-component initiators, the radical formation and thus polymerization initiation is induced by the absorption of a photon. In contrast, the multicomponent initiation requires two or more species to initiate the polymerization: An initiator which is excited by the absorption of a photon and subsequently reacts in a redox reaction with a so-called coinitiator. By this a coinitiator radical is generated, which then initiates the polymerization and thus reacts with the monomer.

With respect to the initiation wavelength, common photoinitiators such as benzophenone, azobisisobutyronitrile (AIBN) or diaryliodonium salts absorb UV light. However, this is disadvantageous because high energy decomposition processes can occur in the polymers for example. An advantage is a variety of lasers with defined wavelengths in the visible range available. In addition, natural light sources such as sunlight can be used. Within the last years increasing activity in developing visible light initiated polymerizations is observed. Examples are reported for atom transfer radical polymerization (ATRP)[209, 210], iniferter-initiated polymerizations[211-213] and visible light mediated ring-opening metathesis polymerization (ROMP).[214, 215] The advantage of visible light-induced polymerization is the avoidance of the side reactions that can caused UV light irradiation.[216] Appropriate photoinitiators for the visible spectral range (> 400 nm), dye-sensitized polymerizations have been demonstrated.[123, 217, 218]

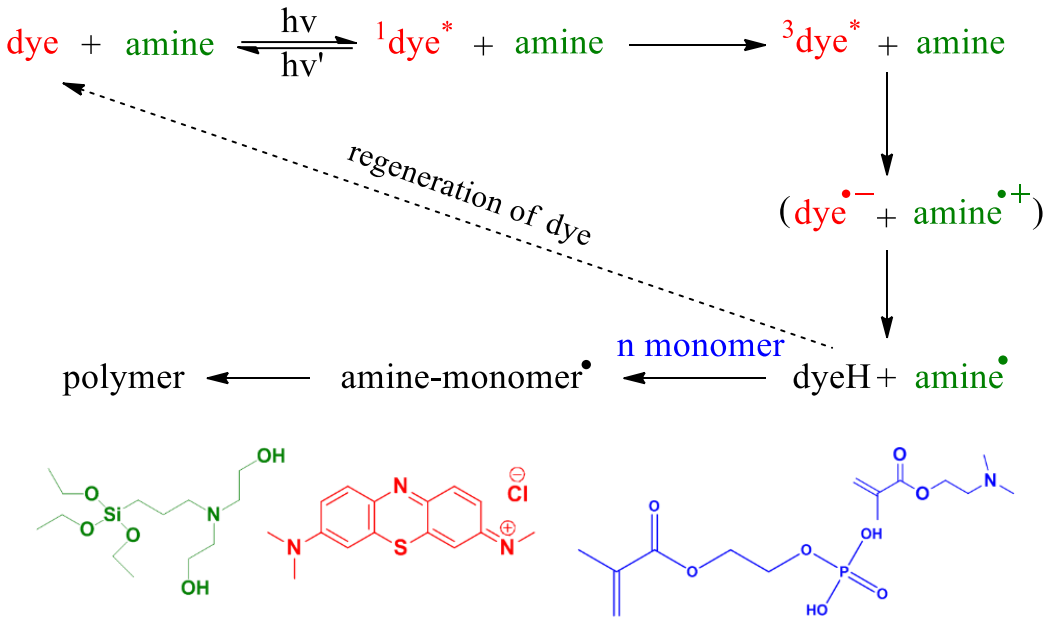

Figure 8. Visible-light activated initiation mechanism of a two-component intiator with methylene blue as a light-absorbing photosensitizer and 3-[Bis(2-hydroxyethyl)amino]propyl-triethoxysilane located on mesoporous silica surface as coinitiator. As monomers the pH-responsive molecules 2-dimethylaminoethylmethacrylate (DMAEMA) and 2-(methacryloyloxy)ethyl phosphate (MEP) are used in this work.

In this work a dye-sensitized polymerization as a two-component initiator which can be initiated using red light is used. The corresponding mechanism, as explained by Kim *et al.*, and summarized in **Figure 8**.[219] The dyes (in this work methylene blue) absorb visible light resulting in an excited electronic state. In this excited electronic state (S1) the dye can either relax to the ground state by emitting electromagnetic radiation of the wavelength, correspondent to the absorbed one. or a non-radiative transition from the electronically excited singlet state (S1) into the electronically excited triplet state (T) occurs. This is called intersystem crossing. In the triplet state the dye can undergo a redox reaction with a tertiary amine. Caused by the electron transfer the generated photoreduction of the dye leads to a semi reduced dye and to the protonated semi reduced dye. The latter represents the colorless leuco form of the dye. Further on, the semi oxidized form of the tertiary amine is formed. By elimination of a proton from the neighboring methyl group, the polymerization initiating form of the tertiary amine is achieved. The leuco form of the dye disproportionate on one hand to the original dye and on the other hand the double protonated dye.

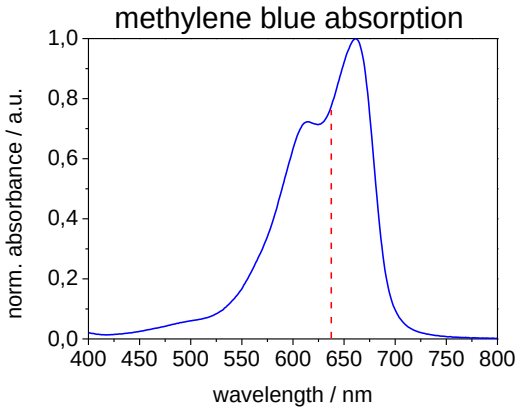

Figure 9. UV-Vis spectrum of methylene blue in 0.1 M aqueous $NaHCO_3$ solution (pH 9). The red line shows the wavelength of the red light He/Ne laser (λ=632.8 nm) used for the polymerizations.

The polymerization should take place at the pore wall within mesoporous silica. A surface initiation is used which means the coinitiator /tertiary amine) has to be covalently bound to the mesopore wall. The dye component methylene blue has been chosen due to its absorption wavelength of 550-700 nm being compatible with a red He/Ne laser (632.8 nm). Methylene blue (red) has a maximal absorption in 0.1 M aqueous $NaHCO_3$ solution at 660 nm as showed in **Figure 9**. As monomers (blue) N, N-dimethylaminoethyl methacrylate (DMAEMA) or phosphoric acid 2-hydroxyethyl methacrylate ester (MEP) are used.

5.2. Surface Plasmon Resonance

Surface Plasmon Resonance Spectroscopy (SPR) is based on the generation of surface plasmons (SP). These are electromagnetic waves that propagate along the interface between a metal and a dielectric. In classical view, plasmons correspond to electrons that oscillate relative to positive ions. SP are described by an exponentially decaying evanescent field perpendicular to the metal (here gold) surface. SP are excited in metals like gold or silver when irradiation with electromagnetic waves is performed at an angle greater than the angle of total reflection. In addition, certain resonance conditions like the incoming electromagnetic wave and the OP need the same wave vector. The wave vector of the SP is described as follows based on the Maxwell equations.[220]

$$k_{x,SP} = \frac{\omega}{c}\sqrt{\frac{\varepsilon_m \varepsilon_d}{\varepsilon_m + \varepsilon_d}}$$

$k_{x,SP}$ = wavevector

ω = angular frequency

c = speed of light

ε_m = dielectric constant of the metal

ε_d = dielectric constant of the dielectric

However, since the momentum of the OP is always greater than the wavevector of the incoming beam in water or air, a special configuration must couple the incoming beam to equalize the momentum. This is made possible, for example, by the Kretschmann configuration, as used in this work. In this case, a prism with optically higher density (refractive index) than that of the air is positioned on the gold-coated glass surface. The higher refractive index of the prism reduces the speed of the light. When the resonance conditions are satisfied, photons interact with the electron gas of the metal layer and an OP is generated. In this case, the excitation of plasmon is possible only with p-polarized (TM: transversely magnetic) light whose electric field is perpendicular to the plane of incidence. The excitation does not proceed with s-polarized (TE: transversely electric) light. The generation of plasmons in the Kretschmann configuration depends on the angle of incidence of the incoming beam and is related to its wave vector.[221]

$$k_{x,Ph} = \frac{\omega}{c}\sqrt{\varepsilon_{prism}}\sin\theta_i$$

$k_{x,Ph}$ = wavevector of photon

ω = angular frequency

c = speed of light

ε_{prism} = dielectric constant of the prism

θ_i = angle of incidence

From this, the resonance condition at a certain angle of incidence is satisfied and surface plasmons are generated at a fixed angular frequency. As already described above, the resonance angle of the OP is greater than the angle of total reflection. Upon the arrival of the laser beam, a part of it is refracted at the interface between the media of different optical density and a part of the beam is reflected at the same angle as the angle of incidence ($\theta_r = \theta_i$). The angle of total reflection can be described by Snell's law using the following equation.

$$\sin\theta_t = \frac{n_1}{n_2}\sin\theta_i$$

θ_t = angle of the transmitted light

θ_i = angle of incidence

n = refractive index of medium i

The angle dependence of the reflection and the transmission can be described in the context of the different refractive indices of the two media and the angle of the transmission with the ratio of the reflected component and the ratio of the transmitted component of p-polarized light.

$$r_P = \frac{n_2\cos\theta_t - n_1\cos\theta_i}{n_2\cos\theta_t + n_1\cos\theta_i}$$

$$t_P = \frac{2n_1\cos\theta_t}{n_2\cos\theta_i + n_1\cos\theta_i}$$

The generation of SP leads to a weakened intensity of the reflected beam and thus to a lowering of the reflectivity in the angular spectrum, since the light is conducted into the SP. As above described, the resonance condition of an SP is dependent on the refractive index of the medium to be analyzed. Therefore, any change in the optical density of the medium over the metal surface in the depth of penetration of the SP affects its wave vector and eventually results in a shift of the resonance angle. Therefore, the SPR is extremely sensitive to changes near the metal surface. A change in the refractive index in the evanescent field of the SP results according to the Fresnel equation to a change in reflectivity. The penetration depth of an SP is smaller than the irradiated wavelength and can be described in the case of total reflection with the following equation.

$$d_P = \frac{\lambda}{2\pi}\sqrt{\frac{n_1^2}{n_2^2}\sin\ ^2\theta_i - 1}$$

d_P = penetration depth

θ_i = angle of incidence

λ = wavelength

n = refractive index

Thus, the SRP is suitable for characterizing optical properties of thin films on metal surfaces without destroying them. With the surface plasmon resonance spectroscopy layer thickness increases or decreases can be detected. The SPR setup is schematically depicted in **Figure 11**. Light is focused on the metal film, after passing the prism and the subsequent reflection is detected. At a certain angle of incidence (resonance angle), the surface plasmons resonate with

the light, resulting in absorption of light and thus decreasing intensity within the reflected beam. The surface plasmon shows a field enhancement which means the calculation of the electric field transfer coefficient based on Fresnels equation shows that the electric field on the low index metal side can be much larger than that on the other side of the metal layer. It is noted that the intensity can be increased very close to the angle of SPR by a factor of more than 30. This is expected to strongly influence plasmon initiated polymerization. [222]

If the thickness of a dielectric layer, here a mesoporous film, on a metal coated substrate is sufficiently thick, optical waveguide mode called transversal mode (TM) are observed at resonance angles below the one of the surface plasmon resonance (**Figure 10**). When using s-polarized light the optical waveguide mode is called (TE) but no surface plasmon is generated.

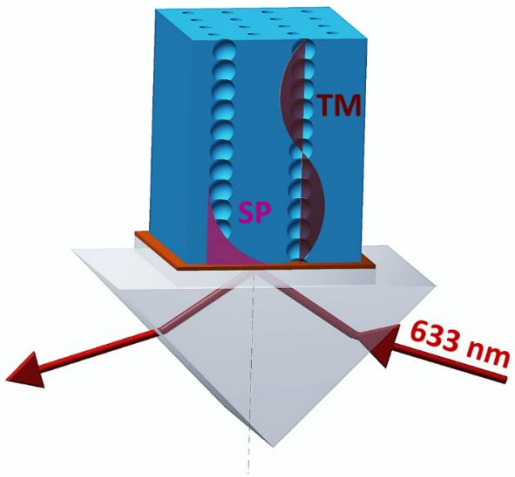

Figure 10. Schematic view of the near-field induced polymerization in the Kretschmann configuration showing surface plasmon (SP) and transversal mode (TM).

In this work the SPR setup depicted in **Figure 11** (RT2005-Spectrometer from Res-Tec) is used. For the measurements the gold coated sample glass slide (n= 1.8449, LaSFN9 glass, Hellma Optik GmbH Jena) is installed into a homemade flow cell (volume ~ 40 μl) and the backside is optically (refractive index) matched with the base of the glass prism using n_D=1,7000 ± 0,0002 index matching oil (Cargille Labs, USA). Monochromatic and linear, transverse-magnetic polarized (Glan-Thompson polarizer, B. Halle) laser light (He/Ne laser, JDSU, 1125P, λ = 632.8 nm) is directed through the prism onto the sample substrate. By variation of the angle of incidence θ (two-cycle goniometer, resolution 0.005°, Huber) and detecting the intensity of the reflected laser light I(θ) with a photodiode (BPW 34B silicon photodiode, Siemens) an angular dependent spectrum is recorded in different sub phases like air, water or polymerization solution.

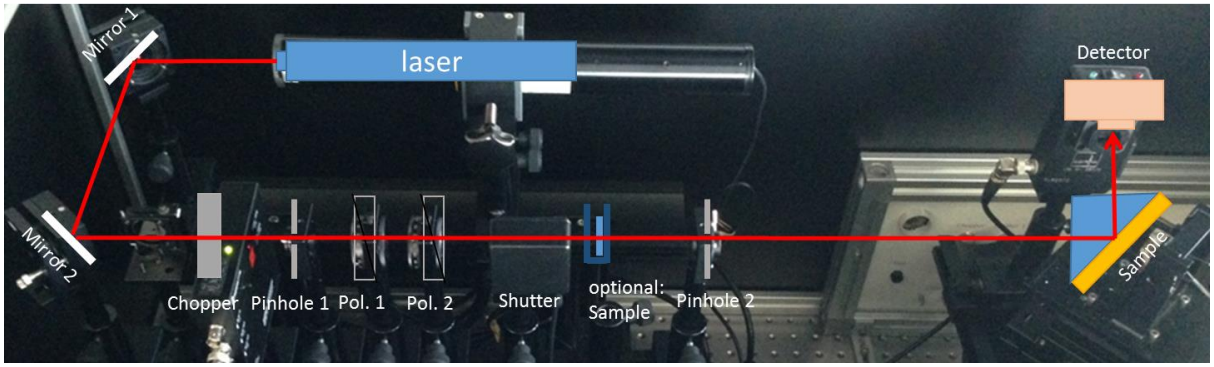

Figure 11. SPR equipment. The laser beam is guided by two mirrors without intensity loss, and directed through a pinhole, a chopper and the polarizer 1 and 2. Polarizer 1 can be used to adjust the intensity of the laser beam. Polarizer 2 regulates the polarization. For example, p- and s –polarized light can be generated. Then the laser impinges the sample in Kretschmann configuration (see **Figure 10**) and ultimately the reflected beam reaches detector (photomultiplier). The sample configuration is shown in **Figure 12**.

The sample preparation is in the first step a thermal evaporation using a Creamet 300 V2 thermal evaporation system (Creavac, 01159 Dresden) of 5 nm chromium on LaSFN9 glass as an adhesion layer followed by a 50 nm gold deposition. The uncoated side of the substrates is covered with sticky tape while dipcoating the sol-gel solution to prepare mesoporous silica like described in experimental section (chapter 8.3). The literature values of the different layers are shown in **Figure 12**. The refractive index of the polymerization solution is measured with a refractometer (AK Prof. Dr. Reggelin, TU Darmstadt) at 589 nm and 20 °C. Also the dielectric constants are given in this figure. They can be calculated by the squares of refractive index.

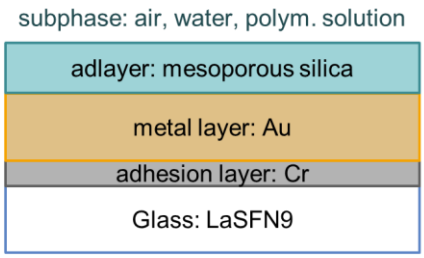

layer	refractive index	ε'	ε''
LaSFN9	1.8449	3.4035	1.5264e-7
chrome	3.1395	-1.1342	20.817
gold	0.18344	-11.753	1.2596
silica (dense)	1.4570	2.122849	-
air	1	1	-
water	1.3317	1.7734	3.9151e-8
polymerization solution	1.3655	1.8649	-

Figure 12. Sample preparation. The optical glass LaSFN9 is coated with chrome as adhesion layer, then the metal layer consisting of gold covered with the mesoporous silica coating. As subphase air, water or polymerization solution is used. in the table the refractive indices of LaSFN9, chrome, gold, dense silica, air, water and polymerization solution are given as well as the dielectric constants ε' and ε'' ($n^2 = \varepsilon$).[223-225]

The procedure for the near-field mode-induced polymerization is shown in **Figure 13**. First the spectrum of a coinitator functionalized mesoporous silica film is measured in contact with air. Subsequently, water is introduced into the cell with a speed of 5 μL/s for approximately 30 minutes followed by recording an angular spectrum. In the following step the polymerization solution is flown into the cell and a fast scan (low amount of measurement points, 0.5 ° steps)

of the spectrum is performed to determine the resonance angle of potential waveguide modes and the surface plasmon. This is important to determine the angle used for polymerization. The sample is subsequently positioned at the chosen polymerization angle and the polymerization is performed. Afterwards the cell is rinsed with water for approximately 30 minutes and a spectrum against water is recorded. The sample is removed from the setup, extracted with water, dried with pressed air and installed in the same way for the recording of a spectrum again in contact with air after polymerization. In addition, samples are characterized by ATR-IR spectroscopy where the C=O stretching vibration at around 1730 cm^{-1} in a Si-O-$Si_{asym.}$ (1070 cm^{-1}) normalized spectra is analyzed to verify polymer functionalization as shown in **Figure 13**b.

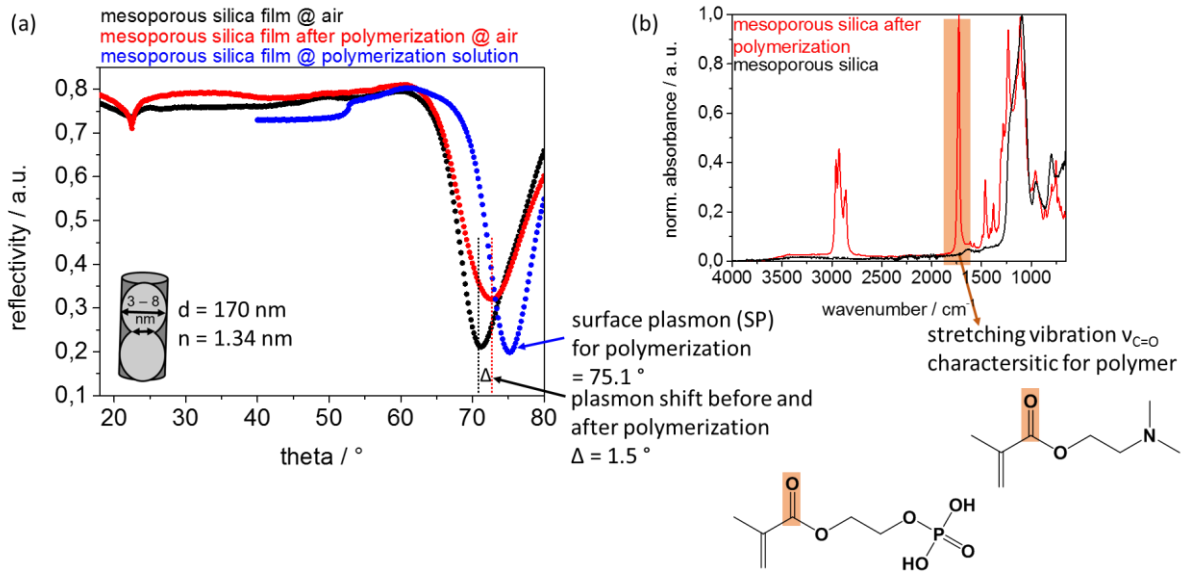

Figure 13. a) SPR spectra of mesoporous silica functionalized with coinitiator measured against air (black, d = 170 nm and n = 1.32), and against polymerization solution (blue) to find the SP for polymerization and mesoporous silica after polymerization, as well as after polymerization and extraction against air (red). The shift of the SP resonance angle between upon polymerization is indicated by the dotted lines. This resonance angle shift to higher angles indicates the change of refractive index and film thickness upon polymerization. b) Additional sample characterization by ATR-IR. Spectra between 4000 and 650 cm^{-1} before polymerization (black) and after polymerization (red) are depicted. The characteristic stretching vibration for the polymers are the C=O bend at around 1730 cm^{-1} (highlighted in orange).

The calculation of the coupled laser power for SP- or TM-induced polymerization is demonstrated in **Figure 14**. The maximum reflectivity is read at an angle lower than the beginning of surface plasmon or transversal mode while the reflectivity of the SP or TM is read at the minima from the SPR spectrum measured against the polymerization solution containing of monomer and methylene blue in 0.1 M $NaHCO_3$ solution.

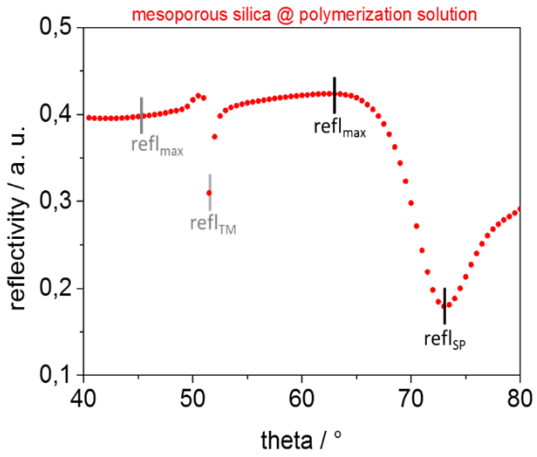

$$coupling\ factor = \frac{ref_{max} - ref_{TM/SP}}{ref_{max}}$$

Figure 14. Exemplary SPR spectrum measured against polymerization solution, showing the position for calculation of coupled laser power. The formula is given next to the spectra.

The laser/light power is important to deduce the available energy for surface plasmon generation and thus for polymerization. This power is measured using a THORLABS PM100A Optical Power Meter after passing the two polarizers 1 and 2 (**Figure 15**). During the measurement polarizer 2 is set constant at 90° which leads to p-polarized light. Polarizer 1 is adjusted which leads to a change in light power coupled onto the sample.

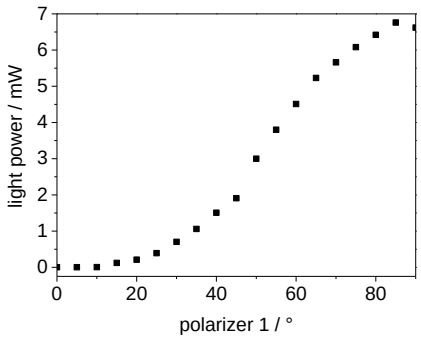

Figure 15. Laser intensity in dependence of polarizer 1, when polarizer 2 is constant at 90° (p-polarized light). Further details in SPR set-up are given in **Figure 11**.

5.3. Cyclic Voltammetry

Cyclic voltammetry is an electrochemical method in which the current at an electrode is measured at varying voltage. The method is used in the elucidation of electrochemical reaction mechanisms, for the determination of redox potentials of molecules, or for determining the kinetics of electron transfer processes.[226, 227] The general cyclic voltammetry measurement setup is composed of three electrodes: working electrode where the electrochemical processes of interest takes place, the reference electrode for measuring the true voltage and the counter

electrode, which compensates for the difference between the measured voltage and the applied voltage. A general overview of cyclic voltammetry is given by Bard and Faulkner and especially for cyclic voltammetry in mesoporous silica the work of Walcarius and co-workers is recommended to the interested reader.[89, 227, 228]

In this work cyclic voltammetry is used to determine the accessibility of mesoporous coatings for small, redox-active probe molecules. Therefore, the substrate located below the mesoporous film which is coated with a conductive layer such as indium tin oxide (ITO) is used as working electrode. The measurement requires a redox-active molecule, here usually $[Fe(CN)_6]^{3-/4-}$ and $[Ru(NH_3)_6]^{2+/3+}$, and a conducting electrolyte, here usually 100 mM KCl. If the voltage at the working electrode is increased, and the redox probe molecule diffuses through the mesoporous film and reaches the electrode, the probe molecule is reduced and the current increases resulting in a maximum current at a certain voltage within the CV. At the potential of the maximum current (E_{pc}), the entire amount of redox active molecule is reduced at the electrode, and a diffusion layer of the reduced molecules forms at the electrode. As a result, less molecules can be reduced and the current decreases reaching an equilibrium state at which the transport of molecules to the electrode determines the detected current. The potential at the working electrode is reversed and the oxidation of the redox probe molecules starts (**Figure 16**, point d). The processes are repeated with the oxidation minimum at point E_{pa} till the starting point (**Figure 16**).

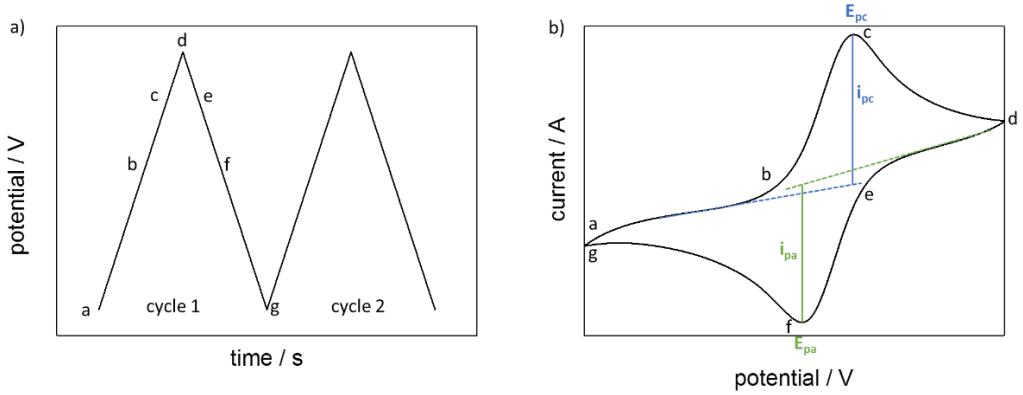

Figure 16. a) Time dependent applied triangle voltage at the working electrode and b) the resulting cyclic voltammogram showing the peak currents E_{pc} and E_{pa}.

The cyclic voltammograms are recorded at different voltage scanrates ν which can provide information about the nature of the molecular transport process. First, the redox-active molecule must reach the electrode, by mass transport, which includes diffusion, convection, and migration. Electron transfer from the redox-active molecule to the electrode can then take place at the electrode. Characteristics in the cyclic voltammogram can help to clarify which

process has the largest contribution to the measured current intensity. A distinction can be made between three cases: the reversible, the quasi-reversible and the irreversible case.

The dividend of the peak currents (I_{red}/ I_{ox}) is 1. The root of the scanrate $\nu^{1/2}$ plotted against the peak currents ($I_{red/ox}$) increase linearly and obeys the Randles-Ševcik equation. With the Randles-Ševcik equation, the slope of the line can be used to determine the diffusion coefficient (D). The other sizes are known.

$$I_P = (2{,}69 \cdot 10^5) \cdot n^{\frac{3}{2}} \cdot A \cdot D^{\frac{1}{2}} \cdot c_i \cdot \nu^{\frac{1}{2}}$$

I_P = current peak for oxidation or reduction [A]

n = number of unreacted electron per molecule

A = surface of the electrode [m2]

D = diffusion constant [m2/s]

c_i = concentration of redox-active molecule [mol/L]

ν = scanrate [V/s]

In the irreversible case, the charge transfer at the electrode is very slow and thus affects the current. Because of the slow charge transfer, molecules can diffuse away from the electrode surface and are no longer available for charge transfer. This widens the distance of the peak potentials (ΔEp) and in some cases only a peak potential is present. In this case the ΔEp > 59/n mV because there is a dependence on the scanrate ν. The peak of the reverse reaction may be missing, so there is possibly only an oxidation or a reduction. The extended Randles-Ševcik equation applies, in which the transfer coefficient α is introduced.

In the quasi-reversible case, the rate of mass transport and charge transfer is of the same order of magnitude. Thus the current strength depends on both processes. At low voltage scanrates, the curve is similar to the reversible case, and at high voltage scanrates, it becomes irreversible.

In the reversible case, the electron transfer is so fast that the current depends on the slower mass transport and is thus diffusion-controlled. Thus, the surface concentration depends only on the potential and it applies the Nernst equation. The peak potential ($E_{red/ox}$) is independent of the voltage scanrate ν. The potential difference is not greater than $\Delta E = | E_{red} - E_{ox} | =$ 59/n mV with n as the number of transmitted electrons.

$$E = E° + \frac{RT}{zF} log \frac{[oxidation]}{[reduction]}$$

E = potential [V]

E = potential [V]

E° = standard potential [V]

R = gas constant (8,31446 J/mol)

T = temperature [K]

F = Faraday constant (96485,34 J/Vmol)

Z = number of transferred electrons

[oxidation]/[reduction] = concentration of the corresponding molecule [mol/L]

For the cyclic voltammetry measurements Autolab PGSTAT302N (Metrohm) is used. For the measurements, the indium tin oxide (ITO) coated glass substrate on which the mesoporous films are deposited is used as the working electrode. Furthermore, two more electrodes are used, a silver / silver chloride electrode (BASi RE-6) as a reference electrode and a graphite electrode as a counter electrode. The measured electrode area is 0.21 cm^2. For pore accessibility two differently charged complexes are used. As a negatively charged complex, potassium hexacyanoferrate ($K_3[Fe(CN)_6]$) and as a positively charged complex hexaaminruthenium chloride ($[Ru(NH_3)_6]Cl_2$) are used. The measurements are carried out with different scanrates ν in the order of 200 mV/s, 100 mV/s, 25 mV/s, 300 mV/s, 1000 mV/s, 200 mV/s. The voltage feed rates of 200 mV/s are measured at the beginning and at the end, and the cyclic voltammograms are only used if they nearly agree. For the determination of the ionic permselectivity, the I_{ox} of 100 mV/s is used. In the films, the influence of the amount of polymer on the ionic permselectivity is examined. The used complexes are dissolved in 0.1 M aqueous potassium chloride solution and thus have a concentration of 1 mM. The appropriate pH is adjusted with sodium hydroxide or hydrochloric acid and checked with pH electrode.

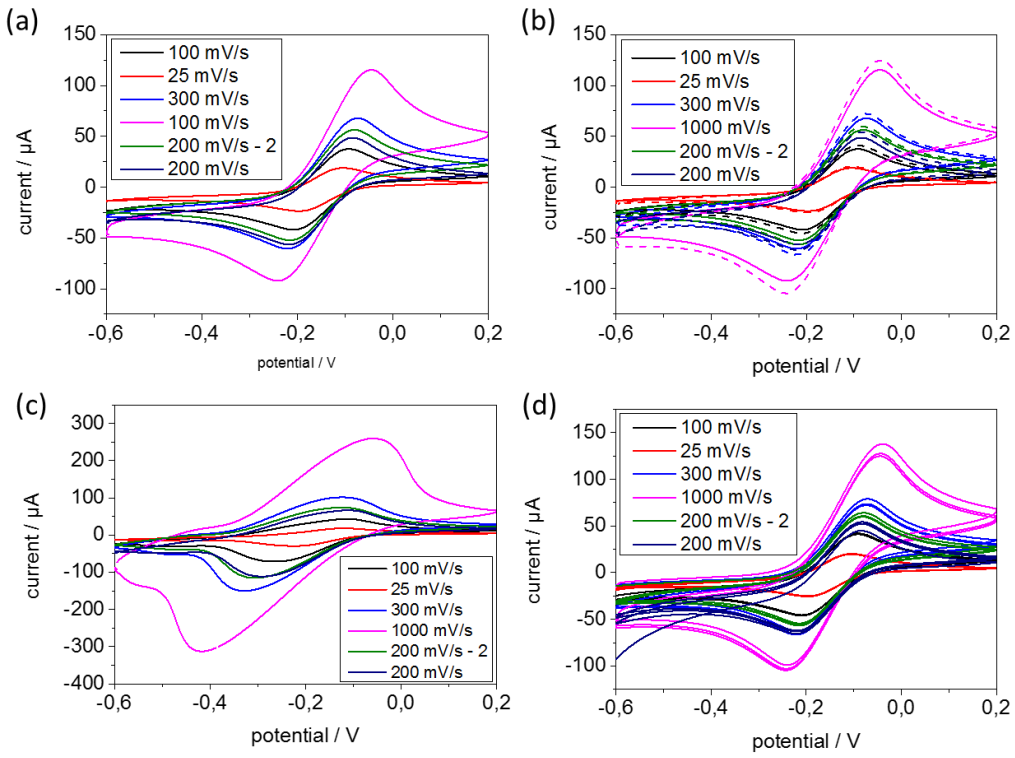

Figure 17. Exemplified qualitiy control in cyclic voltammetry measurements of mesoporous silica. a) Showing the different scan rates measured at pH 3. b) Showing the cyclic voltammograms for all measured scanrates at pH 3 before (line) and after (dashed line) measuring the same scanrates at pH 9. The obtained CV before and after measuring pH 9 are comparable and CV data is only discussed if this is the case. c) Showing the different scan rates including 200 mV/s as first and last scan in basic conditions at pH 9. d) Showing all three cycles measured for each scan rate. Usually the third cycle is shown after validating that the three cycles are comparable. Figure adapted from N. Herzog *et al.* in RSC Adv. 2019, 9, 23570-23578 used by CC BY.

Exemplified qualitiy control in cyclic voltammetry measurements of mesoporous silica dip-coated with 2 mm/s withdrawal speed on ITO coated glass substrates is systematically shown in **Figure 17**. The measurements are performed with 1 mmol $[Ru(NH_3)_6]^{2+/3+}$ dissolved in 0.1 M KCl at pH 3 (**Figure 17**a, b, d) and pH 9 (**Figure 17**c). For all pH values and probe molecules the mentioned scanrates are measured. Thereby, the scanrate 200 mV/s is measured twice at the beginning and at the end after cycling all scan rates three times. Both cyclic voltammograms at this scan rate are very comparable and CV data is only discussed if this is the case (**Figure 17**a and c). In **Figure 17**b cyclic voltammograms measured at pH 3 before (line) and after (dashed line) measuring the same scanrates at pH 9. The obtained CV before and after measuring pH 9 are comparable and CV data is only discussed if this is the case. **Figure 17**d showing the tree cycles of each measured scanrates. Usually the third cycle is shown after validating that the three cycles are comparable.

5.4. Ellipsometry

Ellipsometry is a non-destructive optical method and is used for examining the physical properties, namely the refractive index and the layer thickness of mesoporous films. From the determined refractive indices, the porosities and pore filling after functionalization can be determined based on the Bruggeman approximation.[229] For this purpose, it takes advantage of the fact that the state of polarization of light changes when it is reflected at a surface, especially at silicon wafer substrates. Light can be described as an electromagnetic wave and has a specific frequency or wavelength. The phase and amplitude of two different light waves, passing through a material, can overlap. This may result in different polarizations. If the phase of the oscillation in the x and y directions is equal, the resulting ellipse degenerates into a straight line. A circle is created when the phase shift is exactly ± 90 °. In summary, linear and cyclic polarizations are a special cases of elliptical polarization.[230] The analyzer is rotated so that the light intensity is minimal. From the polarizer and analyzer setting, with minimum intensity, the angle of the phase shift Δ and the amplitude change Ψ can be calculated. Reflecting the light at the surface, some of the light is refracted and Snell's law allows the reflection coefficients of the vertical (r_s) and parallel (r_p) polarizations to be expressed as:

$$r_{01p} = \frac{n_1 \cos(\alpha) - n_0 \cos(\beta)}{n_1 \cos(\alpha) + n_0 \cos(\beta)} \; or \; r_{01s} = \frac{n_0 \cos(\alpha) - n_1 \cos(\beta)}{n_0 \cos(\alpha) + n_1 \cos(\beta)}$$

These equations apply to every interface. In this case, only the boundary layer between air and porous layer (r_{01p}/r_{01s}) is shown. For a single-layer model with two boundary layers (air / porous layer and porous layer / substrate, **Figure 12**, chapter 5.2):

$$R_p = \frac{r_{01p} - r_{12p} e^{-i2\Delta}}{1 + r_{01p} r_{12p} e^{-i2\Delta}} \; or \; R_s = \frac{r_{01s} - r_{12s} e^{-i2\Delta}}{1 + r_{01s} r_{12s} e^{-i2\Delta}}$$

From the measured data, the intensity of the laser beam, for the phase shift of the incident and reflected light Δ and the amplitude ratio Ψ the layer thickness and refractive index of the measured layer is determined by applying the model analysis. The model analysis is based on a layer model, which determines the refractive index and the film thickness of each individual layer. There exist formulas which relate those angles to the ellipsometric angles Ψ and Δ. For the evaluation of the measurement, only these values are used with Δ being the difference of the phase shifts of the vertical and parallel components of the incident (δ_i) and reflective (δ_r) light:

$$\Delta = \delta_i - \delta_r = 2\pi \frac{d_1}{\lambda} \sqrt{n_1^2 n_0^2 \sin^2 \alpha}$$

The second ellipsometric angle can be derived from the Fresnel equations as:

$$tan\psi = \frac{|R_p|}{|R_s|}$$

where Rp is the reflectivity of the p-polarized component of the incident light and Rs the one for the s-polarized component. The fundamental equation of ellipsometry relates Ψ and Δ:

$$e^{i\Delta} \cdot tan\psi = \frac{R_p}{R_s} = \rho$$

If the trajectory of Ψ versus Δ is plotted at a set angle θ, a known wavelength of the incident light λ, and a known refractive index of the surrounding medium (n_0) and the substrate (n_2), an ellipsoid graph is obtained. This means, the optical thickness of the layer examined can be calculated with a periodical result to:

$$d = \frac{\lambda}{2\sqrt{n_1^2 - n_0^2 sin^2\theta}}$$

This ambiguity in the result can be overcome if and are measured at multiple angles of incidence of the light beam. The measurement at two or more incident angles also allows the calculation of the refractive index of the layer of interest.

For the ellipsometry measurements a device of the type nanofilm EP3-SE from the manufacturer Accurion is used. For the measurement the software EP4-View as well as EP4-Model is used for the model analysis of the measured data and for the determination of the refractive index and the layer thickness of the sample. Both are also from the company Accurion. This gadget used the nulling ellipsometry, the light generated by a laser with a wavelength of 658 nm is first polarized linearly by a polarizer and then strikes a compensator. This compensator consists of a π/4 plate and generates circularly polarized light, depending on its position relative to the polarizer. The polarizer-compensator combination enables the generation of elliptically polarized light, which is linearly polarized after reflection. This can pass through another polarizer that is used as an analyzer. If the analyzer is in a 90° position to the axis of the linearly polarized light, the light beam is extinguished. A downstream detector consisting of a light-sensitive CCD camera (charge-coupled device) measures the intensity of the light. In nulling ellipsometry, the angles of the polarizer and the analyzer are varied until the intensity of the light in the detector passes through a minimum. Polarizer, compensator and analyzer can be rotated in a range of 360°. Because of this set-up four alignments are possible. This four zones are shown in **Table 1**. The one-zone measurement is four times faster than four-zone measurements.

Table 1. Fourfold zeroing by four-zone measurement in the ellipsometry.

	Ψ	**Δ**	**C**
Zone 1	A	2 P - 90°	45°
Zone 2	-A	-2 P + 90°	45°
Zone 3	A	2 P + 90°	-45°
Zone 4	-A	-2 P - 90°	-45°

*A = analyzer, P = polarizer, C = compensator.

In this work the same measurement conditions are used for all ellipsometry measurements shown in **Table 2**.

Table 2. Conditions for the ellipsometry measurments.

angle range	38-70°
angular steps	2°
method of measuring	one zone
measuring points	3
rel. humidity	15 %

The relative humidity of 15 % can be adjusted by the humidity controller ACEflow from Solgelway in combination with the chamber recreated from Boissiere *et al.*[72]

As a prerequisite, it is determined by a reference measurement of an unmodified silicon wafer that a 2.8 nm thick silicon dioxide layer is present on the Si wafer. On this layer lies the synthesized mesoporous silica layer. For each spectra modeling, a so-called RMSE value is given. This is the mean square prediction error. The smallest possible error value is ideal since then the modeled values best reflect the measured curve. The one-layer model is used for fitting in the ellipsometry software EP4-Model. In the single-layer model, only the layer thickness on the SiOx layer is assumed. Followed by one value for the refractive index and the layer thickness for the mesoporous silica layer. The error bars specified in the discussion of ellipsometry data are composed of the error (not the RMSE value) output by the EP4 model software and the calculated standard deviation. This is valid for non-functionalized mesoporous silica films. Otherwise the same spot before functionalization and afterwards is marked and measured to have the direct comparison with exclusion of inhomogeneities along the mesoporous silica film.

$$standard\ deviation = \sqrt{\frac{1}{N-1}\sum_{i=1}^{N}(x_i - \bar{x})^2}$$

N = number of values (sample size)

x_i = value for the i-th element of the sample

$\bar{x}$ = arithmetic mean of the sample

The Bruggeman effective medium approximation is used to calculate the volume porosity from the fitted refractive index of the mesoporous silica films.[72, 229, 231] Therefore the following relationship between the dielectric constants and volume fraction of each constituent material exists:

$$V_{pore}\left(\frac{\varepsilon_{pore} - \varepsilon_{mesopSilica}}{\varepsilon_{pore} + 2\varepsilon_{mesopSilica}}\right) + V_{silica}\left(\frac{\varepsilon_{silica} - \varepsilon_{mesopSilica}}{\varepsilon_{silica} + 2\varepsilon_{mesopSilica}}\right) = 0$$

where V_{pore} and V_{silica} correspond to the volume fractions occupied by air and silica, and ε_{pore}, ε_{silica} and $\varepsilon_{mesopSilica}$ correspond to the dielectric constants of air, silica, and the mesoporous silica. Furthermore, the relations $V_{silica}+V_{pore}=1$ and $\varepsilon = n^2$ ($n_{air}=1$ and $n_{silica}=1.46$) are valid so it is possible to gain the following formula and the pore volume/porousity can be calculated. [223]

$$V_{pore}\left(\frac{1 - n_{mesopSilica}^2}{1 + 2n_{mesopSilica}^2}\right) + (1 - V_{pore})\left(\frac{2.1316 - n_{mesopSilica}^2}{2.1316 + 2n_{mesopSilica}^2}\right) = 0$$

6. Results and Discussion

In the following chapters the results are discussed divided into three main chapters shown in **Figure 18**.

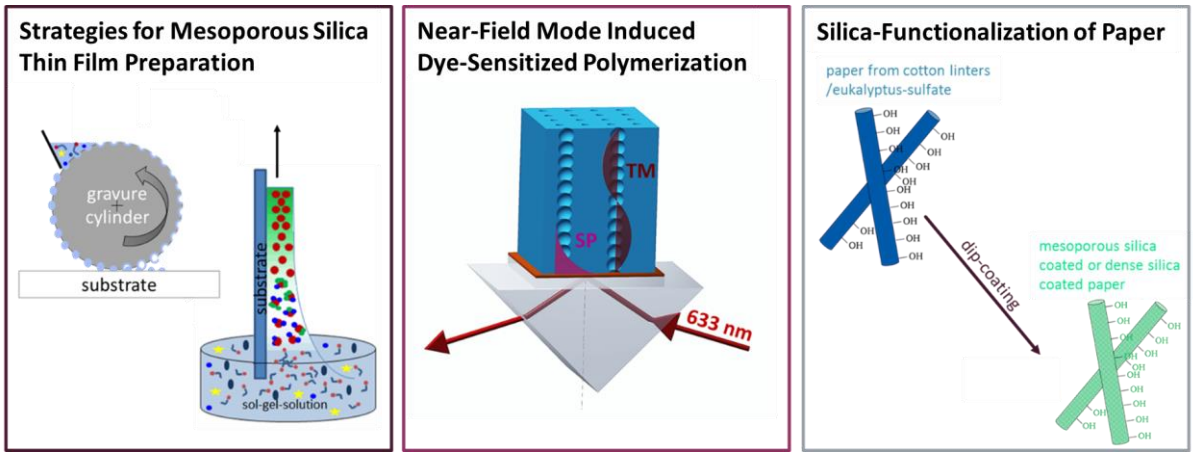

Figure 18. Overview on the three main sub-projects discussed in this chapter.

Chapter 6.1 showing strategies for mesoporous silica thin film preparation comparing dip-coating and gravure printing of mesoporous silica films as well as the in-situ functionalization during silica formation with small molecules during gravure printing. In chapter 6.2 the dye-sensitized polymerization in solution and in mesoporous silica films including the development to near-field induced polymerization by surface plasmon (SP) and transversal modes (TM) is discussed. Chapter 6.3 summarizes the silica-functionalization of paper consisting of two different fiber-types and the investigation concerning water imbibition and silica contribution.

6.1. Strategies for Mesoporous Silica Thin Film Preparation

A procedure for gravure printing of mesoporous films is developed and the two different coating methods for the preparation of mesoporous silica are systematically compared: Mesoporous film preparation by dip coating and by gravure printing. Both film preparation methods are based on the evaporation induced self-assembly (EISA), introduced by Brinker in 1999.[5] Furthermore, the functionalization of mesoporous silica films with the coinitator 3-[Bis(2-hydroxyethyl)amino]propyl-triethoxysilane within a one pot synthesis by co-condensation or within a two-step process via post-grafting is demonstrated as well for gravure printed films.

Parts of this chapter are published in RSC Adv., 2019, 9, 23570-23578.

6.1.1. Mesoporous Silica Preparation via Dip-coating

The mesoporous silica film preparation process combining evaporation induced self-assembly (EISA) and dip-coating is well established and schematically shown in **Figure 1** (chapter 3.1). Thereby, the influence of process parameters such as withdrawal speed, temperature, relative humidity, and composition of the sol-gel solution are systematically controlled and the effect on film characteristics such as film thickness, porosity, pore diameters, and morphology is investigated. When changing the molar ratios between the solvent ethanol, the precursor tetraethyl orthosilicate (TEOS), and the surfactant Pluronic® F127 in the sol-gel solution, the obtained mesopore diameters of the mesoporous silica films change. Two different sol-gel solution compositions have been used resulting in mesoporous silica films with 8 nm maximum pore diameter (small pores) or 16 nm maximum pore diameter (big pores). The formulation for the 16 nm pore diameter films is inspired by Dunphy *et al.* and established by R. Brilmayer for dip-coating. The TEM image (recorded by U. Kunz in AK Kleebe, TU Darmstadt) in **Figure 19**a shows a mesoporous silica film (big pores) with a film thickness of 450 nm. The statistic pore diameter (measuring 20 pores and using the density function of the normal distribution) is calculated with 10.2 ± 1.2 nm. In comparison, the second sol-gel formulation (**Figure 19**b) leads to a mesoporous silica film (small pores) with a thickness of 150 nm and a pore opening diameter distribution of 7.2 ± 0.8 nm. Both films are dip - coated under identical conditions by using a withdrawal speed of 2 mm/s and a climate chamber (50 % RH, 23 °C). The detected film thickness, measured by ellipsometry first decreases with increasing withdrawal speed between 0.1 up to 1 mm/s and then increases with further increasing withdrawal speed for small pore mesoporous films. This observation is in accordance with studies from Grosso *et al.*[77] and Faustini *et al.*[78] which also demonstrate a minimum layer thickness at a withdrawal speed around 0.5 and 1.0 mm/s. This is ascribed to the existence of two different film formation regimes which are dependent on the withdrawal speed. In the capillarity regime at lower withdrawal speeds, the film thickness is governed by evaporation-induced flow. In the draining regime, dominant at higher withdrawal speed the film thickness is mainly dependent on viscous drag flow. The overlapping of both regimes leads to a critical speed and mean minimized layer thicknesses.[79] In accordance with literature, film thicknesses between 60 nm and 400 nm are achieved by dip-coating generating films with maximum 8 nm pore diameter and thickness between 240-1000 nm generating mesoporous silica film with maximum 16 nm pore diameter by varying the withdrawal speed between 0.05 and 30 mm/s as shown in **Figure 19**c.[78] A porosity (pore volume) of 40 - 45 vol% for dip-coated mesoporous silica films for smaller pores and a porosity of 60 vol% for the bigger pores is detected from ellipsometry data (refractive

index) using Bruggeman effective medium approximation (please refer to the appendix, **Table 8** and **Table 9**).

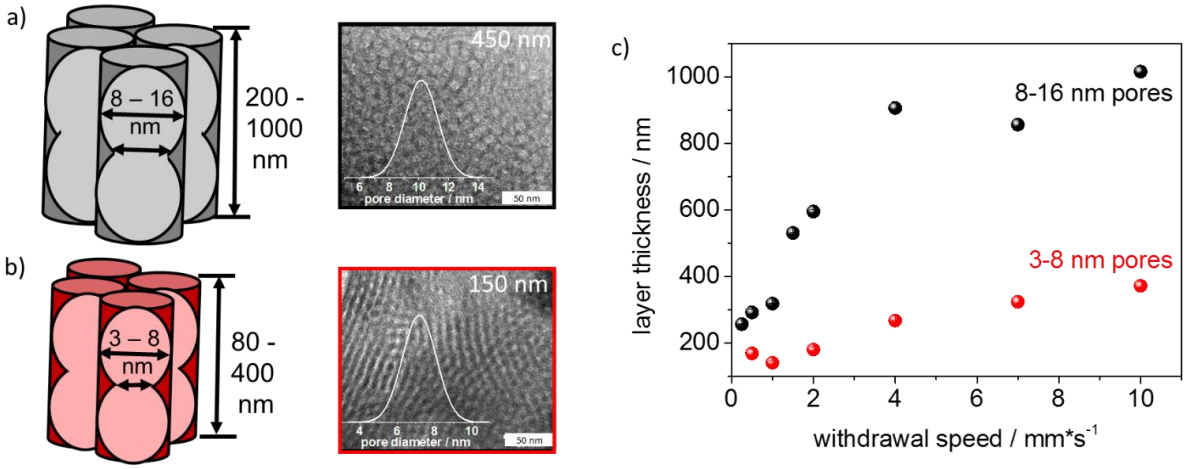

Figure 19. a) TEM image of 8-16 nm pores diameter mesoporous silica films with a statistic pore distribution shown in white. b) TEM image of 3-8 nm pores diameter mesoporous silica film with a statistic pore distribution shown in white. c) Film thickness determined by ellipsometry in dependence of the dip-coating withdrawal speed for 8-16 nm pores (black) and 3-8 nm pores (red). Scale bars are 50 nm in both TEM images.

Functional composition of mesoporous silica films is characterized by using ATR-IR of 350 °C calcinated mesoporous silica films deposited on glass substrates using the two different formulations that lead to different pore diameter (8 nm and 16 nm). Three different silica stretching vibrational bands are observed (**Figure 20**) in accordance with literature:[232] The asymmetric stretching vibration of bridged Si-O-Si at 1260 – 1000 cm^{-1} and the symmetric stretching vibration of Si - O - Si ring structures at around 800 cm^{-1}, both originating from the silica network Si - O - Si as well as the stretching vibrational band of free silanol (Si-OH) groups in the range of 900-980 cm^{-1}.

Thereby ATR-IR spectra can either be measured directly on the glass substrate or after scratching the film. It looks like the $\nu_{asym.}$ Si-O-S band is layer thickness dependent on mesoporous silica films measured directly from the glass substrate in the ATR-IR spectrometer (**Figure 20** a, b). This effect can be attributed to the penetration depth of the evanescent electromagnetic field in ATR-IR. The penetration depth can be calculated using the following equation and depends on the wavelength λ, the angle of incidence θ of the laser beam, as well as on the refractive indices of the ATR crystal n_1 and the sample n_2 used.

$$d = \frac{\lambda}{2\pi\sqrt{n_1^2 sin^2(\theta) - n_2^2}}$$

For the wavelength of λ = 5766 nm (at 1735 cm^{-1}) or 10000 nm (at 1000 cm^{-1}) used and a typical angle of incidence of 45 ° results with n_1 = 2.48 (ZnSe-Diamond)[233] and n_2 = 1,44

(quartz glass)[223] or $n_2 = 1.25$ (mesoporous silica) shows a penetration depth of 917-746 nm or 1590-1294 nm.

As the glass substrate below the mesoporous silica film mainly contains silanol these represent the majority of the detected Si-OH vibrational band absorbance at around 980 cm^{-1} and the symmetric Si-O-Si stretching band absorbance at 780 cm^{-1}. For mesoporous film significantly thinner than the penetration depth, the glass substrate vibrational bands become increasingly dominating with decreasing mesoporous film thickness. With increasing mesoporous film thickness, the asymmetric Si-O-Si vibrational band increases corresponding to the mesoporous silica instead of the supporting glass substrate.

Based on this observation ATR-IR can even be used to indirectly determine mesoporous film thickness, after normalizing all spectra to the Si-OH stretching vibration at 900 cm^{-1} (**Figure 20**e). With increasing mesoporous silica film thickness, the detected ratio between glass substrate and mesoporous silica film and thus the ratio between Si – O – Si asymmetric stretching vibration at 1070 cm^{-1} and Si – O - Si symmetric stretching vibration at around 770 cm^{-1} changes proportionally to film thickness variation. After scratching the calcined (350 °C) mesoporous film off the supporting glass substrate, no influence of film thickness on the detected ATR-IR spectra is observed anymore (**Figure 20**c, d). Consequently, the observed film thickness dependent difference in ATR-IR spectra recorded on substrate supported mesoporous silica films with respect to the symmetrical (800 – 820 cm^{-1}) and asymmetrical (1000 – 1260 cm^{-1}) Si – O - Si stretching vibration and silanol vibrational band (900 – 980 cm^{-1}) can be clearly attributed to the detected mesoporous film thickness dependent ratio of detected glass substrate to mesoporous film.

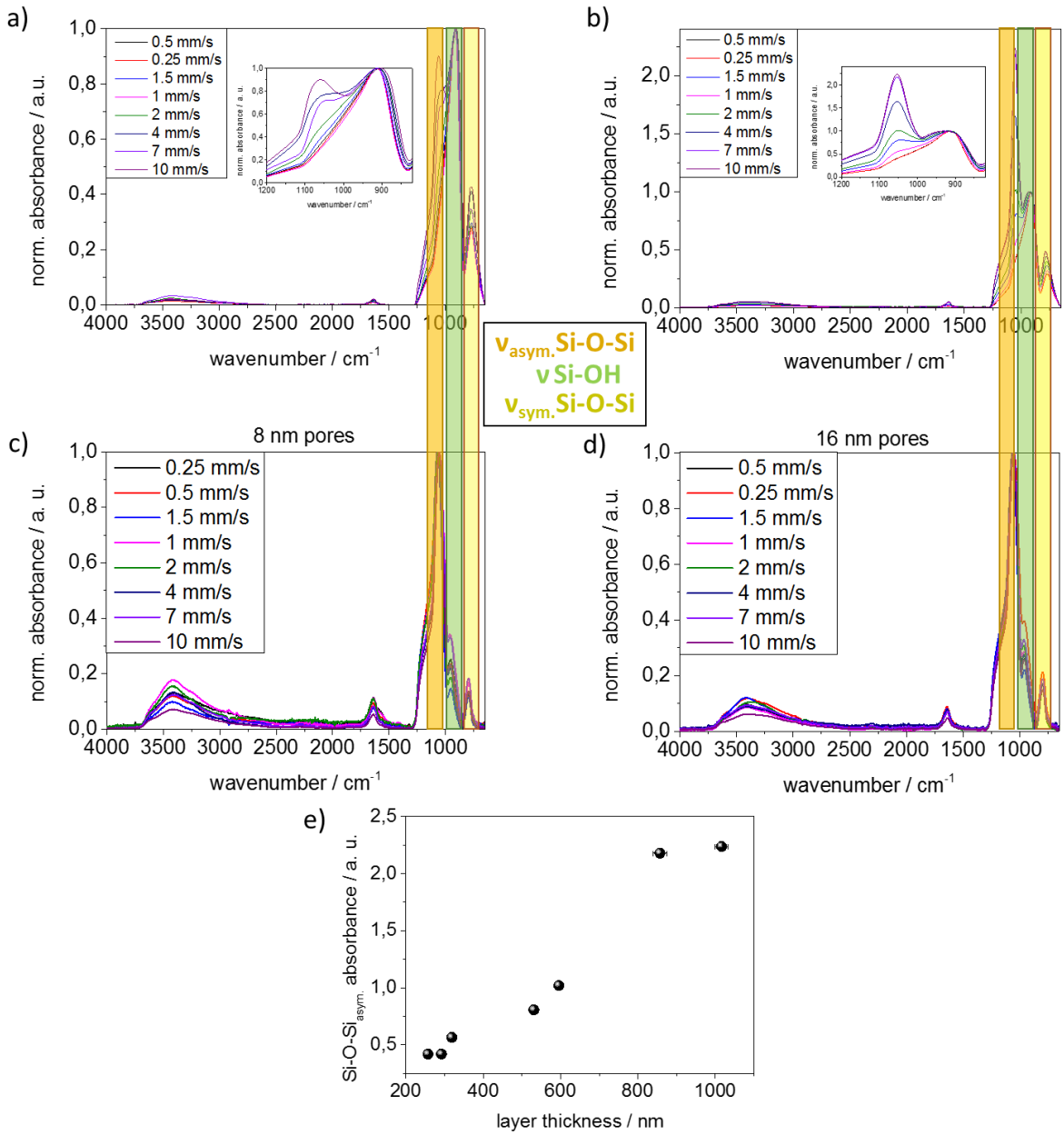

Figure 20. Infrared spectra of the mesoporous film in dependence of the dip-coating withdrawal speed (from 0.25 – 10 mm/s) measured directly on a glass substrate after template calcination at 350°C. a-b) ATR-IR-measurements of mesoporous silica films measured directly on glass substrate prepared via dip-coating and template calcination for both pore sizes 8 nm (a) and 16 nm (b). c-d) ATR-IR-measurements of scratched mesoporous silica films prepared via dip-coating and template calcination for both pore sizes 8 nm (c) and 16 nm (d). The typical silica bands are marked with different colors: Orange = $\nu_{asym.}$Si-O-Si, green = ν Si-OH and yellow = $\nu_{sym.}$ Si-O-Si. e) Si-O-$Si_{asym.}$ absorbance from b) in dependence of the layer thickness of mesoporous silica films evaluated from ellipsometry.

Even thicker mesoporous silica films can be prepared by dip-coating multiple layers. But, multiple layer mesoporous film formation needs a thermal treatment before coating a subsequent layer to condensate the TEOS and avoid dissolution of the previous layer(s). Thereby it has to be ensured that no degradation of the template occurs. Otherwise the solution imbibes into the first layer mesopores during dip-coating of the second layer. This would lead

to an undesired reduction of porosity. In **Figure 21**a the ellipsometry data of the first layer after a stabilizing thermal treatment up to 120 °C or 150 °C are shown. The refractive indices correlate with the porosity of the material and so it can be concluded if the template (Pluronic ® F127) stays within the pores. The polymer has a refractive index of around 1.5 which fits well to dense silica with 1.46. It is visible that the refractive index decreases from 1.45 to 1.38 upon increasing the curing temperature from 120°C to 150°C. This observation correlates with TGA data of the Pluronic® F127 template (Appendix, **Figure 87**) which indicate a thermal degradation of Pluronic® F127 starting at 150 °C. In addition, a reduction in mesoporous silica film thickness from 445 nm to 325 nm curing at 120 °C respectively 150 °C is observed which can be explained by a shrinking of the mesoporous silica film with higher temperatures. This observation is in accordance with literature about silica shrinking during thermal treatment by the research group of F. Schüth.[234]

After subsequent dip-coating of a second layer followed by removal of the polymer template by thermal calcination at 350 ° C refractive indices of 1.2 - 1.25 are detected. This refractive index is comparable to those of one-layer dip-coated mesoporous silica films after calcination at 350 °C as discussed above. The ellipsometry data are supported by profilometer measurements: the steps between substrate, first layer and second layer are visible for thermal treatment till 120 °C (red) and after total calcination to 350 ° C (blue) (see appendix, **Figure 88**). A film thickness of 450 nm for first layer and 600 nm for second layer is observed by calcination to 350 °C. In addition, a film shrinkage of about 30 % from 650 nm to 450 nm upon temperature treatment at 120 °C for the first layer and from 1 μm to 680 nm for the second layer is observed. The complete Pluronic® template removal is proven by ATR-IR spectroscopy. In **Figure 21**b the spectra after curing up to 120 °C (black and red) as well as after curing up to 350 °C (blue) are shown. The characteristic vibrational bands for the polymeric template Pluronic® F127 are the CH_2/CH_3 vibrational band between 2750-3000 cm^{-1} and the C-O vibrational band at 1700 cm^{-1} which are only detected for mesoporous silica films treated only up to 120 °C. In **Figure 21**c the investigation of ionic permselectivity of the two-layer dip-coated mesoporous film with a film thickness of around 600 nm is shown. The cyclic voltammogram looks very similar to the ones discussed for single layer films (chapter 6.1.3, **Figure 24**a-c). At pH 3, both of the two opposite charged probe molecules, $[Fe(CN)_6]^{3-/4-}$ and $[Ru(NH_3)_6]^{2+/3+}$, are diffusing into the mesoporous silica film reaching the electrode below the film (**Figure 21**c). When changing the pH to 9 the silanol groups are deprotonated and a negatively charge on the silica wall is generated. The negatively charged probe molecule $[Fe(CN)_6]^{3-/4-}$ is now electrostatically excluded due to repulsive electrostatic interactions and pore sizes within the Debye Screening length. In contrast to this behavior, the positively charged probe molecule $[Ru(NH_3)_6]^{2+/3+}$ is

preconcentrated showing a 6.5 times higher peak current density as compared to pH 3. This fits perfectly to the results of thickness dependent measurements of ionic permselectivity of mesoporous silica in the next chapter 6.1.2 (**Figure 24**). The films prepared with dip-coating of two layers are also comparable in stability on the supporting substrate and porosity of around 45 % (free pore volume) to prepared one-layer films.

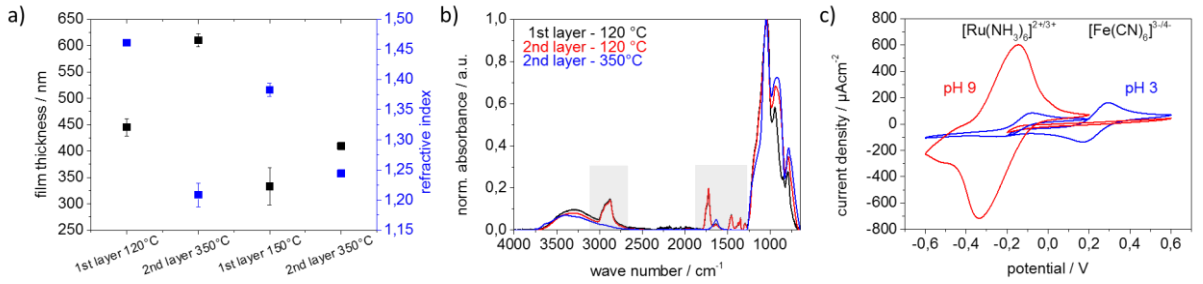

Figure 21. Preparation of mesoporous silica via dip-coating (withdrawal speed 10 mm/s) of two layers to achieve thicker films. a) Ellipsometry measurements revealing the thickness and the refractive indices of first layer treated up to 120 ° C or 150 ° C and the second layer after treatment at 350 ° C. b) ATR-IR spectra normalized to asym. Si-O-Si (1070 cm^{-1}) band and c) cyclic voltammetry of two-layered mesoporous silica cured to 350 ° C using positively and negatively charged probe molecules $[Ru(NH_3)_6]^{2+/3+}$ and $[Fe(CN)_6]^{3-/4-}$ at pH 3 and 9.

In summary, the preparation of mesoporous silica thin films with different film thicknesses and pore diameters could be successfully performed. The film thickness could be controlled by varying the withdrawal speed of the dip-coating process. Furthermore, film thickness can be tuned by repeated dip-coating of sol-gel solution with a thermal treatment step in between.

6.1.2. Mesoporous Silica Preparation via Gravure Printing

Gravure printing has been developed as alternative process for mesoporous film preparation. The sol-gel-solution is transferred from a gravure cylinder to the substrate with a defined cell volume and printing force. In general, gravure printing produces very homogeneous mesoporous silica films on large areas (here up to 12*4 cm^2) in an automated fashion. The known parameters influencing the film thickness of printing are shown in **Figure 22**.

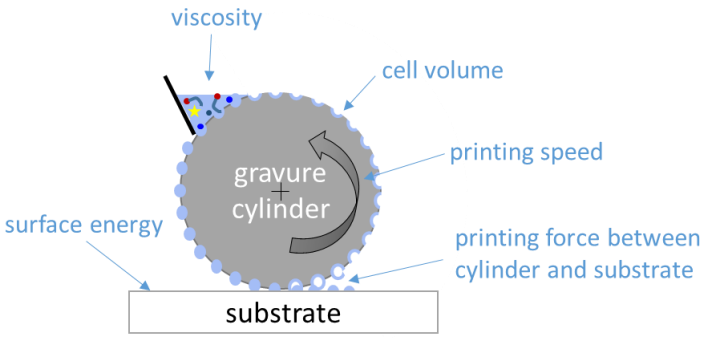

Figure 22. Gravure printing scheme with showing gravure cylinder with cell, the substrate and the doctor blade filled with printing ink. The arrows show the parameters which are influences the film thickness of the printed films according to literature of Spiehl *et al.*.[235]

Structural characterization by transmission electron microscopy (TEM) reveals similar mesoporous structures with pores of 6-8 nm in diameter as compared to dip-coated mesoporous films (**Figure 23**a). Furthermore, SEM images (**Figure 23**c) do not show any microscale cracks or structural defects. Gravure printed films appear to be very homogeneous microscopically as well as macroscopically as deduced from very homogeneous optical interference colors (**Figure 23**d-f). Notably, substrate rim effects resulting in thicker films close to the substrate rims as usually observed upon dip-coating are absent when using gravure printing based on the reflected interference color visible for mesoporous films printed onto silicon wafer substrates. This makes gravure printing a versatile technique to print homogeneous microscopically small area mesoporous film architectures. In contrast to dip-coating, gravure printing allows control of film thickness and film composition patterns by adjusting gravure cylinder cell volume and printing force. Without special optimization, our experiments allow film thickness resolution down to 20 nm while maintaining structural film homogeneity (**Figure 23**b) allowing to homogeneously print ultrathin mesoporous films. In gravure printing, the film thicknesses and homogeneity is mainly determined by the cell volume of the grounded cylinders (1.6 to 24 mL/cm^2) resulting in film thickness variation between 20-240 nm (**Figure 23**b) for a contact force of 500 N. In addition, film thickness can be tuned by varying the contact force between gravure cylinder and substrate. Increasing contact force from 500 N to 700 N leads to increasing film thickness of 10-20 nm (**Figure 23**g). Consequently, gravure printing yields thinner homogeneous films compared to dip-coating. Porosity (pore volume) of 40 - 55 vol% as calculated from ellipsometry data (refractive index) using Bruggeman effective medium approximation (please refer to appendix, **Table 10** and **Table 11**) is detected for gravure printed films. High refractive indices resulting in low porosities of below 20 vol% are observed only in case very small cell volumes of less than 1.67 mL/cm^2 are used. This can be attributed to insufficient ink transfer resulting in inhomogeneous film formation (**Figure 23**h), which is

supported by SEM results (**Figure 23**h). Using a critical cell volume (above 2 mL/cm^2) seems to be crucial for obtaining homogeneous mesoporous silica films by gravure printing with a comparable pore volume to dip-coated mesoporous silica films. Micrometerscale patches are accessible printing individual spots.

Changing the ink composition can introduce functional groups into the mesopore wall (co-condensation) and produce films with varying pore diameters. Here, we demonstrate pore diameters of about 16 nm instead of about 8 nm. These films show higher film thickness under identical gravure printing and the calculated pore volume is slightly larger reaching up to 70 vol% (see appendix, **Table 10** and **Table 11)**. Interestingly, film thickness variation for these films is more sensitive to cylinder volume (**Figure 23**g).

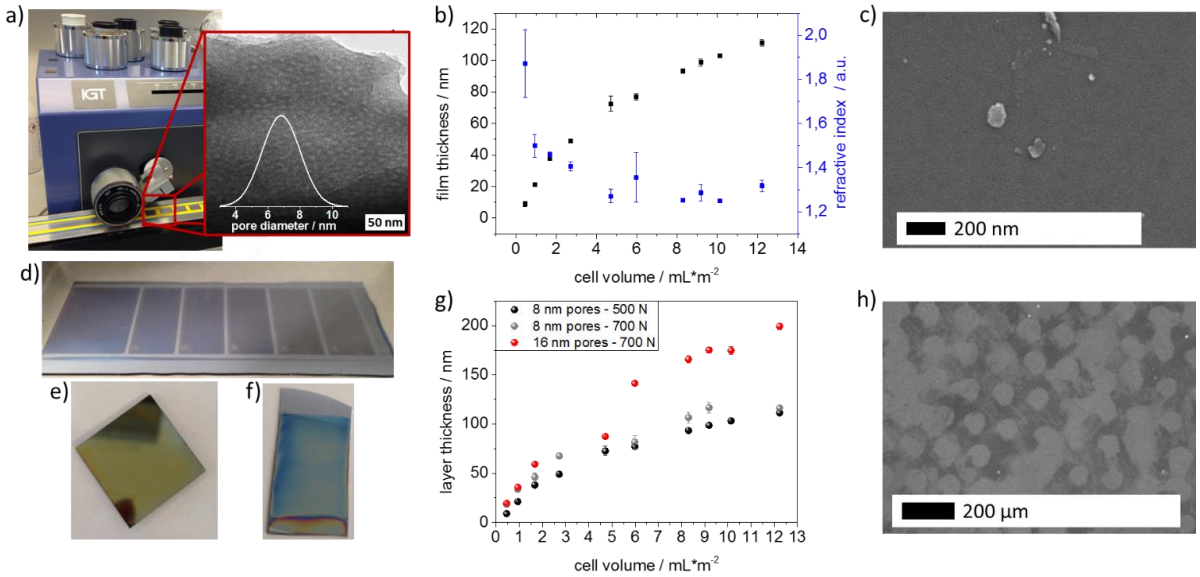

Figure 23. a) Photograph of gravure printed mesoporous silica films and a TEM image of mesoporous silica prepared by gravure printing and calcination at 350 °C using a cylinder with a cell volume of 8.5 mL/m² a statistic pore distribution b) Film thickness (black) and refractive index (blue) determined by ellipsometry in dependence of the cell volume of the used gravure printing cylinder. c) SEM micrographs showing the defect-free homogeneous film structure of various films printed on silicon wafer coated with mesoporous silica printed with an 8.5 mL/m^2 cylinder d) Photograph showing the homogeneity of gravure printed mesoporous silica films with different cylinder cell volume field (9.19 mL/m², 8.3 mL/m², 5.98 mL/m², 4.71 mL/m², 2.72 mL/m² and 1.67 mL/m² from left to right). Using gravure printing it is possible to print mm-scale patterns. e) Image of a printed homogeneous mesoporous silica film prepared with a cell volume of 8.5 mL/m². f) Image of a dip-coated mesoporous silica film prepared with 2 mm/s withdrawal speed. Inhomogeneity's because of edge effects are visible g) Film thickness, as measured by ellipsometry for mesoporous silica films in dependence of the used printing force and the applied ink giving different pore size of 8 nm and 16 nm, gravure printed with different cell volume. h) SEM micrograph showing the printed pattern of the same film. Because of the small cell volume and thus the low amount of transferred sol, the ink has not completely covered the substrate before solvent evaporation and silica film formation. A relatively high refractive index (1.872) indicates that this film may not mesoporous and the silicon wafer effects the high refractive index. Figure adapted from N. Herzog *et al.* in RSC Adv. 2019, 9, 23570-23578 used by CC BY.

In summary gravure printing is an appropriate alternative method for mesoporous silica film preparation which allows a automatization of the process. The film thickness can be adjusted by varying the cell size of the gravure cylinder or the printing force.

6.1.3. Ionic Permselectivity of Mesoporous Silica Films

Mesoporous silica ionic permselectivity and mesoporous silica film ion uptake capability is mainly determined by structural characteristics such as pore size and porosity, together with pore wall functionalization depending interface characteristics such as charge but might as well be affected by mesoporous film thickness. Walcarius and co-workers for example demonstrate an increasing peak current in cyclic voltammetry, representing, according to Nernst equation, an increasing molecule concentration with increasing number of mesoporous silica layers produced by dip-coating.[236] As gravure printing allows very precise adjustment of homogeneous mesoporous layer thickness, the correlation of film thickness and ionic permselectivity is shown in **Figure 24** as detected by the maximum peak current density deduced from cyclic voltammetry. Ionic mesopore accessibility of gravure printed and dip-coated mesoporous silica thin films with increasing film thickness using anionic and cationic probe molecules $[Fe(CN_6)]^{3-/4-}$ and $[Ru(NH_3)_6]^{2+/3+}$ at acidic and basic pH are compared. At basic pH values (**Figure 24** a-c, blue), the silica mesopore wall is negatively charged due to deprotonated silanol groups. Under these conditions, an exclusion of $[Fe(CN_6)]^{3-/4-}$ due to overlapping Debye Screening layers reflected by zero maximum peak current density (j_p) as well as a preconcentration of positively charged $[Ru(NH_3)_6]^{2+/3+}$ in the silica mesopores reflected by increased maximum peak-current densities and peak broadening is expected. At acidic pH values, and thus neutral pore wall charge, no ion discrimination in pore accessibility and thus similar j_p are expected. In accordance with this expectation, both probe molecules show similar and thickness independent maximum peak currents at acidic pH (**Figure 24**, red). As well in accordance with expectation, electrostatic exclusion of $[Fe(CN_6)]^{3-/4-}$ at basic pH is observed indicating a defect-free film structure. Except for very thin films with a film thickness of below 160 nm, a thickness dependent peak current reduction is observed (**Figure 24**d-e) indicating that part of the probe molecule solution may contribute to the cyclic voltammogram. This is as well supported by the evolvement of the CV shape of $[Ru(NH_3)_6]^{2+/3+}$ at basic pH for these thin films. Interestingly, the pre-concentration of $[Ru(NH_3)_6]^{2+/3+}$ at basic pH and the simultaneously observed broadening of the cyclic voltammograms seems to be film thickness and thus preparation process dependent. Reference measurements of unmodified ITO electrodes are shown in appendix **Figure 89**. These measurements do not show any peak

broadening or preconcentration at basic or acidic pH values. In addition, the ATR-IR spectra (**Figure 20**) do not show differences in the Si-O-Si to Si-OH ratio in dependence of film thickness or preparation process, and ellipsometry indicates comparable pore volumes for all investigated films. Together, this indicates that the variation of Si-O-Si$_{asym./sym.}$ to Si-OH band intensity with varying cylinder volume is probably caused by the mesoporous film thickness but not by a difference in Si-OH concentration and thus charge density at the mesopore wall.

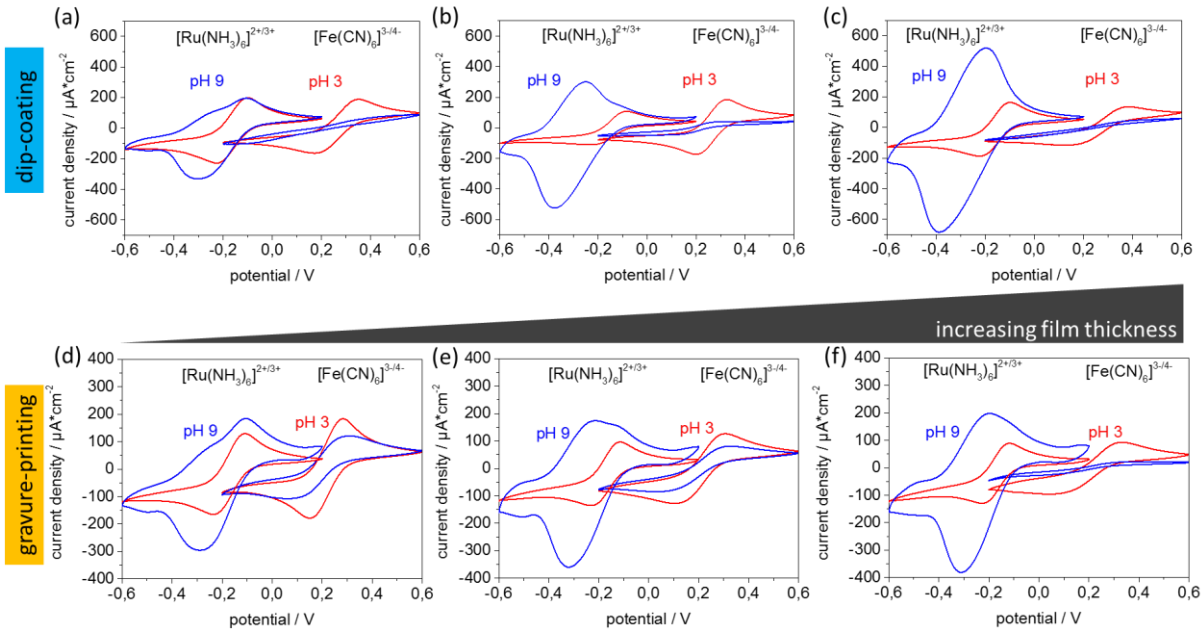

Figure 24. Cyclic voltammograms of mesoporous silica thin films using $[Ru(NH_3)_6]^{2+/3+}$ (-0.6 V - + 0.2 V) and $[Fe(CN)_6]^{3-/4-}$ (-0.2 V - +0.6 V) as an ionic redox probes at pH 3 (red) and 9 (blue). The dip-coated mesoporous silica films are prepared with different withdrawal speeds a) 0.5 mm/s b) 2mm/s and c) 10 mm/s resulting in film thicknesses of a) 140 nm (47 vol% porosity), b) 180 nm (44 vol% porosity), c) 300 nm (39 vol% porosity). Mesoporous silica films prepared by gravure printing are prepared using different cell volumes of d) 8.5 mL/m² e) 16.3 mL/m² and f) 24 mL/m² resulting in film thicknesses of d) 100 nm (48 vol% porosity), e) 162 nm (40 vol% porosity), f) 250 nm (48 vol% porosity). Figure adapted from N. Herzog *et al.* in RSC Adv. 2019, 9, 23570-23578 used by CC BY.

In addition, data evaluation using Randles-Sevcik's equation (**Figure 90**a-f) indicates that non-diffusional transport is significantly detected for mesoporous films thicker than 250 nm at basic solution pH values for positively charged probe molecule $[Ru(NH_3)_6]^{2+/3+}$ and thus in presence of attractive electrostatic interaction between pore wall and diffusing ions. This is reflected by a non-linear correlation of peak currents to the square root of scan rates. All these results indicate good accessibility and a comparable behavior for gravure printed to dip-coated mesoporous silica films.

In summary, the mesoporous silica films prepared by dip-coating as well as gravure printing show a thickness dependent behavior of ionic permselectivity. For thinner films the exclusion of negatively charged probe molecule, $[Fe(CN)_6]^{3-/4-}$, for pH 9 is more pronounced. The

concentration of the positively charged probe molecule, $[Ru(NH_3)_6]^{2+/3+}$, is also lower for this pH value.

6.1.4. In-situ Functionalization and Post-grafting of Mesoporous Silica Films

To broaden mesoporous film functionality and to allow e.g. polymerization different functional molecules should be accessible. Here, the functionalization of mesoporous silica is performed with 3-[Bis(2-hydroxyethyl)amino]propyl-triethoxysilane (called coinitiator). This coinitiator is used because it is one of the components besides a dye needed in dye-sensitized polymerization (chapter 5.1 and chapter 6.2). The surface functionalization is achieved following two different approaches. Firstly, co-condensation during film preparation and secondly post-grafting is investigated. The main advantage of co-condensation is a homogenous distribution of molecules through the mesoporous film, but the structure formation can be impaired. Using post-grafting, structure formation is not affected, but the binding could be inhomogeneous.

To ensure covalent polymer attachment to the mesopore wall, the coinitiator 3-[bis(2-hydroxyethyl)amino]propyl-triethoxysilane is covalently bound to the mesoporous silica thin films. After silica surface modification with the coinitiator, XPS analysis (**Figure 25** and Table 3, Measured by K. Kopp in AK Hess) revealed one coinitiator molecule per approximately 19 silica atoms in case of functionalization of an 170 nm thick mesoporous silica film at an elevated temperature of 80 °C and a 0.01 wt.-% coinitiator concentration in toluene for 1 h. In the case of coinitiator functionalization of 300 nm mesoporous silica one coinitiator molecule per approximately 13 silica atoms is determinable with XPS analysis. Here, the molecule binding is done for 2 h at 80 °C with a 0.05 wt.-% concentration.

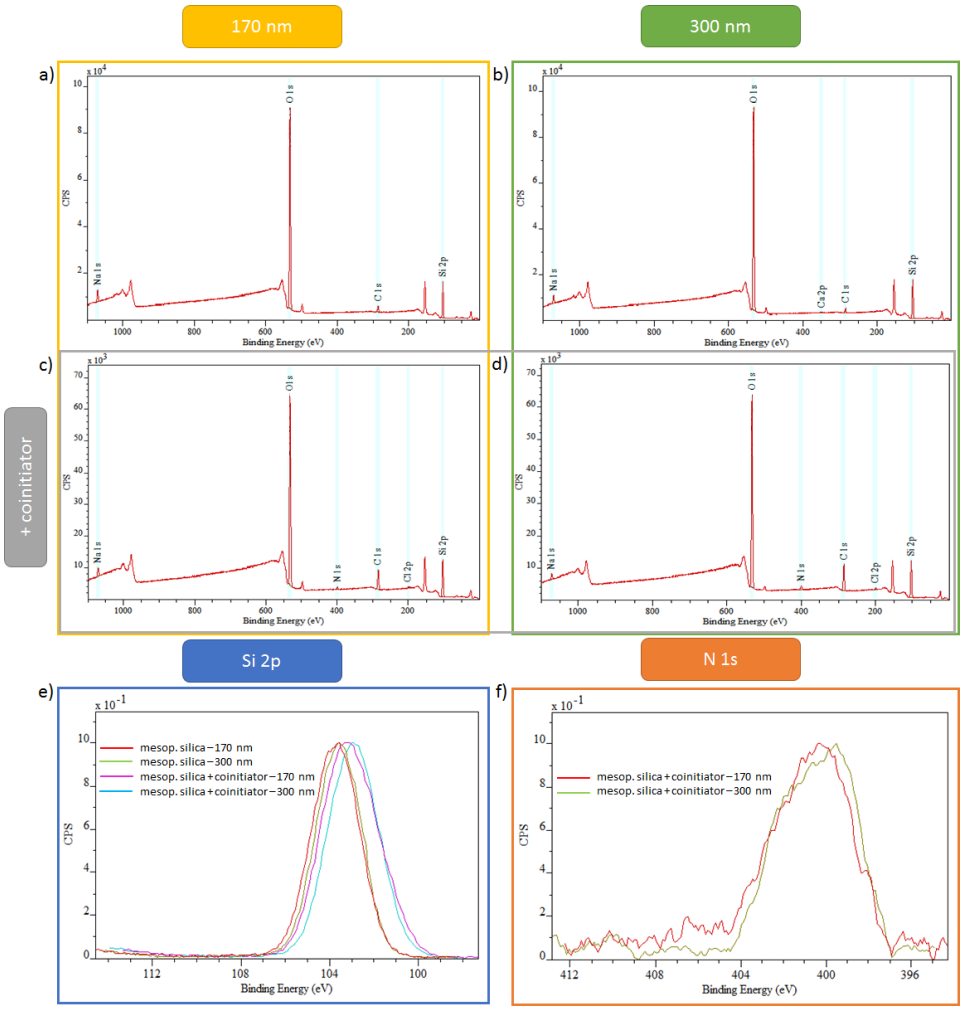

Figure 25. XP survey spectra of the mesoporous silica films with coinitiator (3-[Bis(2-hydroxyethyl)amino]propyl-triethoxysilane) functionalization. a) mesoporous silica with a film thickness of 170 nm b) mesoporous silica with a film thickness of 300 nm. Mesoporous silica after coinitiator functionalization with a film thickness of c) 170 nm and d) 300 nm. e) Zoomed spectra of the e) Si 2p and f) N 1s signal. XPS is measured by K. Kopp (AK Prof. Dr. Hess, TU Darmstadt). Figure adapted from N. Herzog *et al.* in RSC Adv. 2019, 9, 23570-23578 used by CC BY.

Table 3. Surface composition obtained by XPS analysis (**Figure 25**). Please note that not all compositions add up to 100 % due to rounding. XPS is measured by K. Kopp (AK Prof. Dr. Hess, TU Darmstadt).

Sample	C at%	O at%	N at%	Si at%	Ca at%	Na at%	Cl at%	ratio Si:N
Mesoporous silica – 170 nm	6.1	65.1	-	24.3	-	4.5	-	-
Mesoporous silica – 170 nm + coinitiator	13.9	58.3	1.2	23.1	-	3.1	0.4	19:1
Mesoporous silica – 300 nm	3.8	66.7	-	26.2	0.2	3.1	-	-
Mesoporous silica – 300 nm + coinitiator	19.2	55.0	1.7	22.0	-	1.7	0.4	13:1

The coinitator in solution has a pK_a value of 8.7 (calculated using Advanced Chemistry Development (ACD/Labs) Software V11.02 (© 1994-2016 ACD/Labs)). Consequently, the coinitiator is expected to be positively charged at pH-valued below 8.7 and changes to neutral for higher pH-values. Thus, coinitiator functionalization changes the pH-dependent pore wall charge as compared to unmodified mesoporous silica. The cyclic voltammetry measurements of unfunctionalized mesoporous silica films as well as the ones after functionalization with coinitiator using different reaction conditions and mesoporous films with two different film thicknesses of 170 nm (**Figure 26**a, c, e) and 300 nm (**Figure 26**b, d, f) are shown in **Figure 26**. The mesoporous silica films behave in dependent of the film thickness as expected for ionic permselectivity and as discussed above (Chapter 6.1.3, **Figure 24**). The preconcentration of the positively charged probe molecule, $[Ru(NH_3)_6]^{2+/3+}$, as well as the exclusion of negatively charged probe molecule, $[Fe(CN)_6]^{3-/4-}$, is stronger the thicker the mesoporous film is.

After functionalization with a solution of 0.01 wt.-% coinitiator in toluene at 80 °C for 1h for the thinner mesoporous silica film (170 nm), the cyclic voltammogram is shown in **Figure 26**c. At pH 3, the preconcentration of the negatively charged probe molecule $[Fe(CN)_6]^{3-/4-}$ compared to the unfunctionalized mesoporous silica film is visible by higher I_p. The repulsive electrostatic interactions between the positively charged silica walls and the positively charged probe molecule $[Ru(NH_3)_6]^{2+/3+}$ is visible by a very small j_p. At pH 9 the I_P for both, negatively as well as positively charged, probe molecules are comparable. The same coinitiator binding conditions for even longer time (6 h) for the thick film (300 nm) show just a small influence on the ionic permselectivity for both probe molecules (**Figure 26**d in comparison to **Figure 26**c). To achieve a better permselectivity after functionalization the coinitiator binding reaction conditions are adjusted to a coinitiator concentration of 0.05 wt.-% in toluene at 80 °C. Here the thinner mesoporous silica films (170 nm) show no significant difference in cyclic voltammetry measurements between coinitiator binding in thin films with 0.05 wt% for 2h (**Figure 26**e) or 0.01 wt% for 1h (**Figure 26**c). Only the I_p for $[Ru(NH_3)_6]^{2+/3+}$ at pH 9 decreased (**Figure 26**e, red) for functionalization with 0.01 wt% as compared to 0.05 wt% coinitiator solution. This is attributed to a higher degree of functionalization and thus increasing number of positive charges which leads to a electrostatic pore closure. It has to be noted that decreasing pore accessibility for positive molecules is not practical with respect to the use of DMAEMA ($pK_a \sim 8.4$) as monomer for polymerization. DMAEMA is positively charged and for a successful polymerization the diffusion of monomer into the mesopores must to be ensured. The 300 nm thick mesoporous silica film after the functionalization with coinitiator for 2 h at 80 °C with a 0.05 wt.-% solution in toluene (**Figure 26**f) shows comparable ionic permselectivity as the post-grafted mesoporous silica film with a thickness of 170 nm when functionalizing with 0.01 wt.%

for 1 h at 80 °C in toluene (**Figure 26**c). So the cyclic voltammograms in **Figure 26**c and f fit perfectly with the expectations that at pH 3, the coinitiator molecule is positively charged, and the negatively charged, $[Fe(CN)_6]^{3-/4-}$, is electrostatically attracted while the positively charged, $[Ru(NH_3)_6]^{2+/3+}$, diffusion through the functionalized mesoporous silica film is electrostatically hindered. At pH 9, the coinitiator molecule is neutrally charged and thus both probe molecules, positively or negatively charged, are expected to comparably diffuse through the mesopores. An inhibition of $[Fe(CN)_6]^{3-/4-}$ pore accessibility can occur only when negatively charged silanol groups (pH 9) of the silica pore wall dominate. That's why these two different conditions are used for coinitiator binding of mesoporous silica for further experiments.

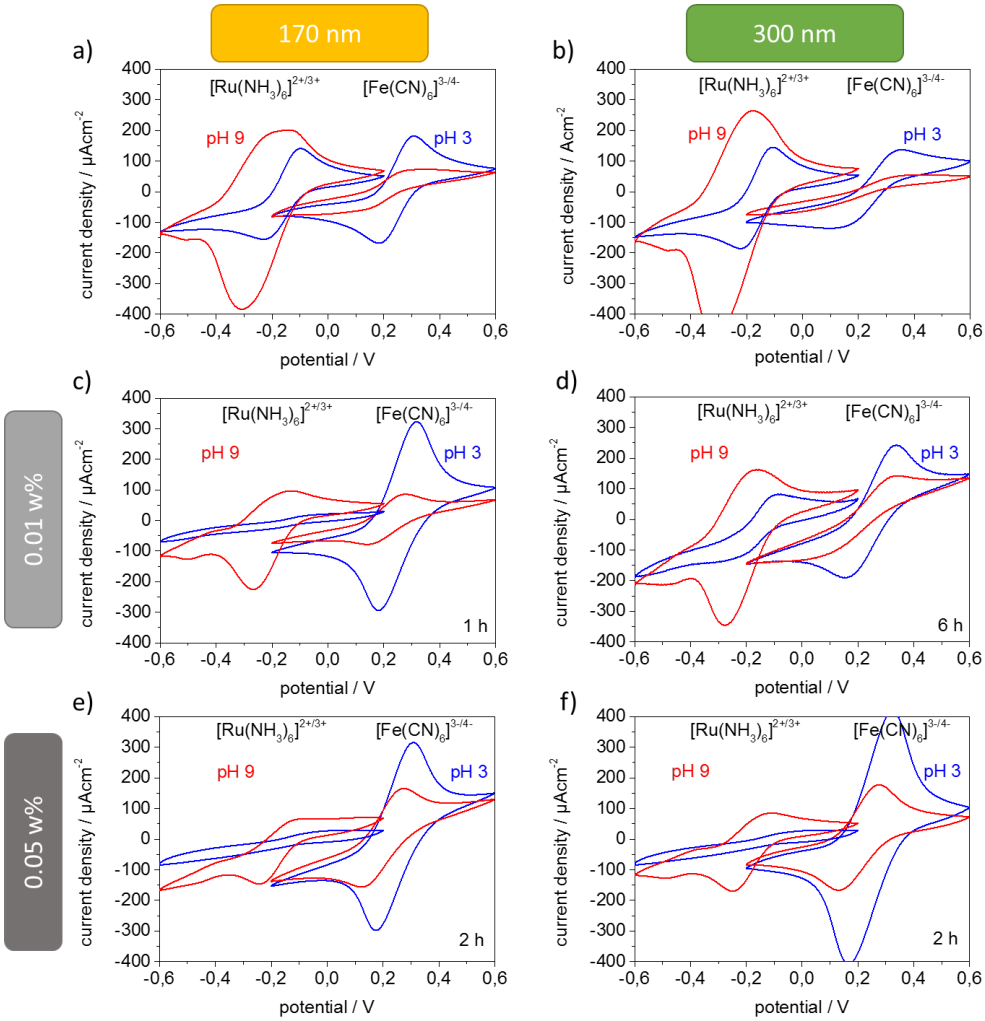

Figure 26. Optimization of coinitiator (3-[Bis(2-hydroxyethyl)amino]propyl-triethoxysilane) post-grafting of mesoporous silica films with 6-8 nm pore diameter of different film thickness (prepared with 2 mm/s = 170 nm and 10 mm/s = 300 nm). The unfunctionalized mesoporous silica with film thickness a) 170 nm and b) 300 nm. The functionalization with 0.01 wt.-% coinitiator in toluene for c) 170 nm film, 1h and d) 300 nm film, 6 h. A functionalization with coinitiator concentration of 0.05 wt.-% in toluene for e) 170 nm film, 2 h and f) 300 nm film, 2 h are shown.

The post-grafted mesoporous silica films prepared with two different withdrawal speeds, namely 2 mm/s and 10 mm/s, are investigated with ellipsometry measurements concerning layer thickness and refractive indices. Therefore, an unfunctionalized mesoporous silica film, a post-grafted mesoporous silica film and the same film after CO_2-plasma treatment[237] to remove the organic molecules from the outer surface of the mesoporous silica film are characterized by ellipsometry and contact angle measurements. The functionalization with coinitiator is now located exclusively inside the mesopores. The mesoporous silica films show film thicknesses of 190 nm and 320 nm respectively as well as refractive indices of 1.195 and 1.265 which result in porosities of 56 vol% and 41 vol%. After the post-grafting with the coinitiator, the refractive indices increase and the porosity decreases. For the 190-200 nm films, the pore filling is calculated (refer to chapter 5.4) to be 15 % of the pore volume. The pore filling of 300 nm thick films is determined to be 29 % of the pore volume indicating higher amount of coinitiator in slightly thicker films. this is consistent with the slightly higher Si:N ration in XPS results (Table 3) and the slightly higher preconcentration for negatively charged probe molecules at pH 3 (**Figure 26.** Optimization of coinitiator (3-[Bis(2-hydroxyethyl)amino]propyl-triethoxysilane) post-grafting of mesoporous silica films with 6-8 nm pore diameter of different film thickness (prepared with 2 mm/s = 170 nm and 10 mm/s = 300 nm). The unfunctionalized mesoporous silica with film thickness a) 170 nm and b) 300 nm. The functionalization with 0.01 wt.-% coinitiator in toluene for c) 170 nm film, 1h and d) 300 nm film, 6 h. A functionalization with coinitiator concentration of 0.05 wt.-% in toluene for e) 170 nm film, 2 h and f) 300 nm film, 2 h are shown.). After CO_2-plasma treatment, the refractive index and thus the pore filling stays relatively constant. In addition, the ellipsometry based pore fillings show successful coinitiator binding but at the same time sufficient remaining porosity allowing further functionalization with polymer.

Functionalization by both post-grafting and co-condensation can be proven by increased contact angles compared to unmodified mesoporous silica. This suggests an increased hydrophobicity due to introduction of organic molecules into the mesopores, and thus successful functionalization. The coinitiator functionalization changes the wetting behavior of water on the mesoporous silica surfaces (**Table 4**). Mesoporous silica is hydrophilic and Young contact angles are around 20-25°. After functionalization with 3-[Bis(2-hydroxyethyl)amino]propyl-triethoxysilane the contact angles increase to 40-45 °. This is an easy and fast investigation method to determine a successful surface functionalization.

Table 4. Values for film thickness and refractive index are obtained by fitting the obtained data to a one-layer model using ellipsometry. V_{pore} values are calculated using the Bruggeman approximation.[229] All samples printed on silicon wafer. Given errors are determined by standard deviation of minimal three measured points. Static contact angles are measured with 2 µL deionized water.

Sample	thickness / nm	refractive index	RMSE	porosity[229] /vol %	contact angle /°
Mesoporous silica – 2 mm/s	193.6 ± 0.3	1.195 ± 0.001	0.692	56	25 ± 1
Mesoporous silica – 2 mm/s + coinitiator	206.5 ± 0.3	1.261 ± 0.001	0.400	42	44 ± 1
Mesoporous silica – 2 mm/s + coinitiator (plasma-treatment)[237]	204.8 ± 0.6	1.261 ± 0.002	1.007	42	-
Mesoporous silica – 10 mm/s	319.8 ± 1.9	1.265 ± 0.004	0.376	41	19 ± 2
Mesoporous silica – 10 mm/s + coinitiator	309.0 ± 1.7	1.388 ± 0.004	0.464	15	41 ± 2
Mesoporous silica – 10 mm/s + coinitiator (plasma-treatment)[237]	310.6 ± 0.6	1.375 ± 0.009	0.917	18	

To allow functionalization of mesoporous films by grafting from polymerizations, initiators or coinitiators have to be present at the pore wall. This can be achieved by co-condensation during the gravure printing process or by dip-coating (**Figure 27**). Co-condensation is performed using different amounts of 3-[Bis(2-hydroxyethyl)amino]propyl-triethoxysilane varied from 5-25 mol%. Changes in mesoporous film structure and porosity as visible by TEM and ellipsometry are investigated with the aim to find optimal experimental conditions meaning at least a critical porosity suitable for mesopore transport and mesopores in the range below 20 nm as well as absence of larger cracks. The co-condensation of mesoporous silica with coinitiator leads to Young contact angles between 30 ° and 40 °. The post-grafting approach leads to higher contact angles of 50-60 ° (**Figure 27**a) indicating higher coinitiator functional density and potentially slight roughness increase. The TEM images of 5 mol% co-condensed mesoporous silica films for two different film thicknesses of 170 nm and 300 nm (**Figure 27**b) show comparable and homogenous mesoscale porous structure. Coinitiator co-condensed mesoporous silica using the same gravure printing conditions like mesoporous silica films without co-condensation show 20 nm higher film thickness in case of co-condensation as compared to the unmodified mesoporous silica (**Figure 27**c). The variation of film thickness between co-condensed film and unfunctionalized mesoporous silica are most probably related to differences in sol viscosity. It

should also be noted that the 5.7 nm thickness increase after coinitiator post-grafting is too large for a monolayer of coinitiator, which is expected to be 1-1.5 nm thick based on its molecular structure. This is most probably due to cross-linking in the TEOS anchoring groups of the coinitiator resulting in multilayer formation. The refractive indices for co-condensed mesoporous silica films are slightly higher than the ones for unfunctionalized mesoporous silica films. Calculations by the Bruggeman approximation[229] show decreased porosity of 37 vol% (n=1.282) for the post-grafted sample compared to the unmodified sample with a porosity of 48 vol%. The co-condensed films ranged between 43-48 vol% at a constant relative humidity of 15 %. A possible explanation for this porosity difference between both functionalization paths indicated a higher functionalization degree in case of post-grafting.

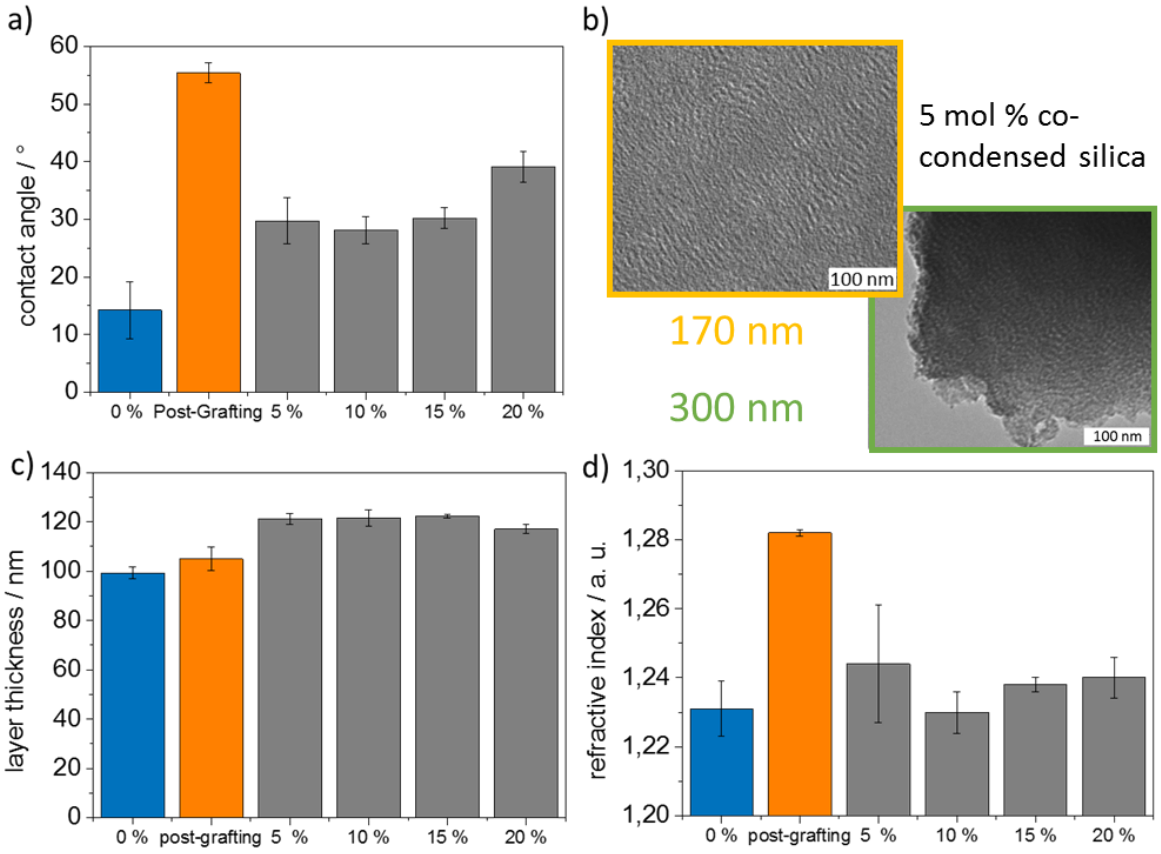

Figure 27. Comparing the functionalization of gravure printed mesoporous silica films with silane (3-[Bis(2-hydroxyethyl)amino]propyl-triethoxysilane) via post-grafting or co-condensation. a) Macroscopic static contact angle measurements with 2 µL water drops for mesoporous silica films with different co-condensation degree b) TEM images of mesoporous silica co-condensed with 5 mol% dip-coated with 2 mm/s and 10 mm/s results in film thickness of 170 nm and 300 nm. Film thickness c) and refractive index d) obtained via ellipsometry for different co-condensation degrees and post-grafting of mesoporous silica prepared with a printing cylinder cell volume of 8 mL/m² via gravure printing. Figure adapted from N. Herzog *et al.* in RSC Adv. 2019, 9, 23570-23578 used by CC BY.

SEM measurements (**Figure 28**) of films of varying amounts of co-condensed coinitiator (0-25 mol% coinitiator) show a microscopically homogeneous film. No cracks are visible. On the

nanoscale for higher amounts <15 mol% of co-condensate, some worm like features are visible with lengths of maximum 160 nm and a diameter of 18 nm (**Figure 28**d, e). The degree of mesoscopic order decreases with increasing concentration of co-condensate $(R'O)_3SiR$ in the sol-gel solution, which leads to more disordered structures as known from literature reports.[103] In general, high amounts of co-condensate in co-condensation reactions cause problems with the different hydrolysis and co-condensation rates of the precursor and co-condensate which leads to a trend towards homo-condensation reactions. The incorporation of organic groups can also lead to reduction in pore diameter and porosity.

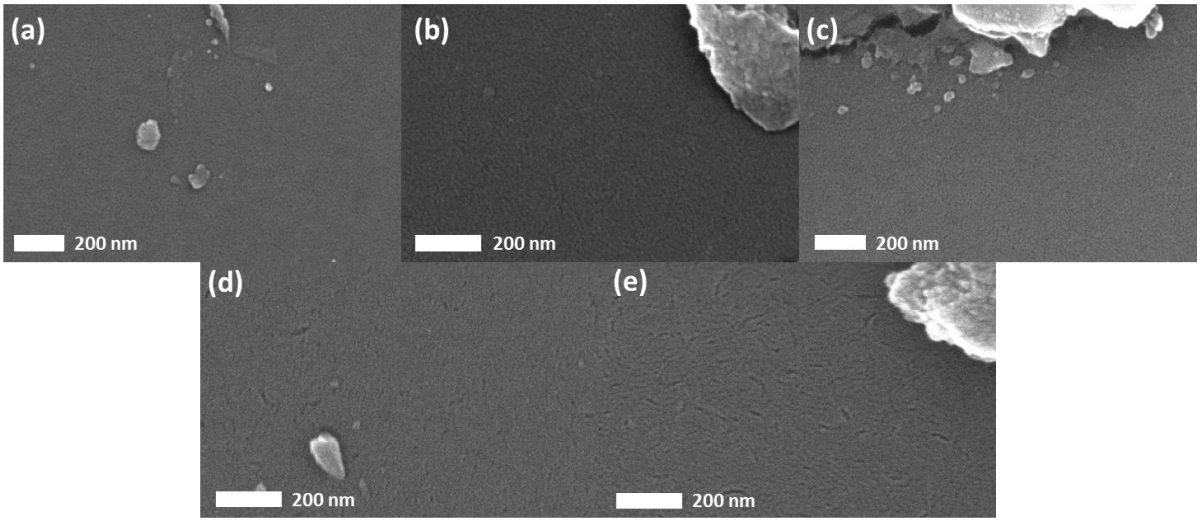

Figure 28. SEM micrographs showing the defect-free homogeneous film structure of various films printed on silicon wafer: (a) unmodified mesoporous silica printed with a 8.5 mL/m² cylinder, (b) co-condensed with a 5 mol% 3-[Bis(2-hydroxyethyl)amino]propyl-triethoxysilane, 8.5 mL/m² cylinder, (c) 10 mol% 3-[Bis(2-hydroxyethyl)amino]propyl-triethoxysilane, 8.5 mL/m² cylinder, (d) 15 mol% coinitiator with 8.5 mL/m² cylinder, (e) 20 mol% 3-[Bis(2-hydroxyethyl)amino]propyl-triethoxysilane, 8.5 mL/m² cylinder. Measurements taken after sputtering samples with a 3 nm platinum-palladium layer. Figure adapted from N. Herzog *et al.* in RSC Adv. 2019, 9, 23570-23578 used by CC BY.

The ionic permselectivity of the co-condensed mesoporous silica films is depicted in **Figure 29** for two different film thicknesses and concentrations of the co-condensate 3-[Bis(2-hydroxyethyl)amino]propyl-triethoxysilane (for profiler measurements see appendix, **Figure 91.** Profilometer measurement for 5 mol% coinitiator co-condensed mesoporous silica films dip-coated with two different withdrawal speeds.). Interestingly, the 5 mol% co-condensed mesoporous silica film prepared with 2 mm/s resulting in 190 nm thick films (**Figure 29**a) shows no influence of the coinitiator molecule in the diffusion of negatively and positively charged probe molecules. Rather the negative charge of the silanol groups of silica surface is visible inducing an inhibited pore accessibility of negatively charged probe molecule $[Fe(CN)_6]^{3-/4-}$ at pH 9 due to repulsive electrostatic interaction. Comparable behavior is observed for thicker films (320 nm) with the same co-condensed coinitiator ratio of 5 mol%

(**Figure 29c**). The higher preconcentration of the positively charged probe molecule $[Ru(NH_3)_6]^{2+/3+}$ at pH 9 as compared to thinner films in case of unfunctionalized mesoporous silica is discussed above (**Figure 26**). The increasing current densities for positively charged $[Ru(NH_3)_6]^{2+/3+}$ at pH 9 indicating preconcentration is dependent on film thickness and with increasing film thickness increasing current density is observed (**Figure 24**). The cyclic voltammograms provide no indication of a positive charge originating from the co-condensed coinitiator molecule at the silica pore walls as no preconcentration of $[Fe(CN)_6]^{3-/4-}$ at pH 3 is observed (**Figure 29**) because of attractive electrostatic interactions between negatively charged probe molecule and positively charged coinitiator functionalized silica wall. When using sol-gel precursor solutions with 25 mol% coinitiator, the ionic permselectivity of negatively charged $[Fe(CN)_6]^{3-/4-}$ at pH 9 of the resulting co-condensed mesoporous silica films changes slightly as compared to 5 mol% co-condesed silica films. For the 190 nm thick film (**Figure 28**b) no total exclusion of the negatively charged probe molecule at pH 9 is observed anymore which can be explained with the wormlike features. Compared to the post-grafted mesoporous silica films (**Figure 26**), the influence of the positive charge in the film is not visible as no preconcentration of negatively charged probe molecule $[Fe(CN)_6]^{3-/4-}$ at pH 3 is observed or as positively charged probe molecule $[Ru(NH_3)_6]^{2+/3+}$ is not excluded at pH 3. In case of features larger than Debye Screening length no exclusion of the probe molecules can be expected. For the thicker film (**Figure 29**d), the reduction of the preconcentration of positively charged $[Ru(NH_3)_6]^{2+/3+}$ for pH 9 is drastically reduced and no further exclusion of $[Fe(CN)_6]^{3-/4-}$ is detectable. These results show that a significant amount of coinitiator molecules are very probably lost in the silica matrix and are not located on the outer silica surface because in cyclic voltammetry measurements, the effect of silanol groups is much more pronounced than the effect of coinitiator molecules. Consequently, coinitiator post-grafting would be the preferred strategy for near-field induced polymerization because of film stability on gold coated glass substrates, while both types of coinitator functionalized mesoporous silica films are used for dye-sensitized polymerization studies. The coinitiator co-condensed mesoporous silica films with low amounts of 5 mol% are favorable for keeping mesoporous structure.

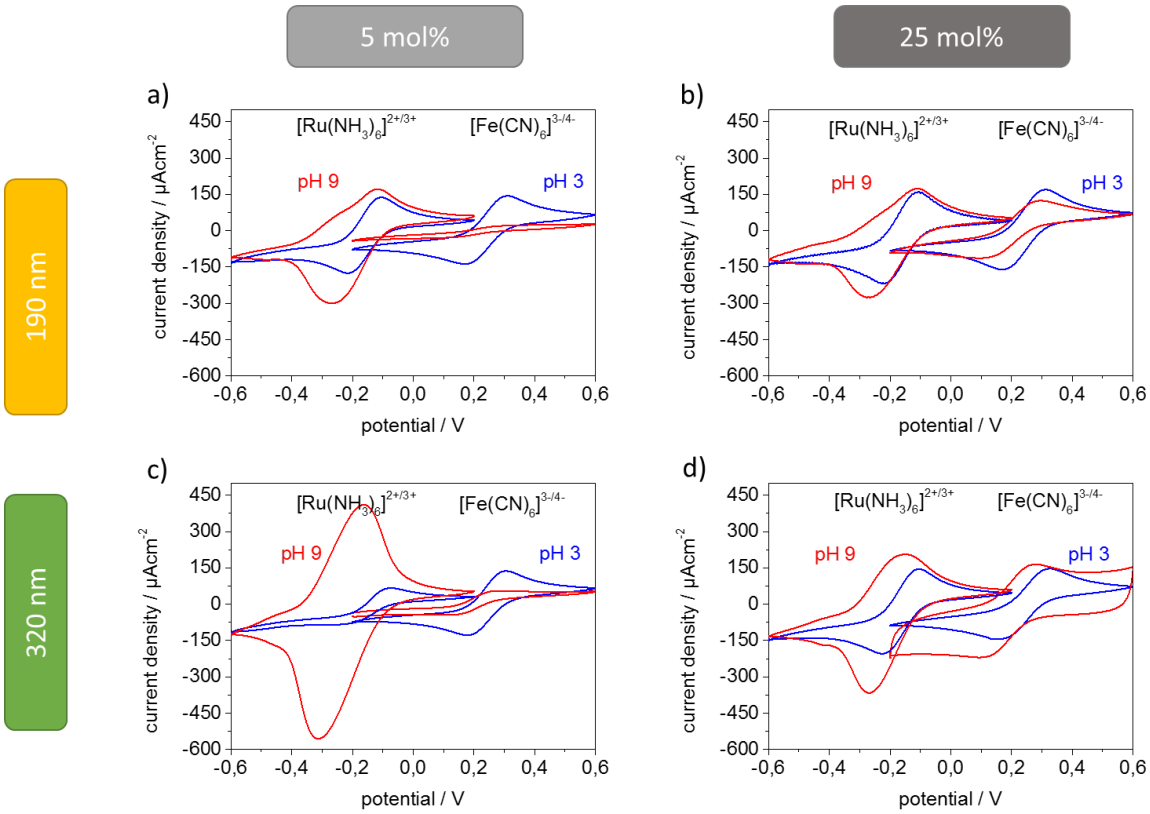

Figure 29. Cyclic voltammograms of mesoporous silica films of different film thickness of 190 nm (a, b) and 320 nm (c, d) prepared by dip-coating with withdrawal speeds of 2 mm/s and 10 mm/s using $[Ru(NH_3)_6]^{2+/3+}$ and $[Fe(CN)_6]^{3-/4-}$ as ionic redox probes at pH 3 (red) and 9 (blue). The amount of co-condensate varies between 5 mol% (a, c) and 25 mol% (b, c) of 3-[Bis(2-hydroxyethyl)amino]propyl-triethoxysilane.

In this chapter the optimal conditions for a post-grafting functionalization of coinitiator could be found. For different film thicknesses the bounding time and concentration of coinitiator in solvent has to be changed to achieve an optimal functionalization with a subsequent pore accessibility related to charged molecules. In a co-condensation process the coinitiator is also suitable for in-situ functionalization with the restriction of worm-like morphologies for higher mol% of the coinitiator.

6.1.5. Preparation of Multifunctional Mesoporous Silica Architectures

Besides the opportunity of printing different inks and thus creating gradient architectures, an advantage of mesoporous film gravure printing is the rapidity of the printing process. The very short contact time between supporting substrate and the sol-gel solution and the low transferred precisely placed liquid volume leads to fast drying, avoiding penetration of sol into a pre-printed layer or dissolution of a pre-printed layer which thus facilitating complex but homogeneous, defect-free multilayer fabrication. This allows for printing of multiple mesoporous silica layers directly on top of one another without using stabilizing temperature treatments between layer

deposition steps, which may negatively affect film homogeneity. Specifically, two-layer gravure printed mesoporous silica films using two different inks resulting in two different functional layers are prepared. The corresponding characterization concerning porosity, contact angles and morphology are summarized in **Figure 30**. The TEM images of the two-layered mesoporous silica films (**Figure 30**a, c) show very homogeneous pore structures. The porosity is calculated with the Bruggeman approximation to 45 -50 %. The film thickness of two layers is around 280-300 nm while one layer is about 130-145 nm. When measuring the wetting behaviors with static contact angles of 2 μL deionized water, the co-condensed mesoporous silica layers as top layer shows slightly higher contact angles as unfunctionalized mesoporous silica surfaces (**Figure 30**b and d).

a)

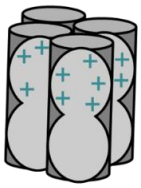

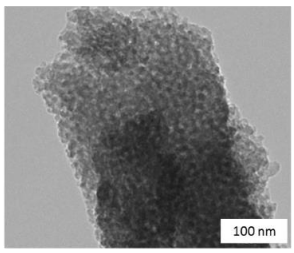

b)

sample	static contact angle / °
mesoporous silica	24 ±1
5 mol% co-condensed mesoporous silica	29 ± 1
1. mesoporous silica 2. 5 mol% co-condensed mesoporous silica	26 ± 1
1. 5 mol% co-condensed mesoporous silica 2. mesoporous silica	22 ± 1

c)

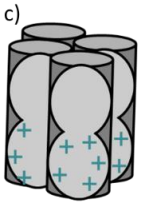

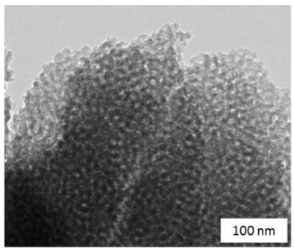

d)

sample	d / nm	n
mesoporous silica	128 ± 2	1.251 ± 0.004
5 mol% co-condensed mesoporous silica	145 ± 1	1.238 ± 0.001
1. mesoporous silica 2. 5 mol% co-condensed mesoporous silica	302 ± 10	1.243 ± 0.010
1. 5 mol% co-condensed mesoporous silica 2. mesoporous silica	297 ± 14	1.229 ± 0.010

Figure 30. a) TEM image of a two-layer mesoporous silica film prepared by gravure printing with two different ink compositions. The first layer of unfunctionalized mesoporous silica and a second layer consists of mesoporous silica with 5 mol% co-condensed 3-[Bis(2-hydroxyethyl)amino]propyl-triethoxysilane. The mesoporous films are thermally treated up to 200 °C and template extracted with acidic ethanol. b) Table with static contact angle measurements (drop size: 2 µL deionized water). c) TEM image of a two-layer mesoporous silica film prepared by gravure printing with two different inks. The first layer consists of mesoporous silica with 5 mol% co-condensed 3-[Bis(2-hydroxyethyl)amino]propyl-triethoxysilane and a second layer of unfunctionalized mesoporous silica. The mesoporous films are thermally treated up to 200 °C and template extracted with acidic ethanol. d) Table with layer thicknesses (d / nm) and refractive indices (n) determined by ellipsometry. The mesoporous silica and 5 mol% co-condensed mesoporous silica are one layer while the other two samples are two layers directly printed after each other.

The SEM cross section of a one-layer printed mesoporous silica film compared to a two-layered printed mesoporous silica film including two different inks is shown **Figure 31** (first layer printed with mesoporous silica containing 5 mol% co-condensed 3-[Bis(2-hydroxyethyl)amino]propyl-triethoxysilane (**Figure 31**a) and a second layer resulting in unfunctionalized mesoporous silica (**Figure 31**b). No interface/separation line between the two

layers is visible indicating a homogenous film preparation. The increasing thickness clearly supports the double layer deposition.

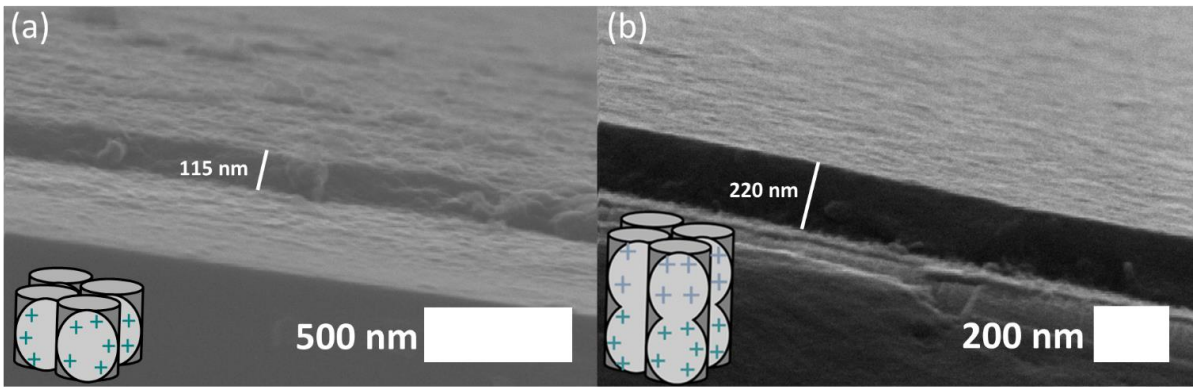

Figure 31. Cross-section SEM image of a gravure printed mesoporous silica film using the gravure cylinder cell volumes 8.5 mL/m² for printing. a) one layer of 5 mol% of 3-[Bis(2-hydroxyethyl)amino]propyl-triethoxysilane co-condensed mesoporous silica with a film thickness around 115 nm and b) two layers consisting of a first mesoporous silica layer containing 5 mol% co-condensed 3-[Bis(2-hydroxyethyl)amino]propyl-triethoxysilane and a second mesoporous silica layer resulting in around 220 nm film thickness. No clear interface between the two layers can be identified indicating a very homogenous structure. The samples are sputtered with Pt/Pd before measuring with SEM. Figure adapted from N. Herzog *et al.* in RSC Adv. 2019, 9, 23570-23578 used by CC BY.

Thereby, a successful multilayer step gradient preparation is supported by XPS measurements (**Table 5**). XPS results (measured by K. Kopp in AK Hess, TU Darmstadt) show one nitrogen atom per seven Si-atoms after printing two layers of 5 mol% co-condensed mesoporous silica. It has to be noted that a significant fraction of these coinitiators are not present at the surface but within the silica network. When printing one layer of 5 mol% mesoporous co-condensed silica followed by a second top layer of mesoporous silica, only one nitrogen atom per 32 Si-atoms is detected by XPS. Printing 5 mol% mesoporous co-condensed silica on top of mesoporous silica leads to one nitrogen atom per 17 Si-atoms. The reference sample of two printed mesoporous silica layers shows no nitrogen within the XPS. In literature the detection of XPS is estimated around 10 nm.[50]

Table 5. Surface composition obtained by XPS analysis. Please note that not all compositions add up to 100 % due to rounding up. XPS is measured by K. Kopp in AK Hess, TU Darmstadt.

	sample	N	C	O	Si	K	Na	In	Cl
		at%	at%	at%	at%	at %	at %	at %	at %
a)	1. mesop. silica 5 mol% co-condensed 2. mesop. silica	0.7	10.2	65.1	23.0	0.3		0.3	0.5
b)	1. mesop. silica 2. mesop. silica 5 mol% co-condensed	1.2	12.2	65.7	20.9				
c)	1. mesop. silica 2. mesop. silica		4.7	69.9	25.5				
d)	1. mesop. silica 5 mol% co-condensed 2. mesop. silica 5 mol% co-condensed	2.9	14.1	60.3	20.7	0.6	0.6		0.7

In **Figure 32**, cyclic voltammetry measurements of double layer gravure printed films consisting of one mesoporous silica layer and one mesoporous silica containing 5 mol% of co-condensed 3-[Bis(2-hydroxyethyl)amino]propyl-triethoxysilane are depicted. The cyclic voltammograms for two-layer films consisting of two identical layers of mesoporous silica, measured as reference, are comparable to those shown above for one layer with a comparable film thickness (**Figure 24**). Co-condensation of 3-[Bis(2-hydroxyethyl)amino]propyl-triethoxysilane results in an inclusion of amino groups with a pK_a value around 8 inducing a change of the mesopore wall charge. This results in a reduced exclusion of the negatively charged probe molecule $[Fe(CN)_6]^{3-/4-}$ at pH 9 visible by a detected j_p of 100 $\mu A/cm^2$ instead of 30 $\mu A/cm^2$ for unmodified mesoporous silica (**Figure 32**c). When printing two layers as a step gradient with different functional composition and individual film thicknesses of 140 nm, here mesoporous silica and 5 mol% co-condensed mesoporous silica (**Figure 32**b), the top layer which is in contact with the probe molecule solution seems to determine the overall transport characteristics. When the 5 mol% co-condensed mesoporous silica film is located on top (**Figure 32**b), the observed pore accessibility is very similar to the pure 5 mol% co-condensed mesoporous silica layers (**Figure 32**c) showing no exclusion of $[Fe(CN)_6]^{3-/4-}$ at 9. But when the unmodified mesoporous silica

layer is located on top of a 5 mol% co-condensed mesoporous film the exclusion of negatively charged $[Fe(CN)_6]^{3-/4-}$ at pH 9 is again observed (**Figure 32**d).

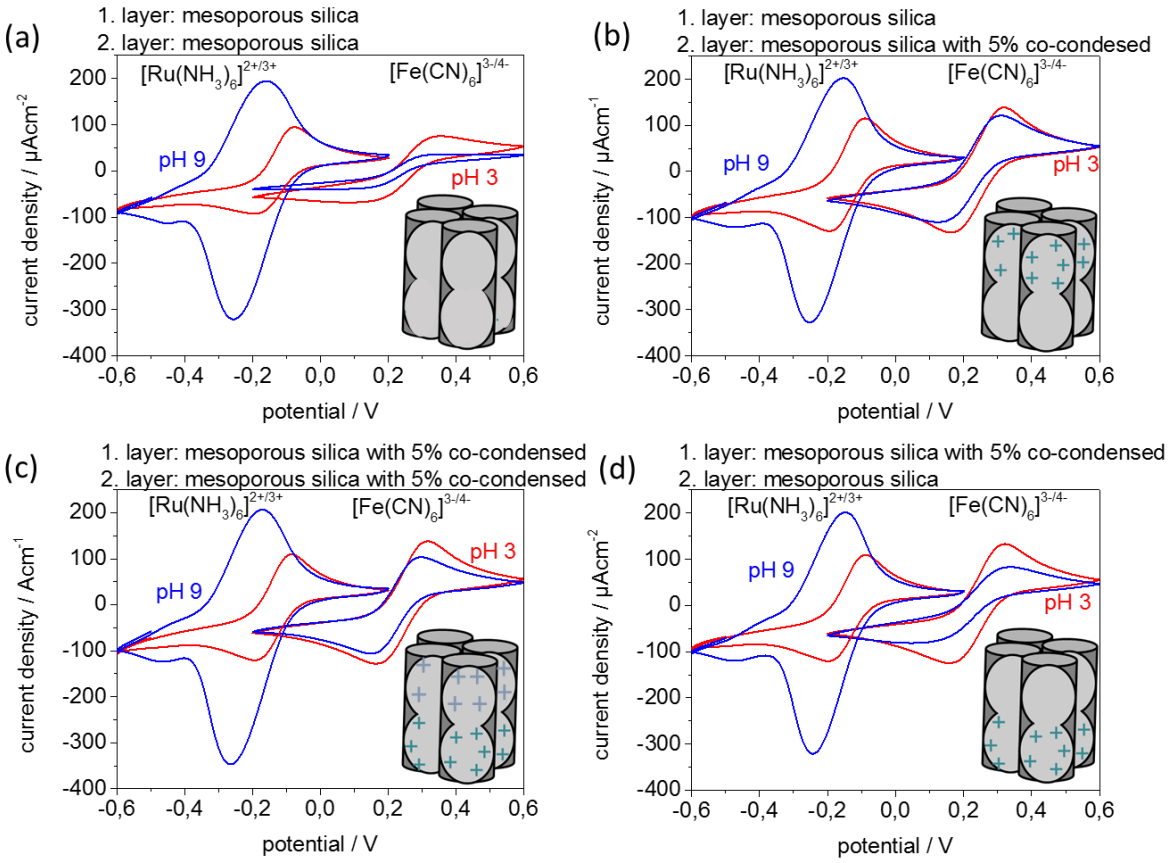

Figure 32. Cyclic voltammograms of mesoporous silica thin films using $[Ru(NH_3)_6]^{2+/3+}$ and $[Fe(CN)_6]^{3-/4-}$ as ionic redox probes at pH 3 (red) and 9 (blue). Mesoporous silica films prepared by gravure printing are prepared using the cell volumes 8.5 mL/m² resulting in film thicknesses 150 nm for one layer and 300 nm for two layers. a) Two gravure printed layers of unfunctionalized mesoporous silica. b) Two gravure printed layers consisting of a first mesoporous silica layer and a second mesoporous silica layer containing 5 mol% co-condensed 3-[Bis(2-hydroxyethyl)amino]propyl-triethoxysilane c) Two gravure printed layers of 5 mol % co-condensed mesoporous silica. d) Two gravure printed layers consisting of a first mesoporous silica layer containing 5 mol% co-condensed 3-[Bis(2-hydroxyethyl)amino]propyl-triethoxysilane and a second mesoporous silica layer. Figure adapted from N. Herzog *et al.* in RSC Adv. 2019, 9, 23570-23578 used by CC BY.

In summary gravure printing is a suitable tool for preparing multifunctional mesoporous silica films without a thermal intermediate step between the layers consisting of different ink.

6.1.6. Outlook

Evaporation induced self-assembly[5] is a well-established preparation method for mesoporous ceramic films. The multiple parameters, such as solution concentrations, pH, evaporation rate and aging conditions among others, allow the process to be tuned to obtain structural variety.[238]

An alternative might be to use photochemical control to produce films. Photochemical induced reaction instead of temperature induced reaction reduces the need to control kinetic variables and gives potential for a simpler production under milder conditions. Another advantage is the possibility of building complex architectures instead of films envisioning light to be locally applied or used in printing processes. One process suitable in this context is the so-called light-induced self-assembly (LISA). UV or visible light is applied to induce photolysis in photo-acid generators (PAGs) creating strong Brönsted acids that catalyze the sol-gel process.[239] Iodonium or sulfonium salts (Ph2I+X-) represent good PAGs for photopolymerization and can be combined with different initiating dyes, based on the type of irradiation to be used.[240] The role of a photosensitizer is to absorb light energy and generate excited species PS* that transfer an electron to the Ph2I+X- resulting in radical cations PS+•. The radical cations are responsible for acid generation (H+X), either by deprotonation of hydrogen donors or by interaction with other radical species. The strong ability of PAGs to initiate hydrolysis and condensation reactions potentially enables mesoporous film synthesis without solvents or water in the sol.[238] Besides simplicity, a remarkable advantage of this method is possibility to use visible light with a suitable PS. Curcumin is an example of such photosensitizer and can be applied with blue light.[88, 101]

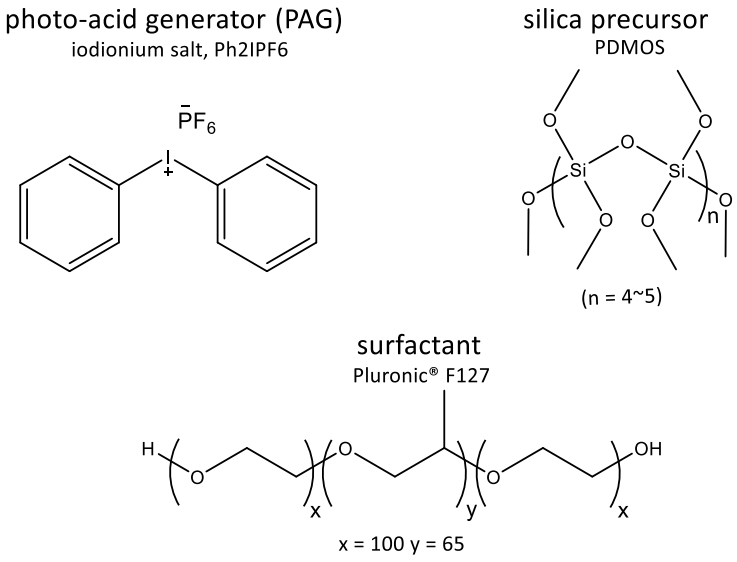

Figure 33. Molecular structures of the photo-acid generator (PAG) (iodionium salt, Ph_2IPF_6), silica precursor (PDMOS) and surfactant (Pluronic® F127) used in LISA process.

The first experiments are performed with UV light initiation in the explained LISA process. PDMOS is used as silica precursor, Pluronic ®F127 as surfactant, Ph_2IPF_6 as PAG together with ethanol and water as solvent (**Figure 33**). In **Figure 34**a the resulting ATR-IR spectra of the prepared structure are shown. The blue reference spectrum corresponds to a free-standing mesoporous silica film showing the three typical silica bands at 1050 cm^{-1}, 950 cm^{-1} and

800 cm^{-1} representing the Si-O-$Si_{asym.}$, Si-OH and Si-O-Si_{sym} vibration. The magenta spectrum corresponds to the reference of the glass substrate to show that the not scratched of printed mesoporous silica is too thick to allow detection of the glass substrate (printing ink is dropped on the glass substrate before UV light exposure. The printing ink spectrum in red shows a lot of vibrational bands because it is a mixture of all components present in the LISA process. Nevertheless, between 1050-800 cm^{-1} clear differences to mesoporous silica are visible. The printed mesoporous silica spectrum in black shows many differences to the printing ink (red). In the black spectra the silica bands for Si-O-Si and Si-OH are clearly visible. It should be mentioned that the surfactant (Pluronic® F127) is still present within the mesoporous silica (CH_3 vibrational band at 2800 – 3000 cm^{-1}). In **Figure 34**b the influence of UV-exposure time changes on ATR-IR spectra is shown. The spectra are nominated to the band at 826 cm^{-1}. With increasing UV exposure time, the Si-OH band and the Si-O-$Si_{asym.}$ increases. In **Figure 34**c a SEM image of the printed mesoporous silica film with the longest UV exposure time of 15 min is shown. A homogenous structure with pores are visible. It does not look like the typical images of optimized mesoporous silica films but very hopeful for further experiments.

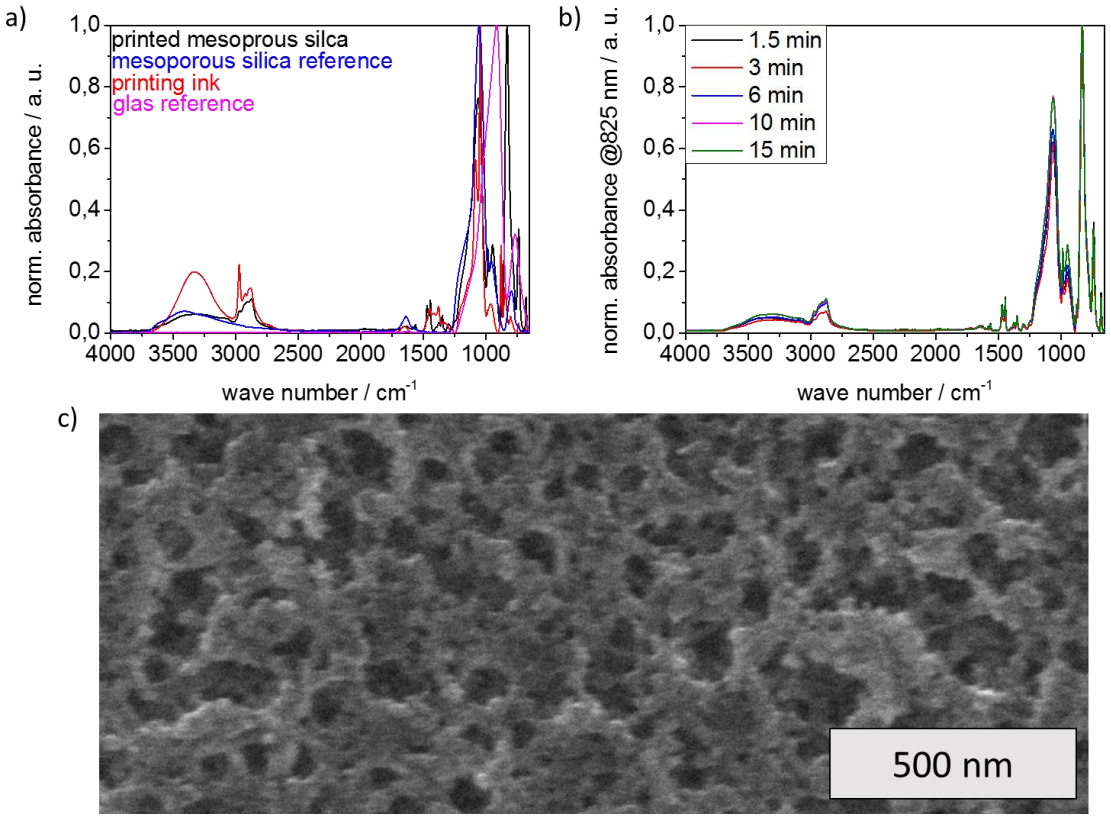

Figure 34. a) ATR-IR spectrum of printed mesoporous silica (black) and reference spectra of mesoporous silica, the printing ink and the glass substrate. b) the time depended exposure of UV light of 254 nm for printing mesoporous silica films varied between 1.5 min and 15 min. c) SEM image of the printed mesoporous silica film with 15 min UV light irradiation with 254 nm. Scale bar is 500 nm.

In further experiments the irradiation is adjusted to visible light of 405 nm. As inspired by Crivello *et al.* and Shi *et al*. curcumin is added to the printing ink in addition to the PAG.[101, 241] Curcumin is matching with an absorbance maximum of 425.8 nm to the laser wavelengths of 405 nm. The UV-Vis spectra collected in ethanol is shown in **Figure 36**a) and the chemical structure in **Figure 36**b). The used laser position can be varied and it is possible to print simple motives. In **Figure 35** images of the substrates with printing solution and after irradiation with the 405 nm laser are summarized. It is possible to see the printed areas indicated by arrows. In **Figure 35**a-e) TEOS is used as precursor and two different PAGs and the burn time of the laser is varied. But in all cases the film is not stably attached to the substrate. Consequently, after rinsing of the not irradiated ink, the entire film is removed. In **Figure 35**f) the precursor is changed to PDMOS and more solution because of higher viscosity could be used. In **Figure 35**g) the printed line is visible after rinsing the substrate with suitable solvent.

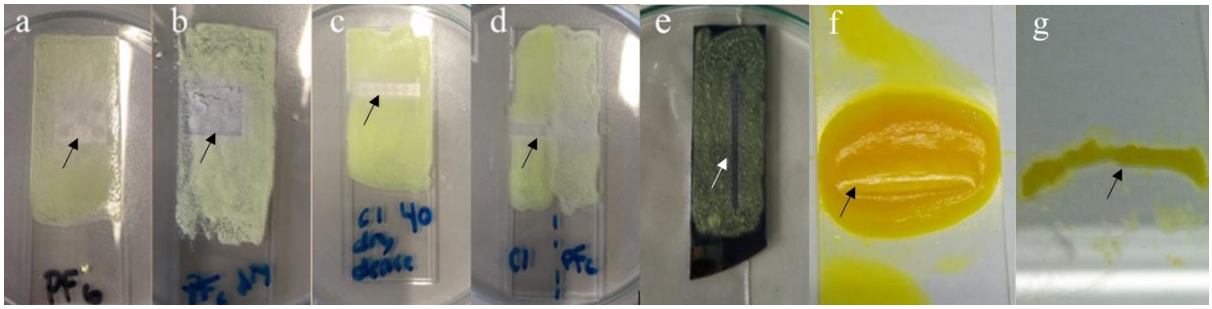

Figure 35. Images of substrates after coating with photoacid sol (Curcumin, one of two PAGs, acetone, TEOS, F127 and water) and irradiation under a 405 nm laser. (a) Diphenyliodonium hexafluorophosphate PAG on glass, burn time of 40 (arbitrary units). (b) Diphenyliodonium hexafluorophosphate PAG on glass, burn time of 60, solution allowed to dry before irradiation. (c) Diphenyliodonium chloride PAG on dense silica, burn time of 40. (d) Comparison of chloride (left)and hexafluorophosphate (right) PAGs on glass, burn time of 40. (e) Diphenyliodonium chloride PAG on dip-coated mesoporous silica, burn time of 40. (f) PDMOS/Iod-Cl/F127 layer before rinsing with solvent and (g) PDMOS/Iod-Cl/F127 layer after rinsing with solvent.

In **Figure 36**c) the ATR-IR spectra of the printed mesoporous silica (scratched of after rinsing with solvent) in black are shown compared to mesoporous silica in blue, bulk PDMOS in green and bulk Pluronic® F127 in magenta. The typical silica bends are visible in the printed silica spectrum (magnification in **Figure 36**d), Especially, the bands at 1050 cm^{-1} for Si-O-$Si_{asym.}$(orange area) is visible after printing compared to the reference spectra of bulk materials no bend in this area can be seen besides the mesoporous silica spectrum but also Si-OH (green area) and Si-O-$Si_{sym.}$ (yellow area). When comparing bulk F127 and the printed mesoporous silica it is visible that the F127 is still in pores after the printing process, which is expected because of no thermal treatment or chemical extraction.

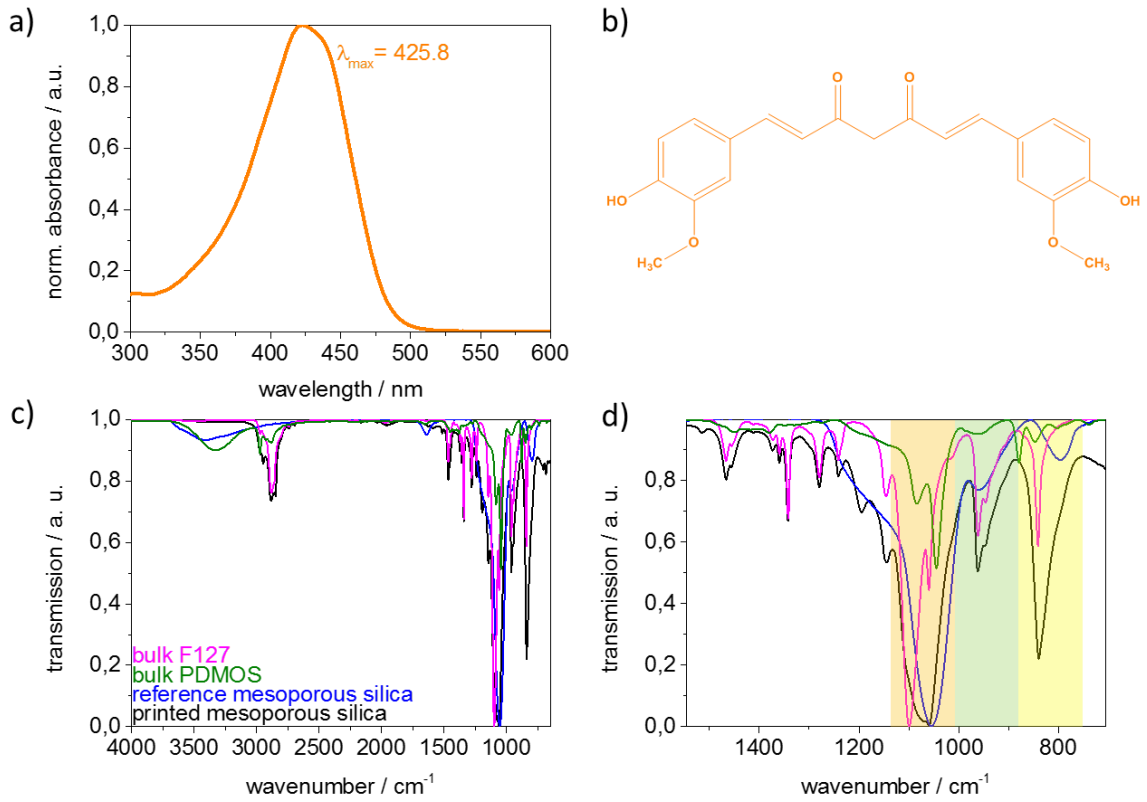

Figure 36. a) UV-Vis of curcumin in ethanol with a maximum of absorbance at 425.8 nm. b) the chemical structure of curcurmin c) ATR-IR spectra of bulk Pluronic ® F127 (magenta), bulk silica precursor PDMOS (green), mesoporous silica as reference (blue) and scratched printed silica (black) shown in **Figure 35** g). d) same spectra in terms of Si-O-$Si_{asym.}$, Si-OH and Si-O-$Si_{sym.}$ band colored in orange, green and yellow.

These first results show the potential of irradiation as an alternative process of printing mesoporous silica. In the next steps this system should be optimized regarding composition and structure formation aiming towards 3D printing. Especially, 3D printer working on a laser-based stereo lithography (SLA) or digital light processing (DLP) system are expected to be suitable. Both systems are working with light in form of laser or projector irradiate a liquid resin and harden it in the right form. Instead of resin it is possible to use the LISA process for printing freestanding mesoporous silica forms.

6.2. Dye-sensitized Polymerization

The mechanism of dye-sensitized polymerization is described in chapter 5.1. The following chapter is divided into four sub-chapters. Firstly, the characteristics of the dye and monomers are summarized. Secondly, the polymerization is investigated in solution (chapter 0). Thirdly, the polymerization in mesoporous silica films initiated with a laser (λ = 632.8 nm) or a LED (λ = 627 nm) is investigated and polymerization parameters such as polymerization time, irradiation energy, applied monomer concentration, etc. (chapter 6.2.3) are varied. Fourthly,

the polymerization in mesoporous films is transferred to initiation by near-field modes such as surface plasmons (SP) or transversal optical waveguide modes (TM) (chapter 6.2.4).

6.2.1. Characteristics of Applied Molecules

The polymerization is conducted using methylene blue as dye, 3-[Bis(2-hydroxyethyl)amino]propyl-triethoxysilane as coinitiator and 2-(Dimethylamino)ethyl methacrylate (DMAEMA) or phosphoric acid 2-hydroxyethyl methacrylate ester (MEP) as monomer. The coinitiator 3-[Bis(2-hydroxyethyl)amino]propyl-triethoxysilane is covalently grafted to the mesoporous silica film via post-grafting or co-condensation. The pH stability of methylene blue in 0.1 M aqueous $NaHCO_3$ solution is investigated with UV-Vis spectroscopy by measuring methylene blue solutions adjusted to different pH-values between 1.3-11.4 to ensure that fluctuations in pH have no effect on the dye solubility and absorption wavelength during polymerization (**Figure 37**a). As can be deduced from **Figure 37**a the maximum absorbance measured in 0.1 M aqueous $NaHCO_3$ solution at 661 nm is not influenced by the applied solution pH. This indicates that the use of different monomers resulting in different pH values in polymerization solution does not affect the methylene blue absorption. **Figure 37**b showing the chemical structure of the methylene blue as blue form on the right side. After interacting with the coinitiator and light irradiation the colorless ‚leuco' form is generated. According to literature the blue form (absorption at 661 nm, **Figure 37**a) is more stable and prefered.[242]

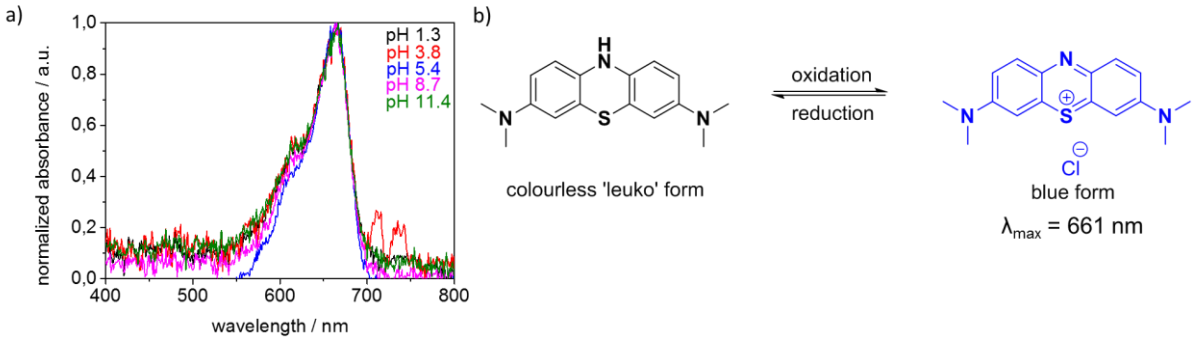

Figure 37. a) UV-Vis spectra of methylene blue dissolved in 0.1 M aqueous $NaHCO_3$ solution at different pH values between 1.3 and 11.4. The absorption maximum of methylene blue in this solvent is located at 661 nm. b) molecular structure of methylene blue in the colorless neutral "leuco" form switching to the positively charged form, knowing as the blue form of the dye.

For dye sensitized polymerization two monomers are selected based on their opposite and pH-responsive charge: 2-Dimethylaminoethylmethacrylate (DMAEMA) and 2-(methacryloyloxy)ethyl phosphate (MEP). DMAEMA (**Figure 38**a) has a calculated pK_a value of 8.18.[243] The titration of the PDMAEMA (polymerized via radical polymerization with AIBN as

initiator) against 0.1 M HCl solution shows a pK_a value at 8.4, which corresponds to the pK_a of the monomer (**Figure 38**a). MEP (**Figure 38**b) has two pK_a values. In literature $pK_{a1} = 4.5$ and $pK_{a2} = 7.7$ is given.[244] When titrating MEP (polymerized via radical polymerization with AIBN as initiator) against 0.1 M NaOH solution pK_a values of 2.5 and 7 are determined, which is slightly lower compared to the monomer values.

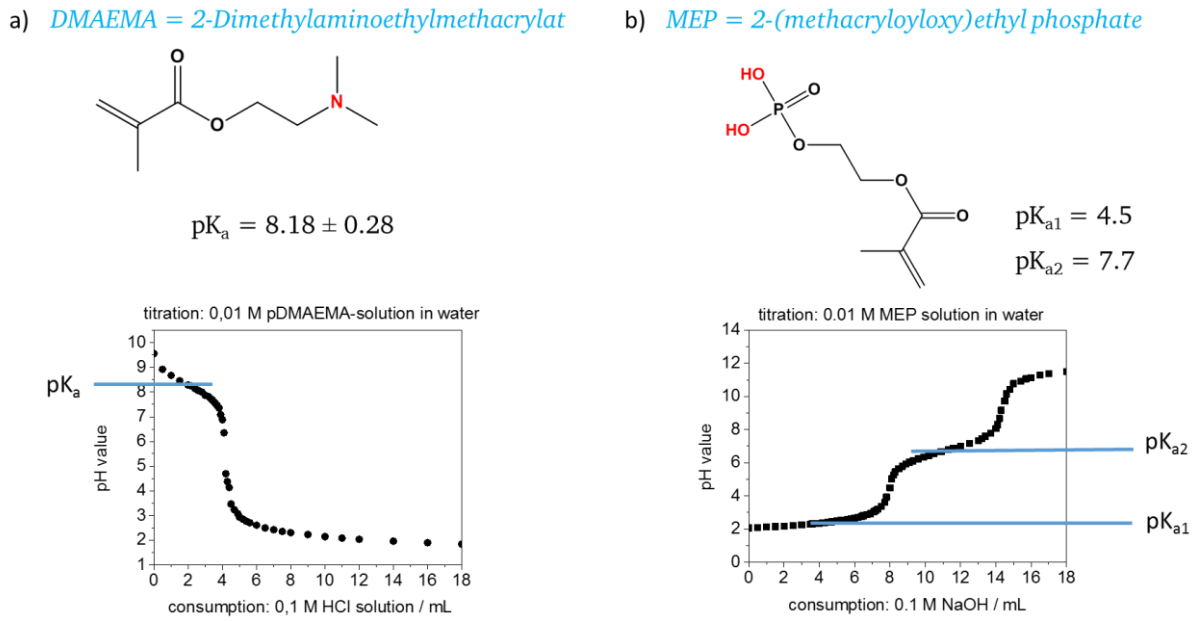

Figure 38. a) Molecular structure of 2- Dimethyaminiethylmethacrylat (DMAEMA) used as monomer in this work. The given pK_a value is predicted using Advanced Chemistry Development (ACD/Labs) Software V11.02 (© 1994-2016 ACD/Labs). The titration curve of a 0.01 M PDMAEMA solution using 0.1 M HCl solution is shown and the pK_a value is also in the calculated area. b) Chemical structure of 2-(methacryloyloxy)ethyl phosphate with known pK_a values of 4.5 and 7.7 from literature.[244] The curve shows the titration of a 0.01 M PMEP solution in water against 0.1 M NaOH solution showing pK_a values at around 3 and 7.

In summary, methylene blue is an ideal initiator because it is stable over a wide pH range and its excitation spectrum ideally matches the red He/Ne laser at 632.8 nm. DMAEMA and MEP are used as pH-responsive monomers/polymers.

6.2.2. Polymerization in Solution

To get first information on the dye-sensitized polymerization for a two-component system consisting of methylene blue as dye and 3-[Bis(2-hydroxyethyl)amino]propyl-triethoxysilane as coinitiator, a secondary amine, polymerization is conducted in solution. For this purpose, the coinitiator, propyldiethanolamine, without the triethoxysilane anchor group, namely a monocationic cholinium-derivative, has to be synthesized because it is not commercially available. Therefore, diethanolamine and 1-brompropan is heated with sodium iodide in

acetonitrile to 60 °C for 5 d (see appendix, **Figure 92**a).[245] The characterization of the anchorless coinitiator (2,2'-(propylazanediyl)bis(ethan-1-ol)) is done with ^{1}H NMR (300 MHz, D_2O) showing that a clean coinitiator is obtained.

The polymerization in solution is performed for up to 120 min under red light irradiation (λ=627 nm) using LED (120 mW/cm²) as irradiation source. To investigate the time dependence, aliquots are taken, cooled down to 0 °C and store in dark to stop polymerization prior to analysis by ATR-IR and ^{1}H NMR. ATR-IR characterization is adapted from Deeb *et al.*[24] monitoring the C=C vibrational band at 1635 cm^{-1}, while the spectra are normalized to the OH vibrational band at 3360 cm^{-1} of the solvent. In this study methyldiethanolamine instead of the propyldiethanolamine is used as coinitiator as it is similar to the surface bound coinitiator used in later studies for polymerization in mesoporous silica films. The C=C vibrational band at 1635 cm^{-1} (**Figure 39**a) decreases with increasing polymerization time indicating the conversion of the monomer double bond to a single bond during polymerization. The monomer conversion of the polymerization is calculated by ^{1}H NMR. Therefore, the ratio of the single proton in the double bond signed with green c in **Figure 39**b to the two terminal protons of the double bond marked with green a and b is compared. Starting with a ratio from the start monomer the conversion is calculated (in %). In **Figure 39**c and d the monomer conversion (blue) and the change in the intensity of the C=C vibrational band is shown for varying methylene blue amounts in the solution. In **Figure 39**d the concentration of dye is one third of compared to **Figure 39**c while monomer and coinitiator concentration is constant. In both cases the C=C vibrational band is decreasing while the monomer conversion is increasing with increasing polymerization time. After 90 minutes polymerization time a conversion of around 20 % is reached. The used methylene blue concentrations do not seem to have a significant influence on the conversion. In both series the critical concentration of methylene blue is exceeded and a polymerization takes place. In the following experiments the methylene blue concentration is always higher than the 0.0003 mg/mL which is expected to lead to a successful polymerization.

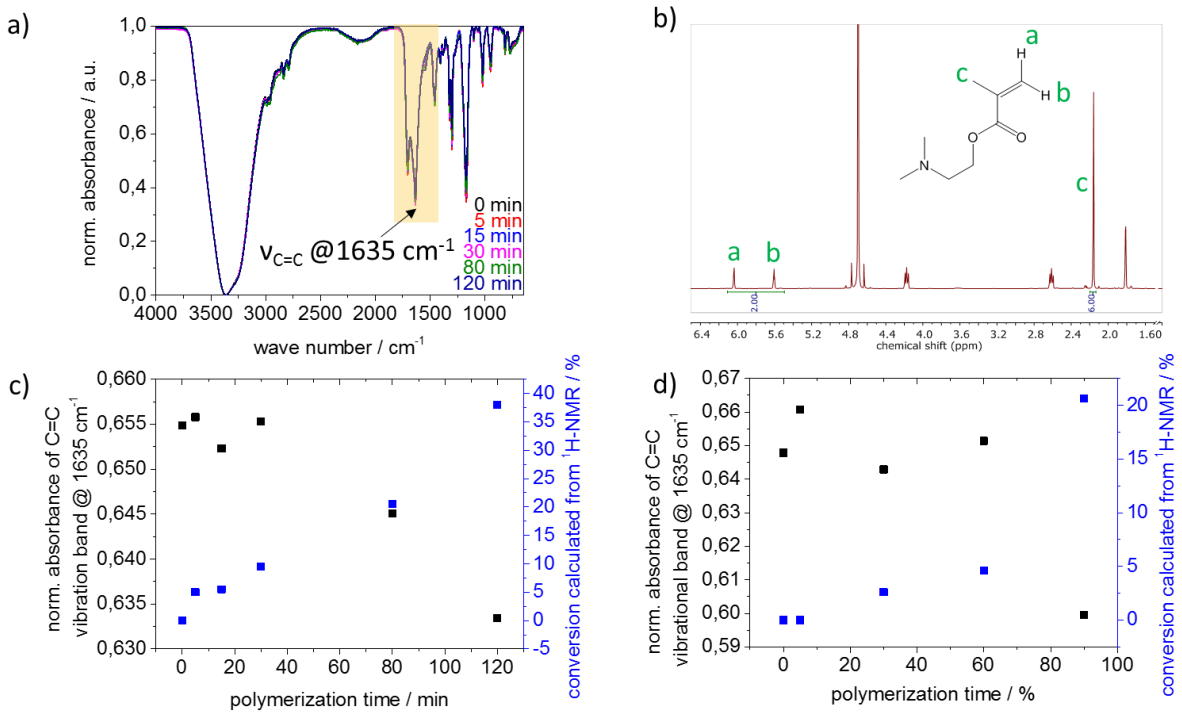

Figure 39. Free radical polymerization of coinitiator/methylene blue system with DMAEMA as monomer. a) ATR-IR spectra of the polymerization solution including a zoom onto the C=C vibrational band at 1635 cm^{-1} (yellow area) in dependence of the polymerization time. b) 1H NMR (300 MHz, D_2O) spectrum of the polymerization solution as an example for calculation of the conversion of the polymerization. The relevant signals are assigned with green letters to the chemical structure of the DMAEMA monomer. c) Characterization of a time dependent polymerization with the coinitiator not carrying an anchor group. Polymerization is done with LED (λ=627 nm, 700 mA). (Polymerization solution: 0.497 g/mL DMAEMA, 0.0011 g/mL methylene blue, 0.0044 g/mL mg propyldiethanolamine in 0.1 M aqueous $NaHCO_3$ solution). d) Time dependent polymerization with anchorless coinitiator using only 0.0003 g/mL of methylene blue. Polymerization is done with LED (λ=627 nm, 700 mA).

It is important to note that the methylene blue can be regenerated after polymerization. Without irradiation the methylene blue switches back from 'leuko' form to the colored form (**Figure 37**b). Methylene blue dye regeneration within the polymerization solution is monitored by UV-Vis spectroscopy using the kinetic mode for 780 min (**Figure 40**a). The maximum absorbance of methylene blue in polymerization solution (DMAEMA, 0.1 M $NaHCO_3$ solution → pH 9) is located at 660 nm. Plotting the absorbance at 660 nm in dependence of time shows that methylene blue regeneration is a relatively slow process reaching an almost constant value after 600 minutes (**Figure 40**b). Under the applied conditions after 13 h, 75 % of the initial absorbance are recovered indicating simultaneously occurring dye bleaching and regeneration, during the polymerization.

In addition to dye consumption inhibition by present oxygen has to be considered as explained in detail in mechanism postulated by research group of O. Soppera in chapter 5.1 (**Figure 8**). Oxygen can react with the triplet state of the dye to a peroxide radical which is not active for

polymerization and reduced the effectivity of the polymerization.[24] On one hand, the protonated dye radical can react with another protonated dye radical to the leuco form, which is responsible for dye bleaching. On the other hand, the protonated dye radical can react in a disproportionation reaction with other radicals. The dye is regenerated in the original form, the active species and can used for polymerization again. This means the bleaching and the regeneration of the dye is a competitive process. In order to achieve comparable conditions in this study, the degassing of the polymerization solution is always carried out directly before polymerization and is kept constant for all experiments.

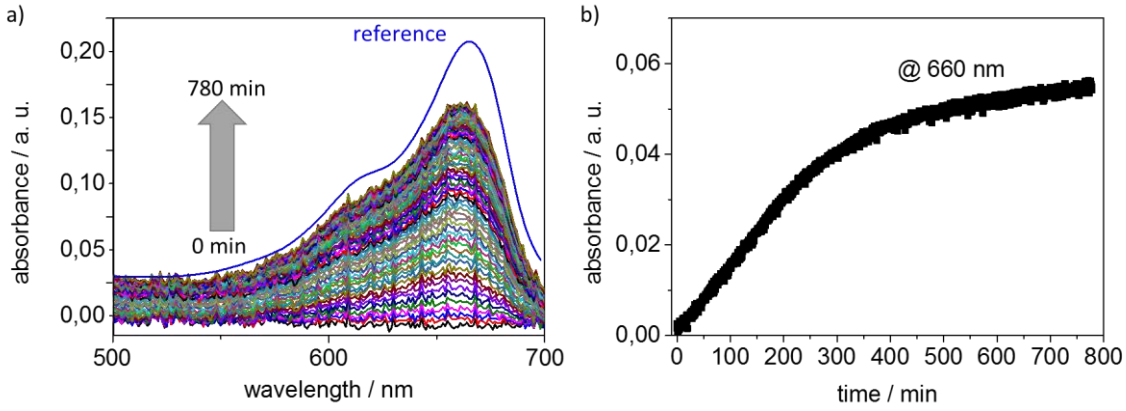

Figure 40. Methylene blue recovery. a) UV-Vis spectra over time for 780 min after 30 min polymerization with Lumatec®Lamp (32 mW/cm²) for 30 min showing a growing absorbance of the methylene blue. b) Plot of the maximal absorbance at 660 nm against the recovery time.

With the aim to go towards near-field induced and localized polymer functionalization of mesoporous films the dye sensitized polymerization is intended be applied as a surface-induced polymerization in mesoporous silica films. As chemical kinetics are specific on this length scale and cannot be extrapolated from microscales the polymerization has to be explored in these pores as a next step using the here determined suitable conditions.[24] For polymerization in mesopores diffusion processes are expected to play an important role, as the diffusion of molecules at the nanoscale takes less time than the exposure time and might be strongly determined by surface forces and for example by electrostatic interaction. Therefore, the intensity of the radiation probably plays a decisive role. In addition, the amount of chemical species present is limited, so all photochemical reactions, including the regeneration of the dye, can play a major role.

6.2.3. Polymerization in Mesoporous Silica

To investigate the diffusion of the reaction components, used for dye sensitized polymerization, into the mesoporous silica films adsorption experiments are performed and characterized with ATR-IR spectroscopy and UV-Vis spectroscopy. To analyze the accessibility for example, a mesoporous film is incubated in methylene blue solution followed by subsequent analysis of UV-Vis absorption of these films after incubation as well as after incubation and extraction. This experiment reveals the adsorbed dye amount as well as the suitability of the extraction conditions to remove unbound dye. To characterize the adsorption of monomer the corresponding experiments are performed in combination with characterization by ATR-IR spectroscopy. **Figure 41** shows the UV-Vis measurements after methylene blue incubation. The corresponding ATR-IR data after monomer incubation are shown in **Figure 42** and **Figure 43** for mesoporous films with coinitiator functionalization using post-grafting (**Figure 41**a and **Figure 42**) or co-condensation (**Figure 41**b and **Figure 43**), respectively. When using mesoporous silica films directly after functionalization the coinitiator is located inside the mesopores and on the top surface of the mesoporous film (**Figure 42**a and b). After the mesoporous film surface is treated with CO_2 plasma[237] for 12 s the organic groups on top of the mesoporous silica films are removed and functionalization exclusively inside the mesopores is achieved (**Figure 42**c and d). Two monomers, positively charged or neutral DMAEMA and negatively charged or neutral MEP are used. Mesoporous silica films functionalized with coinitiator are incubated into the monomer, methylene blue and polymerization solution for 30 minutes each to investigate the accessibility of molecules required for polymerization. Subsequently, the incubated films are dried with pressed air and measured with UV-Vis and ATR-IR spectroscopy.

Methylene blue in aqueous solution shows an absorbance at 661 nm (see chapter 6.2). When incubating the coinitiator functionalized mesoporous silica films deposited on a glass substrate with methylene blue dissolved in water (**Figure 41**, blue and magenta line) an absorption maximum between 600-670 nm is detected indicating methylene blue infiltration and adsorption into the mesoporous film. After incubation with polymerization solution, consisting of 9:1 vol. ratio of monomer and methylene blue solution (9:1 monomer : MB = 225 mg/mL DMAEMA, 0.0052 mg/mL MB in 0.01 M $NaHCO_3$) no absorbance for methylene blue is observed. There are two possible reasons for this observation: firstly, methylene blue is present in the mesoporous silica films but cannot be detected because of low concentration in mesoporous silica films. Secondly, the monomer present in this solution suppresses the methylene blue diffusion and adsorption into the mesoporous silica film. In **Figure 41**c a coinitiator functionalized mesoporous silica coated substrate after incubating with

a highly concentrated methylene blue solution (left picture) is shown. Incubating this strong blue colored substrate into the polymerization solution results in a colorless substrate afterwards (right picture) indicating the visible blue color is washed of the glass supported mesoporous silica film. In all other experiments the concentration of methylene blue and polymerization solution is identical to the polymerization experiments using 225 mg/mL DMAEMA, 0.0052 mg/mL MB in 0.01 M $NaHCO_3$. Methylene blue as well as the coinitiator and DMAEMA can be positively charged, whereby repulsive electrostatic charges can be carefully excluded by the successful incubation in coinitiator functionalized mesoporous silica films of pure methylene blue as well as pure monomer solution. In addition, the polymerization solution as well as the monomer solution has a pH value of 8-9. This high pH value is chosen to guarantee a neutrally charged coinitiator and a negatively charged mesopore wall due to remaining deprotonated silanol groups. This negative charge is expected to favor pore accessibility for methylene blue and DMAEMA/MEP (both are neutral charged). Thereby, the absorbance intensity of the C=O vibrational band for both monomers is not directly comparable, because of different extinction coefficients.

When changing the monomer to negatively charged MEP the incubation with polymerization solution show no detectable adsorption of methylene blue in mesoporous silica films (**Figure 41**) compared to incubation of pure (monomer-free) methylene blue solution. These experiments lead to the conclusion that the second assumption is probably correct and that the presence of the monomer seems to hinder the diffusion of the dye into the mesopores. This has to be kept in mind for further polymerization experiments. Because of polymer formation seen in **Figure 42** and **Figure 43** the dye-sensitized polymerization is a working system and further used for polymer functionalization in mesoporous silica films.

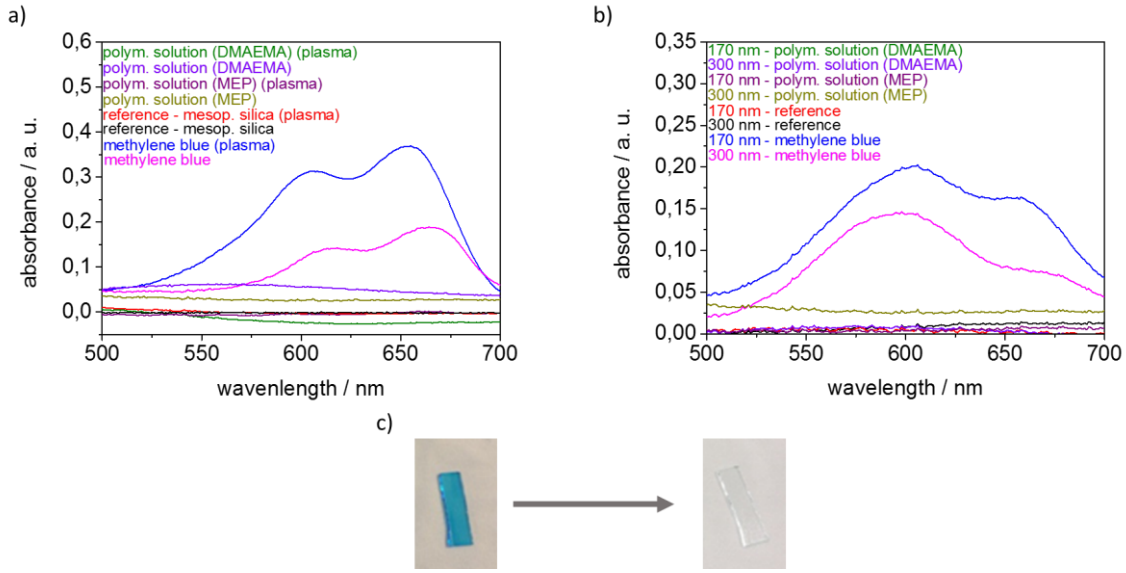

Figure 41. UV-Vis spectra of the incubation experiments in a) **Figure 42** and b) **Figure 43** measured after drying with compressed air after incubation with the solution given in the legend. c) Showing a blue colored mesoporous silica film with coinitator incubated in a methylene blue solution and dried afterwards changing to colorless mesoporous silica film incubating in polymerization solution consisting out of DMAEMA and methylene blue in 0.1 M $NaHCO_3$ solution.

After looking at the methylene blue adsorption in absence or presence of monomer, the monomer adsorption in absence or presence of methylene blue is investigated. The monomer is thereby detected using ATR-IR spectroscopy looking at the C=O vibrational band at 1730 cm^{-1}. In accordance to the methylene blue adsorption experiments (**Figure 41**) the mesoporous silica films are post-grafted with the coinitiator. In all samples (**Figure 42**a-d), a C=O vibrational band is observed for mesoporous films incubated into monomer solution as well as for mesoporous silica films incubated into polymerization solution containing monomer and methylene blue. This ensures that monomer is present in the mesoporous silica films under all conditions and especially under polymerization conditions.

In addition, one mesoporous film is polymer functionalized for 1 h under laser irradiation (λ = 632.8 nm, 5 mW) and measured before (green) and after (dark blue) extraction with water to analyze the covalently grafted polymer amount in comparison to the maximum amount of only adsorbed and thus extractable monomer. Monomer and polymer amount is analyzed based on the C=O vibrational band at 1730 cm^{-1} in Si-OH (900 cm^{-1}) normalized spectra. The presence of methylene blue in the mesoporous silica films (magenta) cannot be investigated by ATR-IR, since no characteristic functional groups are visible compared to the reference mesoporous silica film. In order to show that the monomer is also available for polymerization inside the mesoporous silica films, the coinitiator bound to the outer surface is removed by CO_2 plasma treatment[237]. Upon monomer extraction the C=O vibrational band for

PDMAEMA/PMEP functionalized mesoporous silica films is reduced to more than a half (from 0.02 to 0.0075, **Figure 42**a, green, dark blue) of the original absorbance after polymerization before extraction of unbound monomer. This indicates that a significant amount of unreacted monomer or solution polymer is removed by extraction with water. In a reference experiment the complete extraction of adsorbed monomer in mesoporous silica films with water is shown (see appendix, **Figure 93**).

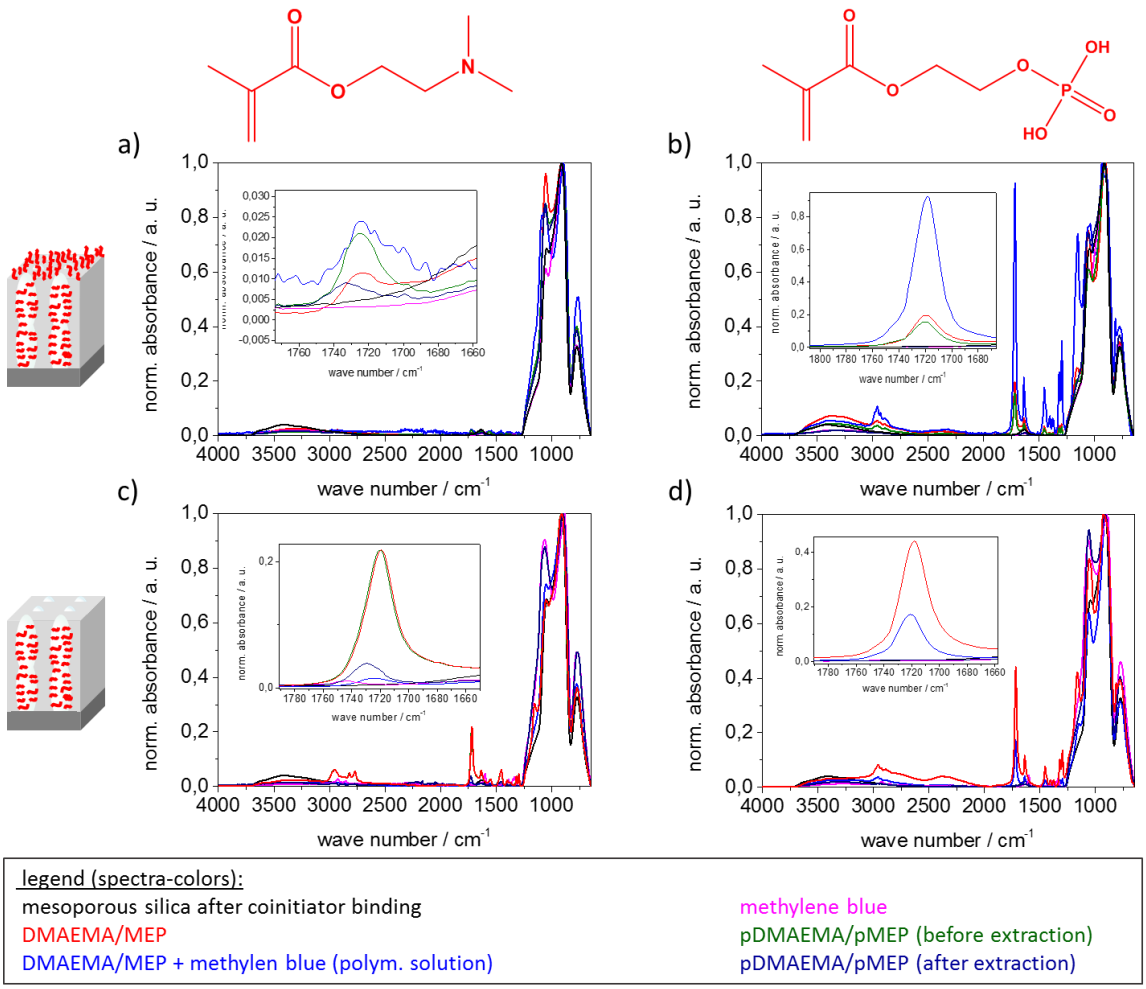

Figure 42. Reference experiments showing ATR-IR spectra after incubation of the coinitiator functionalized mesoporous silica films into monomer solution in the absence and presence of methylene blue as well as a polymer functionalized mesoporous silica film (1 h, 5 mW laser power) before and after extraction with water. The magnification is showing the C=O vibrational band at 1730 cm^{-1} in Si-OH (900 cm^{-1}) normalized spectra. Incubation of mesoporous silica films into DMAEMA a) and MEP b) polymerization into a 350 nm thick mesoporous silica film without CO_2 plasma treatment. 350 nm thick mesoporous silica film after plasma treatment[237] afterwards and incubation experiments with DMAEMA d) same conditions like in c) but with MEP as monomer.

The same incubation experiments are performed with coinitiator co-condensed mesoporous silica films for both monomers, DMAEMA (**Figure 43**a and c) and MEP (**Figure 43**b and d). In addition two mesoporous film thicknesses, 170 nm (**Figure 43**a and b) and 300 nm (**Figure 43**c and d) are characterized. It has to be noted that the ATR-IR spectra are recorded directly

from glass substrate and so the penetration depth of the evanescent field into the mesoporous silica coated glass substrates are varying using different mesoporous film thicknesses (compare chapter 8.2.1).

The polymerization solution as well as the monomer adsorb into the mesoprous silica which is confirmed by the detected C=O vibration band at 1730 cm^{-1}. In addition, the ATR-IR spectra after polymerization before extraction show a C=O absorbance which is more than twice as high as after polymerization and extraction. This shows again that a lot of unpolymerized monomer remains in the mesoporous films. This is absolutly fine because in solution polymerization under identical polymerization conditions a monomer conversion of 40 % could be achieved after a polymerization of 2 h. In **Figure 43**c, d the mesoporous film thickness is higher, which show no problems for the polymerization solution to diffuse into the films.

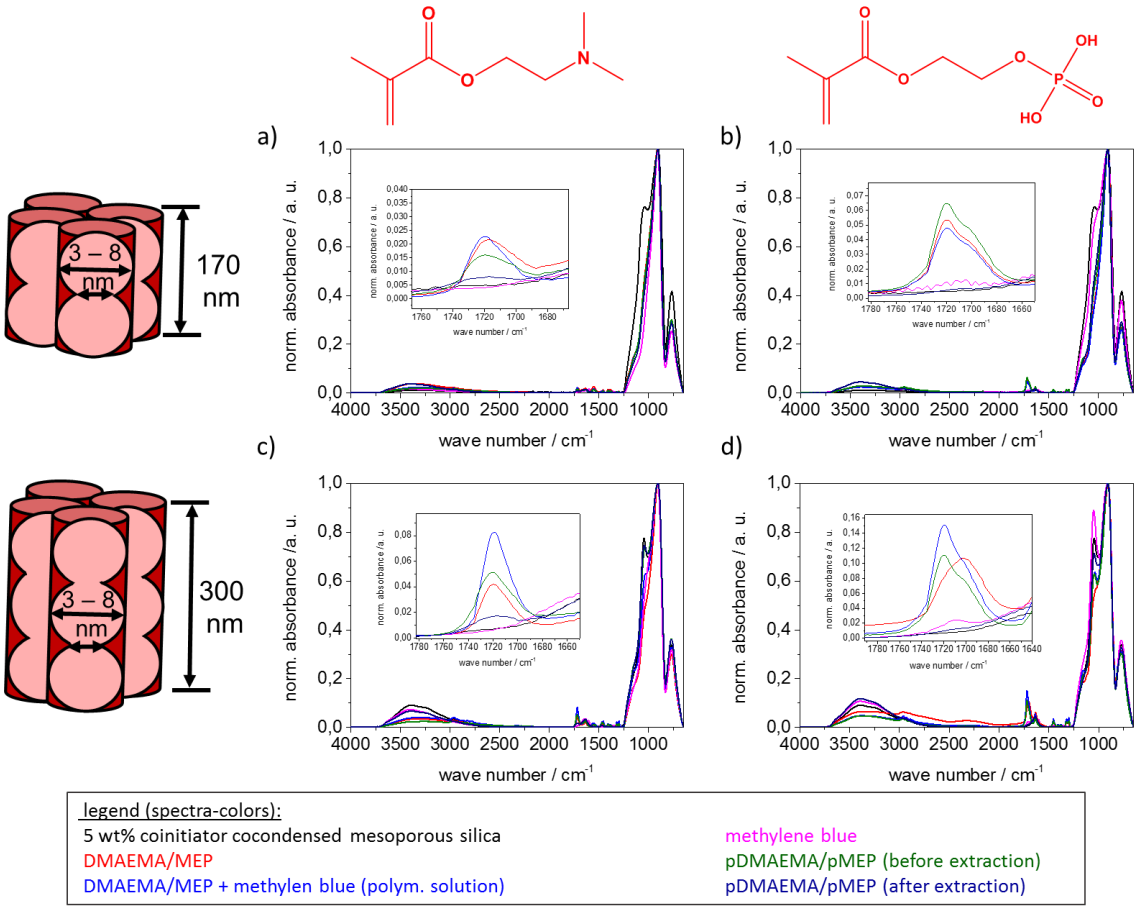

Figure 43. Reference experiments showing ATR-IR spectra after incubation of the 5 mol% coinitiator co-condensed mesoporous silica film into monomer solution in the absence and presence of methylene blue as well as a polymer functionalized mesoporous silica film (1 h, 5 mW laser power) before and after extraction with water. The magnification is showing the C=O vibrational band at 1730 cm^{-1} in Si-OH (900 cm^{-1}) normalized spectra. Incubation of mesoporous silica films into DMAEMA (a) and MEP (b) and polymerization into a 170 nm thick mesoporous silica film. 300 nm thick mesoporous silica film with incubation experiments of DMAEMA d) same conditions like in c) but with MEP as monomer.

Although, no significant absorbance related to dye adsorption into the mesoporous silica films could be observed in case the monomer is present (polymerization conditions) (**Figure 41**) while monomer is adsorbed (**Figure 42** and **Figure 43**) dye sensitized polymerization takes place under irradiation. It has to be noted that polymerization under the same conditions in absence of methylene blue could not be detected (see appendix, **Figure 94**). Polymer formation using dye sensitized polymerization inside mesopores is proven after removing the coinitiator from the outer surface with CO_2 plasma[237] for 12 s as indicated by the C=O vibrational band at 1730 cm^{-1} (**Figure 43**c and d). Consequently, the amount of methylene blue in the pores, although not detectable by UV-Vis spectroscopy, seems to be sufficient to start a polymerization upon visible light irradiation.

Light can heat liquids as a function of its energy. For example, a 10-minute exposure to visible light (400-700 nm) with 936 W/m² can heat the polymerization solution by 2 °C measured in an experiment with Lumatec®Lamp. The thermal initiation of the dye sensitized polymerization with methylene blue and DMAEMA is investigated to exclude that the polymerization is in fact initiated by temperature. In **Figure 44** the ATR-IR spectra of the test of thermal polymerization with the dye sensitized system is shown. The coinitiator functionalized mesoporous silica film is incubated into polymerization solution and heated to 70 °C for 1 h. The spectra after extracting the polymerization solution without (blue) and with heating (red) are shown and compared to the reference spectrum (black). Here no differences and especially no C=O vibrational band at around 1730 cm^{-1} are visible. Consequently, a thermal initiation of the dye-sensitized polymerization can be excluded under the applied conditions.

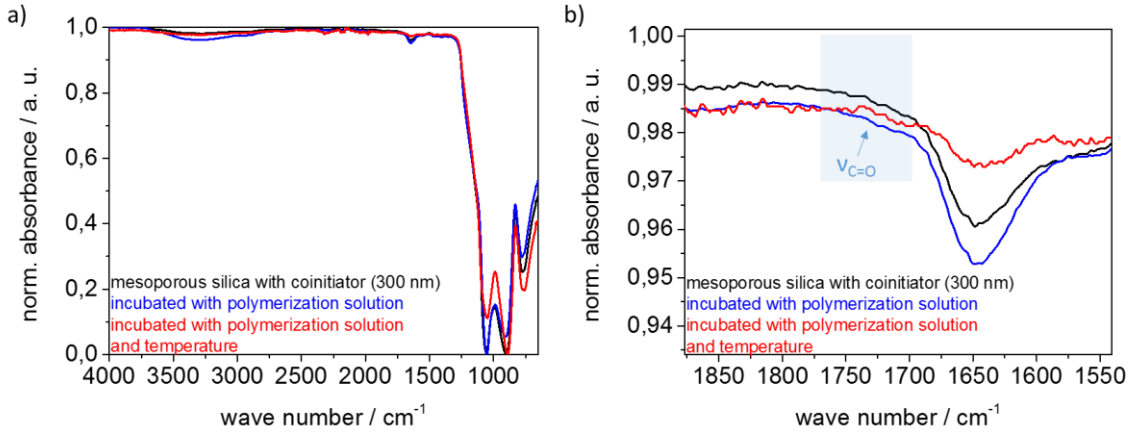

Figure 44. Thermal initiation of the dye sensitized polymerization. a) ATR-IR spectra of coinitiator functionalized mesoporous silica film of 300 nm thickness (black) and of coinitiator functionalized mesoporous silica after contact with the polymerization solution and extraction with (blue) and without (red) heating at 70 °C for 1h. b) Zoom onto the range of 1825-1550 cm^{-1}. The area of the C=O vibrational band at around 1730 cm^{-1} is highlighted in blue.

The C=O vibrational band intensity at 1730 cm^{-1} can be correlated with the free pore volume calculated by Bruggeman effective medium theory based on changes in refractive indices before and after polymerization detected by ellipsometry. To give an indication on the correlation of pore filling and ATR-IR signal intensity, **Figure 45**a shows ATR-IR and ellipsometry data which are extracted from a study of Dr. Jessica C. Tom *et al.* published in *Polymers,* 2017, 9(10), 539.[135] The shown data are produced by using iniferter-initiated polymerization using DMAEMA as monomer in mesoporous silica films (170 nm film thickness). According to this data already an absorbance of 0.017 of the C=O vibrational band (normalized to Si-OH band, ATR-IR measured directly from substrate of 170 nm thick mesoporous silica films) leads to a polymer filled mesoporous silica film visible by a free pore volume of less than 5 vol% (blue). **Figure 45**b showing ATR-IR spectra of scratched mesoporous silica (black) and scratched mesoporous silica after polymerization with dye sensitized polymerization of DMAEMA/methylene blue system with Lumatec®Lamp. The data from previous research published in *Chem. Commun.*, 2015, 51, 11697-11700.[136] show a C=O vibrational band absorbance of 0.056 (normalized to Si-O-$Si_{asym.}$ (1070 cm^{-1}) vibrational band) correlates to a polymer with a molecular mass of 760 – 825 g/mol (polymer is degrafted with TBAF according R. R. Patil *et al.*[246]). When the molecular weight of the monomer (157.21 g/mol) is taken into account, this corresponds to 4-5 monomers per chain. This low amount of repetition units generated in the mesoporous silica is also shown in previous studies using iniferter induced polymerization of Silies *et al.*.[134] The amount of polymer in the mesopores is not determined by the chain length but by the number of chains, regardless of whether the mechanism is a controlled or free radical polymerization.

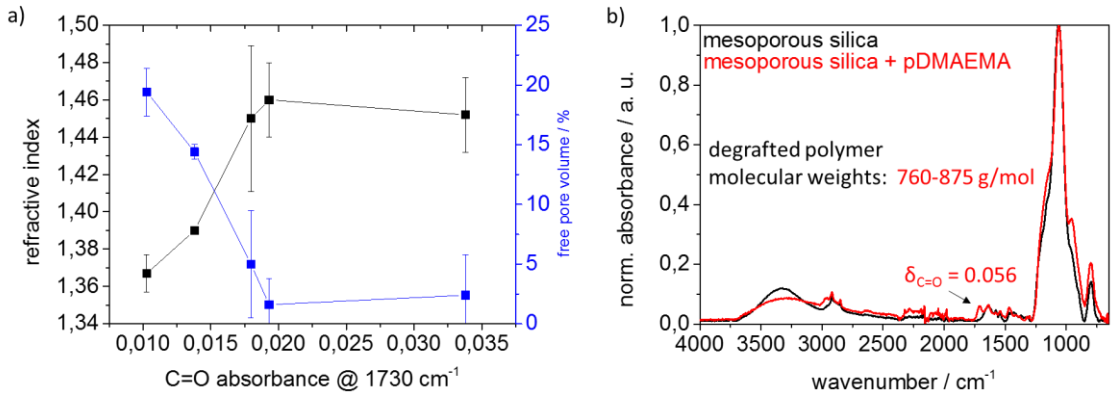

Figure 45. In experiments from Jessica C. Tom published in Polymers 2017, 9, 539 the C=O absorbance at 1730 cm^{-1} and data for pore filling during the iniferter induced polymerization with DMAEMA calculated from the refractive indices knowing from measurements with ellipsometry are combined and shown in a). The film thickness is 230 nm. Figure adapted from J. C. Tom *et al.* in Polymers 2017, 9, 539 used by CC BY. In b) the ATR-IR spectra of polymer of a dye sensitized polymerization with DMAEMA on mesoporous silica is shown. The analog degrafted polymer show molecular weights in GPC and MS of around 760-875 g/mol. The C=O band absorbance is 0.056.

In the example polymerizations with comparable mesoporous silica films used in **Figure 45**a and monomer DMAEMA during the incubation experiments the absorbance of the C=O vibrational bands could be reached with about 0.01 at a polymerization of 1 h at 5 mW (**Figure 43**a, 170 nm film thickness). This indicates that the mesopores are not completely filled with polymer because around 20 % of free pore volume is still available.

Polymerization with red light LED (λ = 627 nm)

In **Figure 46** the dye sensitized polymerization of DMAEMA and MEP with methylene blue and coinitiator covalently bound to the mesoporous silica surface is investigated in dependence of the polymerization time (ATR-IR spectra see appendix, **Figure 95**, **Figure 96** and **Figure 97**). The light intensity of the red light LED (λ = 627 nm) is set constant to 120 mW/cm^2. The error bars represent repeated measurements on one substrate. In **Figure 46**a, b the coinitiator is co-condensed in mesoporous silica films of 170 nm (**Figure 46**a) and 300 nm (**Figure 46**b) film thickness, while the coinitiator is post-grafted in case of **Figure 46**c. The C=O vibrational band at 1730 cm^{-1} in Si-OH normalized spectra belonging to DMAEMA is plotted against the polymerization time. In addition, the difference between polymerization inside the mesopores (CO_2-plasma treated, dark color) and on the outer surface as well as inside the mesopores (light color) is depicted. For all conditions the C=O absorbance increases with increasing polymerization time up to 60 minutes, which would be expected for a free radical polymerization. Deep *et al*. shows that for a free radical photopolymerization the monomer conversion is limited in dependence of used energy and show a degressive course.[24] This means the monomer conversion increases more and more slowly and approaches a final value. In addition, a rapid increase in monomer conversion is evident in the initial period of polymerization up to 60 min (**Figure 46**).

Considering the error bars, the values for the C=O absorbance for the polymer-functionalized mesoporous silica films with or without plasma treatment are comparable. As the ATR-IR spectra are measured on the substrate the measured C=O band intensities of different film thicknesses cannot be directly compared because of the different penetration depths of the evanescently decaying optical field of the ATR-IR into the mesoporous silica films as discussed in chapter 6.1 and 8.2.1. Nevertheless, the time dependence of polymer formation can be compared between both film thicknesses (170 nm and 300 nm) even if the absolute values are affected by the film thickness. The time dependent C=O vibrational band in Si-OH (900 cm^{-1}) normalized spectra for post-grafted coinitiator and PDMAEMA functionalized mesoporous silica films (**Figure 46**c) behaves equal to the previously discussed polymerization on co-condensed

mesoporous silica films showing an increasing polymer amount with increasing polymerization time. This is clearly shown in **Figure 46**c (post-grafted coinitiator functionalization, 170 nm, red and 300 nm, blue) where, the C=O absorbance of PDMAEMA functionalized mesoporous silica films and coinitiator co-condensed silica films functionalized with PDMAEMA (170 nm, **Figure 46**a and 300 nm, **Figure 46**b) are compared with regard to the C=O vibrational bands in Si-OH (900 cm^{-1}) normalized spectra showing absorbance in the same areas. When changing the monomer to MEP, polymer amount increases with polymerization time up to comparable absorbances as for DMAEMA (**Figure 46**d). The error bars are significant, which is attributable to a worse solubility of MEP in aqueous 0.1 M $NaHCO_3$ solution and a resulting inhomogenous monomer distribution in solution due to low solubility. This can be avoid by using DMF as solvent showing in Brilmayer *et al.*[247]. But as polymerization is intended to be carried out in an SPR setup and not under a fume hood later, the polymerization conditions here have not been changed and aqueous solution is preferred. Nevertheless, the increase of PMEP amount with time is visible (**Figure 46**d). The comparable maximum C=O absorbances can be well explained by the maximum monomer conversion at the same polymerization energies. In comparison to **Figure 45**, a complete pore filling (less than 5 % of free pore volume) for the 170 nm thick mesoporous silica films polymerized with DMAEMA (**Figure 46**a, c, red) can be achieved with polymerization times longer than one hour. Absorbance of 0.02 reached after 60-90 minutes. With respect to the obtained refractive index in ellipsometry measurements (**Figure 45**) this is translated into more than 95 % pore filling considering the data of Dr. Jessica Tom assuming polymer formation exclusively occurs within the mesopores and not on the outer mesoporous film surface. The latter is probable as the mesoporous films were CO_2-plasma treated and thus coinitiator at the outer surface was destroyed before polymerization.

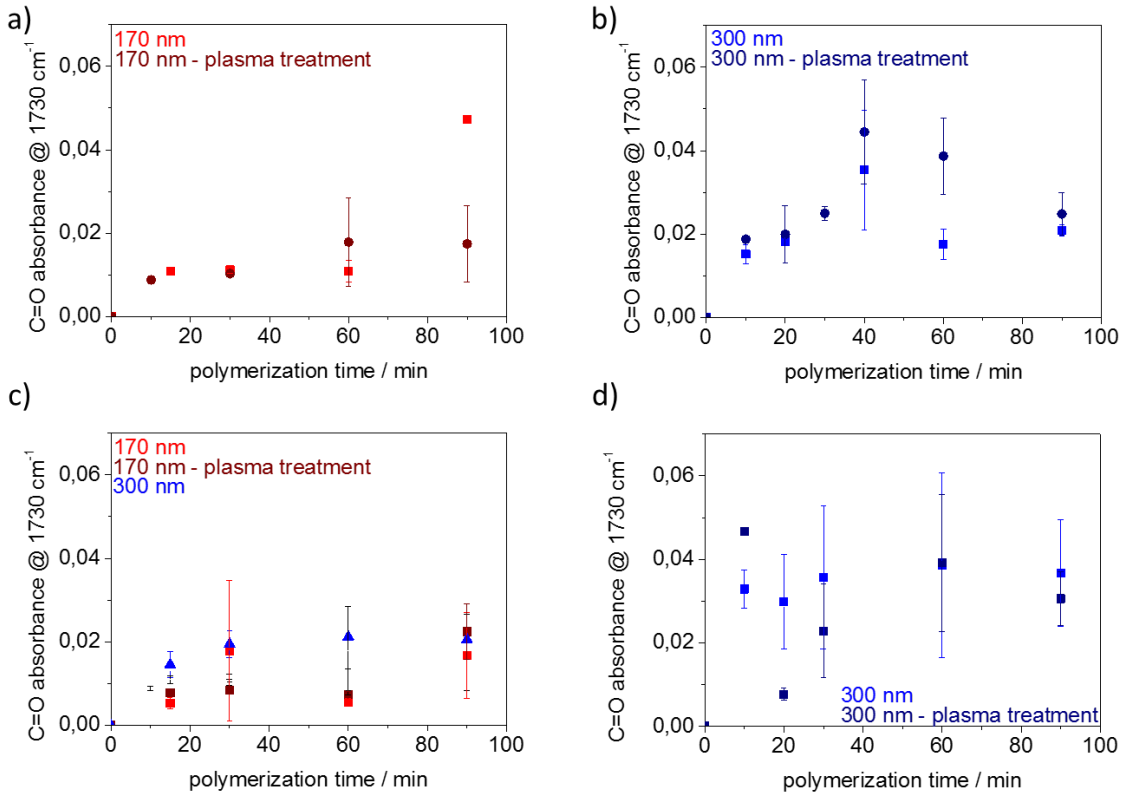

Figure 46. Time-dependent polymerization with red-light LED (λ= 627 nm, 700 mA). The C=O band at 1730 cm^{-1} in Si-OH (900 cm^{-1}) normalized spectra of ATR-IR spectra is shown in dependence of polymerization time. Comparison of 5 mol% coinitiator co-condensed mesoporous film with a thickness between a) 170 nm and b) 300 nm with and without plasma treatment[237]. DMAEMA is the used monomer c) same conditions like a) and b) but the mesoporous silica films are post-grafted with coinitiator. d) Polymerization of MEP in 300 nm thick mesoporous silica films post-grafted with coinitator. In the dark red series, the mesoporous silica films functionalized with coinitiator are plasma treated[237] before polymerization. Error bars are caused by multiple measurements on a substrate and the calculated standard deviations.

In addition to the influence of irradiation time (**Figure 46**) the influence of irradiation power of the dye sensitized polymerization on mesoporous silica films is investigated. A constant polymerization time of 30 minutes is used as **Figure 46** revealed that longer polymerization times do not further increase the obtained polymer amount under the applied conditions. As a LED ($\lambda = 627$ nm) is applied as irradiation source, the light intensity is adjustable by the incoming current of the LED. In **Figure 47** the resulting C=O absorbance at 1730 cm^{-1} in Si-OH (900 cm^{-1}) normalized ATR-IR spectra is shown (ATR-IR spectra see appendix, **Figure 98**). The energy dependent C=O absorbance relatively well follows the light intensity. With increasing light intensity, the C=O band intensity and thus the polymer amount increases. The C=O band intensities cannot be directly compared in terms of pore filling, since these mesoporous films are thicker mesoporous silica films (300 nm). Nevertheless, the obtained polymer amount correlates well with the irradiation power for the polymerization in the mesoporous films and on the outer surface (**Figure 47**a) as well as for polymerization exclusively inside the mesopores

(**Figure 47**b) after having removed the coinitiator from the outer surface using a CO_2 plasma treatment.

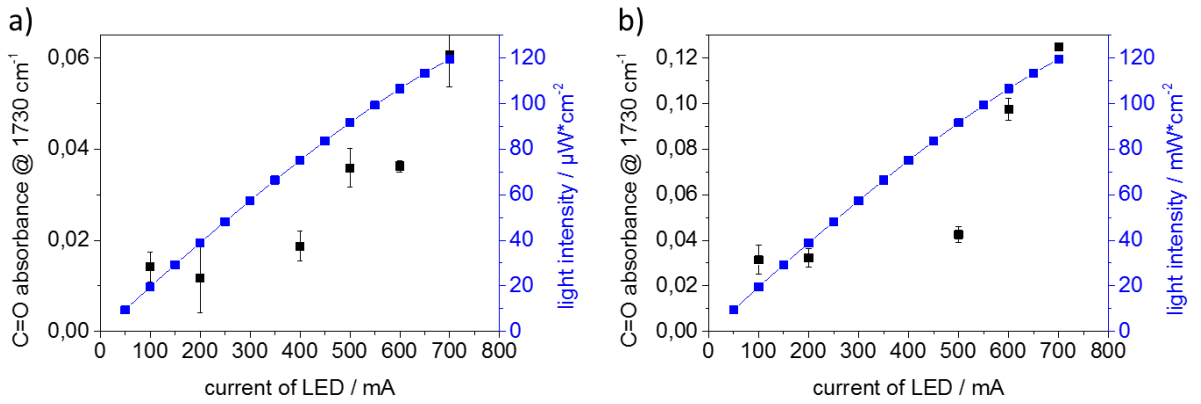

Figure 47. Energy dependent polymerization of DMAEMA with red-light LED (λ = 627 nm, 30 min) of 300 nm thick mesoporous silica film (small pores) co-condensed with 5 mol% coinitiator. a) without CO_2 plasma treatment. b) After coinitiator functionalization the mesoporous silica films are CO_2 plasma treated to remove coinitiator from outer surface. The C=O absorbance in Si-OH (900 cm^{-1}) normalized spectra is shown (black). Error bars showing differences in measurements from one substrate. Blue points show the light intensity in dependent of the used current.

In summary, the control of polymer amount using dye sensitized polymerization in mesoporous silica films is possible by adjusting irradiation power and reaction time. Thereby the generated polymer amount can much better be adjusted by irradiation power than by irradiation time. In addition, already relative short polymerization times of a few minutes generate detectable polymer amounts. This is encouraging with respect to initiation of polymerization using surface plasmons and potential local control as these surface plasmons consist of a highly localized exponentially decaying electromagnetic field (chapter 5.2). Thus short irradiation pulses are desired while energy can be adjusted.

Polymerization with red He/Ne laser (λ = 632.8 nm)

LED light as used in **Figure 46** and **Figure 47** provides a large-area illumination. A laser, in contrast, is focused to one individual millimeter or sub-millimeter spot. Laser illumination in one spot to induce polymer functionalization thus offers an opportunity to investigate the local limitation of polymer functionalization of mesoporous films but of course also affects the choice of suitable characterization methods. In this sub-chapter the polymerization upon irradiation with a He/Ne laser (λ = 632.8 nm) is investigated. Parameters such as irradiation power but as well monomer and dye concentration are varied. It has to be mentioned that all polymerizations done with laser as light source are done with p-polarized light. The complete experimental set-up is shown in chapter 5.2 (**Figure 11**). Polymer amount as reflected by the

absorbances of the C=O vibrational band at 1730 cm^{-1} in Si-OH (900 cm^{-1}) normalized (900 cm^{-1}) is measured within the irradiated laser spot on the mesoporous silica coated glass substrate (experimental details in chapter 5.2, **Figure 11**) (**Figure 48**) (ATR-IR spectra see appendix, **Figure 99**). In **Figure 48**a the influence of the monomer / dye volume ratio on PDMAEMA formation is investigated. A monomer solution concentration of 250 mg/mL in aqueous $NaHCO_3$ (0.1 M) and a methylene blue solution concentration of 1.3 mg/25 mL are used. Increasing DMAEMA amount per methylene blue dye leads to increasing polymer amount. Under the applied conditions a volume ratio of 9:1 (225 mg/mL DMAEMA, 0.0052 mg/mL methylene blue in 0.1 M $NaHCO_3$) provides the highest C=O absorbance under the applied irradiation conditions and thus the highest polymer amount within the laser spot. By changing the volumetric ratio of monomer (250 mg/mL) to dye (0.052 mg/mL) solution, the final concentration of both monomer and methylene blue in the polymerization solution change. But as even very low methylene blue concentration such as 0.0003 mg/mL does not seem to limit polymerization under the applied conditions (**Figure 48**a) the main influencing parameter seems to be the monomer concentration. This is supports the increasing PDMAEMA amount with increasing DMAEMA concentration (**Figure 48**b). The monomer solution concentration is varied between 250-1000 mg/mL while the relative ratio of both solutions (monomer: dye solution) is kept constant at 9:1 (volume changes are negligible). At the same time the viscosity of the solution increases with increasing monomer concentration as visible by eye. This increasing viscosity might be difficult for later SPR experiments because of flowability trough the flow cell. For this reason, all further experiments are performed with a monomer solution consisting of 250 mg/mL or 500 mg/mL. In **Figure 48**c the effect of varying methylene blue concentration is investigated. No clear influence of the methylene blue concentration on the PDMAEMA amount is observed indicating, that even the lowest concentration is sufficient for the polymerization of the present monomer amount. In addition, this effect might as well result from the limited accessibility of methylene blue into the mesopores in the presence of monomer (**Figure 41**). Further experiments are conducted with a methylene blue concentration of 0.0052 mg/mL in final polymerization solution. Finally, the influence of polymerization solution pH value (9:1 DMAEMA : MB = 450 mg/mL DMAEMA, 0.0052 mg/mL MB in 0.01 M $NaHCO_3$) is investigated. The polymerization solution in aqueous 0.1 M $NaHCO_3$ solution shows a pH value of 9. This composition is originally selected because at this pH, DMAEMA and the coinitiator are neutrally charged. It has to be considered, that adjustment of solution polymerization pH value leads to a dilution of the solution resulting in lower concentrations of monomer. Comparing the pH-dependent polymerizations regarding PDMAEMA amount in the laser spot, the untreated polymerization solution with pH 9 show no disadvantage, leads to the

highest polymer amount because of no dilution of the polymerization solution (see appendix, **Figure 100**).

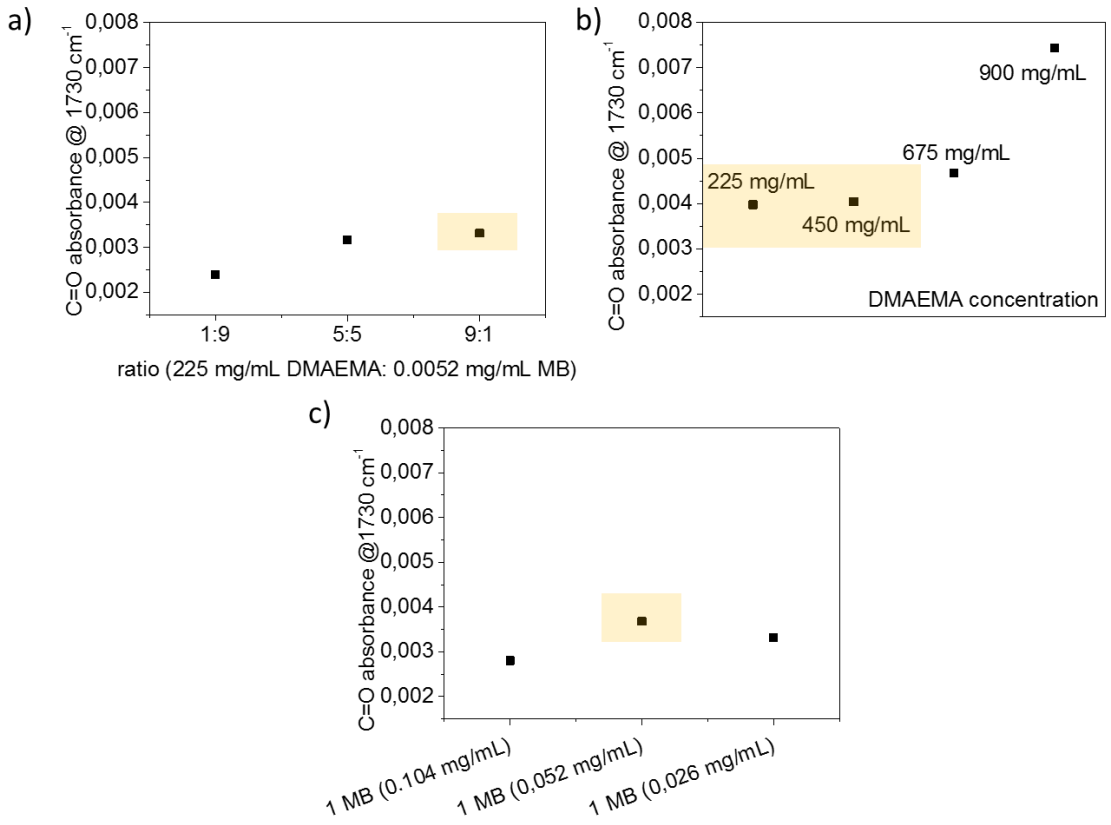

Figure 48. In all figures the C=O vibrational band absorbance at 1730 cm^{-1} extracted from ATR-IR spectra in the laser spot normalized to the Si-OH band at 900 cm^{-1} are depicted. The mesoporous silica films with a film thickness of 300 nm are post-grafted with coinitiator. The polymerizations are performed with a He/Ne laser (λ = 632.8 nm) with a power of 1.5 mW (Pol. 1=40 °, Pol. 2=90 °) for 30 min with DMAEMA as monomer and methylene blue as dye. a) Varying ratio of DMAEMA to methylene blue solution resulting in 1:9 (25 mg/mL DMAEMA, 0.047 mg/mL methylene blue), 5:5 (125 mg/mL DMAEMA, 0.026 mg/mL methylene blue) and 9:1 (225 mg/mL DMAEMA, 0.0052 mg/mL methylene blue) volume ratio. b) Influence of monomer concentration with constant methylene blue concentration in the polymerization solution of 0.0052 mg/mL (volume changes are negligible). c) Influence of methylene blue concentration at constant DMAEMA concentration of 450 mg/mL.

Besides the solution composition and above all the monomer concentration the laser power is expected to influence polymer formation as observed for LED irradiation. Within the SPR-setup the He/Ne laser power can be adjusted by changing the polarizer 1 angle from 0-90° while keeping the position of polarizer 2 constant at 90° and thus p-polarized light (see experimental set up in chapter 5.2, **Figure 11**). While varying the polarizer 1 angle from 0-90° the irradiation power follows a sinus function (chapter 5.2, **Figure 15**). **Figure 49** depicts the results of the energy dependent laser induced dye sensitized polymerization (ATR-IR spectra see appendix, **Figure 101**). Keeping the polymerization time constant at 25 min (**Figure 49**a, b) the C=O

absorbance at 1730 cm^{-1} in Si-OH (900 cm^{-1}) normalized spectra increases proportionally to the irradiation power increase. Black (**Figure 49**a) and red (**Figure 49**b) data points encode different film thicknesses of mesoporous silica films on glass substrates and a different monomer concentration. As the film thickness is different absolute values cannot be directly compared due to the different penetration depth of the ATR-IR evanescent field (please refer to chapter 8.2.1) but the energy dependence seems to be comparable for both film thicknesses of 300 nm and 170 nm and the obtained polymer amount clearly follows the increase in irradiation power. In **Figure 49**c the polymerization time is prolonged to 4 h. All other conditions such as mesoporous film thickness and monomer concentration are chosen similarly to the black data points in **Figure 49**a. Regarding energy dependence, the polymer amount is significantly increasing with increasing laser beam power from 3 mW to 6.5 mW by a factor of 1.8. This tuning of polymer amount by the irradiation power and monomer concentration is in accordance with the prior experiments under LED irradiation.

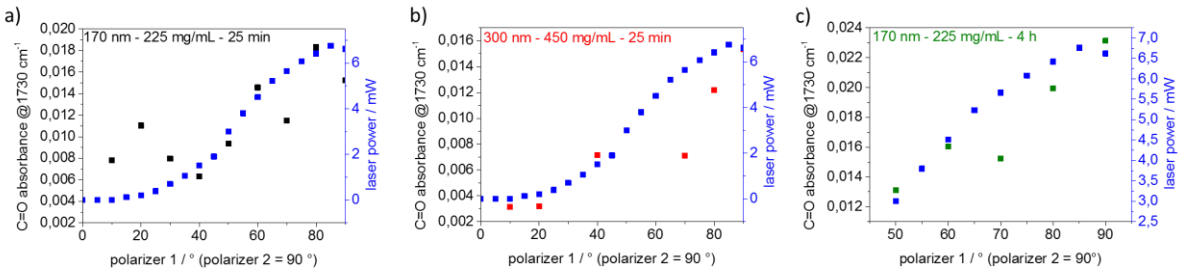

Figure 49. Energy dependent polymerization with He/Ne laser (λ = 632.8 nm). The C=O vibrational band absorbance at 1730 cm^{-1} in Si-OH (900 cm^{-1}) normalized spectra (black) within laser spot is shown as well as the laser power (blue) against the used polarizer 1 angle. a) Results for 25 min polymerization time in a 170 nm thick mesoporous silica film post-grafted with coinitiator is polymerized with DMAEMA (225 mg/mL DMAEMA, 0.0052 mg/mL MB in 0.01 N $NaHCO_3$) and b) for a 300 nm film using a DMAEMA with higher concentration (450 mg/mL DMAEMA, 0.0052 mg/mL MB in 0.01 N $NaHCO_3$). c) Results for 4 h polymerization time under polymerizations conditions identical to a).

The time dependence of laser-induced mesoporous film polymer functionalization is investigated in detail in **Figure 50** (ATR-IR spectra see appendix, **Figure 103** and **Figure 102**). In **Figure 50**a a time dependent polymer amount increase as expected for a free radical polymerization is observed for a laser power adjusted to 6.5 mW (polarizer 1 angle of 90 °) and a low monomer concentration of 225 mg/mL (DMAEMA 225 mg/mL and 0.0052 mg/mL methylene blue in 0.1 M $NaHCO_3$ solution) in black data points. Reducing the laser power to 0.2 mW (Polarizer 1 angle of 20 °) while increasing the DMAEMA monomer concentration from 225 mg/mL to 450 mg/mL (**Figure 50**a, red) results in slightly lower C=O vibrational band absorbance and thus PDMAEMA amount.

When changing the monomer from DMAEMA to pH-dependently, negatively charged MEP the obtained polymer amount is increasing with increasing polymerization time, too (see appendix, **Figure 104** and **Figure 105**). Here, the difference in absorbance of C=O vibrational band in Si-OH (900 cm^{-1}) normalized spectra with regard to the impact of energy is noticeable and higher irradiation powers lead to higher polymer amounts in the mesoporous silica films. When polymerizing MEP exclusively inside the pores by using CO_2-plasma treatment[237] after coinitiator binding, the absorbance of the C=O vibrational band only increases to one third of the maximum C=O absorbance after polymerization inside as well as outside of the mesoporous silica film. In **Figure 50**b the polymerization of 5 mol% coinitiator co-condensed mesoporous silica films with DMAEMA and MEP as monomer is compared to each other by plotting the absorbance of C=O vibrational band in Si-OH (900 cm^{-1}) normalized spectra in dependency of polymerization time. All four series show a time dependence according to a radical polymerization mechanism. This means that the polymer amount is increasing with increasing polymerization time. The polymerization with MEP is to be evaluated with errors because of the polymerization located in the laserspot and the inhomogeous monomer distribution in polymerization solution. The polymerization with DMAEMA as monomer shows that the C=O absorbance is higher for the thicker (300 nm) mesoporous silica films as compared to thin films (170 nm). This is in accordance to the film thickness effect observed for the comprehensive polymerization with LED as light source (**Figure 46**). Because of the penetration depth of the evanescent field of the ATR-IR, no statement can be made here about the amount of polymer in comparison to the different layer thicknesses. With respect to the obtained refractive index in ellipsometry measurements (**Figure 45**a) this is translated into 10 % free pore volume after 90 minutes of polymerization time (**Figure 50**b, blue data spots) considering the data of Dr. J. Tom assuming polymer formation exclusively occurs within the mesopores and not on the outer mesoporous film surface.

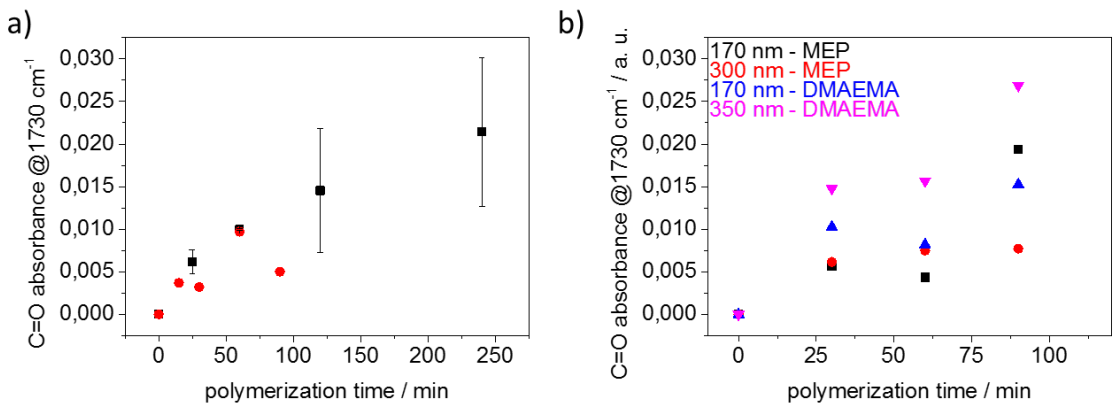

Figure 50. Time dependent polymerization with red light He/Ne laser (λ = 632.8 nm). The C=O vibrational band at 1730 cm^{-1} in Si-OH (900 cm^{-1}) normalized spectra is plotted against the polymerization time. C=O absorbance in Si-OH (900 cm^{-1}) normalized spectra is measured in laser spot. In a) a 170 nm thick mesoporous silica film post-grafted with coinitiator is polymer functionalized with DMAEMA (225 mg/mL DMAEMA, 0.0052 mg/mL methylene blue in 0.1 M $NaHCO_3$ solution) with 6.5 mW laser power (pol. 1 = pol. 2 = 90 °) (black). The red spots show the polymerization with 0.2 mW laser power (pol. 1 = 20 °, pol. 2 = 90 °, 300 nm filmthickness). DMAEMA (450 mg/mL DMAEMA, 0.0052 mg/mL methylene blue in 0.1 M $NaHCO_3$ solution) is used as monomer. In b) the comparison between two film thicknesses, 170 nm and 300 nm, for both monomers DMAEMA and MEP is shown for 5 mol% coinitiator co-condensed silica films.

As the polymer amount can be adjusted with adjusting irradiation power and polymerization time the laser induced dye-sensitized polymerization is investigated regarding its potential for local resolution starting by comparing the laser spot area to the surrounding area in the x-y plane (**Figure 51**a). It has to be noted, that the transition of methylene blue (blue solution) into the colorless leuco-form preferably occurs within and close to the laser spot at the mesoporous silica coated glass substrate (**Figure 51**a) as visible by eye. The area of this decolored zone in the polymerization solution seems to increase with increasing polymerization time and increasing laser power. In **Figure 51**b the ATR-IR spectra (zoom of the C=O vibrational band at 1730 cm^{-1}) at different positions (**Figure 51**a scheme) and distances to the laser spot area are shown. The C=O absorbance (**Figure 51**b, magenta/red) within the laser spot is significantly higher than the C=O absorbance in some millimeter distance in x- (green) or y-direction (black/blue). The C=O absorbance in dependence of the distance from the laser spot for all measured spots is shown in **Figure 51**c. The local functionalization around the polymerization spot is clearly visible. The exact gradient in x-y direction around the laser spot is dependent on the polymerization parameters. Here, a polymerization time of 30 minutes with a laser power of 1.8 mW and a monomer (DMAEMA) concentration of 225 mg/mL is chosen while the mesoporous silica film is 300 nm thick with pore diameters of 3-6 nm (TEM images see **Figure 19**, 6.1.1).

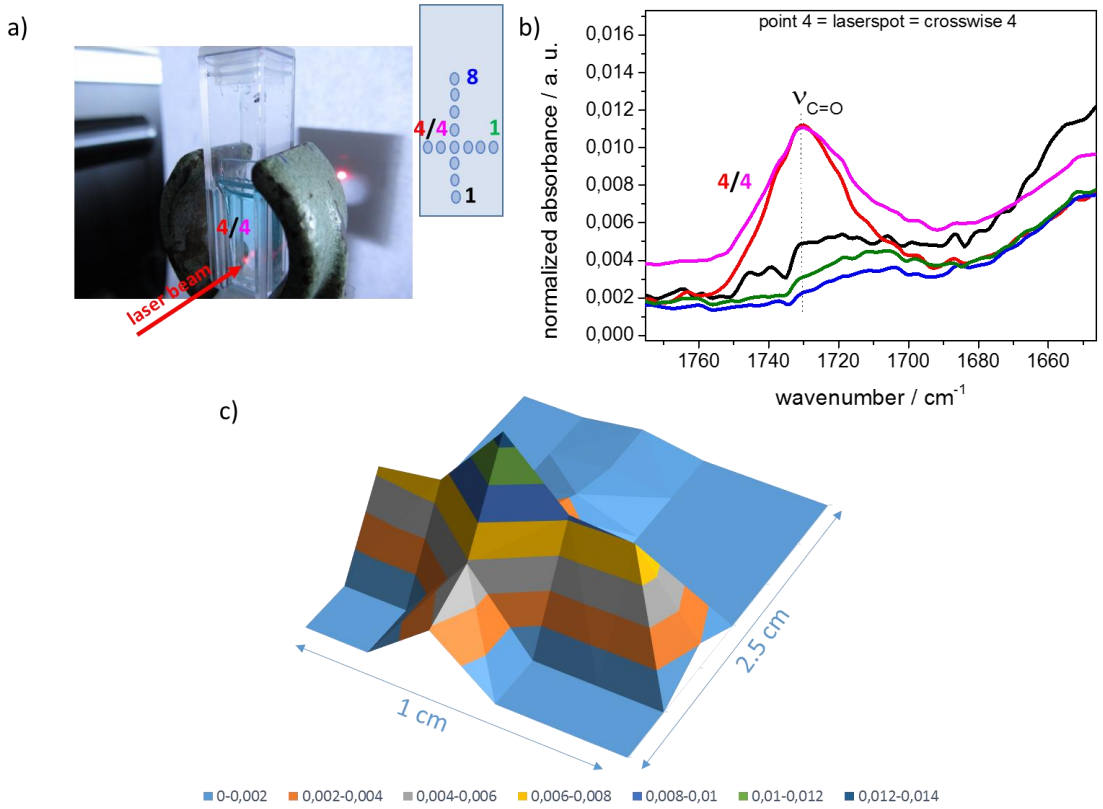

Figure 51. X-y localized He/Ne induced polymerization. The polymerization takes place for 30 minutes using DMAEMA (225 mg/mL DMAEMA, 0.0052 mg/mL methylene blue in 0.1 M $NaHCO_3$ solution) as monomer on a 300 nm thick coinitiator functionalized mesoporous silica film with a laser power of 1.8 mW (pol 1=40°, pol 2=90°) a) shows a picture of the dye sensitized polymerization with red laser as light source. The spot where the laser crosses the mesoporous silica coated substrate is clearly visible. After polymerization the switch from colored methylene blue to the leuco form is visible in dependence of the parameters only in this spot. In b) the magnification of the ATR-IR spectra, especially of the C=O band at 1730 cm^{-1} in Si-OH (900 cm^{-1}) normalized spectra, is shown. The measured spots are marked in a) and same colors are used. c) shows a 3D mapping of the measured substrate by using the C=O band extracted from the ATR-IR spectra.

Increasing the laser power from 1.8 mW (**Figure 51**) to 5.6 mW (**Figure 52**b, blue) the local limitation (x-y resolution) of polymer amount distribution around the directly irradiated laser spot region in mesoporous silica films is lost for a polymerization time of 30 minutes (**Figure 52**) (ATR-IR spectra see appendix, **Figure 106**). The scheme of spot position and ATR-IR measured spots are shown in **Figure 52**a. The related C=O vibrational band absorbance at 1730 cm^{-1} in Si-OH (900 cm^{-1}) normalized spectra is shown in **Figure 52**b. For lower laser power of 0.2 mW (pol.1 = 10°, polymerization spot = 3) and 1.8 mW (**Figure 51**) the highest polymer amount is detected within the laser spot. Increasing the laser power (**Figure 52**, pol.1 = 70°, 80°, 90°, polymerization spot = position 3 for polarizer angle 70°,80°, position 4 for polarizer angle 90°) the detected polymer amount (C=O vibrational band absorbance) becomes comparable for all measured spots and the x-y resolution is lost.

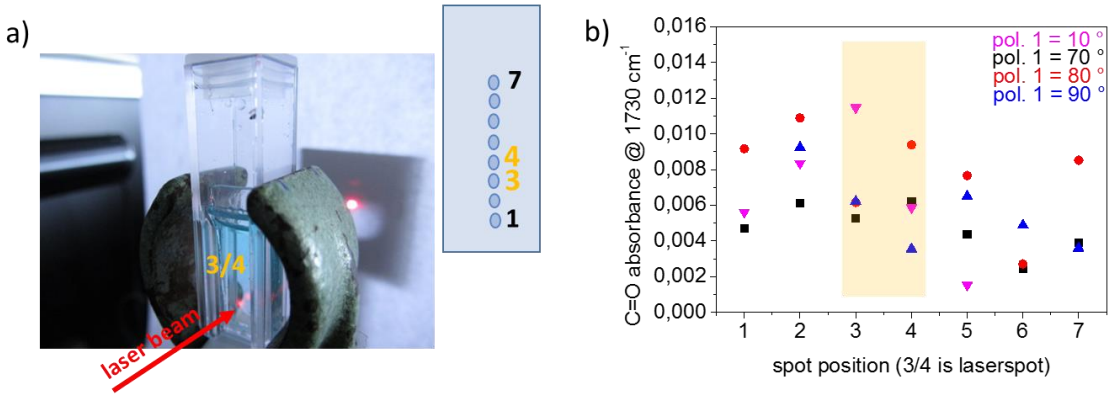

Figure 52. Further results to x—y resolution of the dye-sensitized polymerization with red laser and methylene blue as dye and DMAEMA as monomer. a) shows a picture of the dye sensitized polymerization with red laser as light source. The spot where the laser crosses the mesoporous silica coated substrate is clearly visible. After polymerization the switch from colored methylene blue to the leuco form is visible in dependence of the parameters only in this spot. b) The C=O absorbance in Si-OH (900 cm^{-1}) normalized spectra are plotted against the vertical line of the polymerized mesoporous silica film. The polymerization conditions are the same like in **Figure 51** but other laser powers are used. The laser spot is 3 for magenta, black and red, 4 for blue series.

In summary, the dye sensitized polymerization seems to be a very suitable tool for the polymerization initiated with red light using different light sources such as Lumatec®Lamp (λ=400-700 nm)[136], LED (λ=627 nm) or He/Ne laser (λ=633 nm). The polymer amount within/on the mesoporous silica films can be adjusted by varying the polymerization parameters such as irradiation power, polymerization time or monomer concentration. By removing the coinitiator molecules from outer surface by CO_2 plasma treatment[237] the polymerization exclusively occurs within the mesopores. With a laser as light source a control in x-y direction on mm-scale is possible which is an important result for the aim of local polymer functionalization with near-field modes.

6.2.4. Polymerization with Near-Field Modes

In this chapter the polymerization with near-field modes, such as surface plasmons (SP) and leaky transversal optical waveguide modes (TM) is investigated. The final aim is to investigate potential local control of mesoporous film polymer functionalization by combining nanoscale optical fields with wavelength compatible free radical dye-sensitized polymerization. The sample preparation for the experiments discussed in this chapter is shown in chapter 5.2, there is also a detailed explanation of the experiment setup and the emergence of such near-field modes. The mechanism of dye-sensitized polymerization is explained in detail in chapter 5.1.

As a first question the influence of polymer formation (refractive index increase as compared to liquid or air filled mesopores) on the surface plasmon resonance angle and thus the sensitivity of in-situ polymer detection has to be investigated. Ideally, polymer formation is expected to result into a refractive index increase again resulting into a shift of the surface plasmon resonance to higher resonance angles. According to the experimental results shown in **Figure 53** in-situ detection of polymer formation using the surface plasmon is not unambiguously possible because of three reasons: Firstly, when measuring in solution and not against air the sensitivity is extremely low due to index matching between the polymerization solution and silica as compared to air-filled mesopores due to similar refractive indices between solvent (water or polymerization solution) and polymer functionalized mesoporous silica films. The simulated SPR spectra using the software Winspall (Restec) of a 170 nm thick mesoporous silica film with a refractive index of 1,25 (porosity 44 vol%) in contact with air (red) and water (blue) is shown in **Figure 53**a. Upon polymer functionalization the refractive index is assumed to increase to 1.4 while the thickness is kept constant. The resulting shift in the SP resonance angle (**Figure 53**a, light red and dark red) are clearly visible and a shift of the SP minimum from 44° to 61° (air as surrounding medium) and 50° to 65° (water as surrounding medium) is obtained. In reality the measured spectra rather look like the ones shown in **Figure 53**b. The coinitiator functionalized mesoporous silica film coated on gold substrate is placed into the flow cell in SPR set-up (see chapter 5.2) and measures against air, subsequently water is constantly flow through cell with 5 μL/s and a spectra is recorded with water as surrounding medium. In a next step the cell is filled with polymerization solution, a quick spectrum is recorded for localizing the SP minimum. The angle is set to the SP resonance angle and polymerization is carried out. After polymerization the cell is flushed with water, and a SPR spectrum is recorded. Afterwards the substrate is removed and cleaned again with water, dried with compressed air and rearranged in the SPR set-up at the same position. A spectrum with air as ambient medium is recorded after the polymer functionalization. The SP resonance angle shift is visible for high polymer amounts (compare C=O vibrational band absorbance at 1730 cm^{-1}, **Figure 53**c), when measuring against air. More detailed a SP resonance angle shift from 62 to 72 ° is observed for a C=O vibrational band absorbance normalized to Si-O-Si_{assym} (1070 cm^{-1}) of 0.4. This high C=O absorbance indicates clearly a completely filled pore (no free pore volume available) and even polymer on top of the mesoporous film. But even in this case when measuring against water no significant SP resonance angle shift to higher angles is observed (**Figure 53**b, blue). The measuring against water can also include swollen polymer trapped in the polymerization flow cell which changes the refractive index and leads to an index matching with the polymer functionalized mesoporous silica film.

Secondly, it has to be considered that even in case a SP resonance angle shift towards higher angles, for example 62 ° to 72 ° (**Figure 53**b), is observed this might be explained by polymer filling of the mesoporous silica and an increasing refractive index. But the polymer PDMAEMA can act as a hydrogel storing water, which might not be removable by heating and drying under mild conditions.[248] Thus a shift of theta is an indication of a successful polymerization but not necessarily proportionally related to the amount of polymer bound in the mesopores. Consequently, a characterization using other characterization methods such as ATR-IR spectroscopy is essential to be able to make a statement about the polymer functionalization. Water in the silica mesopores is also visible in ATR-IR spectra (**Figure 53**c) of the polymer functionalized mesoporous silica film by the strong OH vibrational band at 3600-3000 cm^{-1}. To investigate the effect of humidity on refractive index and layer thickness of PDMAEMA functionalized mesoporous films ellipsometry measurements under controlled and varying humidity are performed (**Figure 53**d). The pores are filled with 30 % of PDMAMA calculated by Bruggeman approximation.[229] The PDMAEMA functionalization of mesoporous silica is located inside and outside the mesopores, this explains the constant swelling of thickness. At 75 % relative humidity the thickness increases stronger probably due to condensation effects. The refractive index increases constantly up to a relative humidity of 75 %, followed by a sudden increase probably due to water adsorption and condensation into the mesopores.

Thirdly, an interesting observation has to be mentioned here: interestingly the SP resonance angle shift towards higher angles is usually observed for relatively high polymer amount formation. When generating low amount of polymer under SP-irradiation, the SP resonance angle shift often towards smaller resonance angles. This is only observed for SP-induced polymerization and not for laser-induced polymerization, for example. This resonance angle shift to smaller angles indicates a reduction in film thickness or refractive index. One possible explanation might be etching of the mesoporous silica films, because of local heating and the harsh conditions of polymerization solution (pH9). This effect might be overcompensated when having a high polymer amount after polymerization then again inducing a resonance angle shift to higher angles. The thermal initiation of the dye-sensitized polymerization can be excluded shown in **Figure 44** (see chapter 6.2.3). Recently, etching processes of ordered silica structures are used to allow ultrathin mesoporous silica film generation. [65] John *et al.*[249] showed that the polymerization solution, used same monomer but different dye, reduced the mesoporous silica layer thickness in contact with the polymerization solution within 2 h to 50 % of the initial film thickness. When using SP induced polymerization also local heat spots seem to play an important role.[274] In the work of John *et al.* from our research group mesoporous silica coated on silver substrates are functionalized with polymer using irradiation at an angle in the

beginning of a SP, where the enhancement factor of evanescence field is the weakest. The polymerization time is set to 30 min showing a thickness decrease of 85 % by cross-section SEM measurements.

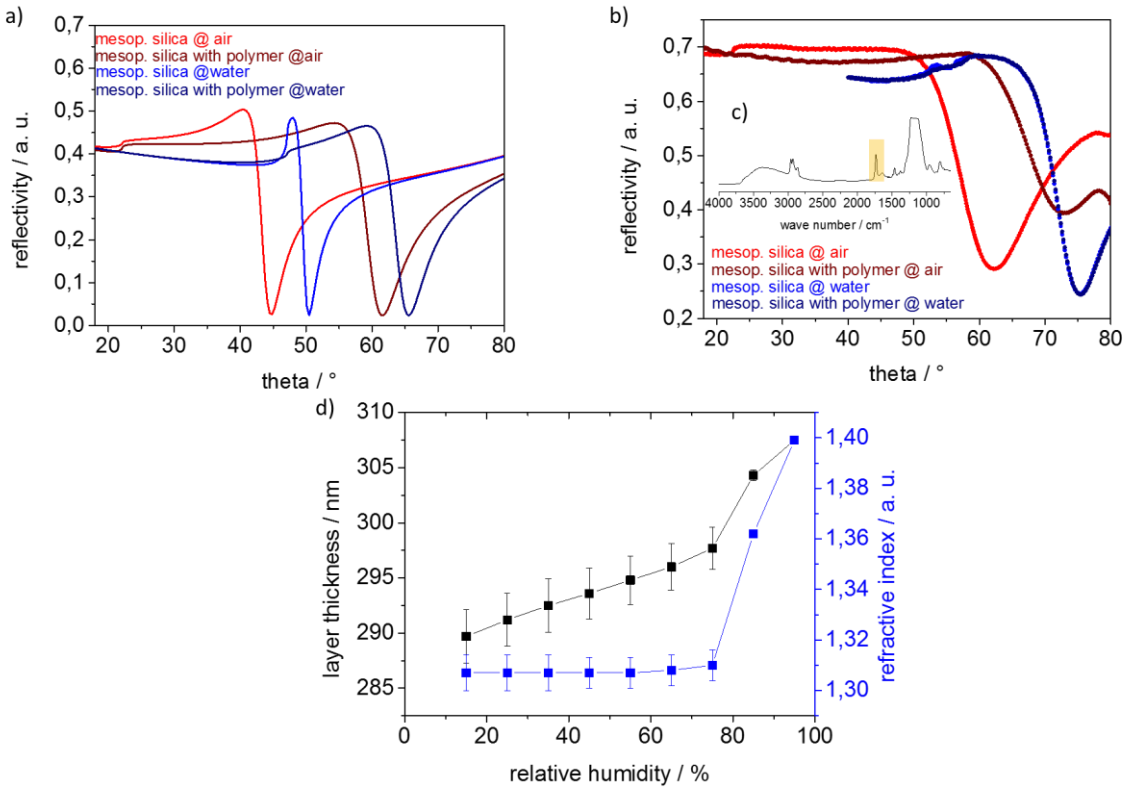

Figure 53. a) Model spectra of mesoprous silica (170 nm) with a refractive index of 1.25 on 50 nm gold coated on LaSFN9 glass with 5 nm chromium as liability mediator. Polymer functionalization is simulated by refractive index increase to 1.4. The surrounding medium is air and water. b) Real measured spectra of mesoporous silica films functionalized with PDMAEMA proofed in c) as ATR-IR spectrum with highlighted C=O vibrational band at 1730 cm^{-1} in Si-O-$Si_{asym.}$ (1070 cm^{-1}) normalized spectra. d) Ellipsometry measurements of an PDMAEMA functionalized mesoporous silica film under increasing relative humidity from 15 to 95 %.

In conclusion the shift of the SP resonance angle without additional characterization is no unambiguous indicator of a successful polymer functionalization. That's why every polymerization is characterized using ATR-IR following the C=O band at 1730 cm^{-1} as sign for a successful PDMAEMA or PMEP functionalization.

In the following of this chapter every individual Figure represents one polymerization series. In series the film preparation including chromium and gold thermal evaporation on LaSFN9 glasses and coating of mesoporous silica as well as coinitiator binding is performed identically for all samples. This is very important for comparison of polymerization because minimal changes in thickness and quality of gold and chromium and thickness and porosity of mesoporous silica influence the coupling efficiency of the surface plasmon. The energy coupling

has a strong influence on polymerization as this determines the provided energy and the enhancement factor of evanescent field of SP. The coupled energy during the polymerization is the difference between the reflectivity at the beginning and the minimum of the SP.

The penetration depth of the SP is dependent on refractive indices of coinitiator functionalized mesoporous silica and the surrounding medium as well as the wavelength and the critical angle. The penetration depth can be calculated with the following formula.[250]

$$l = \frac{\lambda}{2\pi\sqrt{n_1^2 sin^2(\emptyset_c) - n_2^2}} \; with \; n_2 < n_1$$

In the experiments the wavelength of 632.8 nm is used. The critical angle of the polymerization solution is at 50 ° and has a refractive index of 1.3655. The refractive index of the dielectric layer gold is 0.19609. Using these parameters, the penetration depth of the evanescent field in the polymerization system is calculated with approximately 100 nm. The transversal mode (TM) is guided through the entire mesoporous silica film independently of the layer thickness (**Figure 54**). The investigation of SP induced polymerization is performed with mesoporous silica films of different film thicknesses caused by different film preparation on gold coated glass substrates.

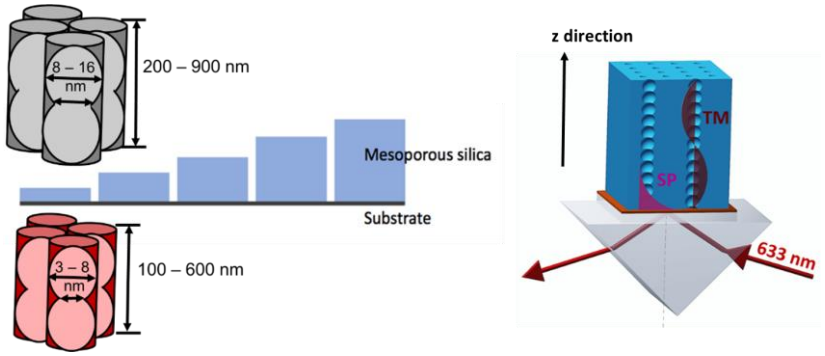

Figure 54. Schematic demonstration of the different possible mesoporous silica film thicknesses prepared with dip-coating or gravure printing on gold coated LaSFN9 gold substrates. The SP has a definite penetration depth in dependence of the dielectric medium (mesoporous silica) and the surrounding medium (air, polymerization solution). TM is guided through the hole dielectric layer.

Different layer thickness of small pores with a pore diameter of 3-6 nm are prepared on gold-coated LaSFN9 substrates. To prepare mesoporous silica films with different film thickness two approaches are followed. Firstly, the withdrawal speed while dip-coating is varied between 2 and 10 mm/s resulting in single layer films with a film thickness between 160 and 365 nm. Secondly, the withdrawal speed of 2 mm/s is dip-coated two times, as described in chapter 6.1.1, resulting in two-layer films with a total film thickness of 365 nm. The resulting layer thickness of the two-layer films is comparable to the one-layer films dip coated using a withdrawal speed of 10 mm/s. The porosity (deduced from the refractive index using

Bruggeman's approximation) seems to be lower for double layer films. A porosity of 31-32 vol% for single layer and a porosity of 22 vol% for double layer films both functionalized with coinitiator are detected. These films are subsequently used for PDMAEMA functionalization using SP irradiation. Although performing the polymerization under identical conditions for all films, thicker films seem to be functionalized with a significantly higher polymer amount comparing the C=O vibrational band absorbance at 1730 cm^{-1} in Si-O-$Si_{asym.}$ (1070 cm^{-1}) normalized ATR-IR spectra (**Figure 55**a and c) but the amount cannot be quantified compared because the normalization of the spectra contains errors. The polymer has some bands in the same wave number area than the silica matrix (1000-1250 cm^{-1}) overlaying the Si-O-$Si_{asym.}$ band (1100 cm^{-1})(see appendix, **Figure 107**). The different amounts of polymer in films of different thicknesses cannot be explained intuitively, since the ratio of polymer to silica (normalization) should be comparable. One hypothesis could be that it is caused by destructive effects that occur simultaneously with polymerization. Thin films are proportionally etched faster and thus polymer is also detached faster than thicker films.

The comparison of the C=O bands in Si-O-$Si_{asym.}$ (1070 cm^{-1}) normalized spectra is possible even with different layer thicknesses, because the reflective gold layer underneath the film prevents the visibility of the underlying glass substrate (see chapter 8.2.1, **Figure 84**), but excluded when polymer amount is incredibly high. Having a high polymer amount leading to a masking of the typical mesoporous silica bands indicated by the changing Si-O-Si vibrational band at 1070 cm^{-1}. In addition, the very strong C=O absorbance (**Figure 55**a, green color) with a maximum peak intensity of 0.98 indicates a high polymer amount which cannot only be explained by polymer formation within the mesopores. The high polymer amount is also visible by eye directly on the substrate (see appendix, **Figure 108**) This is in accordance with the selected relatively high polymerization time of 2 h at the highest possible laser power of 5 mW (Pol.1 = Pol.2 = 90°). It can also be concluded, that the mesoporous films prepared by a two step dip-coating process are less suitable for SP induced polymer functionalization as compared to single layer films with identical film thickness. The reason for this is the coupling efficiency of the SP, visible by the depth of the surface plasmon resonance (**Figure 55**d, red color). Two-layer films show significantly more "loss of light" and thus broadening and SP resonance not going to almost zero reflected beam intensity (y-axes in SPR spectra) (**Figure 55**b, blue or green color) as compared to single-layer films. The coupling efficiency in case of two-layer films reduced to 44 % of the initially available energy extracted at the SP resonance angle of 60° (**Figure 55**b and d, green and red). This might indicate optical inhomogeneities along the mesoporous film thickness.

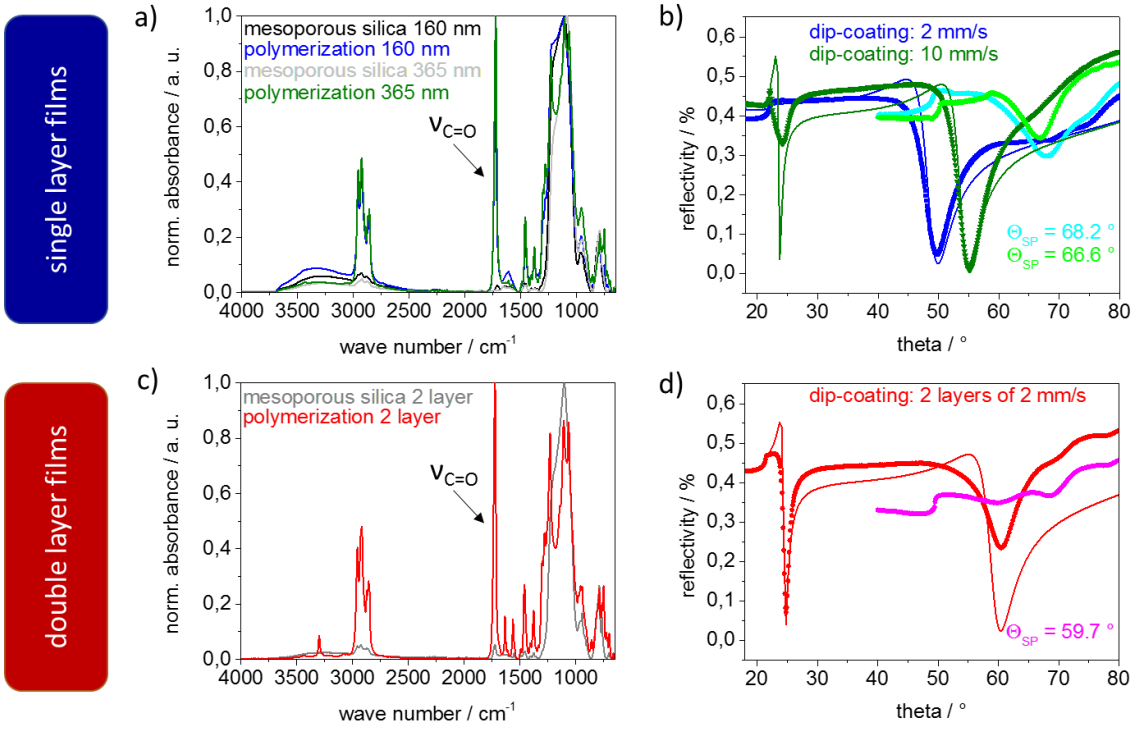

e)

Sample	Layer thickness / nm	Refractive index
2 mm/s	160	1.308
2 mm/s – 2 layer	360	1.356
10 mm/s	365	1.311

Figure 55. Polymerization with DMAEMA as monomer (450 mg/mL DMAEMA, 0.0052 mg/mL methylene blue in 0.1 M $NaHCO_3$-solution) in mesoporous films post-grafted with coinitiator under SP irradiation at the SP resonance angle (minimum) for 2 h using a laser power of 5 mW (λ = 632.8 nm). ATR-IR spectra before and after mesoporous silica film PDMAEMA functionalization using different film thicknesses for a) a single layer (blue = 160 nm, green = 365 nm) or c) a double layer (red = 360 nm) film. Gray and black spectra show the corresponding with coinitiator functionalized mesoporous silica films. The corresponding SPR spectra are shown in b) 160 nm film (blue) and 365 nm film (green) and d) 360 nm double layer film. The SPR spectra measured against polymerization solution are shown in cyano (b) for 160 nm films and bright green (b) for 365 nm single layer films while the magenta spectrum (d) show the double layer film with 360 nm. e) Table summarizing the values for layer thickness and refractive index resulting from model fitting (one layer) of SP measurements. For details on the fitting procedure please refer to chapter 5.2.

To improve multilayer mesoporous film design gravure printing of mesoporous silica on gold substrates is used. In **Figure 56** the SPR spectra of coinitiator post-grafted mesoporous silica films prepared by gravure printing with small pores (**Figure 56**a, b, d) and big pores (**Figure 56**c) and varying layer thicknesses are shown. In **Figure 56**e the ATR-IR spectra after the PDMAEMA functionalization are shown. **Figure 56**f shows the C=O absorbance of the Si-O-$Si_{asym.}$ (1070 cm^{-1}) normalized spectra as an indication of polymer amount plotted against layer thickness. The polymerization under SP irradiation is performed by while scanning from 40-80 ° (each scan needs 8 min for 40-60° in 0.1° steps and 60-80° in 0.2° steps) for 2 times. Only

the SP irradiation depicted in **Figure 56**b is performed for 10 minutes at 79 ° after the first and before the second scan. After polymerization the refractive indices of polymer functionalized mesoporous silica films are larger than 1.45 ($\varepsilon = n^2$). This indicates completely filled mesopores. The polymer amount especially for magenta and green spectra in **Figure 56**e is very high in the mesoporous silica films because the polymer bands overlay the typical band for mesoporous silica, namely Si-O-Si_{asym}, Si-OH, Si-O-$Si_{sym.}$. As the experiments in **Figure 56**a, b and d are comparable regarding the coupled energy of the SP (65 %, ~ 0.13 mW). Two statements can be deduced. Firstly, comparing **Figure 56**a and b the longer polymerization time leads to a higher polymer amount and a higher shift of SP resonance angle (**Figure 56**a: $\Delta = 11°$, **Figure 56**b: $\Delta = 17°$). The observed higher SP resonance angle shift for **Figure 56**a (red) as compared to **Figure 56**b (magenta) fits well to the expectation, that increasing polymer amount leads to a higher refractive index resulting into a higher value for the SP resonance angle. Secondly, the increasing film thickness leads also to a higher polymer amount comparing ATR-IR spectra (**Figure 56**e, red and blue) related to **Figure 56**a and **Figure 56**d. **Figure 56**c showing a mesoporous silica film with a bigger pore diameter (8-16 nm) and a film thickness of 201 nm. The coupled energy of the SP during polymerization is slightly higher (75 %, ~ 0,15 mW). This experiment (**Figure 56**c) shows that SP induced polymerization is possible in these bigger mesopore films, too.

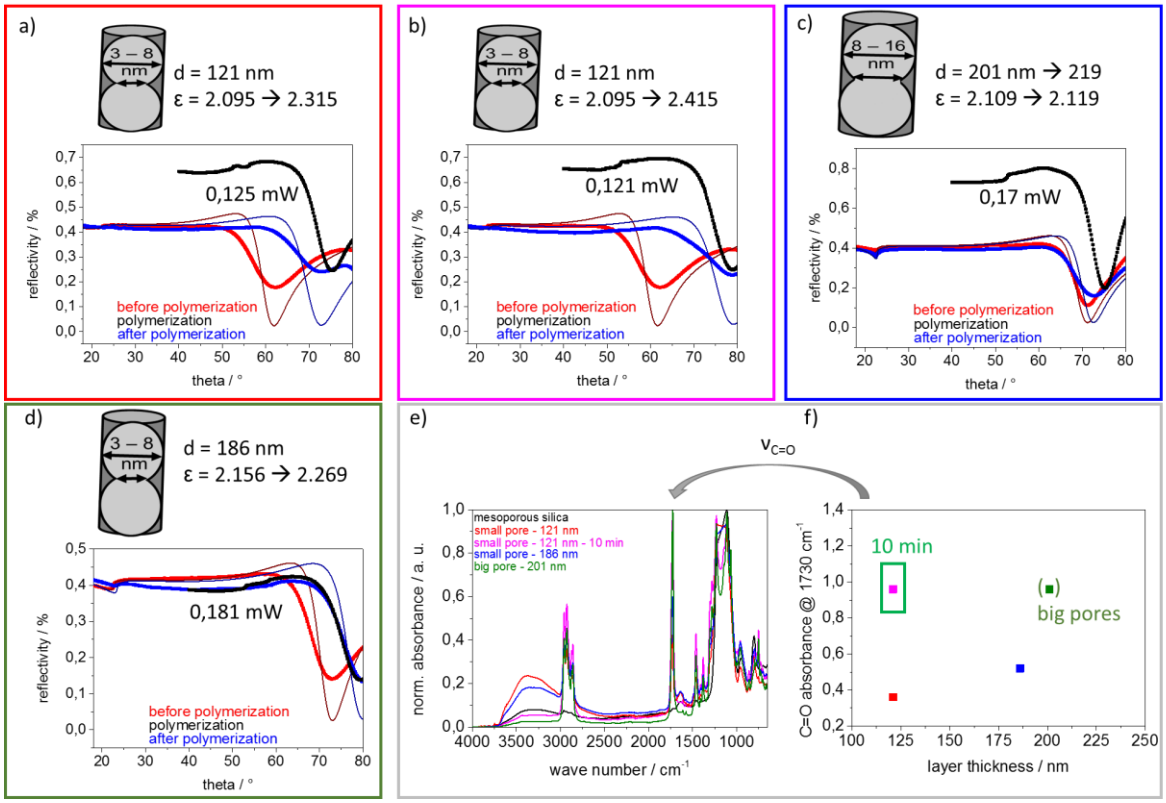

Figure 56. SP-induced polymerization in mesoporous silica films post-grafted with coinitiator prepared by gravure printing on gold coated glass substrates. The SPR spectra of untreated mesoporous films in contact with air are shown in red, the SPR spectra in contact with polymerization solution are shown in in black and the SPR spectra after polymerization in contact with air are shown in blue. Polymerization shown in a, c and d are performed using 0.8 mW laser power (λ=632.8 nm) for two slow scans (each scan needs 8 min for 40-60° in 0.1° steps and 60-80° in 0.2° steps). Only the polymerization in b) is performed using a hold of 10 min at θ_{SP}= 78.9° after the first and before the second scan. The film thickness of the mesoporous silica is different for each experiment a) and b) 121 nm, d) 186 nm with pore diameters of 3-8 nm and c) 201 nm with pore diameter of 8-16 nm. e) ATR-IR spectra recorded directly from gold-substrate normalized to Si-O-$Si_{asym.}$ (1070 cm^{-1}) vibrational band. C=O absorbance @ 1730 cm^{-1} in Si-O-$Si_{asym.}$ (1070 cm^{-1}) normalized spectra in contrast to layer thickness (polymerization time for a) and b)) is shown in f).

The detected high amounts of polymer (experiments in **Figure 55** and **Figure 56**) might indicate polymerization not exclusively initiated by SP because the film thickness of the mesoporous silica film (120 – 360 nm) is thicker than the calculated SP penetration depth (100 nm) using the equation above. Therefore, other effects such as radical diffusion may also play a role. With a laser power of 5 mW and a time of 10-60 min, not such high polymer amount is expected, based on the preliminary experiments with the laser or LED. The higher polymer amount is explainable with the enhancement of the evanescent field of SP in SP induced polymerization. The calculation of the transfer coefficient of the evanescent field based on the Fresnel equations for an interface shows that the electric field on the side of the metal with a low refractive index can be much larger than that on the other side of the metal layer. The transfer coefficient is the ratio of the reflected or transmitted amplitude to the incident wave. The field enhancement as a function of the angle of incidence of the incoming beam depends

on the thickness of the gold layer. It is shown that very close to the SPR resonance angle of planar gold films in contact with water (68°) the SP field intensity can be enhanced by a factor of more than 30 for a 50 nm thick gold film.[251] This field enhancement might explain the much higher polymer amount as expected based laser irradiation under comparable laser power. The SP resonance angle and coupling efficiency, which varies minimally from film to film, also have an enormous effect on polymerization, since even the smallest differences have a very strong effect due to this amplification.

As demonstrated in chapter 6.2.3, the polymer amount generated during dye-sensitized polymerization is dependent on the monomer concentration in the polymerization solution like shown for LED or laser induced polymerization in mesoporous silica films (**Figure 48**b).

In first experiments the influence of the monomer concentration on SP-induced mesoporous film polymer functionalization is investigated (**Figure 57**). Therefore, two polymerization series with small pore mesoporous silica (film thickness of 245 nm, **Figure 57**a, b) and with big pore mesoporous films (film thickness of 525 nm, **Figure 57**c, d) in dependence of the monomer (DMAEMA) concentration are shown. Polymerization is performed at the SP resonance angle (minimum) measured against polymerization solution. The characterization is performed using ATR-IR spectra recorded directly from gold substrates. The influence of increasing monomer concentration on the generated polymer amount in SP-induced polymerizations is investigated in **Figure 57** for small pore (**Figure 57**a-d) and big pore (**Figure 57**e-g) mesoporous silica films. For constant monomer solution flow of 5 μL/min, the ATR-IR spectra before and after SP-induced polymerization in small pore mesoporous silica films (**Figure 57**a,c, red and blue) clearly show higher polymer amount (higher C=O vibrational band at 1730 cm^{-1}) after polymerization with doubled monomer concentration (red, blue). In the ATR-IR spectra the change of the Si-O-$Si_{asym.}$ vibrational band shape at around 1100 cm^{-1} caused by the high polymer amount and overlaying polymer vibrational bands is visible. This indicates a very high amount with a majority of polymer growing on the outside surface of the mesoporous film. In case the monomer flow is stopped and thus only the monomer present within the cell at the beginning of the polymerization is available for polymerizations (**Figure 57**c, green) the polymerization is also successful but resulting smaller C=O vibrational band in the ATR-IR spectrum indicating a lower polymer amount of approximately factor 2.4 for the given experimental conditions. Although the SPR-spectra (**Figure 57**b, d) cannot be used for detailed evaluation of polymer formation, as discussed above, a stronger SP resonance angle shift for **Figure 57**d as compared to **Figure 57**b would be expected. Considering the extremely strong C=O absorbance in Si-O-$Si_{asym.}$ (1070 cm^{-1}) normalized spectra in the ATR-IR a much stronger SP resonance angle shift as the observed 4° (**Figure 57**d) would be expected. This might

support the hypothesis of SP enhancement induced film degradation processes during SP induced polymerization caused by the harsh conditions (pH, temperature) in combination with the SP enhancement acting on the mesoporous film but a definite explanation can currently not be deduced.

In analogy to small pore mesoporous silica films (3-8 nm pore diameter) increasing polymer amount when increasing the monomer concentration is observed for big pore mesoporous silica films with pore diameters of 8-16 nm with a thicker film thickness upon SP-induced polymerization (**Figure 57**c) analyzing the C=O vibrational band at 1730 cm^{-1}. Although, the C=O vibrational band intensity is not as high as for smaller mesopore films, the C=O absorbance in $Si\text{-}O\text{-}Si_{asym.}$ (1070 cm^{-1}) normalized spectra nevertheless surpasses a value of 0.2. Avoiding a polymerization on the outer surface in a next step removing of coinitiator on the outer surface by CO_2 plasma treatment is studied.

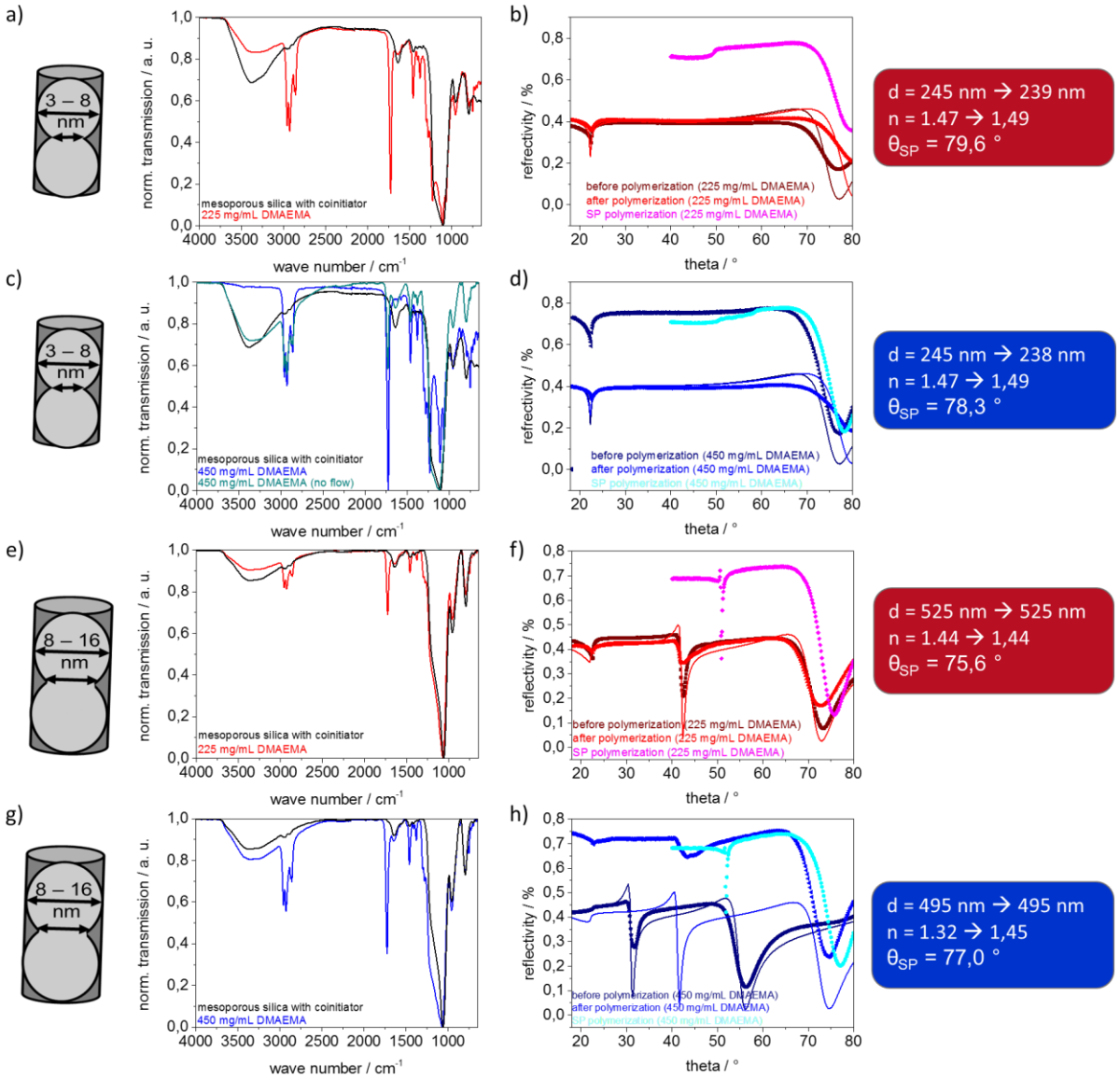

Figure 57. SP-induced polymerization (laser power 0.8 mW, 632.8 nm). The polymerization occurred during one angular scan of around 5 minutes (0.1 °/s von 40-60°, 0.2 °/s von 60-80°) using different monomer concentrations of 225 mg/mL (red) and 450 mg/mL (blue) DMAEMA in water (9:1 volume ratio with methylene blue solution). a) ATR-IR spectra of mesoporous silica films (post- grafted coinitiator, layer thickness of 245 nm, pore diameters of 3-8 nm before polymerization (black), after polymerization with 225 mg/mL monomer concentration (red), and after polymerization with 450 mg/mL (blue) monomer concentration. Both polymerizations are performed under constant flow of polymerization solution (flow rate of 5 µL/min.). For comparison while the turquoise spectra are done with a static polymerization solution (no fluid flow). b) The SPR spectra corresponding to the ATR-IR spectra in a are shown. Dark color (dark red and dark blue) shows measurements before polymerization while bright colors (red and blue) showing measurements after polymerization against air. Magenta and cyano showing the measurement against polymerization solution. c) mesoporous silica films post-grafted with coinitiator with a layer thickness of around 500 nm and pore diameters of 8.16 nm. ATR-IR spectra using the same color code like in a). d) showing also same experiments like in b). In SPR spectra the dotted line is the measured data, while the lines are the fitted data.

To further investigate the distance dependence of the SP induced polymerization and if polymerization on the outer mesoporous film surface can be avoided by destroying all

coinitiator at the outer mesoporous film surface SP induced polymerization upon CO_2 plasma treatment[237] and thus destruction of the coinitiator at the outer mesoporous films surface is investigated. The comparison between SP-induced polymerization with and without plasma treatment for DMAEMA is shown in **Figure 58**. Comparable data for MEP are shown in the appendix (**Figure 109**).

The characterization of PDMAEMA amount using ATR-IR spectroscopy is shown in **Figure 58**a. After CO_2 plasma treatment of coinitiator functionalized mesoporous films a small C=O vibrational band at 1730 cm^{-1} in Si-O-$Si_{asym.}$ (1070 cm^{-1}) normalized ATR-IR spectra is detectable (**Figure 58**a, grey) especially when compared to untreated coinitiator functionalized mesoporous silica films (**Figure 58**a black). Since this phenomenon of C=O vibrational band in ATR-IR spectrum of coinitiator functionalized mesoporous silica is not observed on previous measurements it is reasonable to assume that the CO_2 plasma generates C=O groups at the surface. Performing the polymerization for both films under identical polymerization conditions (time, energy, concentration) successful polymer formation indicated by C=O absorbance at 1730 cm^{-1} in Si-O-$Si_{asym.}$ (1070 cm^{-1}) normalized spectrum is observed in both cases (**Figure 58**a red, blue). A comparable C=O absorbance of 0.05 is detected. This C=O absorbance can originate only from the mesopores in the mesoporous films. Comparing this C=O absorbance to a position next to the SP spot (0.4 cm distance) showing only 0.03 C=O absorbance indicating a local limitation of the polymerization. For the CO_2 plasma treated mesoporous silica films also the smaller absorbance on a position next to the SP spot is visible which indicates a changed functionality in the pores after being in contact with solvents for a long time (~2h). But the direct comparison between plasma and non-plasma treated mesoporous silica films has to be taken very carefully, as the coinitiator functionalized mesoporous films showing a high refractive indices against air after plasma treatment indicating a very low porosity, although the films have been treated exactly the same except for the plasma treatment (**Figure 58**b). In general, the C=O absorbance are lower compared to the experiments shown before because of lower laser power (0.012 mW) and lower energy coupling (85 % no plasma, 70 % with plasma). Because of the changed SPR spectra and the low porosity of the CO_2 plasma treated gold substrates coated with coinitiator functionalized mesoporous silica this route will not be followed in further experiments.

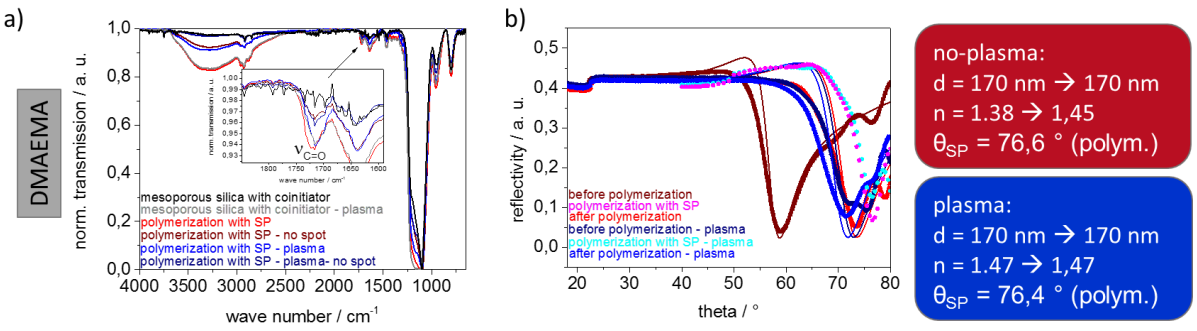

Figure 58. Polymerization of mesoporous silica films post-grafted with coinitiator with SP with and without plasma treatment after coinitiator binding. a) ATR-IR spectra, b) SPR spectra showing in red polymerization with SP and in blue polymerization with SP after Plasma treatment. DMAEMA (225 mg/mL DMAEMA, 0.0052 mg/mL methylene blue in 0.1 M $NaHCO_3$ solution) is used as monomer. Polymerization is done for 30 min with a laser power of 0.012 mW (λ = 632.8 nm). The film thickness is around 170 nm. In both cases the pore diameters are between 3-8 nm.

To more precisely adjust polymer amount, the reaction time has to be adjusted in addition to irradiation power. To investigate the time-dependence of the SP-induced polymerization two different laser powers are used and the polymerization time is varied from 0 to 120 min. The resulting ATR-IR spectra are shown in **Figure 59**. The corresponding SPR spectra are summarized in the appendix (**Figure 110**), always showing the spectra before and after polymerization as well as the spectrum in contact with the polymerization solution (here SP determined and assumed to be constant during polymerization). The SP induced polymerization has been performed at the SP resonance angle (minimum of SP). For both laser power (0.05 mW, **Figure 59**a and 2 mW, **Figure 59**b) a time dependent increase in the C=O vibrational band absorbance at 1730 cm^{-1} in Si-O-$Si_{asym.}$ (1070 cm^{-1}) normalized spectra is observed (**Figure 50**c). The lower power shows a time dependence as expected for a free radical polymerization. The polymer amount increases with reaction time up to a C=O vibrational band intensity at 1730 cm^{-1} of 0.7 after 60-120 minutes (**Figure 53**c, black). For the higher energy of 2 mW laser power, a reduction of polymer amount between 30 and 40 minutes polymerization time is observed which would not be expected and might be related to film degradation without being able to proof this hypothesis to date for the here investigated films. The SP induced polymerization compared in time dependence shows that longer polymerization times again leads to higher polymer amounts in mesoporous silica films as well in case of SP induced polymerization.

Comparing SP-induced polymerization with LED induced polymerization in mesopores reveals again higher polymer amount for SP-induced polymerization as compared to LED-induced polymerization indicating the SP field enhancement: The laser spot area is around 1 mm in diameter, which corresponds to an area of 0.008 cm^2. The laser power is set at 0.05 mW and

2 mW, whereby only 70 % of the energy is coupled in the SP as deduced from the depth of the SP in the SPR spectrum and thus the reflected laser beam intensity. Thus, the coupled laser intensity is estimated to be approximately 4.4 mW/cm^2 and 175 mW/cm^2 respectively. The C=O vibrational band intensity achieved by LED induced polymerization in chapter 6.2.3 with 120 mW/cm^2 (**Figure 46**) reached a maximum value of 0.06 at 100 min polymerization time. With SP-induced polymerization using 95 % less coupled laser intensity the comparable C=O vibrational band intensities are achieved after 45 min. This shows the massive effect of SP field enhancement which is reported to be a factor of 20-30.[220, 222]

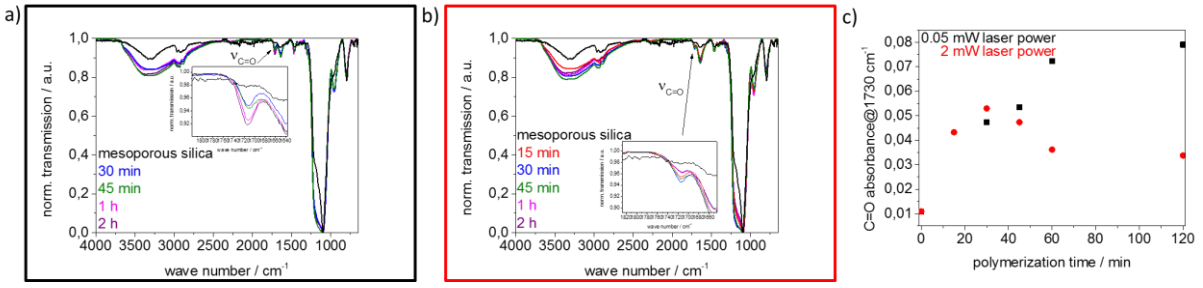

Figure 59. Time-depended SP-induced polymerization using two different laser powers (black = 0,05 mW and red = 2 mW (λ = 632.8 nm)). The mesoporous silica films post-grafted with coinitiator has a film thickness around 170 nm and a pore diameter of 3-6 nm. DMAEMA is used as monomer with 225 mg/mL DMAEMA, 0.0052 mg/mL methylene blue in 0.1 M $NaHCO_3$ solution. a) ATR-IR spectra of the mesoporous silica films after polymerization with different times. The laser power is constant at 0,05 mW. The zoom shows the C=O band in Si-O-Si$_{asym.}$ (1070 cm^{-1}) normalized spectra. b) ATR-IR spectra of polymerization with SP with higher laser power of 2 mW. The polymerization time is varied the same using the same color code for ATR-IR spectra. The zoom shows the C=O band@1730 cm^{-1} in Si-O-Si$_{asym.}$ (1070 cm^{-1}) normalized spectra. c) Plot of the C=O absorbance@1730 cm^{-1} in Si-O-Si$_{asym.}$ (1070 cm^{-1}) normalized spectra resulting from a) black and b) red against the polymerization time. (SPR spectra in **Figure 110**, appendix).

To investigate the energy dependence of SP induced polymerization with the aim to adjust the amount of generated polymer envisioning a nanolocal functionalization in mesoporous silica films. In general, a rather short reaction time is favored to avoid film degradation and thus control the amount of polymer and its location and to allow fast polymer writing in future.

In **Figure 60** two series of energy dependent SP-induced polymerization are discussed. In the first series (**Figure 60**a, b) a polymerization time of 30 min is used, since this is observed to be potentially the limit before film degradation and the decreasing of polymer amount takes place for the highest energy (**Figure 59**c). The corresponding SPR spectra are shown in the appendix (**Figure 111** and **Figure 112**). The ATR-IR spectra show an increasing absorbance of the C=O vibrational band at 1730 cm^{-1} and thus an increase in polymer amount with irradiation power (**Figure 60**b). Although the polymer amount stays relatively small. It is clearly visible that the polymer amount can be precisely controlled by the irradiation laser beam power. When changing the monomer concentration and the polymerization time from 225 mg/mL DMAEMA

and 30 minutes (**Figure 60**a, b) to 450 mg/mL DMAEMA and 10 minutes (**Figure 60**c, d), the energy dependence of the polymer formation is still observed. The polymer amount increases with increasing irradiation power and the highest power of 6.4 mW (80°) leads to a factor 3 higher C=O absorbance of 0.9 (normalization is not possible because of overlaying polymer bands to silica in ATR-IR spectrum) as compared to 0.02 mW (20°) (**Figure 60**b). This value of the C=O absorbance already indicates that polymer formation cannot be limited to inside the mesopores and polymer formation at the outside planar surface of the mesoporous silica film occurs. Comparing light-induced polymerization in mesoporous silica showing a C=O absorbance of 0.017 at a laser power of 6.8 mW to SP-induced polymerization, where 35 % energy is coupled into the SP, leading to an estimated power of 2.3 mW a C=O absorbance of 0.022 is obtained. This again demonstrates the field enhancement within the surface plasmon without which the observed C=O vibrational band intensities could not be explained. The polymer amount generated with SP induced polymerization is higher than the polymer amount generated with light induced polymerization in mesoporous silica films using less laser power.

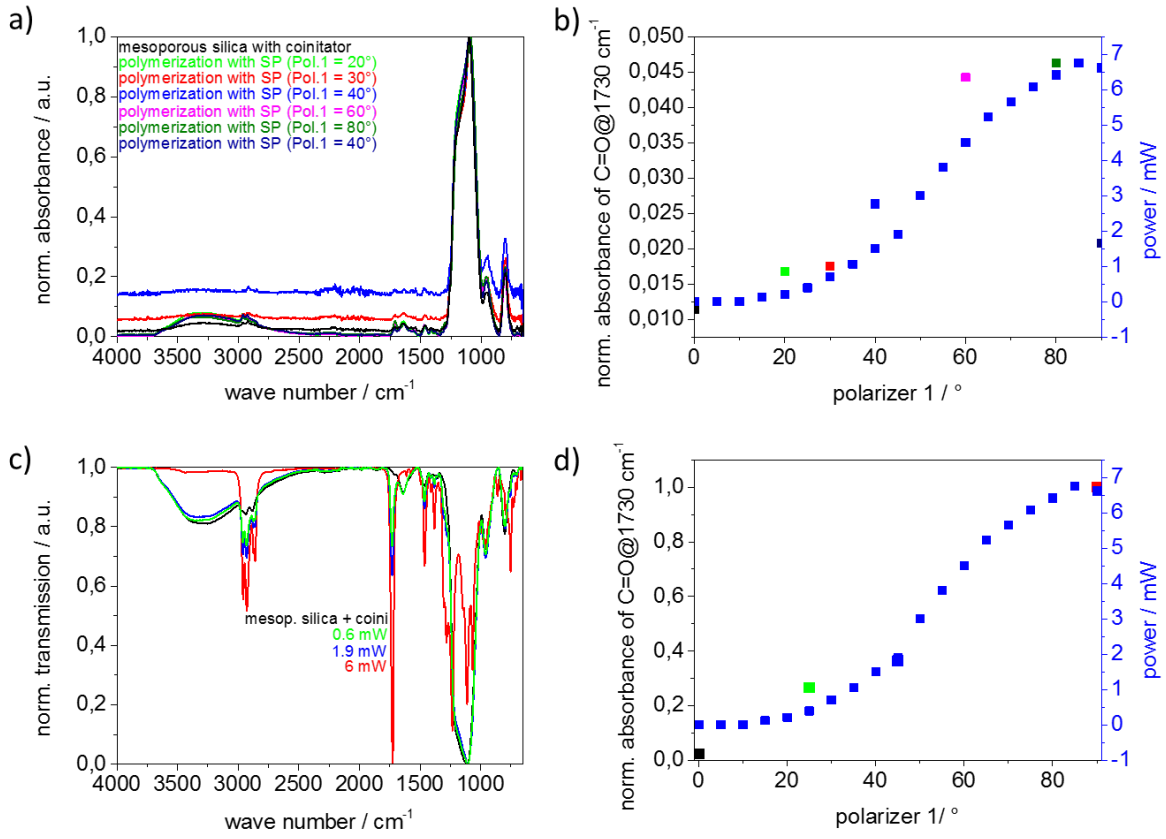

Figure 60. Energy-dependent SP-induced polymerization. a) ATR-IR spectra of DMAEMA (250 mg) polymerization using different irradiation powers with a constant polymerization time of 30 min. The film thickness is around 170 nm with a pore diameter of 3-8 nm. b) The C=O absorbance@1730 cm^{-1} in Si-O-$Si_{asym.}$ (1070 cm^{-1}) normalized spectra (black) plotted against the polarizer 1 (Pol. 2=90°) which results in the laser power shown in blue. c) and d) showing the same experiment like a and b using higher monomer concentration (450 mg/mL DMAEMA, 0.0052 mg/mL methylene blue in 0.1 M $NaHCO_3$ solution) and a shorter polymerization time of 10 min.

The tuning of polymer amount via laser beam power of the incoming laser during a SP induced polymerization could be successfully demonstrated. In the presence of thick mesoporous silica films not only the surface plasmon but an additional near field mode is appearing, the leaky transversal mode (TM). Thus, the polymerization can be induced with the surface plasmon but as well by the transversal mode (TM). This is especially interesting as both modes are characterized by a very different field distribution along the mesoporous film thickness (**Figure 10**, chapter 5.2). The TM is distributed over the entire film cross-section and no enhancement of the energy occurs (see **Figure 53**). A mesoporous silica film thickness larger than 400 nm is required to allow TM formation in liquid surrounding medium. In addition, this film thickness should be larger than the penetration depth of the surface plasmon.

To investigate the differences between SP-induced and TM-induced polymer functionalization of mesoporous silica films the polymerization is initiated once at the SP resonance angle of 67.5 ° and subsequently with the TM at a resonance angle of 52.8 ° (see SPR spectra recorded against polymerization solution in **Figure 113** in appendix). Both polymerizations are performed using the same sample in two separate spots (**Figure 61**). Polymer formation on the outer film surface is investigated using AFM as absence of polymer on the outer surface while simultaneously detecting polymer in the ATR-IR spectra would be an indication towards local limitation. The SP-induced polymerization is not successful in this experiment because no polymer is detected in ATR-IR spectrum (see appendix, **Figure 114**). In contact with polymerization solution the coupling effeciency for the TM is 69 % of laser power (5 mW). After the TM induced polymerization the SP resonance angle as well as the TM angle is shifted to higher angles. SP sensitive to 100 nm (penetration depth) while the TM is sensitive to the entire film thickness (480 nm). In the corresponding ATR-IR spectra (**Figure 61**b) the C=O vibrational band of PDMAEMA at 1730 cm^{-1} in Si-O-$Si_{asym.}$ (1070 cm^{-1}) normalized spectra indicates the presence of polymer for TM-induced polymerization under the applied experimental conditions (**Figure 61**b, blue). The outer mesoporous silica film surfaces are additionally characterized using atomic force microscopy (AFM) before polymerization (**Figure 61**c), after 1 h contact with polymerization solution (**Figure 61**d) and with TM-induced polymerization (**Figure 61**e). In case of TM-induced polymerization polymer formation on the outer surface is clearly observed which is explainable with the polymerization through the entire film. The contact with polymerization solution provides no changes on the silica surface compared to the reference sample. In summary, a successful TM-induced polymerization can be shown with a proof that the polymer functionalization is done through the entire film including the outer surface for a mesoporous film thickness of more than 400 nm.

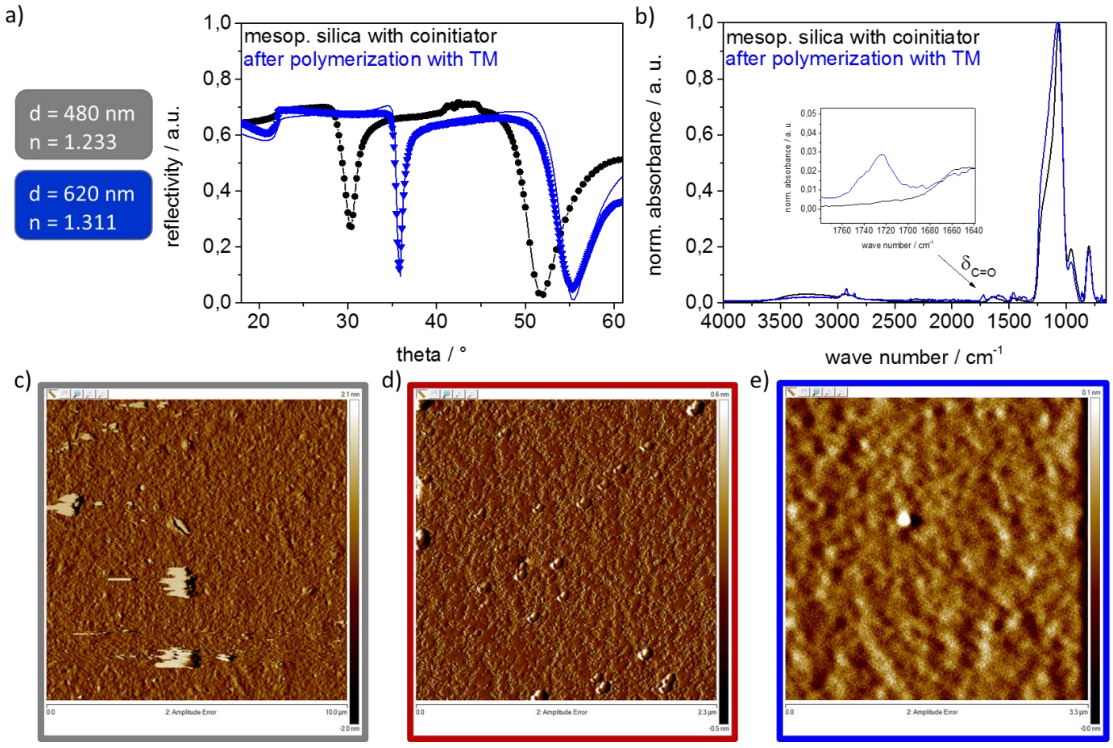

Figure 61. Polymerization of DMAEMA with TM (blue) in a mesoporous silica film functionalized with coinitiator (black) with a layer thickness of 480 nm and pore diameters of 3-8 nm. The used laser power is 5 mW (λ =632.8 nm) and 1 h time with a constant flow of polymerization solution of 5µL/s a) SPR spectra measured against air (dots) before polymerization (black) and after polymerization (blue). The fit curves are shown as line. b) ATR-IR spectra of mesoporous silica films before and after polymerization with TM belonging to SPR spectra. c-f) AFM images of the surfaces of mesoporous silica functionalized with coinitiator c) after polymerization with SP d) and TM e) (measured by Beatrice Fickel, AK Prof. Dr. Biesalski, TU Darmstadt).

Within individual polymerization series the results are consistent but not directly comparable with other series for example with respect to absolute C=O vibrational band intensity values characterizing polymer amount. For example in **Figure 59**c the SP-induced polymerization for 30 min with 2 mW lase power shows C=O vibrational bands of 0.055 while in **Figure 60**b SP-induced polymerization under same conditions generates C=O vibrational bands of 0.025. In the future, a main focus must be placed on process optimization from sample preparation via film optimizing to SP-induced polymerization, since automation of the processes is extremely useful to ensure comparability of the full results. It has to be noted as well that during the work with near-field induced polymerization a not to be neglected number of failed experiments (no detectable C=O vibrational band) after SP-induced polymerizations were obtained (70 % of SP-induced polymerizations are successful). However, the trend of higher C=O vibrational band intensity in ATR-IR spectra observed for TM induced polymerization as compared to SP induced polymerization is observed for the high majority of experiments (90 %) for which polymer formation was observed.

Polymer functionalization of SP-irradiation and TM-irradiation is compared for bigger pore mesoporous silica films. These mesoporous silica films with pore diameters of 8-16 nm are chosen for this comparison as they can be prepared more easily as single layer films with film thickness larger than 500 nm. As mentioned for the experiment in **Figure 61** this thickness is required to allow TM formation. In **Figure 62**a the mesoporous film coated gold substrates after SP-induced and TM induced polymerization are shown. Next to the photograph of the film a scheme indicating the spots measured with ATR-IR and ellipsometry are depicted. Thereby the spot 5 (slightly above) is the spot in which polymerization has been performed. The TM-induced polymerization shows a C=O vibrational band at 1730 cm^{-1} in Si-O-$Si_{asym.}$ (1070 cm^{-1}) normalized spectra within all analyzed spots (1-5) (**Figure 62**b). The C=O vibrational band intensity is varying between 0.06 and 0.16 where in the upper area (above spot 5) the C=O absorbance is higher. The SP resonance angle shifts to higher angles after polymer functionalization (**Figure 62**c). The increase in C=O absorbance in Si-O-$Si_{asym.}$ (1070 cm^{-1}) normalized spectra and refractive index as deduced from the SP spectra fit upon polymerization are plotted in **Figure 62**d (filled symbols). For this sample, SP-induced polymerization (**Figure 62**e) only results in a relatively small C=O vibrational band of 0.005 for all measured spots. This is not surprising noting the limited penetration depth of the SP, the TM propagating in the entire film thickness and assuming no exchange of monomer and dye takes place with the polymerization solution in the bottom parts of the mesoporous film. The film degradation plays a non-negligible role for SP-induced polymerizations which can be seen in decreasing film thickness in fitted SP spectrum (**Figure 62**f) and ellipsometry data (**Figure 62**d, non-filled circles) after polymerization. The SPR spectrum (**Figure 62**f) after SP-induced polymerization shows a SP- and TM- resonance angle shift to slightly higher angles for TM and significantly higher resonance angle for SP indicating higher refractive indices. But for the SP-induced polymerization a film degradation is visible in the fitted film thickness after polymerization. The determined refractive indices and layer thicknesses based on fitting the SPR spectra in red box (**Figure 62**c, TM-induced polymerization) and blue box (**Figure 62**f, SP-induced polymerization) are in agreement with ellipsometry measurements (**Figure 62**d) as well fitted with a one-layer model. The values for layer thickness (black) and refractive indices (blue) (**Figure 62**d) for SP (circle)- and TM (filled square)-induced polymer functionalization fit well to the SPR model. The coupled energy for SP and TM induced polymerization is 1.69 mW respectively 0.75 mW (laser power = 3 mW, coupling efficiency for SP =56 % and TM=25 %). In a reference experiment of He/Ne-laser induced polymerization on a mesoporous silica film with related film parameters (big pores, 500 nm film thickness), polymerization solution and polymerization time the C=O absorbance is 0.03 for the highest possible laser power of 6.5 mW (pol. 1 =90°).

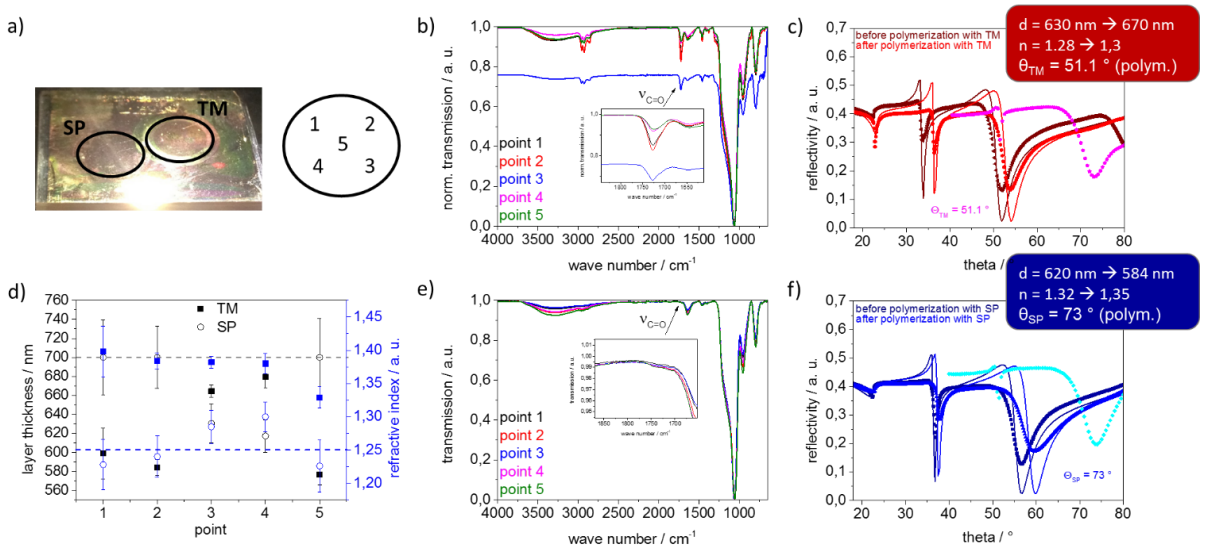

Figure 62. Polymerization with SP and TM using DMAEMA (225 mg/mL DMAEMA, 0.0052 mg/mL methylene blue in 0.1 M $NaHCO_3$ solution) as monomer. The polymerization time is 30 min with a laser power of 3 mW (λ = 632.8 nm). Mesoporous silica films are post-grafted with coinitiator. The film thickness is around 600 nm and has a pore diameter of 8-16nm. a) image of the mesoporous silica film on gold coated glass after the polymerization showing the two rings of the flow cell from SPR set up with the five spots measured with d) ellipsometry (one-box fitting model for layer thickness and refractive index) and ATR-IR. b) ATR-IR of polymerization with TM. c) SPR spectra before polymerization (red) and after polymerization (dark red) with TM mode. Magenta spectrum shows the spectra where the resonance angle of TM is evaluated for polymerization. e) ATR-IR of polymerization with SP. c) SPR spectra before polymerization (blue) and after polymerization (dark blue) with SP. Cyano spectrum shows the spectra where the resonance angle of TM is evaluated for polymerization.

In summary, both near-field modes, SP and TM, initiate polymerizations. Thereby SP induced polymerization generates apparently less polymer than TM induced polymerization although SP shows field enhancement compared to laser-induced polymerization. This is a good indication that local limitation of polymerization in several hundred nanometer thick mesoporous films works, because otherwise, especially in contact with the polymerization solution, significantly more polymer formation would be expected on the outer surface, as it is observed for thinner films in SP induced polymerizations.

To investigate the effect of laser beam power, the experiment shown in **Figure 62** is repeated with 2 mW (**Figure 63**) instead of 3 mW (**Figure 62**). Considering the coupling efficiency (depth of the corresponding SP or TM in the SPR spectrum) the energy coupling for TM is estimated to be ~0.2 mW while the SP is estimated to be 1 mW (**Figure 63**a, laser power = 3 mW, coupling efficiency for SP=50 % and TM=10 %). The polymerization is evaluated based on ATR-IR measurement within the irradiated spot as well as next to it in the flow cell. In addition as reference spot on the same substrate but located outside of the flow cell is measured as indicated in **Figure 63**e. In addition the SP- versus TM-induced polymerization is carried out for DMAEMA (**Figure 63**b) as well as for MEP (**Figure 63**f). For

the polymerization with DMAEMA the mesoporous silica film thickness is varied between 500 nm and 800 nm using two different withdrawal speeds during dip-coating. The ATR-IR measurements (**Figure 63**c) of 500 nm thick mesoporous silica films after SP- and TM-induced PDMAEMA functionalization show clear C=O vibrational bands at 1730 cm^{-1} in Si-O-$Si_{asym.}$ (1070 cm^{-1}) normalized spectra detected within the polymerization spot (magenta and red). The spectra next to the polymerization spot show no C=O vibrational band intensity for SP-induced polymerization (blue) and less C=O vibrational band intensity for TM-induced polymerization (magenta) as compared to the irradiated spot. This observation is reproduced for the polymerization with MEP as monomer in 500 nm thick mesoporous silica films (**Figure 63**g) and with DMAEMA in mesoporous silica films with 800 nm thickness (**Figure 63**d). The detected C=O vibrational band intensity for PMEP functionalized mesoporous silica films showing a higher polymer amount by TM-induced polymerization than SP-induced polymerization. In case of 800 nm thick mesoporous silica films the SP-induced polymerization leads to higher polymer amounts that the TM-induced polymerization. The corresponding SPR spectra are depicted in the appendix in **Figure 115**. The TM- and SP-induced polymerization is always carried out on the same substrate, first with the SP and then with the TM. Therefore, the refractive indices of the mesoporous films before polymerization are comparatively high in the latter, because the substrates probably still have residual moisture in the pores due to the extraction with water. All SP-induced polymerizations shown in **Figure 63** result into a shift of SP resonance angle as well as TM resonance angle to larger angles which fits well to the relatively high C=O vibrational band intensity for SP-induced polymer functionalization visible in ATR-IR spectra. The TM-induced polymerization shows no big differences in SPR spectra before and after polymerization but this can be explained by the previously filled pores (film is wetted before because of SP-polymerization in the same sample before) or if the coupled energy is too low to generate a thick polymer layer on top which can be seen by a shift in TM resonance angle.

When comparing the small C=O absorbance in Si-O-Si_{asym} (1070 cm^{-1}) normalized spectra for SP-induced polymerization in **Figure 62** with the higher polymer amount in **Figure 63** it is obvious that smallest differences in the mesoporous film characteristics or in the performance of near-field induced polymerization have strong effects e.g. on coupling and field enhancement and cannot yet be fully controlled in such detail, so that absolute values between different samples are not directly compared.

Comparing the polymer amount directly in the irradiated spot with position next to it, the SP-induced polymerization results in a significantly higher C=O absorbance in Si-O-$Si_{asym.}$ (1070 cm^{-1}) normalized spectra, within the irradiated spot as compared to a spot (distance

~2 mm) next to it (compare magenta and blue spectra in **Figure 63**c,d and g). In contrast the TM-induced polymerization shows a broadened area of polymer functionalization with an decrease of polymer amount in a 2 mm distance to the polymerization spot (compare red and magenta spectra in **Figure 63**c,d and g). This behavior is a first indication for a working local resolution with respect to x-y-direction.

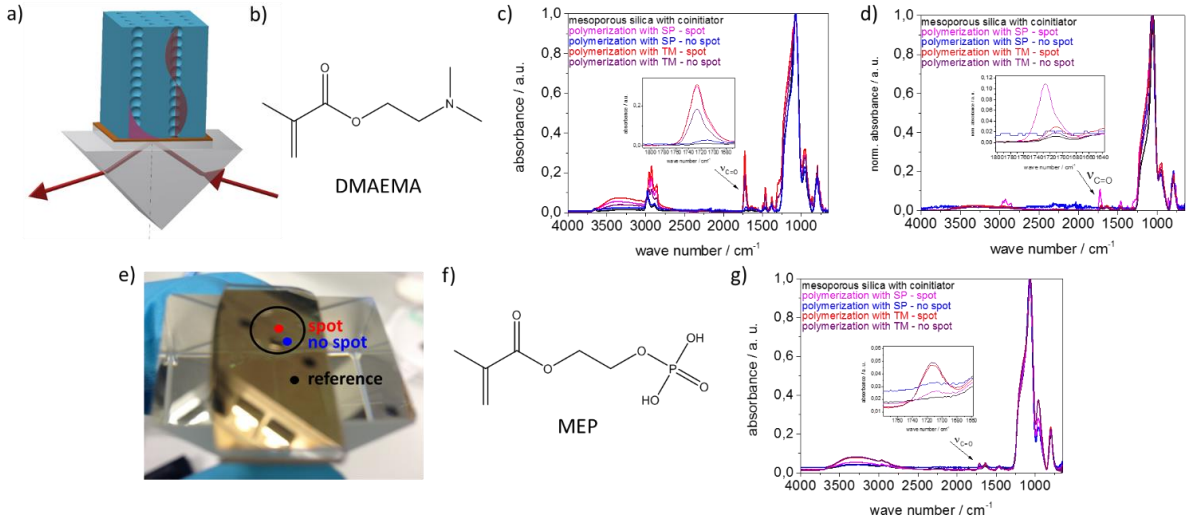

Figure 63. Polymerization of SP and TM with two different monomers. Polymerization time is 30 min at a constant flow of 5 µL/min and a concentration of 225 mg/mL of monomer (laser power = 2 mW). Pore diameters of mesoporous silica films are between 8-16 nm. a) Scheme of the difference between SP and TM. b) chemical structure of monomer DMAEMA. c) ATR-IR spectra of mesoporous silica films with around 500 nm film thickness before and after polymerization measured with the set-up in e). d) showing the same polymerization parameters but using thicker films with film thickness around 800 nm. e) image of mesoporous silica film on gold coated glass substrate with circle of the flow cell marked with spot of laser (red), no spot (blue) and the reference (black) as measuring set up for ATR-IR measurements. f) chemical structure of monomer MEP. g) ATR-IR spectra of the polymerization with MEP with TM (red=spot, magenta= no spot) and SP (magenta = spot and blue=no spot).

In summery the SP induced polymerization in mesoporous silica can be controlled with respect to the generated polymer amount by varying the polymerization time and the power. With respect to energy not only the adjustable laser power but as well the coupling efficiency and shape of the SP and TM have to be considered. This depends on the optical quality of the film and it is very difficult to reproduce and optimize within the applied preparation procedures. If this concept of SP- and TM-induced polymerizations should be further developed towards precise and nanoscale local resolution and polymer amount control at the nanoscale optimizing and reproducible adjusting the optical film quality and stability will be very important. The latter complicates exact reproducibility as optical film parameters seem to vary slightly between different films. These slight variations, which are not significantly affecting classical polymerization, seem to have a pronounced effect in SP-induced polymerizations as they strongly affect field enhancement for example. By comparing the generated C=O vibrational

band intensity and thus the generated polymer amount between SP-induced and LED induced polymerizations the enhancement of SP is demonstrated. It is also possible to use the TM to initiate polymer functionalization. It can be shown that the SP induced polymerization is locally limited in x-y direction while TM-induced polymerization is more distributed in the area. In the case that both SP and TM induced polymerizations on one substrate (same film parameter), less polymer is detected in thick films (d >> penetration depth of the SP) for the SP induced polymerization than for TM induced polymerization although the SP has an enhancement factor. This fact clearly indicates that the polymer is formed as well on the outer surface in case of TM induced polymerization. Understanding the exact reason for this requires the systematic investigation of many parameters (monomer distribution along the film, dye distribution along the film, simulation for field distribution and amplification, etc). thereby, it has to be noted that the changes induced by SP or TM polymerization are not necessarily resolved by routine characterization techniques such as SEM or TEM and even characterization by BET is extremely challenging if not impossible due to the low material amount. A future direction might therefore not only look at the polymer functionalization and local control but as well on the development of suitable characterization procedures for these scales in combination with such low material amount of mesoporous films.

A critical aspect of this polymerization is the influence of the quality of the gold substrate and mesoporous film and so the reproducibility of polymerization. Since the coupling of the energy of the SP and thus energy and field enhancement varies from film to film, it is not yet possible to derive generally valid parameters such as required energy and polymerization time to obtain a local resolution in x-y and z-direction, but in principle a control of the polymer quantity is possible and a nanolocal resolution is very likely.

6.2.5. Outlook

Another possibility to generate an evanescent field without using metal coatings such as old is using total internal reflection when a laser beam is reflected under total reflection from a glass substrate, (**Figure 64**). This configuration is implemented in total internal reflection microscopy setups. The interface mesoporous silica to cover slip is a perfect combination because the difference in refractive indices fulfill the requirement that n_1 (sample) is less than n_2 (cover slip). In a first experiment, in collaboration with Dr. Tobias Meckel (AK Prof. Dr. Biesalski, TU Darmstadt), a self-constructed TIRF microscope equipped with a red light laser (pulsed every 10 ns, $\lambda = 650$ nm, power 100 mW) is used to verify if methylene blue initiated polymerizations can be performed at this wavelength using a TIRF microscope.

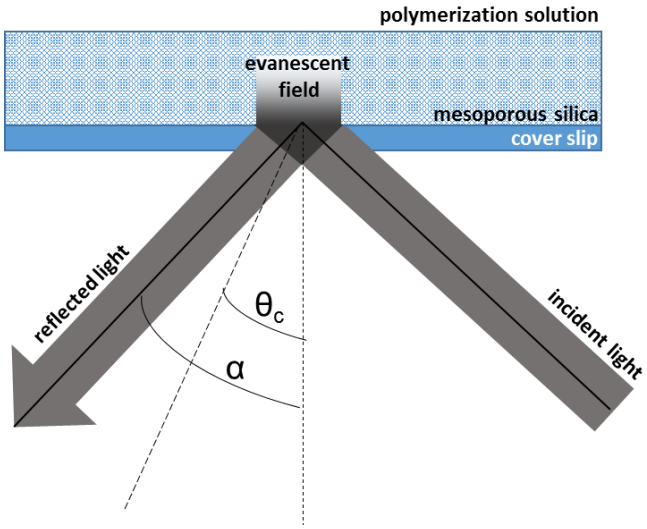

Figure 64. Total internal reflection fluorescence (TIRF). The excitation laser beam (λ = 650 nm, power 100 mW) pass the sample with the incidence angle α, which is greater than the critical angle, θ_c (indicated by the dashed line). The excitation beam is reflected off the cover-slip–sample interface with angle α and an evanescent field is generated on the opposite side of the interface, in the sample. The refractive index of the sample (n_1) must be less than the index of refraction of the cover slip (n_2) to achieve total internal reflection.

The mesoporous silica is coated on one side of cover slip by dip-coating with 2 mm/s withdrawal speed and afterwards functionalized with coinitiator. The same polymerization solution as for SPR experiments (DMAEMA (450mg/mL) and methylene blue (0.0052 mg/mL) in aqueous 0.1 M $NaHCO_3$ solution) is used (Chapter 8.3.2, 8.4 and 8.7). The polymerization is performed for 10 minutes and 20 minutes irradiation with 30 % laser intensity (3.8 mW) and 10 min with 60 % laser intensity (8 mW). After polymerization the sample is characterized using ATR-IR spectroscopy. The Si-OH (900 cm^{-1}) normalized ATR-IR spectra are shown in **Figure 65**. The C=O vibrational band at 1730 cm^{-1} is characteristic for a successful polymerization because the C=O function could only result from polymer PDMAEMA (zoom in in **Figure 65**). In this initial proof of concept experiment a C=O vibrational band at 1730 cm^{-1} and thus polymer formation is only observed for 20 min polymerization time and 30 % laser intensity (3.8 mW) (green). Compared to polymerizations with the He/Ne laser with the same laser power but using a lower monomer concentration of 225 mg/mL the C=O absorbance of Si-OH (900 cm^{-1}) normalized spectra is in the same area at 0.01 – 0.011. This indicates a free pore volume of 20 % (**Figure 45**). Although the polymer amount is very low, this is a proof of concept allowing to further investigate the potential of TIRF-induced polymer functionalization of mesoporous films and with this broadening the application of such visible light and nanolocal optical field induced polymerizations.

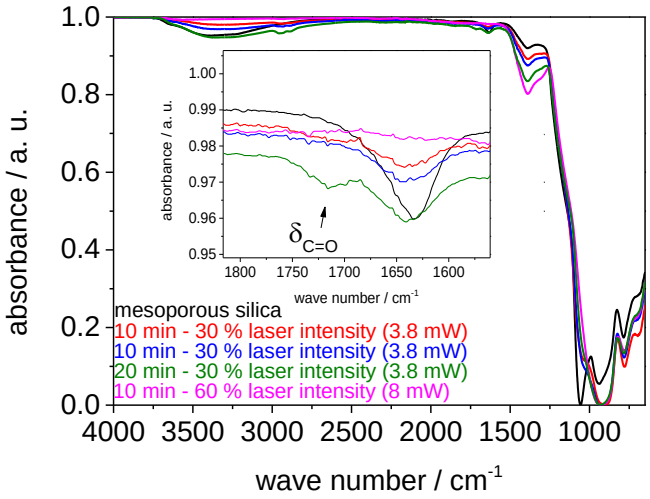

Figure 65. ATR-IR spectra of mesoporous silica prepared (black) and mesoporous silica after near-field induced polymerization under different condition with DMAEMA. The spectra are recorded directly on glass substrate (cover slips) and normalized to Si-OH bend at around 900 cm^{-1}. The area between 1800 – 1575 cm^{-1} is enlarged in the figure. The C=O vibrational band at 1730 cm^{-1} in Si-OH (900 cm^{-1}). normalized spectra is an indicator for successful polymer functionalization (dark green).

The opportunity of varying film thickness and therefore changing the range of evanescent field in the z-direction into the film could lead to a functionalization on the nanoscale. When optimizing the parameters like porosity and film thickness also a multilayer design is imaginable. This 3D nanolocal polymer writing in confinement of mesoporous structures should be investigated regarding the transport with respect to selectivity, direction and rate adjustment.

6.3. Silica-Functionalization of Papers as Hierarchical Porous Material

This chapter is divided into two sections. In the first section, the silica functionalization of cotton linter papers and the functionalization with redox-responsive polymer regarding the design of wettability and water imbibition are investigated and discussed. In the second section, the silica functionalization of eucalyptus-sulfate papers with focus on silica distribution and engineering asymmetric wettability is demonstrated.

6.3.1. Silica-Functionalization of Cotton Linters

Parts of the results discussed in this chapter are published in *Langmuir* 2017, 33, 332-339. The functionalization of paper sheets with silica based on preliminary work of Christelle Dubois. She focused on the functionalization of the silica-paper hybrid materials with hydrophobic silanes.

Paper-based microfluidic devices have been studied for a variety of applications from delivery, lab-on-chip devices to sensors and membranes since their introduction by Whitesides.[140, 252] The adjustment of flow in paper-based materials with respect to paper homogeneity and density, fluid viscosity, environmental conditions and channel dimensions are being studied in nowadays research.[152, 156, 157, 253-255]

To understand the role of nanoscale pores and especially mesopores on paper material characteristics cotton linters paper sheets are coated with a nonporous (dense) and a mesoporous (template Pluronic® F127) coating using EISA and dip-coating on previously lab engineered paper sheets. The procedure of coating cellulose fibers in a paper sheet with mesoporous silica is depicted in **Figure 66**a. Using sol-gel chemistry and evaporation induced self-assembly, mesoporous silica coatings with and without mesopores (called mesoporous or dense respectively) are prepared in paper sheets depending on the presence or absence of the micelle forming block copolymer template in the coating solution. Based on this procedure, dense or mesoporous silica-paper hybrid materials or pure silica paper-derived materials are prepared depending on the final temperature used for curing. In case samples are heated up to 200 °C, the cellulose-fiber based paper stays intact and a hybrid material is obtained (see TGA measurement in appendix, **Figure 117**). Differently, heating up to 500 °C results in a degradation of the cellulose fibers and an unmodified silica material derived from paper is obtained.

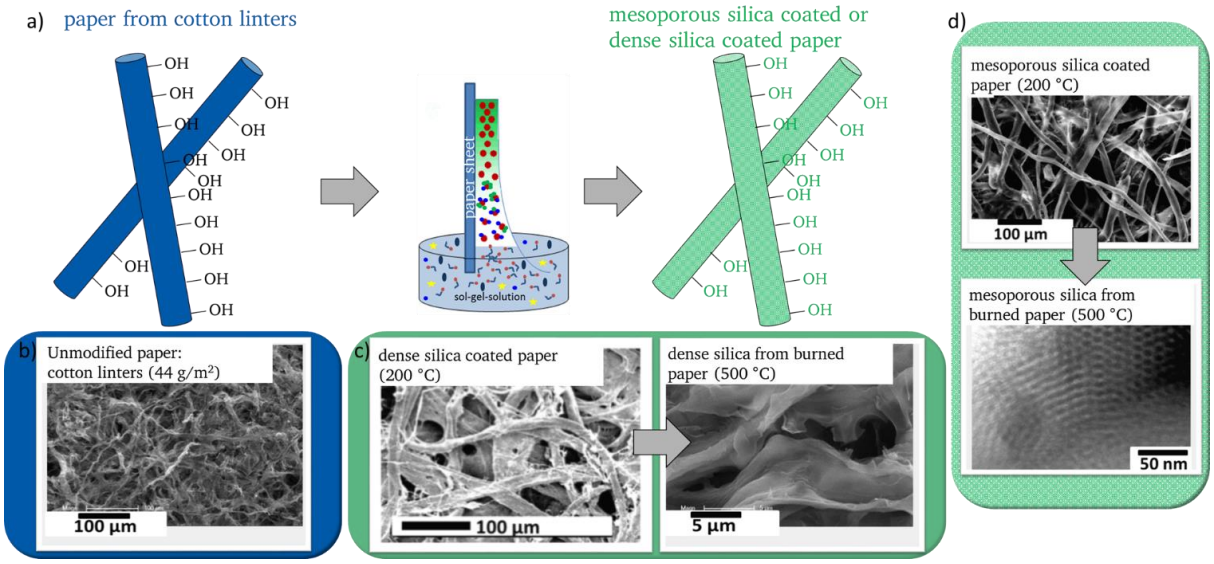

Figure 66. Schematic illustration of the preparation of paper-derived mesoporous silica sheets. Electron microscopy images of b) cotton linters (44 mg/m²) and paper-derived silica structures. c) SEM images of dense silica paper-derived silica treated until 200 °C and non-mesoporous paper-derived silica treated until 500 °C. d) SEM images of mesoporous (F127) paper-derived silica treated until 200 °C without destroying the cellulosic paper structure and TEM images resolving the mesoporous structure of mesoporous (F127) paper-derived silica treated until 500 °C. SEM images are recorded by Dr. A. Geißler (AK Prof. Dr. Biesalski, TU Darmstadt). TEM image is recorded by U. Kunz (AK Prof. Dr. Kleebe, TU Darmstadt). Adapted with permission from *Langmuir* 2017, 33, 332-339. Copyright 2017 American Chemical Society.

The fibrous and mesoporous structure of dense and mesoporous silica-paper hybrid and unmodified silica materials is characterized using scanning electron microscopy (SEM) as well as transmission electron microscopy (TEM) and compared to unmodified paper sheets (**Figure 66**b). **Figure 66**d clearly shows an intact fibrous structure of a mesoporous silica coated cotton linters hybrid paper sheet after being treated up to 200 °C. The same sample, treated up to 500°C to remove the cellulose fibers, shows the disruption of the fiber structure. Nevertheless, a mesoporous structure with ordered pores smaller than 10 nm is clearly visible in case the mesopore template Pluronic® F127 is present as depicted in the TEM image of **Figure 66**d. By coating the same paper structure with dense silica, comparable disrupted fiber structures are observed after heating up to 500 °C as it can be seen in the SEM images (**Figure 66**c).

A further characterization of the silica functionalized paper sheets is performed using ATR-IR spectroscopy (**Figure 67**). The reference spectrum is paper consisting of cotton linter fibers (black). The spectrum shows the typical OH stretching vibration of polysaccharides between 3500 and 3000 cm^{-1} and the CH stretching vibration at around 2800-2900 cm^{-1}. At 1630 cm^{-1} the band of the water molecules absorbed in cellulose are visible. Between 1500- 850 cm^{-1} the stretching and bending vibrations of CH_2, CH, OH and CO are visible. In **Figure 67**a the functionalization with mesoporous silica is investigated. No differences between the reference

papers and the mesoporous silica coated papers (with, blue and without extraction, red, for template removal) are visible concerning additional functional groups. The magenta spectrum (**Figure 67**) showing the residual what after treatment until 500 °C and thus after calcination of all cellulose components. After this calcination of the paper cellulose fibers the functional groups of silica are visible by Si-OH and Si-O-Si_{sym} vibrational band at around 1000 cm^{-1} and 800 cm^{-1}. This shows in combination with TEM images in **Figure 66**d that mesoporous silica is present in low amounts in the modified paper sheets although not visible in the ATR-IR spectra before cellulose calcination. **Figure 67**b shows the same characterization for dense silica coated cotton linters papers. In magenta the silica spectrum after paper calcination (500 °C) shows the same characteristic silica bands as discussed for mesoporous silica coated cotton linters after calcination (**Figure 67**a). In red the dense silica functionalized cotton linters paper is shown. Here, it is visible that the bands from reference uncoated paper and unfunctionalized silica are overlapping which is the proof that silica is coated in and on the cotton linter paper.

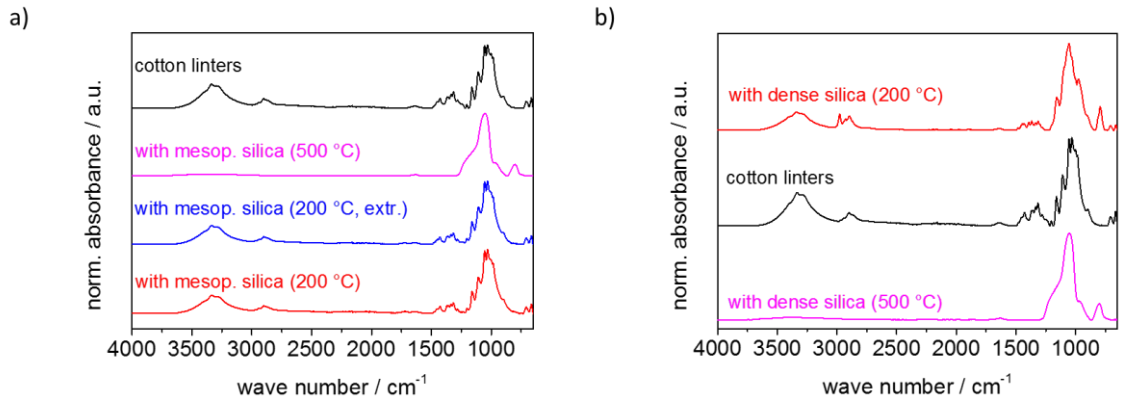

Figure 67. Infrared spectra of a) mesoporous silica functionalization and b) dense silica functionalization. Untreated paper sheets (cotton linters, 44 g/m²) are shown in both spectra in black. The mesoporous silica or dense silica functionalized papers treated till 200 °C are shown in red. For mesoporous silica hybrid paper sheets treated with 200 °C and extracted with ethanolic hydrochloric acid to remove the polymeric template the spectrum is blue. The mesoporous silica and dense silica residues when burning the paper substrate are colored in magenta.

The systematic investigation of the influence of paper fibrous structure on wetting behavior of cotton linters papers regarding their water imbibition after coating with dense or mesoporous silica (before and after template extraction) has been performed using different paper grammages between 18 and 101 g/m^2.

In **Figure 68**a the water imbibition of dense silica coated cotton linter papers is shown. In addition, a grammage dependent water exclusion is observed by contact angle measurement over more than three minutes (**Figure 68**a). This grammage dependence for the water exclusion is as well observed for water imbibition in dense silica coated paper (**Figure 68** b). A time-dependent rise of the water front is observed. Plotting the travelled water front distance against

the square root of the time macroscopically a linear dependence in analogy to the Lucas-Washburn-equation is observed. Under the applied experimental conditions and using identical material preparation conditions and especially a constant sol-gel solution concentration, water is no longer excluded for dense silica coated hybrid cotton linters papers when the grammage reaches a value of 44 g/m^2 or higher. The exact value of this critical grammage seems to strongly depend on the paper fiber morphology and hierarchical sheet porosity. This indicates the dependence of water imbibition due to the silica coating amount per fiber according to the Lucas Washburn equation. However, the situation clearly seems to be complex: no linear relation between grammage and water fluid flow is observed. When measuring the static contact angle (**Figure 68**a) of the water excluding samples, the water droplet stays stable for a few minutes, but then the contact angle slightly decreases due to evaporation of water. For the dense silica coated samples with high grammages, an intrusion of water can be achieved within the first 30 s.

Water imbibition into the mesoporous silica coated papers is investigated with and without the presence of the mesopore forming template Pluronic® F127. When template is present in the mesoporous silica coating the mesopore accessibility is hindered because pores are filled. Interestingly, the comparison of mesoporous silica coated hybrid papers before (**Figure 68**c) and after template extraction (**Figure 68**d) show no significant differences with respect to water imbibition considering the error bars (obtained from three independent measurements). This indicates that other structural effects, e.g. fiber swelling or pinning might be dominating water imbibition. In general, and in contrast to the effect of dense silica coatings, the mesoporous silica coating does not seem to affect the water imbibition significantly supporting the role of nanoscale porosity for paper characteristics.

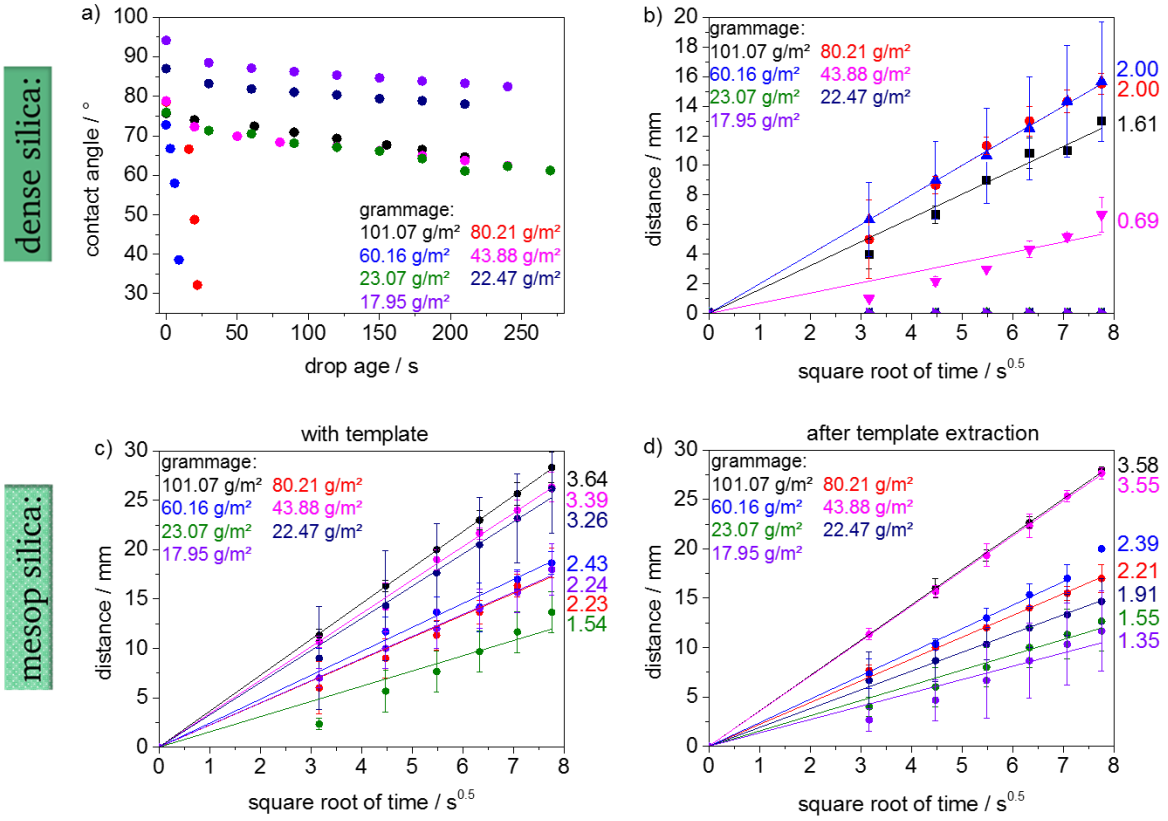

Figure 68. Paper grammage dependent water imbibition for dense and mesoporous silica hybrid cotton linters paper sheets. a) Grammage and time-dependent static contact angle of dense silica hybrid cotton linter papers. b) Grammage and time-dependent water fluid of dense silica hybrid cotton linter papers. c) Grammage and time-dependent water fluid of mesoporous silica hybrid cotton linter papers without template extraction. d) Grammage and time-dependent water fluid of mesoporous silica hybrid cotton linter papers after template extraction. Adapted with permission from *Langmuir* 2017, 33, 332-339. Copyright 2017 American Chemical Society.

Coating a cotton linters paper sheet only partially with dense silica by preheating the oven used for the aging process (**Figure 69**e, f), a fluid stop barrier is created even visible by eye. Water imbibes into the silica-free half of the paper sheet and the water front stops when reaching the dense silica coated half. This clearly demonstrates the effect of the dense silica coating as already described above. Thereby this effect cannot be related to classical hydrophobization: The contact angle of water on dense silica is considerably small (reference dense silica on glass: CA = 35 °), still water is not rising likely due to small capillary forces. These observations indicate that water imbibition is not only affected by the inter-fiber porosity, which is usually used for explanation of Lucas-Washburn-like capillary fluid flow, but is as well strongly affected by fiber morphology. In order to observe this effect at the microscale in more detail, fluorescence microscopy analysis on water imbibition in which the aqueous phase carries a dissolved FITC-Dextran, causing a green fluorescence, and the dense silica coated cellulose fibers showing a red autofluorescence has been investigated together with T. Meckel (**Figure 69**a-d). The solution including the dye is taken up by the uncoated half of the paper strip

(**Figure 69**g) and does not propagate/penetrate into the dense silica coated area, although the fibers clearly continue and inter-fiber space does not change at the observed scales. Only a few streaks of liquid show capillary transport of the FITC-Dextran solution on the surface of probably incompletely coated cellulose fibers within the border region (arrow heads). The obtained fluorescence microscopy images suggest the capillary uptake of FITC-labeled dextran containing water within the unmodified cotton linters paper sheet and that capillary-driven fluid flow comes to a stop at the border with the dense silica coated region of the paper sheet. The fiber morphology (red fluorescence) is clearly visible not showing any difference between unmodified and dense silica coated fibers.

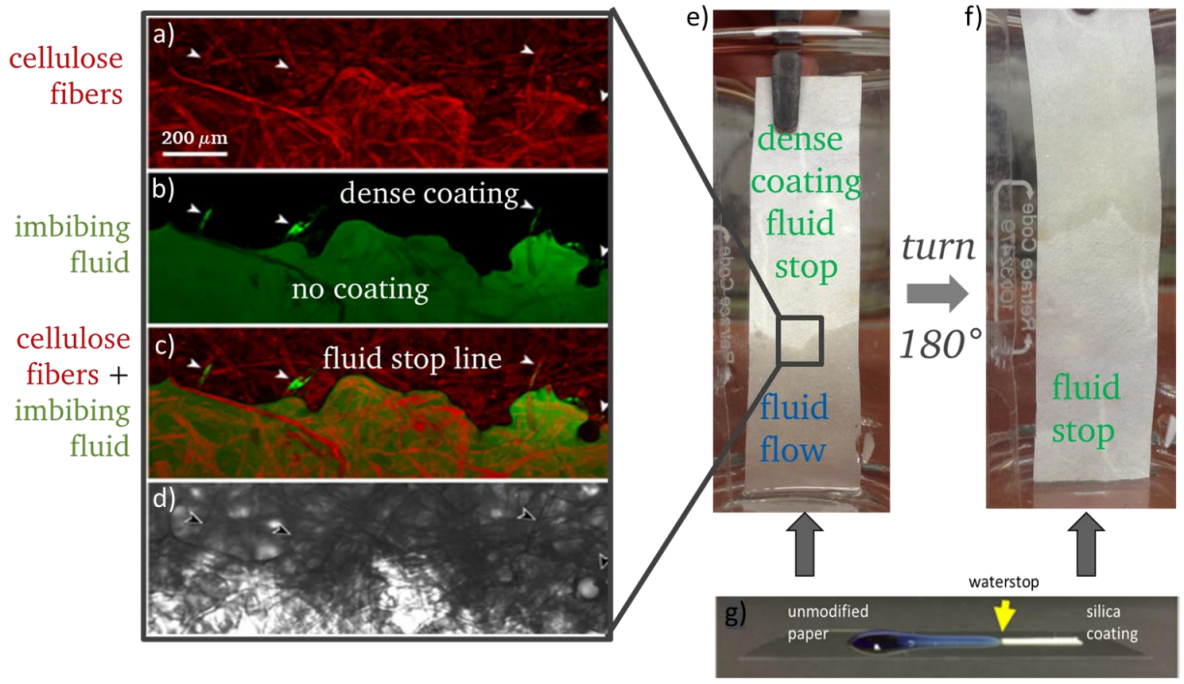

Figure 69. Maximum projection of a stack of confocal images taken at the border between the uncoated (bottom) and dense silica coated (top) area of a paper strip. Autofluorescence of cellulose fibers (a, red), FITC-dextran solution (b, green), overlay of a+b (c) and a bright-field image (d). Water capillary uptake of cotton linter paper sheets coated half with dense silica shows a fluid stop when starting in the uncoated area (e) and no water uptake when starting with the dense silica coated area (f). Photograph of the stopping dye containing water fluid front (g). Fluorescence images are taken by Dr. Tobias Meckel (AK Prof. Dr. Biesalksi, TU Darmstadt). Adapted with permission from *Langmuir* 2017, 33, 332-339. Copyright 2017 American Chemical Society.

As mentioned above mesoporous silica coated cotton linter papers do not show the fluid stop observed for dense silica coated cotton linters paper. Therefore, further functionalization strategies are necessary to implement fluid barriers into these papers or as well to switch fluid flow in such papers. In cooperation with Dr. C. Rüttiger (AK Gallei/Rehahn, TU Darmstadt), the silica coated cotton linter papers are post-grafted with the redox-responsive polymer poly(2-(methacryloyloxy)ethyl ferrocenecarboxylate) (PFcMA) (**Figure 70**a) via atom transfer radical

polymerization (ATRP) using a grafting from approach. The PFcMA has been chosen as it can be oxidized with $FeCl_3$ or tris(4-bromophenyl)ammoniumyl hexachloroantimonate (magic blue) and reduced with ascorbic acid or decamethyl cobaltocene ($CoCp^*_2$) and with this changes its charge and wetting behavior. The ATR-IR spectra after PFcMA functionalization of silica coated paper are shown in **Figure 70**b. Characteristic vibrational bands are located at 1728 cm^{-1} corresponding to the C=O vibration of the PFcMA and at 1070 cm^{-1} corresponding to the asymmetric Si−O−Si stretching vibration. The cellulose paper fibers give a complex infrared spectrum (**Figure 70**, black) that overlaps with the silica vibrational bands at 1070 cm^{-1} (**Figure 70**, red). Nevertheless, the silica structure can clearly be proven after destroying the cellulose fibers at 500 °C for two hours (**Figure 70**, green). After this removal of the original paper structure the infrared spectrum clearly shows the presence of unfunctionalized silica. The PFcMA functionalization becomes visible by a very small absorbance at 1728 cm^{-1} corresponding to the C=O vibrational band of the PFcMA. The relatively small absorbance can be referred to the low ratio of polymer compared to cellulose in the mesoporous silica coated hybrid paper. Additionally, no difference in the C=O vibrational band at 1728 cm-1 relative to the Si-O-Si matrix stretching at 1070 cm^{-1} can be observed before and after oxidation of PFcMA with $FeCl_3$. This clearly indicates that differences in the interaction with water upon oxidation and reduction are due to the different surface energies and not due to material instability.

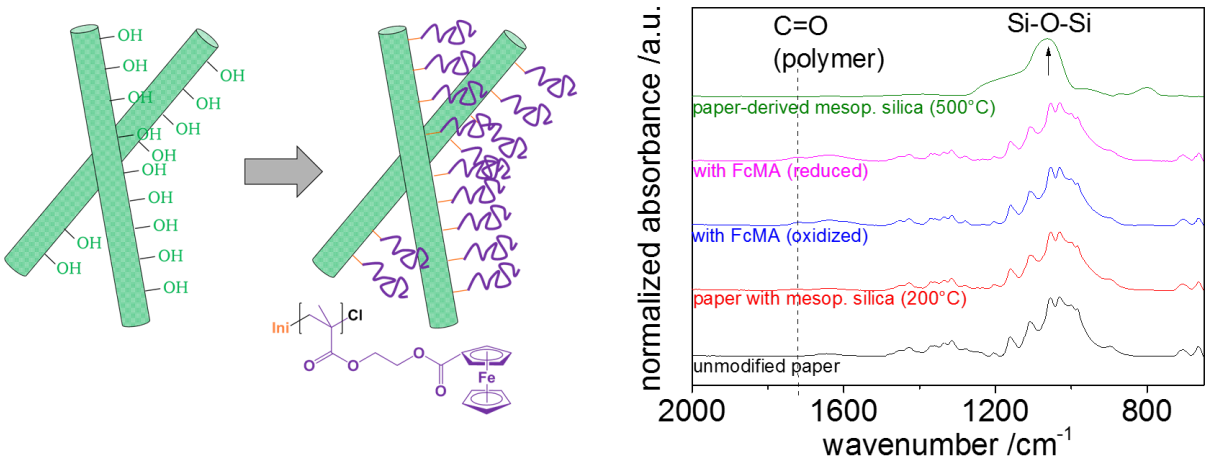

Figure 70. a) Schematic illustration of a grafting-from approach on mesoporous silica and dense silica coated hybrid cotton linter papers to generate a redox-responsive polymer coating. The polymer functionalization is prepared by Dr. C. Rüttiger (AK Gallei/Rehahn, TU Darmstadt). b) Infrared spectra of untreated paper sheets (cotton linters, 44 g/m², black), mesoporous silica hybrid paper sheets (200 °C) (red), mesoporous silica hybrid paper sheets (200 °C) functionalized with PFcMA in an oxidized (blue) and reduced (magenta) state and paper-derived mesoporous silica after destroying the cellulose paper fibers at 500 °C (green). Adapted with permission from *Langmuir* 2017, 33, 332-339. Copyright 2017 American Chemical Society.

The successful functionalization is confirmed by 29Si CP-MAS NMR spectra measured before and after grafting of PFcMA in cooperation with Torsten Gutmann (AK Prof. Dr. Buntkowsky, TU Darmstadt). The spectra shown in **Figure 71**a, b illustrate the typical spectra pattern for non-functionalized porous silica represented by Q_n groups between approximately 80 ppm and -115 ppm. After functionalization of the mesoporous hybrid paper-based silica with PFcMA (**Figure 71**c), T_n groups in the range of -60 ppm to -70 ppm appear which clearly show a covalent binding of functional groups (PFcMA ATRP initiator) to the silica via silane anchor groups. Additionally, the relative intensities of the Q_n signals between -80 and -115 ppm change after functionalization with PFcMA (**Figure 71**b). Although the ^{29}Si CP MAS spectra cannot be discussed quantitatively, a reduction of the relative amount of the OH bearing groups (Q1, Q2 and Q3) compared to Q4 is observed. This is a clear indication for the reaction of silica hydroxyl groups with silane anchor groups. Interestingly, in both spectra Q1 groups at approximately -81 ppm are detected. This is uncommon for unmodified mesoporous silica materials such as SBA-3 or MCM-4142 as well as for cellulose/silica hybrid materials.[256-260] In these materials usually only Q2, Q3 and Q4 groups are observed. This indicates an influence of the paper matrix on the organization and linking of the TEOS during the sol-gel silica coating process resulting in a restricted crosslinking of TEOS precursor in comparison to conventional silica materials in which a high degree of cross-linking is reached and thus no Q1 groups are detected. The change in the relative intensities of the different Q groups in the ^{29}Si CP MAS spectra for paper-based hybrid mesoporous silica (200 °C) and paper-derived mesoporous silica (500 °C) (**Figure 71**a, b) indicate that the cross-linking process is stimulated by heating. Nevertheless, the structural framework of the silica which is given by the organization on the paper template seems to be mostly preserved during the calcination since the Q1 signals are still observed.

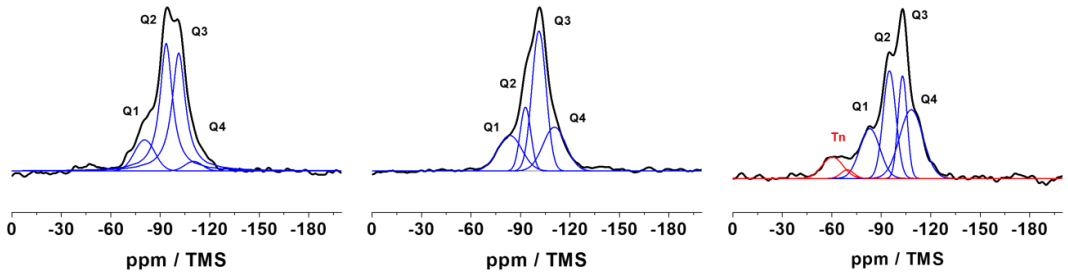

Figure 71. ^{29}Si CP MAS spectra measured at 8 kHz spinning of a) paper hybrid mesoporous silica (200 °C) and b) of paper derived mesoporous silica (500 °C). c) ^{29}Si CP MAS spectra measured at 8 kHz spinning of PFcMA functionalized paper hybrid mesoporous silica (200 °C). Solid-State NMR Spectroscopy is done in cooperation of Dr. Torsten Gutmann (AK Prof. Dr. Buntkowsky, TU Darmstadt). Adapted with permission from *Langmuir* 2017, 33, 332-339. Copyright 2017 American Chemical Society.

Redox-responsive PFcMA polymers show a great potential for switching between hydrophilic-hydrophobic on planar surfaces and mesoporous silica.[178, 261] Wetting characteristics are

determined using Young contact angle measurements in the reduced- and in the oxidized state for the redox-responsive polymer (**Figure 72**). In case of PFcMA, higher contact angles of around 110-120° for mesoporous silica and dense silica paper hybrid sheets are observed and therefore water imbibition is prevented. After oxidation, the contact angles drop to approximately 70-80°, and thus changes from a hydrophobic to a hydrophilic state inducing a change from a Cassie-like wetting behavior to a Wenzel-type wetting.[262] Comparing the measured contact angles for silica paper hybrid materials with (mesoporous) and without (dense) mesopores, a significantly higher contact angle is observed for the unmodified dense silica paper hybrid materials compared to the mesoporous silica paper hybrid materials. This fits to the water imbibition characteristics in **Figure 68**. The difference between mesoporous and dense silica coating might indicate that water penetration is strongly affected by the fiber surface or the fiber interior. Nevertheless, the redox gating after polymer functionalization works in a comparable way for both materials. This effect is due to a swelling of the fibers and therefore a resulting damage of the coating (see reference experiments for eucalyptus-sulfate fibers, **Figure 80**). For the dense and mesoporous silica hybrid paper (200 °C) after functionalization with PFcMA in the reduced state, contact angles of higher than 100° are observed corresponding to water exclusion from the fibrous matrix. After oxidation of PFcMA, the measured contact angles drops to values of 60°-80° allowing water to penetrate the silica hybrid paper sheet. This oxidation based change of fluid flow is reversible and a repeated reduction leads again to contact angles above 100 °C even if the absolute values are slightly lower than before oxidation.

Capillary water uptake is fast for unmodified paper as well as for mesoporous silica-paper hybrid materials. Dense silica-paper hybrid materials show water exclusion and a grammage dependence as discussed above (**Figure 72**d, h). The functionalization of dense or mesoporous silica-paper hybrid materials with redox-responsive PFcMA in its reduced state results in complete water exclusion (**Figure 72**, blue). Gating of water imbibition is achieved upon oxidation of PFcMA in case a sufficient amount of ferrocene units are oxidized (**Figure 72**, magenta). A linear fitting according to Lucas Washburn equation results in slope values of 1.9 and 1.7 for the mesoporous silica-paper hybrid material and the dense silica-paper hybrid material, respectively. This as well supports the observation of a difference in water imbibition in case the fiber surface is coated with dense silica, although the difference after functionalization with PFcMA in its oxidized state is much smaller than for the unmodified silica paper-hybrid sheet. Furthermore, the slope value of 1.9 for the PFcMA-functionalized mesoporous silica-paper hybrid material is relatively close to the one of polymer free mesoporous silica-paper hybrid material, which is 2.1, showing a real gating of water

imbibition. These results clearly show that redox-gating of water imbibition into paper-derived materials is possible if a change from Cassie-type wetting to Wenzel-type wetting can be achieved.

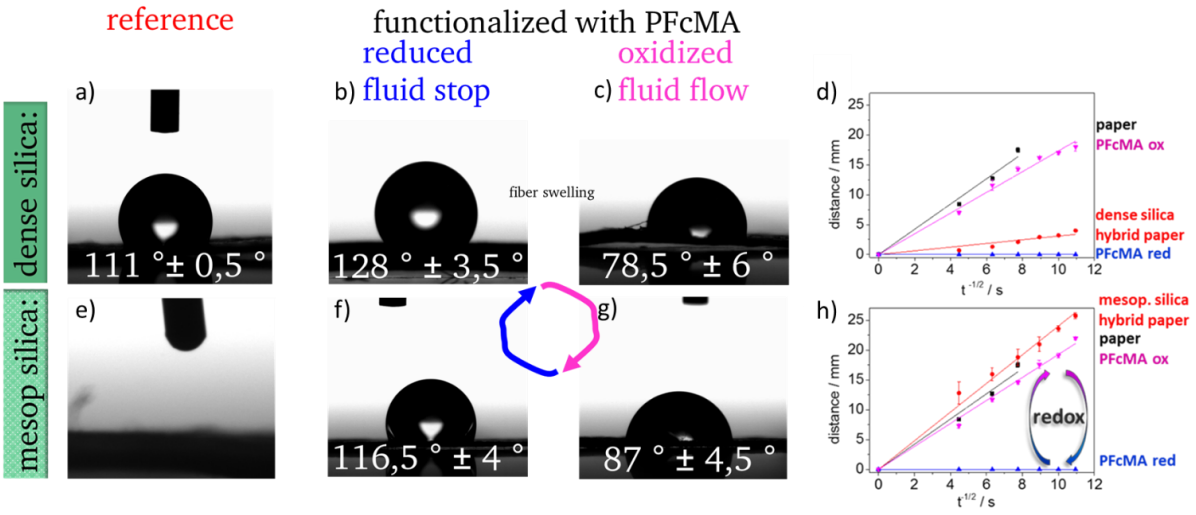

Figure 72. Static contact angle (drop volume is 2 µL) of silica modified hybrid paper before (a, e) and after (b-c, f-g) PFcMA modification of a) dense silica hybrid paper e) mesoporous silica hybrid paper. The influence of reduced PFcMA in dense (b) and mesoporous (f) silica hybrid paper versus chemically oxidized PFcMA in dense (c) and mesoporous (g) silica hybrid paper is clearly visible and indicating a Cassie-Wenzel-like transition. d, h) Capillary water fluid flow measured for d) cotton linters paper (44 g/m²) (black), dense silica hybrid paper (200 °C, red), dense silica hybrid paper after PFcMA modification in the reduced (blue) state and after oxidation with $FeCl_3$ (magenta). h) Capillary water fluid flow measured for cotton linters paper (44 g/m²) (black), mesoporous silica hybrid paper (200 °C, red), mesoporous silica hybrid paper after PFcMA modification in the reduced (blue) state and after oxidation with $FeCl_3$ (magenta). Adapted with permission from *Langmuir* 2017, 33, 332-339. Copyright 2017 American Chemical Society.

In summary, cotton linter paper functionalization with mesoporous or dense silica allows to design nanoscale porosity into paper. Choosing the right paper grammage together with hydrophilic but non-porous (dense) silica coatings allows to generate fluid stop barriers in paper. The functionalizing of silica coated paper with redox-responsive PFcMA enables switching between fluid stop and fluid flow using redox stimuli.

6.3.2. Silica Functionalization of Eucalyptus Sulfate Fibers

On the basis of the results summarized in this chapter, a patent DE 102018124255.7 (01.10.2018) has been registered. Furthermore, the results have been published in *Adv. Mater. Interfaces* 2019, 1900892 (DOI: 10.1002/admi.201900892). The entire work in this chapter is based on an intensive collaboration with Dr. M. Nau (AK Prof. Dr. Biesalski, TU Darmstadt). While the silica coating of paper sheets and investigation of wetting behavior has been performed by myself Dr. M. Nau performed the imaging and calculation of silica layers in the paper sheet crosssection. This work is the scientific basis for the project of the Pioneer Fund of the Technical University of Darmstadt, which is approved in March 2020. This project is allocated to Prof. Andrieu-Brunsen and Prof. Biesalski with Dr. M. Nau and myself as coordinators.

The reproducibility and possibility of transfer the fluid barrier generation based on dense silica coatings to different fiber types should be verified. Papers consisting of bleached eucalyptus sulphate fibers are used for this purpose. Compared to cotton linters fibers with a length of >3 mm these fibers are shorter with a length of < 2 mm.[263, 264] In addition, cotton linters usually contains a comparatively high amount of α-cellulose and thus low proportions of lignin and hemicelluloses.[265] The fiber shape and the fiber diameter is evenly tubular. Eucalyptus sulphate fibers, on the other hand, consist of different fiber types and vascular cells (tracheids, tracheas) and thus different fiber geometries.[266]

The grammage of the papers using eucalyptus-sulfate fibers and the concentration of the silica coated have to be varied to generate the same wetting behavior for silica functionalized eucalyptus-sulfate papers compared to papers prepared from cotton linters fibers (chapter 0).

The silica coating (**Figure 73**a) containing ethanol-water based solution is adapted from prior work on cotton linters (chapter 0).[151] The curing procedure is adapted to a heat-treatment at 130 °C and atmospheric pressure (**Figure 73**b) or at reduced pressure (**Figure 73**c). The temperature of 130 °C has been chosen, because it is nondestructive to eucalyptus paper (TGA, **Figure 74**a, black curve) but allows acid-catalyzed hydrolysis and condensation of TEOS, resulting in silica formation.[151, 267] Using a simple dip-coating – curing process, and varying the initial TEOS concentration in the coating solution, wetting characteristics are observed to progress from hydrophilic to Janus type and hydrophobic in a controlled fashion by adjusting a precise and simple gradient design. Investigation by eye, microscope, and SEM do neither show macroscopic changes to the eucalyptus paper structure nor alterations on the micrometer scale

(**Figure 73**b and c) compared to unmodified paper sheets (**Figure 73**a) can be observed. This apparent lack of discernible topographical and morphological differences indicates that the relevant features of the coating and its thickness has to be smaller than the resolution limit of the SEM at the given conditions (2500x/76 nm^2). Unfortunately, SEM nanoscale analysis of the silica coated eucalyptus paper sheets is not trivial due to high energy needed for imaging, which can destroy the organic matrix of the hybrid material. Consequently, further analysis is followed via correlated TGA, CLSM and BET analysis in order to gather information at sub-micron scale.

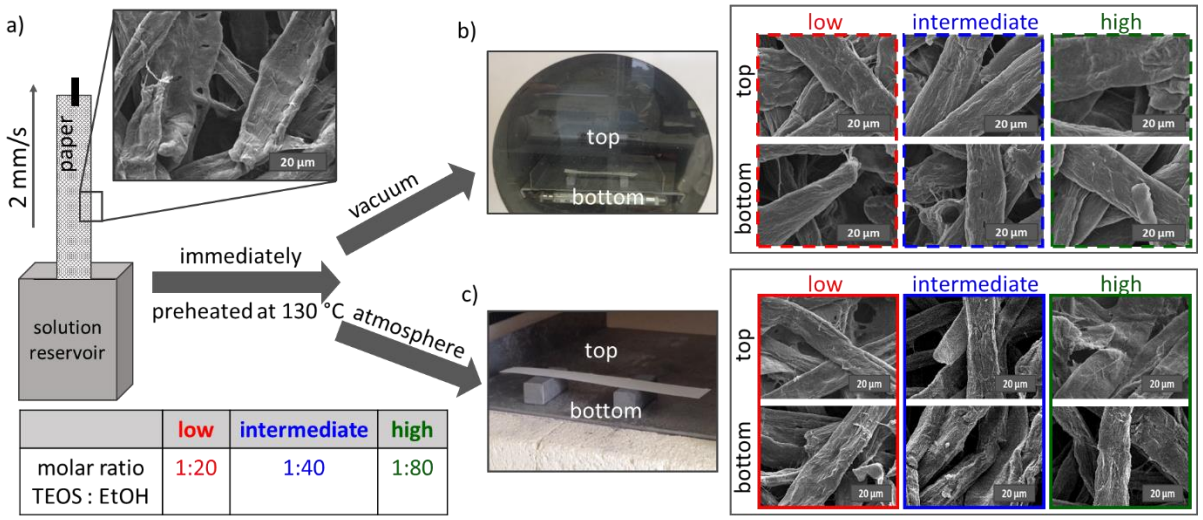

Figure 73. Schematic illustration of the preparation of silica coated paper sheets. The paper sheet is dip coated in three different precursor solutions having defined amounts of dissolved TEOS as described in the inserted table. Subsequently, the samples are cured in preheated ovens at 130 °C under atmospheric pressure and vacuum, respectively (b) and c). Inserted scanning electron microscopy images show examples of non-modified eucalyptus-sulfate paper (80 g/m², a)), and silica-modified eucalyptus-sulfate paper (80 g/m², b) and c)), respectively. Adapted with permission from *Adv. Mater. Interfaces* 2019, 1900892. Copyright 2019 Royal Chemical Society.

The amount of deposited silica within the eucalyptus paper sheet is determined via TGA analysis (**Figure 74**). Due to the apparently very low amount of silica, TGA is the method of choice, because of the very small errors/deviation compared to alternative methods such as standard gravimetric analysis, especially for small sample amounts. During a TGA measurement, the silica content of coated paper sheets has been determined by thermal removal of the paper which only leaves silica (stable up to 1700 °C) and ash. The determined amount of silica is calculated considering the ash-content, 5.8 wt.-%, of the base-paper deduced from a reference measurement. This shows that in the low TEOS concentration coated papers the silica content is 0.5 wt.-%, for intermediate TEOS concentration 1.5 wt.-% and for the high TEOS concentration coated papers contain around 3.7 wt.-% silica.

Further analysis using Krypton-BET (measured by Dr. J. Schmidt, TU Berlin) reveals a specific surface for uncoated samples of 0.54 m^2/g which is in poor agreement with values reported by

mercury-porosimetry (6.35 m²/g) for these papers. Since both methods are complimentary, and the applied Hg porosimetry equipment detects a pore diameter range from macropores down to pore-opening of 10 nm, while Kr-BET only detects pores up to 50 nm diameter this gives an information on the mesopore content. Kr BET is used because only a surface area of 0.05 m² and thus a small sample quantity is required. Kr adsorbs as well as N_2 or Argon. The resulting isothermal curve reflects the pore size.[268, 269] With these samples (see appendix, **Figure 118**) an increase of volume at low partial pressures, which indicates the presence of micropores. The strong increase at high partial pressure (>0.75) is caused by macropores, which are not considered for the surface determination. This fits to the results of Maloney *et al.*.[149] After coating the eucalyptus paper sheets with low silica amount, the macropores are unaffected as is evident through SEM imaging (**Figure 73**) but the Kr-BET specific surface changed to 0.59 m²/g (low), 0.43 m²/g (intermediate), and 0.27 m²/g (high), respectively (**Table 6**). This decrease in surface area, indicates that the mechanism of the silica induced hydrophobization is not based on the generation of micro- or nano structure, but rather on the masking of the micro pores presented by the fiber surface. This hypothesis is supported by the rather miniscule decrease in free surface energy from cellulose (63.8 mN/m) to silica (59.2 mN/m) that are determined on model surfaces (**Table 7**).

a)

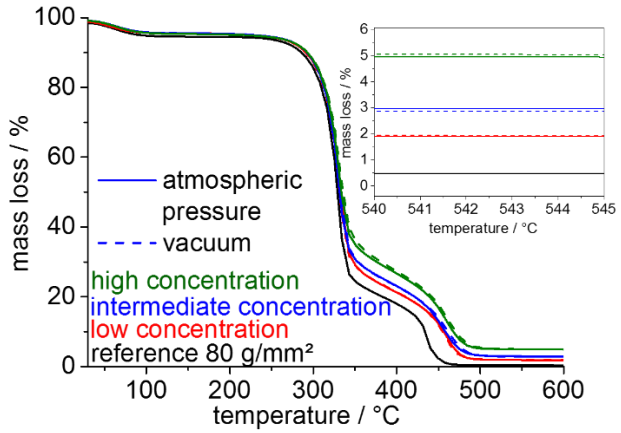

b)

samples	drying mode	mass loss / %	silica amount / %
reference 80 g/m²		94.2	-
low concentration	atmosphere	93.6	0.5
low concentration	vacuum	93.7	0.5
intermediate concentration	atmosphere	92.6	1.6
intermediate concentration	vacuum	92.8	1.4
high concentration	atmosphere	90.5	3.7
high concentration	vacuum	90.5	3.7

Figure 74. a) Thermogravimetric analysis of silica coated eucalyptus-sulfate paper (80 g/m²) sheets. The amount of coating is determined by the TEOS concentration in the initial coating (red, blue and green) and, to a much smaller degree, by the curing process (atmospheric pressure = line and vacuum = dotted line). b) Table of mass loss between 120 °C and 600 °C in % and the calculated silica amount in wt.-%. Reprinted with permission from *Adv. Mater. Interfaces* 2019, 1900892. Copyright 2019 Royal Chemical Society.

Table 6. Kr-BET (87 K) of paper reference (80 g/m²) and silica coated paper with different concentration cured with atmospheric pressure and for intermediate silica concentration also cured in vacuum. Hg-Porosimetry of eucalyptus-sulfate paper with grammage of 80 g/m².

Sample	Hg-Poro. in m^2g^{-1}	Kr BET in m^2g^{-1}
Reference (80 g m^{-2})	6.35	0.54
Low Conc. – oven		0.59
Intermediate Conc. – oven		0.43
Intermediate Conc. - vacuum		0.49
High Conc. - oven		0,27

Table 7. Contact angle data of silica and cellulose (regenerated) of 2 µL droplets of different solvents. From this data the surface energy is calculated according to the model of Owens, Wendt, Rabel and Kaelble.

Solvent	CA cellulose / °	CA silica / °
Water	27 ± 8	34 ± 7
N,*N*-dimethylformamide	0 ± 0	19 ± 2
Dimethylsufoxide	5 ± 3	26 ± 3
n-Hexane	7 ± 1	6 ± 2
Toluene	8 ± 1	20 ± 4
Calculated surface energy in mN m^{-1}	**63.8 (R^2: 1)**	**59.2 (R^2: 1)**

Young contact angle (CA) measurements of the top and bottom surfaces of all silica coated eucalyptus-sulfate papers (**Figure 75**) have been carried out to study the influence of silica coating on the wetting behavior of the hybrid paper. All samples prepared with high TEOS concentrations exhibit hydrophobic wetting characteristics with static contact angles of 120°-130°. It is noteworthy that the chemical surface of cured TEOS is composed entirely of hydrophilic hydroxyl functions. No difference between the macroscopic static water contact angles of the top and bottom surface is observed, regardless of the orientation during curing and the curing pressure, i.e. ambient pressure vs. vacuum oven, respectively. In contrast, eucalyptus paper sheets coated using low TEOS concentration in the dip-coating process do all exhibit a hydrophilic wetting behavior. Neither any difference of top versus bottom side wetting behavior, nor any differences in the wetting of the hybrid materials using the two different curing strategies can be found. Interestingly, the eucalyptus paper sheets coated with

intermediate TEOS concentrations show a very different and curing process dependent wetting behavior: if these samples are cured in an oven under ambient pressure, the top side exhibits hydrophobic wetting behavior with static contact angles of about 120°, whereas the bottom side exhibits hydrophilic macroscopic static contact angles of 0° going along with water exclusion at the top and instant, complete water imbibition at the bottom side. As the top surface is water repellent, while the bottom side absorbs water immediately, a Janus-type or amphiphilic membrane has been created. This result can be explained by the positioning of the sample in the oven, as well as considering migration of the TEOS during the drying procedure (wick effect). The sample is placed in the oven during drying in a horizontal position, favoring a directed migration of the TEOS due to preferred ethanol evaporation at the top of the paper sheet. If ethanol evaporation and silane hydrolysis as well as condensation now takes place at similar time scales, a gradient in silica distribution along the eucalyptus paper cross section is obtained. Curing eucalyptus paper sheets coated with identical intermediate TEOS concentration in an oven under reduced pressure results in hydrophilic behavior/surface at both sides of the paper sheets. The latter can be explained by the fact that evaporation of the solvent is now much faster than migration of the TEOS and thus homogeneous paper characteristics with respect to the silica coating are obtained.

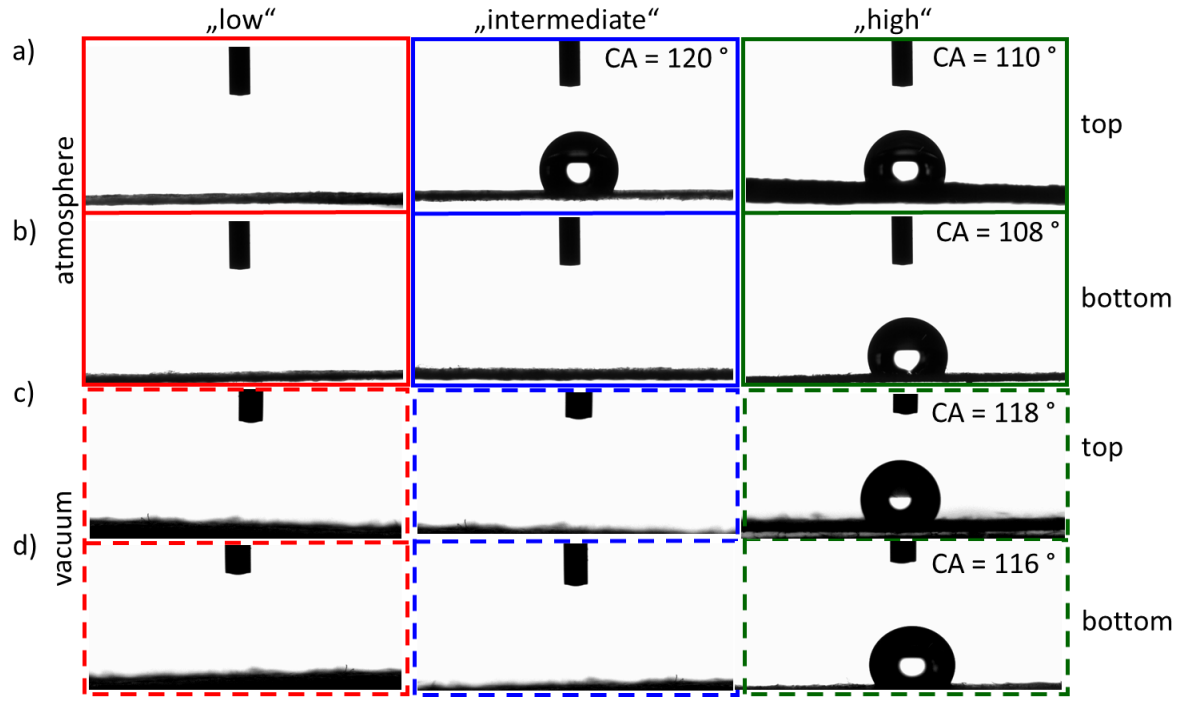

Figure 75. Static contact angle measurements of 2 µL water (MiliQ) droplets on silica coated eucalyptus-sulfate paper sheets (~80 g/m²). The papers are coated with the three different TEOS concentrations, "low", "intermediate", and "high". a) shows the top surface and b) the bottom side of the paper after curing in a preheated oven, and c) shows the top surface and d) the bottom side of the paper after curing in a vacuum oven. Reprinted with permission from *Adv. Mater. Interfaces* 2019, 1900892. Copyright 2019 Royal Chemical Society.

To explain the Janus paper characteristics in a next step, the cross-sectional silica distribution is determined to address e.g. the question if a characteristic/critical coating amount per surface area exists that leads to the hydrophobic properties (i.e. no further wicking of a water drop into the material is observed). The relative silica distribution is obtained by using CLSM imaging. Representative CLSM image stacks of cross sections of the hybrid paper material are depicted in **Figure 76**. The untreated cellulose sheets are stained with Calcofluor White prior to dip-coating with Rhodamine B labeled silica-precursor solution. The silica (Rhodamine B channel) is colored in magenta while the eucalyptus fibers (CFW channel) are colored in cyan.

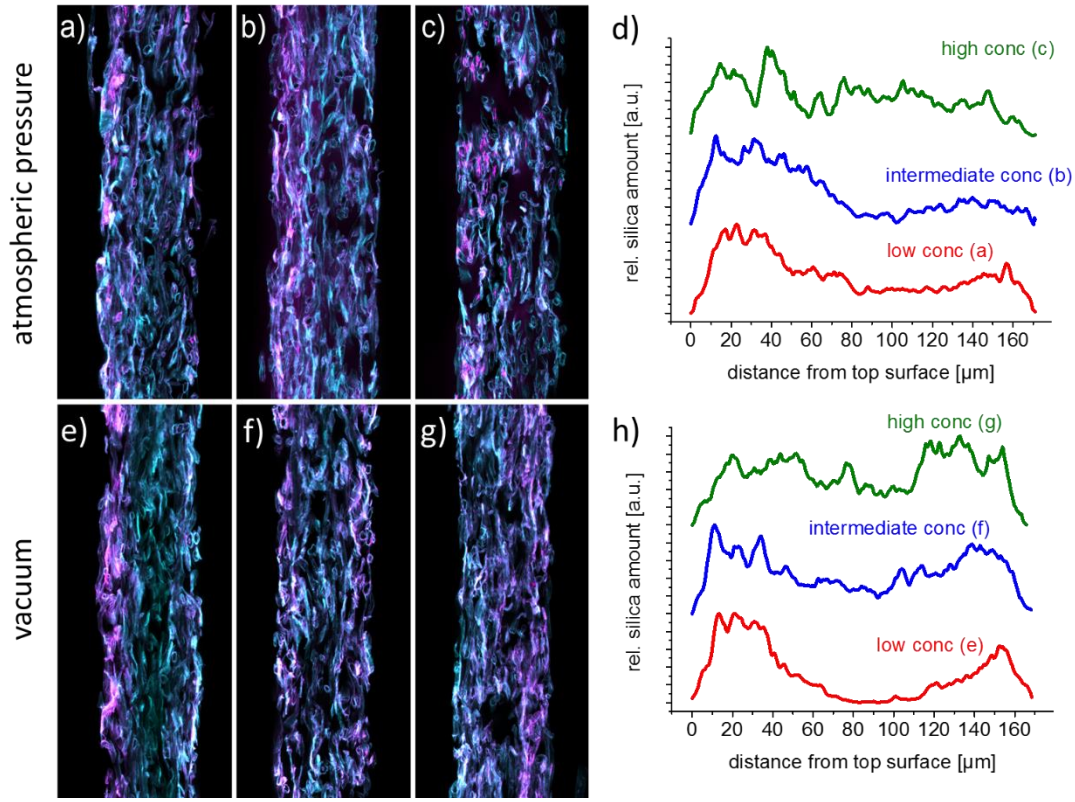

Figure 76. CLSM images of cross sections of hybrid papers prepared from a) low TEOS conc., cured under ambient pressure b) intermediate TEOS conc., cured under ambient pressure c) high TEOS conc., cured under ambient pressure d) low TEOS conc., cured under vacuum e) intermediate TEOS conc., cured under vacuum f) high TEOS conc., cured under vacuum. All images are z-projections of stacks with 20 to 25 individual images, respectively. d) Comparison of Rhodamine B fluorescence for samples coated with all three TEOS concentrations and cured at ambient pressure. h) Comparison of Rhodamine B fluorescence for samples coated with all three TEOS concentrations and cured in vacuum. Data evaluation is carried out by Dr. M. Nau. Adapted with permission from *Adv. Mater. Interfaces* 2019, 1900892. Copyright 2019 Royal Chemical Society.

For the three different applied TEOS concentrations during dip-coating (compare **Figure 76**a-c and **Figure 76**e-f) and each curing method (ambient pressure and reduced pressure, **Figure 76**a,e; b,f; c,g), similar silica distributions are observed. TEOS coated eucalyptus paper sheets cured under vacuum show bathtub like silica distribution along the cross section with an increased silica amount at the top and bottom surfaces of the paper cross section. The relative

difference of deposited silica between the outer paper sheet surfaces, compared to the center of the cross section is increasing with decreasing TEOS concentration in the dip-coating solution. This implies, that the TEOS concentration within the coating solution affects the movement of the liquid phase during TEOS hydrolysis and condensation, e.g. via changes in the fluidic properties (such as viscosity) and different interaction with the fibrous eucalyptus paper substrate.

Contrary to this, eucalyptus paper sheets cured under ambient pressure show up to twice the relative silica concentration on the top of the samples compared to the bottom. The silica gradient along the cross section of the hybrid paper is less pronounced if the initial coating solution contains higher TEOS concentrations. The reason for this can again be related to the evaporation kinetics, and thus, the relation of material transport versus hydrolysis-condensation speed determining the chemical gradient formation of the silica-modified hybrid paper.

To gain further insight into absolute mass distributions, the relative measurements are numerically integrated (along the cross section), normalized, and the relative partial integral for each 10 μm cross section segment of the paper sheet cross section is calculated and multiplied with the coat weight as determined by TGA. This data evaluation is carried out by Dr. M. Nau. This allows to determine the distribution of absolute volumetric coat weights displayed in **Figure 77**a (cured under vacuum) and **Figure 77**b (cured under ambient pressure). Correlating the obtained silica distribution with the static contact angle described earlier, indeed a correlation between silica amount and wetting is observed: The threshold silica amount when the paper sheet becomes hydrophobic is located between the highest coat weight (still resulting in hydrophilic wetting), and the lowest silica coat weight (just inducing hydrophobic wetting).

The highest amount of silica of a hydrophilic sample (lower threshold boundary) is observed at the top surface of the samples coated with intermediate TEOS concentration and cured under vacuum **Figure 77**a, blue), while the lowest already hydrophobic material is observed with the corresponding sample cured under atmospheric pressure (**Figure 77**b, blue). While the sample cured under atmospheric pressure is still hydrophobic with a specific coat weight of 10.3 mg/cm^3 (**Figure 77**b), the sample cured under vacuum is hydrophilic at a specific coat weight of 9.3 mg/cm^3 (**Figure 77**a), which defines the threshold between those two boundaries. Consequently, a minimum silica content between 1.85 wt.-% and 2.05 wt.-% with respect to eucalyptus sulfate fibers is necessary to obtain hydrophobic hybrid membrane behavior. Through correlation of these data with the specific surface area, the threshold in terms of coating weight is located between 2.9 mg/m^2 and 69 mg/m^2. The apparent absence of

microscale changes is subsequently self-explanatory because the density of silica (2.65 g/cm²) translates to - with respect to paper coatings - ultrathin coating thicknesses between 1.1 nm and 26 nm.

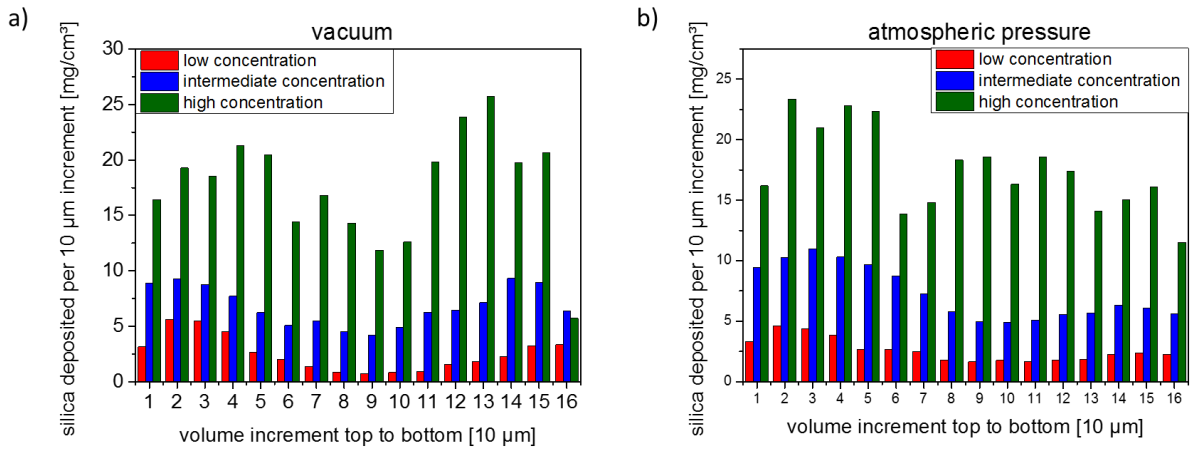

Figure 77. Absolute amount of silica per volume increment calculated through correlation of CLSM and TGA data, for a) samples cured under vacuum and b) samples cured under ambient pressure. Data evaluation is carried out by Dr. M. Nau. Reprinted with permission from *Adv. Mater. Interfaces* 2019, 1900892. Copyright 2019 Royal Chemical Society.

To show the versatility of asymmetric paper-based Janus membranes, their ability to separate oil and water can be demonstrated: For this purpose, a two-phase water-oil system consisting of water and cyclohexane is used. Cyclohexane has been chosen as oil component to eliminate effects based on high viscosity. The investigated paper sheet is located at the interface between water and cyclohexane (**Figure 78**b). By use of the three different TEOS-concentrations for eucalyptus paper coating and facile orientation it is possible to create all possible permeation combinations for this system as depicted in **Figure 78**a. The paper sheets coated with “low” and “high” amount of TEOS behave as expected. If a FITC labelled water drop is placed onto the hydrophilic paper membrane (i.e. “low” TEOS coating, **Figure 78**e), the membrane allows water permeation. At the same time, the same membrane does not allow any visible permeation of the unpolar oil. The opposite behavior is observed for the hydrophobic paper (i.e. “high” TEOS coating, **Figure 78**d): the Rhodamine B labelled oil droplet is capable to permeate the fibrous network, whereas the water droplet does not penetrate the surface of the paper. Most interestingly, the Janus-type paper (i.e. “intermediate” TEOS coating, dried under ambient pressure) is acting as a “double diode”: both, water and oil, are capable to permeate through the membrane, however only with a specific direction and in opposite directions relative to each other (**Figure 78**c,f). This prohibits a reverse permeation as demonstrated by the fact that one orientation of the Janus-Paper (hydrophobic side facing towards the water, **Figure 78**c) will let

water pass through from the oil-side and vice versa. In the opposite orientation (hydrophobic side facing towards the oil, **Figure 78**f) permeation is blocked in both directions.

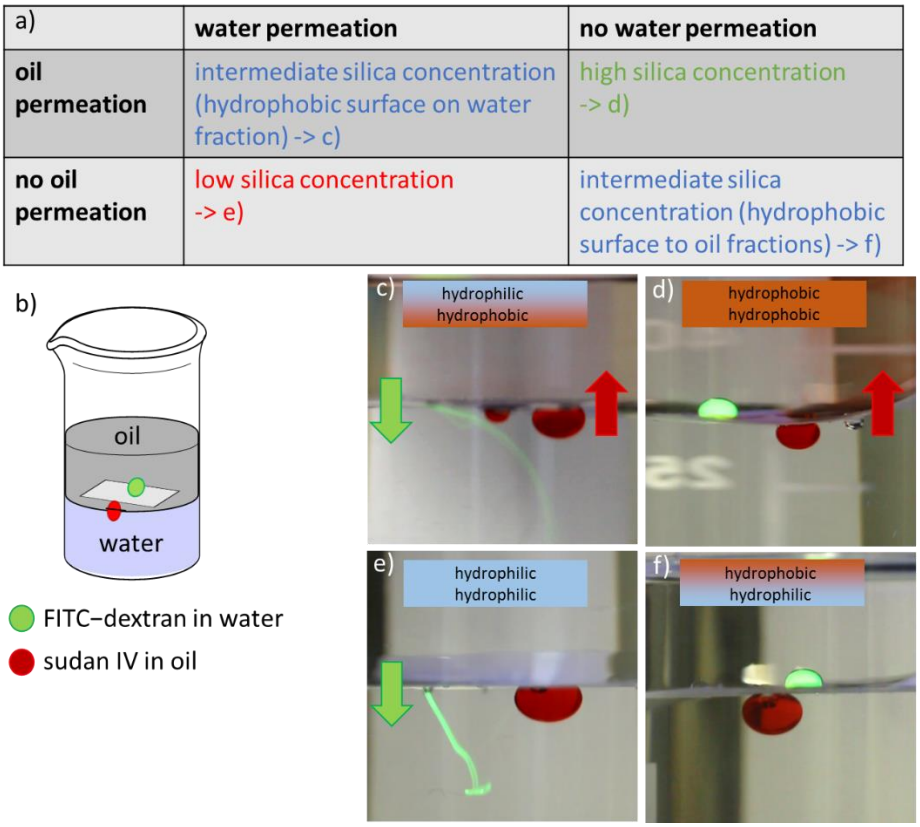

Figure 78. a) Table showing the oil/water infiltration or exclusion through different eucalyptus paper sheets prepared with different amount of silica coating cured under atmospheric pressure. b) Experimental set-up with a membrane between water phase on the bottom and oil phase on the top. An oil droplet colored with Sudan IV and water droplet colored with FITC-dextran are positioned on the opposite side to take a look on droplet permeation. Images of the four combinations of permeation/exclusion are shown in c) through f): c) Janus membrane, where the hydrophobic interface lays on the water phase. d) hydrophobic silica coated paper membrane e) hydrophilic silica coated paper and f) Janus membrane, where the hydrophilic interface lays on the water phase. Adapted with permission from *Adv. Mater. Interfaces* 2019, 1900892. Copyright 2019 Royal Chemical Society.

Finally, with respect to potential upscale and industrial process implementation, the investigation of solvent-free TEOS formulations as coating agent for paper samples are performed. The presence of small amounts of water is required to successfully achieve crucial condensation reaction and thus a permanently, chemically stable hydrophobic coating. TGA revealed that with solvent-free TEOS formulations, combined with small amounts of water as precursor, even less material is needed on the paper sheets (**Figure 79**a and b) as compared to coating from ethanolic solution in order to achieve stable hydrophobic surfaces with static contact angles of about 130°. In contrast to this “wet” TEOS, using solvent free and dry TEOS as coating agent leads to a slower water imbibition compared to untreated samples. This can

be explained by partial condensation of the TEOS due to residual moisture present in the fibers (around 5 wt.-%).

a)

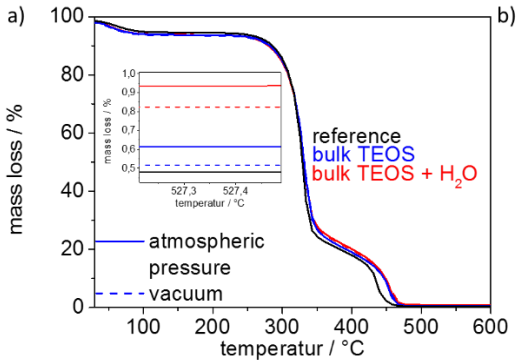

b)

sample	drying method	top / °	bottom / °
reference	-	-	-
bulk TEOS	atmospheric pressure	127.9**	-*
bulk TEOS	vacuum	128.7**	128.3**
bulk TEOS + H_2O	atmospheric pressure	128.2	128.8
bulk TEOS + H_2O	vacuum	125.8	127.6

* drop infiltrates directly
** drop infiltrates after 20 s completely

Figure 79. TGA analysis of silica coated eucalyptus-sulfate paper sheets (80 g/m²) prepared from solvent free TEOS or solvent free TEOS with a drop of water and treated with 130 °C at atmospheric pressure or in vacuum. b) The table shows the macroscopic static contact angle measurements from top and bottom of the silica coated paper sheets.

The influence of solvents to ultrathin dense silica coating is investigated using tetrahydrofuran (THF). In **Figure 80**a the SEM-image of a high concentration dense silica coated eucalyptus-sulfate paper is shown as well as a water drop (2 μL) showing hydrophobic wetting behavior. The paper sheet is treated with THF for 20 min followed by drying**. Figure 80**b showing the SEM image after this solvent treatment and imbibition of water droplet (2 μL). In the SEM images no differences on microscopic scale are visible. But fibers are known for swelling in solvents like DMSO, THF or acetic acid[270, 271], so the silica coating possibly crack or breaks because of new orientation of the fibers which results in a hydrophilic paper.

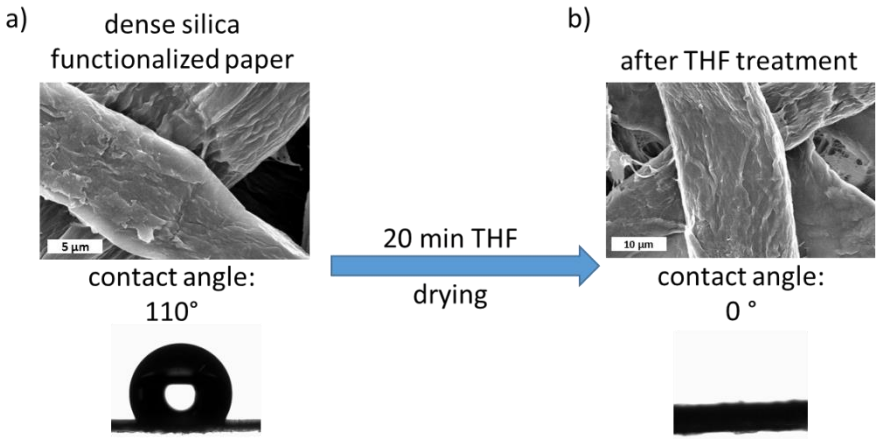

Figure 80. a) SEM image of dense silica coated eucalyptus-sulfate fibers (80 g/m²) with high concentration resulting in hydrophobic wetting behavior. b) After 20 min in tetrahydrofuran (THF) and drying the samples show a hydrophilic wetting behavior.

In summery eucalyptus-sulfate paper functionalization with dense silica in a EISA-dipcoating process allows to design silica gradients by controlling the drying process. When choosing the right paper grammage together with right silica distribution along the paper sheet cross-section allows to generate papers with janus-type wettability. The achieved wetting behavior is due to the reduction of nanoporosity by the thin coating. The silica functionalized papers show great potential for application as oil/water separation membrane in first investigations.

6.3.3. Outlook

Targeted pore space design and its accessibility (through pore functionalization) on or even in paper fibers is of great interest to the development of new applications and the key to tailored, complex functional papers, e.g. for dynamic controllable fluidics or sensors. This raises the question whether nanoporous spaces in paper can be specifically designed and selectively functionalized and thus their influence on paper properties, such as the capillary fluid and molecular transport, systematically understood and adjusted. The use of sol-gel chemistry for the production of mesopores offers the possibility of selectively functionalizing by means of co-condensation mesopores and e.g. transport-determining parameters, such as pore charge and wetting, directly incorporate in the manufacturing process. In combination with fiber functionalization prior to papermaking, this should enable to establish not only structurally, but also functionally hierarchical papers. The correlation of pulp fiber properties (morphology, length, wall thickness, etc.) of cellulosic fibers with the design of (meso) pores prior to papermaking can be investigated on the basis of sol-gel chemistry. In addition, the production of papers from differently functionalized fibers and their evaluation in terms of mechanical properties as well as potential applicability depending on fiber type, fiber distribution and fiber functionalization in paper may also be of interest compared to post-functionalized papers.

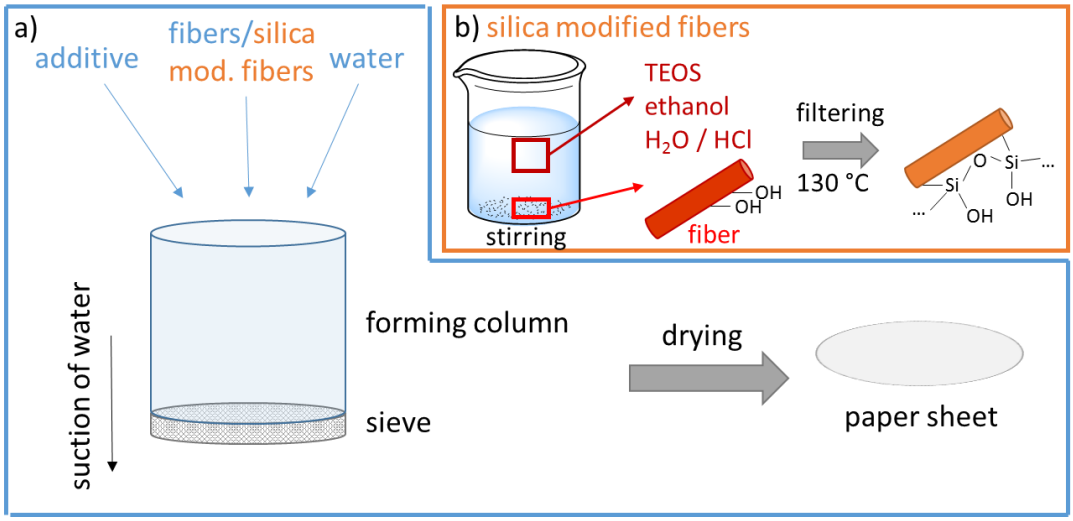

Figure 81. a) Schematic illustration of sheet forming with conventional Rapid-Koethen hand sheet maker according to DIN 54358 and ISO 5269/2. In forming column or filling chamber the fibers dispersed in water is filled in with possibly additives. This is diluted with more water, whirled up and sucked off through the sieve using vacuum. The formed paper sheet is dried for several minutes at 93 °C. b) Fiber functionalization with dense silica: The fibers are stirred for 24 h in a silica precursor solution containing TEOS, ethanol, water and HCl. The fibers are filtered off and dried in oven for 2 h at 130 °C before using for sheet forming.

In the two previous chapters' 0 and 0 the silica coating of two different fiber types (cotton linters and eucalyptus sulfate) are successfully demonstrated. In the future, silica fiber functionalization prior to paper fabrication should be investigated to enable higher degree of freedom in paper composition design. In a first proof of concept experiment, the functionalization of fibers with silica via sol-gel chemistry has been performed (**Figure 81**b). The functionalized cellulose fibers are used in the laboratory paper sheet building process (**Figure 81**a) as described in the experimental section (Chapter 8). The papers made of functionalized fibers have a non-optimal homogeneity, but are sufficiently stable both in the dry (left) and in the wet (right) state as shown in **Figure 82**c,d. Another complementary approach is the in-situ functionalization of cellulose fibers with sol-gel-solution during the paper building process by using the precursor as additive (**Figure 82**b). The reference paper (eucalyptus-sulfate) are shown in **Figure 82**a.

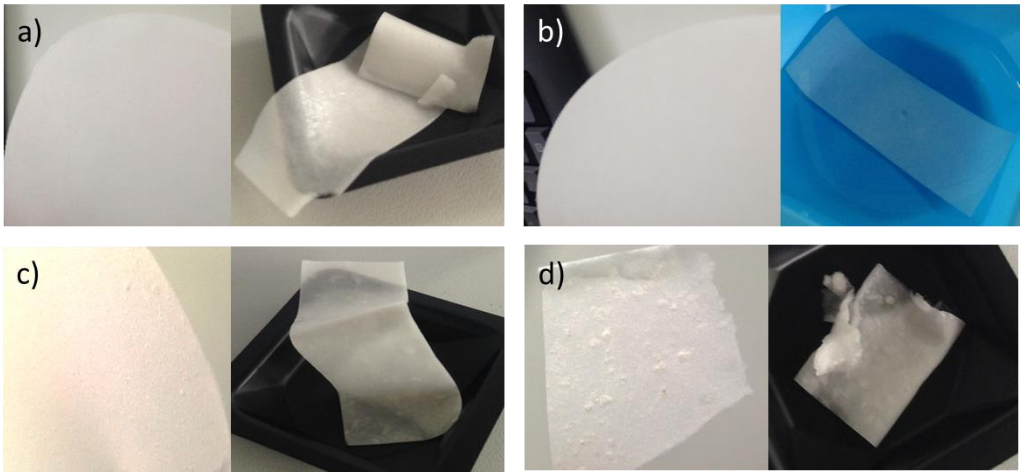

Figure 82. Images of different paper sheets in dry state (left) and wet state (right). a) eucalyptus sulfate paper b) eucalyptus sulfate paper with silica-precursor solution as additive c) paper made out of 50 % unfunctionalized and 50 % silica functionalized eucalyptus sulfate fibers d) paper made out of silica functionalized eucalyptus sulfate fibers.

A silica functionalization of eucalyptus-sulfate fibers/papers could be detected by TGA measurements (**Figure 83**). The ash content of unmodified eucalyptus-sulfate (89 g/m²) is about 0.55 wt.-%. The papers sheets that had a silica-precursor solution as additive showed no differences in TGA measurements. When using silica functionalized fibers for paper making (paper grammage: 55 g/m²), the residual of around 3.5 wt.-% after temperature treatment to 600 °C can be correlated to silica which is stable till 1400 °C. When using a mixture of silica functionalized and unfunctionalized fibers (paper grammage: 112 g/m²) for paper making, the residual (ash content) is with 1.27 wt.-% in between the unfunctionalized or fully functionalized papers. However, no differences concerning ash content compared to unfunctioalized paper in TGA measurements are observed when using the sol-gel-precursor as additive (paper grammage: 69 g/m²).

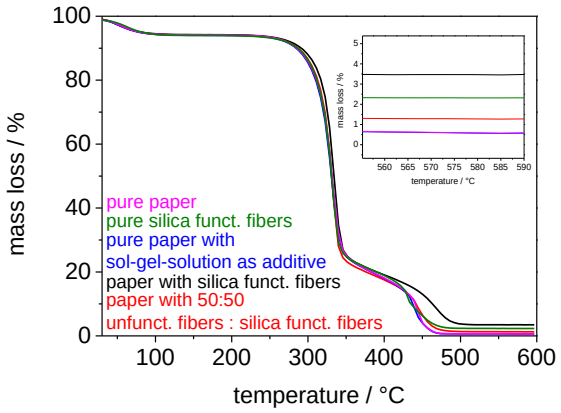

Figure 83. Thermogravimetric analysis of eucalyptus-sulfate paper (magenta), silica functionalized eucalyptus-sulfate fibers (black) and paper made out of these fibers (green and red) as well as eucalyptus-sulfate paper made with silica-precursor solution as additive (blue).

This very first result, indicates a successful silica functionalization of fibers and paper making, can be used for further experiments with respect to water imbibition. In general, the optimization in terms of functionalization, fiber and paper properties is required.

A targeted design of pore spaces and their accessibility functionalized pores in paper fibers and on paper sheets is of great interest for the development of new applications and is the key to tailor-made, complex functional papers, e.g. for dynamically controllable fluidics or sensor technology.

7. Summary and Outlook

This thesis is divided into three sections (**Figure 18**). In the first chapter the automation of the production of mesoporous silica by means of gravure printing is successfully carried out. The films are compared with films produced by conventional dip-coating processes and in both processes the EISA process is used as mechanism for nanopore formation by template assembly and silica formation by hydrolysis and condensation of silanes. The process parameters are optimized to produce mesoporous silica films with different layer thicknesses. In general, gravure printing produces very homogeneous mesoporous silica on large areas in an automated fashion. By using a co-condensate, gravure printing could be used as a fast and easy method for the production of multifunctional layers, which allows exciting new architectures. Furthermore, the binding of the coinitiator on silica surface for different layer thicknesses is investigated and an optimum is found. In the outlook a further promising method for the automated production of mesoporous silica films and even structures could be presented. In first tests a 3D printing process, which works with photoinitiated silica, is shown to be useful.

The results concerning coinitator functionalized mesoporous silica films are used in the second chapter for the targeted polymer functionalization using visible light and near-field modes. The successful dye-sensitized polymerization of DMAEMA with methylene blue and a secondary amine with red light as initiator could be performed. When the amine is bound to the surface, polymer grafting to the mesoporous silica surface occurs. In different experiments a time, concentration and energy dependent adjustment of polymer amount could be shown. Both positively and negatively charged monomers could be successfully polymerized. By using a laser as a light source, a spatially resolved polymer functionalization in x-y direction could be realized using the appropriate reaction parameters. The free radical dye-sensitized polymerization is combined with nanoscale optical fields like surface plasmons (SP) or leaky transversal optical waveguide modes (TM). The SP induced polymerization in mesoporous silica can be controlled with respect to the generated polymer amount by varying the polymerization time and the energy. In terms of energy, not only the adjustable laser power, but also the coupling efficiency and the shape of the SP and TM have to be considered. This is highly dependent on the optical quality of the film and is very difficult to reproduce and optimize within the applied preparation methods. By comparing the generated C=O vibrational band intensity and thus the generated polymer amount between SP- induced and light induced polymerizations the enhancement of SP is demonstrated. It is also possible to use the TM to initiate polymer functionalization. It can be shown that the SP induced polymerization is locally limited in x-y direction while TM-induced polymerization is more distributed in the area. In the case that both SP and TM induced polymerizations takes place in the same mesoporous silica film, less polymer is detected for the

SP induced polymerization than for TM induced polymerization although the SP has an enhancement factor. This fact clearly indicates that the polymer is formed as well on the outer surface in case of TM induced polymerization. To avoid the inequality of gold-substrate preparation with mesoporous silica, a proposal for the use of an evanescence field induced polymerization generated by TIRF is shown in the outlook. In initial experiments a successful polymerization could be shown by using an evanescent field.

In the third part of this thesis the local functionalization with silica on hierarchically porous paper is shown. The focus is on the introduction of new structures, namely mesoporous silica and dense silica, into pre-prepared paper. A variation including the formation of a fluid stop barrier for the water imbibition in the functionalized papers could be shown successfully by exclusively using silica for paper functionalization. It could be shown that the grammage of the silica-functionalized paper plays a decisive role. The most probable mechanism is based on pinning at the three-phase contact line on the rough microstuctured paper, which is enabled by the fact that coated fibres do not allow subsequent swelling of the cellulose material. This hypothesis is supported by a rather tiny decrease in surface free energy from cellulose to silica, which was determined on model surfaces. By varying the amount of silica added and the drying process, the distribution of silica along the paper cross sections can be adjusted in terms of hydrophobicity. In initial tests, the application as a membrane for oil-water separation is successfully demonstrated. A subsequent functionalization with the redox-responsive polymer PFcMA is able to cause the switching of the papers in relation to the wetting, and the first tests of initial functionalization of the fiber and subsequent paper formation are described in the report, which is successfully carried out. This system may allow multifunctional functionalization in papers in the future and thus produce new tailor-made papers. By using a simple dip-coating process and tuning the initial TEOS concentration in the coating solution and drying process, the wetting characteristics progress from hydrophilic to Janus type and hydrophobic in a controlled fashion by adjusting a precise and simple gradient design. If ethanol evaporation and silane hydrolysis as well as condensation now occur on similar time scales, a gradient in silica distribution and thus a tailored adjustment along the paper cross-section is obtained.

8. Experimental Section

8.1. Used chemicals and materials

Chemicals

1-Bromopropane	Sigma-Aldrich, 99 %
2-(Dimethylamino)ethyl methacrylate (DMAEMA)	Sigma-Aldrich, 98 %
3-[Bis(2-hydroxyethyl)amino]propyl-triethoxysilane	ABCR, 62 %
acetonitrile	AppliChem, 99,9 %
aluminium oxide (AlOx)	Sigma-Aldrich
calcoflour white	Sigma-Aldrich
diethanolamine	Sigma-Aldrich, 98 %
ethanol	EMPLURA®, Merck, 99 %
hexaammineruthenium(II) chloride	VWR, 99 %
hydrochloric acid (37 %ig)	VWR
iodine	99,5 %
methylene blue	Sigma-Aldrich
phosphoric acid 2-hydroxyethyl methacrylate ester (MEP)	Sigma-Aldrich
Pluronic® F127	Sigma-Aldrich, 99 %
potassium chloride	Sigma-Aldrich
potassium hexacyanoferrate(III)	Sigma-Aldrich, 99 %
rhodamine B	Sigma-Aldrich, 95 %
sodium hydrogen carbonate	Sigma-Aldrich
sodium iodid	VWR, 99 %
tetraethyl orthosilicate (TEOS)	Sigma-Aldrich, 98 %
tetrahydrofuran (THF)	AppliChem, 0,5 ppm water
toluene	AppliChem, 0,5 ppm water

Materials

chromium nuggets (Cr)	Alfa Aesar
gold nuggets (Au)	ESG, Scheideanstalt
index matching oil (n_D=1,7000 ± 0,0002)	Cargille Labs
indium-tin-oxide coated glass slide (ITO), SiO2 passivated	VisioTEK, Rs = 4-8 Ω

LaSFN9, optical glass with $n_{632.8} = 1.84489$	Schott
microscope slide	VWR/Roth
silicon-wafer, 525 ± 25 μm, type P/Bor, <100> orientation	Si-Mat, 2-5 Ω resistivity

8.2. Used equipment

In the following, all used characterization methods and relations used for data evaluation are briefly introduced. The methods ellipsometry, CV and SPR described in chapter 5 are not considered again.

8.2.1. Infrared spectroscopy

ATR-IR spectroscopy is applied for functional characterization and allows the independent determination of silica (Si-O-Si and Si-OH stretching vibration) and polymer (C=O vibration). The ATR-IR spectroscopy is performed on a spectrum One (Perkin-Elmer) in the attenuated total reflection mode. The porous silica films are scratched from the glass substrate for measurement or measured directly on the supporting substrate. The spectrum is recorded between 4000-650 cm^{-1} and background corrected automatically after the measurement. The spectra are normalized to the asymmetric stretching vibration of ~ 1070 cm^{-1} in case of scratched or in case of mesoporous films supported on gold coated glass substrate, or to the stretching vibration of Si-OH at around 900 cm^{-1} in case the mesoporous films are measured directly on the substrate (**Figure 84**). The polymer content is determined by the absorption of the C = O valence vibration of the ester group at ~ 1730 cm^{-1}. Three different kinds of silica stretching vibrations are known from literature in silica spectra.[232] Two belonging to the silica network Si-O-Si divided into asymmetric stretching vibration of bridged Si-O-Si at 1260 – 1000 cm^{-1} and the symmetric stretching vibration of Si-O-Si ring structure at around 800 cm^{-1}. The third typical silica vibration is the stretching vibration of free silanol groups Si-OH in the range of 900-980 cm^{-1} as indicated in **Figure 84**. Of course only mesoporous films treated identically can be directly compared.

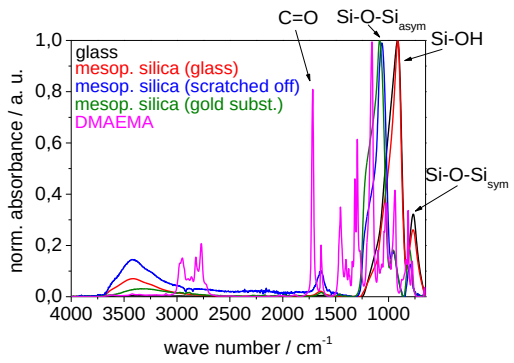

Figure 84. ATR-IR spectra of glass substrate (black), mesoporous silica on glass (red), mesoporous silica scratched off (blue), mesoporous silica on gold coated glass substrate (green) and DMAEMA (magenta) showing the characteristic silica stretching vibration Si-O-Si_{asym},, Si-O-Si_{sym} and the polymer typical C=O vibration. Bends are marked with arrows.

8.2.2. UV/VIS

UV/VIS absorption measurements are carried out using a Cary 60 UV/VIS-spectrometer from Agilent. The recording of measured data is done using the software package Agilent Cary WinUV-Software. The background is corrected prior to each measurement.

8.2.3. Contact Angle

Contact angle measurements are carried out using Model TBU90E DataPhysics Instruments GmbH with the Programm SCA-Software. All samples are measured at three to five positions, and the average value is calculated with standard deviation. For static contact angle measurements, a water drop volume of 2 μL is used.

8.2.4. Transmission Electron Microscope (TEM)

Transmission electron microscopy (TEM) micrographs are recorded using a FEI CM20 TEM microscope with a maximum resolution of 2.3 Å equipped with a LAB-6 cathode (200kV) and a CCD camera (Olympus) from Frau Ulrike Kunz (AK Prof. Dr. Klebe/ TU Darmstadt). Samples are dispersed in a few droplets of ethanol before being dropped onto a copper TEM grid to image.

8.2.5. Scanning Electron Microscope (SEM)

Scanning electron microscopy (SEM) micrographs are captured using a JEOL JSM-6510 scanning microscope operated at an acceleration voltage of 20 kV. Samples are coated with a platinum/palladium (80:20) layer of several nanometers with a Cressington 208 HR.

8.2.6. X-ray Photoelectron Spectroscopy (XPS)

XPS are recorded by K. Kopp (AK Prof. Dr. Hess, TU Darmstadt) using a Surface Science Laboratories SSX-100 X-ray photoelectron spectrometer equipped with a monochromatic Al Kα X-ray source (100 W). The X-ray spot size is 250−1000 μm. The binding energy scale of the system is calibrated using Au 4f7/2 = 84.0 eV and Cu 2p3/2 = 932.67 eV signals from foil samples. A Shirley background is subtracted from all spectra. Peak fitting is performed with Casa XPS using 70/30 Gaussian-Lorentzian product functions. Atomic ratios are determined from the integral intensities of the signals, which are corrected by empirically derived sensitivity factors.

8.2.7. Profilometer

Profilometric measurements are performed as complementary methods to SPR and ellipsometry measurements (Kompetenzzentrum Materialcharakterisierung, TU Darmstadt). The profiler device Dektak XT from Bruker with a vertical resolution to 1 Å, horizontal resolution of 120,000 points and a force on top of 1 mg is used. Each measurement is scanned in Hills & Valley mode.

8.2.8. Light-emitting Diode (LED)

An Autolab Optical bench from Metrohm equipped with an Autolab LED Driver with 700 mA output is used as LED light source. As LED is a LDC627 with red light and a wavelength of 627 nm is used. The spectrum and the intensities of the lamp is shown in **Figure 85**. The intensity can be varied by changing the incoming current of LED.

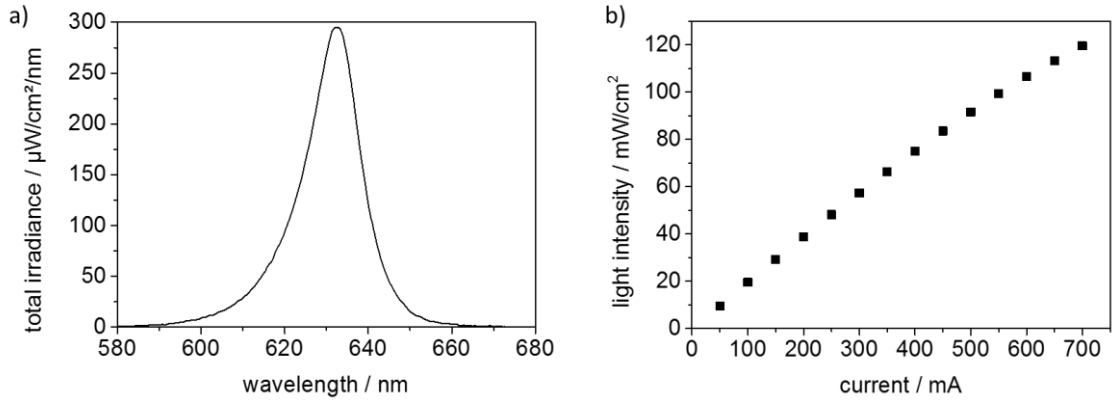

Figure 85. a) spectrum of the LED described with the wavelength 627 nm. b) light intensity of the LED when changing the current input of the LED between 50 and 700 mA.

8.2.9. Lumatec®Lamp

A Lumatec UV-Technik Superlite 410 lamp is used as the light source for reference polymerisations in mesoporous silica. The wavelength ranged from 400 to 700 nm (visible light). Each polymerisation is carried out in a polystyrene (PS) cuvette with substrate perpendicular to light beam and positioned 10 cm away from the light source in an aluminum foil-lined box. In **Figure 86** a spectrum of Lumatec®Lamp with filter 0 (400-700 nm) and the intensity of Lumatec®Lamp at filter 0 is shown.

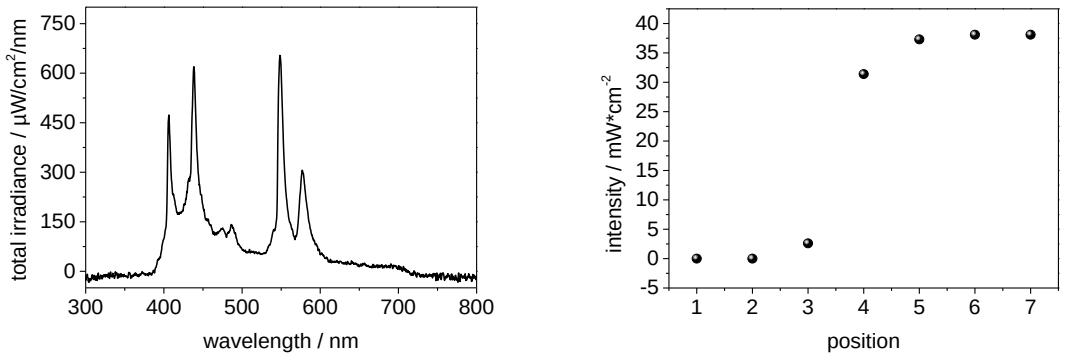

Figure 86. a) Spectrum of Lumatec®Lamp with filter 0 (400-700 nm) and b) intensity of Lumatec®Lamp at filter 0.

8.3. Silica Film Preparation

The mesoporous silica films are synthesized evaporation induced self-assembly (EISA)[5] using sol-gel chemistry. The different substrates types are covered with the precursor solutions on

two different routes by dip-coating or gravure printing. The chapter is divided into a formulation part (chapter 8.3.1) and the preparation part (chapter 8.3.2).

8.3.1. Formulations of Sol-Gel Solution

Mesoporous silica

Mesoporous silica films are synthesized via sol-gel-chemistry using tetraethyl orthosilicate (TEOS) in the presence of the template Pluronic® F127. The precursor solutions (1 TEOS: 0.0075 F127: 40 EtOH: 10 H_2O: 0.2 HCl) resulting in 8 nm mesopores (called small pores) or (1 TEOS: 0.02 F127: 40 EtOH: 34.5 H_2O: 0.08 HCl)[272] resulting in 16 nm mesopores (called big pores) are stirred for 24 h at room temperature before being used.

Mesoporous silica with co-condensate

The mesoporous silica with co-condensate where synthesized the same way like unfunctionalized mesoporous silica but with the changed formulation ((1−x) TEOS: x 3-[Bis(2-hydroxyethyl)amino]propyl-triethoxysilane: 0.0075 F127: 40 EtOH: 10 H2O: 0.2 HCl) with x being between 0 and 25 mol %.

8.3.2. Preparation via Sol-Gel Solution

Mesoporous silica

Mesoporous silica films are synthesized by evaporation induced self-assembly (EISA)[5] on silicon wafer, glass or indium tin oxide coated glass substrates at 40-50 % relative humidity and 298 K. The mesoporous silica films are dip-coated with varying withdrawal speeds between 0.1 mm/s and 30 mm/s or gravure printed (G1-5 - IGT Testing Systems, Dr. Dieter Spiehl, AK Prof. Dr. Dörsam, TU Darmstadt) with different gravure cylinders cell volumes between 0.2 mL/m² and 24 mL/m². A printing speed of 0.6 m/s and a printing force of 700 N are used. Freshly deposited films are stored at 50 % relative humidity for 1 h. In case of printing two layers the cylinder with 8.5 mL/m² cell volume is used. Between the first and the second layer an aging time of 10 min is used. After deposition of the second layer films are kept at 50 % relative humidity for 1 h followed by a stabilizing thermal treatment and extraction like for films treated to 200 °C. After successful film deposition a stabilizing thermal treatment is carried out in two successive

1 h steps at 60 °C and 130 °C. Consecutively, the temperature is increased to 350 °C, or to 200 °C in case of co-condensed mesoporous silica films, with a gradient of 1 °C/min. This final film stabilization temperature is applied for 2 h. Finally, the films treated up to 350 °C and are rinsed with ethanol and stored under ambient conditions. Template extraction of the films with co-condensed organic groups, treated only up to 200 °C, are treated with acidic ethanol (0.01 M HCl in abs. ethanol) for 3 days to remove the mesopore template.

8.4. Surface Grafting of Initiator Molecules

Mesoporous silica films are prepared by dip coating with two different withdrawal speeds 2 mm/s and 10 mm/s for further functionalization via post-grafting approach with the formulation resulting in 8 nm. The binding with the coinitiator (3-[Bis(2-hydroxyethyl)amino]propyl-triethoxysilane) is done with 0.01 wt.-% in toluene for 1 h (2 mm/s) and 0.05 wt.-% (10 mm/s) for 2 h at 80° in nitrogen atmosphere. Afterwards an extraction of mesoporous silica film with toluene takes place.

When post-grafting the coinitiator on mesoporous silica films with pore sizes of 16 nm prepared by dip-coating and all mesoporous silica films prepared by gravure printing the conditions of 1 h and a concentration of 0.01 wt.-% in toluene at 80 °C are used. The functionalization takes place in nitrogene atmosphere. Afterwards an extraction of mesoporous silica film with toluene takes place.

8.5. Plasma Treatment with CO_2

The CO_2 plasma treatment is carried out according to a protocol of Mr. Babu (AK Prof. Dr. Schneider, TU Darmstadt).[237] The plasma treatment is carried out with carbon dioxide with a Diener Electronic Femto equipment, at a pressure of 0.4 mbar and a power of 20 % for 12 seconds.

8.6. Adsorption-tests of Polymerization

The mesoporous silica films are separated and incubated for 1 h with different solutions. The solutions are the dye solution (methylene blue, 3 mg/50 mL 0.1 M aqueous $NaHCO_3$ solution), monomer solution (DMAEMA or MEP, 500 mg/mL 0.1 M aqueous $NaHCO_3$ solution) or 9:1 ratio monomer:dye solution (450 mg/mL monomer, 0.0052 mg/mL methylene blue in 0.1 M $NaHCO_3$ solution = polymerization solution). The mesoporous silica films are dried with

compressed air and freshly measured in ATR-IR and UV-Vis. Simultaneously the mesoporous silica film is polymerized with the same solution for 1 h with the laser (Pol.1 =Pol, 2 = 90°, 5 mW). Then the substrate is measured in ATR-IR without extraction just dried with compressed air, then the extraction with water takes place, the film is dried and measured again in ATR-IR.

8.7. Polymer-Functionalization of Surface

The dye sensitized polymerization is used as a surface initiated photopolymerization explained in chapter 5.1. The polymer functionalization of mesoporous silica films of different film thickness and pore sizes are done with different initiation systems, light induced with different light sources like laser, LED or Lumatec®lamp of red light or near-field induced with surface plasmons or transversal modes.

8.7.1. Light Induced Polymerization

Initiator solutions are prepared by dissolving 3 mg methylene blue dye in 50 ml aqueous 0.1 M aqueous $NaHCO_3$ solution. The monomer DMAEMA (destabilized over AlOx) is as well dissolved in an aqueous $NaHCO_3$ solution. As DMAEMA concentrations mostly 225 g/L or 450 mg/mL are used. Before polymerization the dye solution and the monomer solution are mixed in a ratio of 1:9 and the solution is degassed for 10 min by nitrogen or argon bubbling under the exclusion of light and in the presence of the coinitiator functionalized mesoporous film. For polymerization the mesoporous film is irradiated with red light (light source: LED, Laser or Lumatec®lamp) with a defined intensity and with a defined polymerization time. For the LED and Lumatec®lamp light source the mesoporous silica film is located in a distance of 10 cm, positioned perpendicular to the waveguide. For the laser light source, the mesoporous silica is located as shown in **Figure 11**, chapter 5.2 and the laser dot crossing the mesoporous film is marked for characterization. After polymerization the mesoporous film is extensively extracted in water.

8.7.2. Near-Field Induced Polymerization

More information of the experimentation set up is given in chapter 5.2.

The laser power is adjusted to 100 % reflectivity (Pol. 1 ~ 22 °, Pol. 2 = 90 °) in the detector whithout sample. After installation of sample in the Kretschmann configuration a spectrum

measured against air is recorded.[220] Than water is constantly flown with 5 μL/min flow rate through the sample and a second spectrum is recorded. Afterwards the polymerization solution prepared analogous to light induced polymerization is flown constantly during the experiment at a flow rate of 5 μL/min. The spectrum is recorded in a very fast way, to avoid a starting polymerization. After determination of the surface plasmon maximum (SP) or transversal mode (TM) the corresponding resonance angle and the intensity of laser is set and the polymerization is running for the desired time. After this the extraction with water is done in the flowing cell and after minimum 30 min a spectrum is recorded. Then the sample is removed, extracted again and dried and build in the set up again for a renewed measurement against air after polymerization.

8.8. Papersheet Formation

For the preparation of lab-engineered paper substrates eucalyptus sulfate pulp (curl: 16.2 %; fibrillation degree: 1.3 %; fines content: 15.2 %) is used. The pulp is refined in a Voith LR 40 laboratory refiner. Refining is performed with an effective specific energy of 16 kWh/t (750000 rotations). Laboratory-engineered paper substrates are prepared from eucalyptus sulfate pulp with a grammage of 80 ± 0.9 g/m^2 by using a Rapid-Köthen sheet former according to DIN 54358 and ISO 5269/2. (REF: ISO 5269-2:2004(E), Pulps – Preparation of Laboratory Sheets for Physical Testing – Part 2: Rapid Köthen Method, 2004.) No additives or fillers are used. After sheet formation, the paper substrates are equilibrated at a temperature of 23 °C, and a relative humidity of 50 % in a climate-controlled room for at least 24 h before further characterization and functionalization is performed.

For the preparation of the cotton linter paper substrates, bleached, dry cotton linter pulp is used. The pulp is refined in a Voith LR 40 laboratory refiner. Refining is performed with an effective specific energy of 200 kWh/t. Cotton linter paper sheets with a grammage of 42−44 g/m^2 are fabricated using a conventional Rapid-Köthen hand sheet maker according to DIN 54358 and ISO 5269/2 in the absence of additives and fillers. After sheet formation, the paper substrates are equilibrated at a temperature of 23 °C, and a relative humidity of 50 % in a climate-controlled room for at least 24 h before further characterization and functionalization is performed.

The cotton linter paper sheets with other grammages used in this work are formed in the research group of Markus Biesalski from Tizian Venter.

8.8.1. Silica Functionalization of Paper Sheets

These coatings are synthesized via sol−gel chemistry based on the oxide precursor tetraethoxysilane (TEOS) in the presence of a Pluronic® F127 template. Dynamic light scattering (DLS) measurements under the conditions used in the coating procedure of this study (acidic ethanol) reveal a concentration-independent micelle diameter of 6.8 ± 0.5 nm for Pluronic F127 concentrations between 0.3 and 9.3 g/mL. This indicates the Pluronic® F127 forms spherical micelles under the coating conditions used. To prepare mesoporous silica coatings, the precursor solution is prepared using the following molar ratios: 1 TEOS:0.075 Pluronic® F127:24 EtOH:5.2 H_2O:0.28 HCl. Dense silica coatings are prepared similarly, but in the absence of the Pluronic® F127 template. The precursor solution is stirred for 24 h.

Cotton linter paper (fibers are provided by Fachgebiet Papierfabrikation und Mechanische Verfahrenstechnik PMV, TU Darmstadt) sheets (prepared by S. Richter and T. Venter, AK Prof. Dr. Biesalski, TU Darmstadt) are dip coated with sol gel solution for mesoporous silica (8 nm) or dense silica with the intermediate concentration at 40−50 % relative humidity and 298 K at a withdrawal speed of 2 mm/s. Freshly deposited films are stored at 50 % relative humidity in a climate chamber for 1 h. A consecutive thermal treatment is then carried out in two successive 1 h steps at 60 °C and 130 °C, followed by a temperature increase to either 200 °C or 500 °C, respectively, at a rate of 1 °C/min. This final temperature is held for 2 h before cooling to ambient temperature. The prepared samples are then rinsed with ethanol and stored under ambient conditions. The samples that are treated up to a temperature of 200 °C are then immersed into acidic ethanol (0.01 M HCl) to chemically extract the Pluronic® F127 template. To prepare cotton linter paper sheets that are coated only within one- half with dense silica, the samples are stored in a preheated oven at 130 °C for 1 h immediately after dip-coating, followed by a temperature increase to 200 °C at a rate of 1 °C/min.

Eucalyptus-sulfate paper sheets (1 cm* 8 cm) are dip coated at 50 % relative humidity and 23 °C at a withdrawal speed of 2 mm/s. Freshly deposited films are directly brought in a 130 °C preheated vacuum drying oven or a muffle furnace. The samples are kept in a horizontal position with a minimal bearing surface at 130 °C for 2 h before cooling to ambient temperature. Three different concentrations of dip-coating solution are prepared with the following molar ratios:

- 1 TEOS:80 EtOH:20 H_2O:0.04 HCl → low concentration (l_c)
- 1 TEOS:40 EtOH:10 H_2O:0.02 HCl → intermediate concentration (i_c)
- 1 TEOS:20 EtOH:5 H_2O:0.01 HCl → high concentration (h_c)

The precursor solutions are stirred for 24 h. The samples are marked on the top side of the sheets.

List of Figures

List of Tables

List of Abbreviation

AFM	Atomic force microscope
APTES	(3-Aminopropyl)triethoxysilane
ATRP	Atom transfer radical polymerization
BET	Brunauer-Emmett-Teller
CA	Contact angle
CLSM	Confocal laser scanning microscopy
CMC	Critical micelle concentration
CSA	Cooperative self-assembly
CV	Cyclic voltammetry
CVD	Chemical vapor deposition
DLP	Digital light processing
EISA	Evaporation induced self assembly
GPC	Gel permeation chromatography
IR	Infrared
ITO	Indium-tin-oxide
IUPAC	International Union of Pure and Applied Chemistry
LCT	Liquid crystal templating
LED	Light-emitting diode
LISA	Light-controlled self-assembly
LSP	Localized surface plasmon
MSS	Module steady state
NMR	Nuclear magnetic resonance
PAG	Photoacid generators
PDI	Polydispersity
PDMAEMA	Poly(2-(Dimethylamino)ethyl methacrylate)
PDMS	Polydimethylsiloxan
PET	Polyethylenterephthalat
PFcMA	Poly(2-(methacryloyloxy)ethylferrocene-carboxylate)
PMEP	Poly(2-(methacryloyloxy)ethylphosphat)
PMO	Periodic mesoporous organosilica
PTFE	Polytetrafluorethen

PS	Photosensitizer
RAFT	Reversible addition-fragmentation chain transfer
ROMP	Ring-opening metathesis polymerisation
SEM	Scanning electron microscopy
SLA	Stereolithography
SPR	Surface plasmon resonance
STED	Stimulated emission depletion
TEM	Transmission electron microscopy
TEOS	Tetraethylorthisilicat
TGA	Thermo gravimetric analysis
TIRF	Total internal reflection fluorescence microscopy
UV	Ultraviolet
Vis	Visible
XPS	X-ray photoelectron spectroscopy

Literature

1. Nie, Z.; Kumacheva, E., Patterning surfaces with functional polymers. *Nature materials* **2008,** *7*, 277-290.
2. Sanchez, C.; Belleville, P.; Popall, M.; Nicole, L., Applications of advanced hybrid organic–inorganic nanomaterials: from laboratory to market. *Chem. Soc. Rev.* **2011,** *40*, 696-753.
3. Andrieu-Brunsen, A.; Micoureau, S.; Tagliazucchi, M.; Szleifer, I.; Azzaroni, O.; Soler-Illia, G. J. A. A., Mesoporous Hybrid Thin Film Membranes with PMETAC@Silica Architectures: Controlling Ionic Gating through the Tuning of Polyelectrolyte Density. *Chemistry of Materials* **2015,** *27* (3), 808-821.
4. Soler-Illia, G. J.; Azzaroni, O., Multifunctional hybrids by combining ordered mesoporous materials and macromolecular building blocks. *Chem. Soc. Rev.* **2011,** *40* (2), 1107-50.
5. Brinker, C. J.; Lu, Y.; Sellinger, A.; Fan, H., Evaporation-Induced Self-Assembly: Nanostructures Made Easy. *Adv. Mater.* **1999,** *11* (7), 579-585.
6. Murdan, S., Electro-responsive drug delivery from hydrogels. *Journal of Controlled Release* **2003,** *92* (1-2), 1-17.
7. Hunter, G.; Vander Wal, R.; Evans, L.; Xu, J.; Berger, G.; Kullis, M.; Biaggi-Labiosa, A., Nanostructured material sensor processing using microfabrication techniques. *Sensor Review* **2012,** *32* (2), 106-117.
8. Yan, X.; Wang, F.; Zheng, B.; Huang, F., Stimuli-responsive supramolecular polymeric materials. *Chem Soc Rev* **2012,** *41* (18), 6042-65.
9. Huber, D. L.; Manginell, R. P.; Samara, M. A.; Kim, B.-I.; Bunker, B. C., Programmed Adsorption and Release of Proteins in a Microfluidic Device. *Science* **2003,** *301* (5631), 352-354.
10. Choi, M.; Kleitz, F.; Liu, D.; Lee, H. Y.; Ahn, W.-S.; Ryoo, R., Controlled Polymerization in Mesoporous Silica toward the Design of Organic-Inorganic Composite Nanoporous Materials. *J. Am. Chem. Soc.* **2005,** *127*, 1924-1932.
11. Schoch, R. B.; Han, J.; Renaud, P., Transport phenomena in nanofluidics. *Reviews of Modern Physics* **2008,** *80* (3), 839-883.
12. Barbey, R.; Lavanant, L.; Paripovic, D.; Schuwer, N.; Sugnaux, C.; Tugulu, S.; Klok, H. A., Polymer brushes via surface-initiated controlled radical polymerization: synthesis, characterization, properties, and applications. *Chem Rev* **2009,** *109* (11), 5437-527.
13. Jordan, R.; Ulman, A.; Kang, J. F.; Rafailovich, M. H.; Sokolov, J., Surface-Initiated Anionic Polymerization of Styrene by Means of Self-Assembled Monolayers. *J Am Chem Soc* **1999,** *121*, 1016-1022.
14. Matsuno, R.; Yamamoto, K.; Otsuka, H.; Takahara, A., Polystyrene- and Poly(3-vinylpyridine)-Grafted Magnetite Nanoparticles Prepared through Surface-Initiated Nitroxide-Mediated Radical Polymerization. *Macromolecules* **2004,** *37*, 2203-2209.
15. Sun, Y.; Ding, X.; Zheng, Z.; Cheng, X.; Hu, X.; Peng, Y., Surface initiated ATRP in the synthesis of iron oxide/polystyrene core/shell nanoparticles. *European Polymer Journal* **2007,** *43* (3), 762-772.
16. Li, Y.; Benicewicz, B. C., Functionalization of Silica Nanoparticles via the Combination of Surface-Initiated RAFT Polymerization and Click Reactions. *Macromolecules* **2008,** *41*, 7986-7992.
17. Wildanger, D.; Patton, B. R.; Schill, H.; Marseglia, L.; Hadden, J. P.; Knauer, S.; Schönle, A.; Rarity, J. G.; O'Brien, J. L.; Hell, S. W.; Smith, J. M., Solid Immersion Facilitates Fluorescence Microscopy with Nanometer Resolution and Sub-Ångström Emitter Localization. *Advanced Materials* **2012,** *24* (44), OP309-OP313.
18. Eliseev, S. P.; Korolkov, A. E.; Vitukhnovsky, A. G.; Chubich, D. A.; Sychev, V. V., STED nanolithography of three-dimensional plasmonic structures. *Nanotechnologies in Russia* **2016,** *11* (3), 200-207.

19. Fischer, J.; Wegener, M., Three-dimensional direct laser writing inspired by stimulated-emission-depletion microscopy [Invited]. *Opt. Mater. Express* **2011,** *1* (4), 614-624.
20. Wollhofen, R.; Katzmann, J.; Hrelescu, C.; Jacak, J.; Klar, T. A., 120 nm resolution and 55 nm structure size in STED-lithography. *Optics Express* **2013,** *21* (9), 10831-10840.
21. Ueno, K.; Misawa, H., Surface plasmon-enhanced photochemical reactions. *Journal of Photochemistry and Photobiology C: Photochemistry Reviews* **2013,** *15*, 31-52.
22. Baffou, G.; Quidant, R., Nanoplasmonics for chemistry. *Chem Soc Rev* **2014,** *43* (11), 3898-907.
23. Álvarez, M.; Best, A.; Unger, A.; Alonso, J. M.; del Campo, A.; Schmelzeisen, M.; Koynov, K.; Kreiter, M., Near-Field Lithography by Two-Photon Induced Photocleavage of Organic Monolayers. *Advanced Functional Materials* **2010,** *20* (24), 4265-4272.
24. Deeb, C.; Ecoffet, C.; Bachelot, R.; Plain, J. r. m.; Bouhelier, A.; Soppera, O., Plasmon-Based Free-Radical Photopolymerization: Effect of Diffusion on Nanolithography Processes. *Journal of the American Chemical Society* **2011,** *133* (27), 10535-10542.
25. Tijunelyte, I.; Kherbouche, I.; Gam-Derouich, S.; Nguyen, M.; Lidgi-Guigui, N.; de la Chapelle, M. L.; Lamouri, A.; Lévi, G.; Aubard, J.; Chevillot-Biraud, A.; Mangeney, C.; Felidj, N., Multi-functionalization of lithographically designed gold nanodisks by plasmon-mediated reduction of aryl diazonium salts. *Nanoscale Horiz.* **2017**.
26. Pieke, S. Experimentelle Untersuchungen zur effizienten Vernetzung von Oberflächenbeschichtungen mit UV-Strahlung. Universität Karlsruhe (TH), KIT Scientific Publishing, 2009.
27. Ogawa, K. A.; Goetz, A. E.; Boydston, A. J., Developments in Externally Regulated Ring-Opening Metathesis Polymerization. *Synlett* **2016,** *27* (02), 203-214.
28. Pascual, L. M. M.; Dunford, D. G.; Goetz, A. E.; Ogawa, K. A.; Boydston, A. J., Comparison of Pyrylium and Thiopyrylium Photooxidants in Metal-Free Ring-Opening Metathesis Polymerization. *Synlett* **2016,** *27* (05), 759-762.
29. Allegrezza, M. L.; DeMartini, Z. M.; Kloster, A. J.; Digby, Z. A.; Konkolewicz, D., Visible and sunlight driven RAFT photopolymerization accelerated by amines: kinetics and mechanism. *Polymer Chemistry* **2016,** *7* (43), 6626-6636.
30. Konkolewicz, D.; Schröder, K.; Buback, J.; Bernhard, S.; Matyjaszewski, K., Visible Light and Sunlight Photoinduced ATRP with ppm of Cu Catalyst. *ACS Macro Letters* **2012,** *1* (10), 1219-1223.
31. Xiao, P.; Frigoli, M.; Dumur, F.; Graff, B.; Gigmes, D.; Fouassier, J. P.; Lalevée, J., Julolidine or Fluorenone Based Push–Pull Dyes for Polymerization upon Soft Polychromatic Visible Light or Green Light. *Macromolecules* **2014,** *47* (1), 106-112.
32. Fouassier, J.-P.; Morlet-Savary, F.; Lalevée, J.; Allonas, X.; Ley, C., Dyes as Photoinitiators or Photosensitizers of Polymerization Reactions. *Materials* **2010,** *3* (12), 5130-5142.
33. Fouassier, J. P.; Lalevée, J., *Photoinitiators for Polymer Synthesis*. Wiley-VCH Verlag & Co. KGaA,: Weinheim, Germany, 2012.
34. Jung, J. H.; Park, M.; Shinkai, S., Fabrication of silica nanotubes by using self-assembled gels and their applications in environmental and biological fields. *Chemical Society Reviews* **2010,** *39* (11), 4286-4302.
35. Wang, Z.; Yang, X.; Cheng, Z.; Liu, Y.; Shao, L.; Jiang, L., Simply realizing “water diode” Janus membranes for multifunctional smart applications. *Materials Horizons* **2017,** *4* (4), 701-708.
36. Walther, A.; Müller, A. H. E., Janus Particles: Synthesis, Self-Assembly, Physical Properties, and Applications. *Chem. Rev.* **2013,** *113* (7), 5194-5261.
37. Tian, X.; Li, J.; Wang, X., Anisotropic liquid penetration arising from a cross-sectional wettability gradient. *Soft Matter* **2012,** *8* (9).
38. Shah, A. A.; Schultz, B.; Zhang, W.; Glotzer, S. C.; Solomon, M. J., Actuation of shape-memory colloidal fibres of Janus ellipsoids. *Nat. Mater.* **2015,** *14* (1), 117-24.

39. Yang, H. C.; Hou, J.; Chen, V.; Xu, Z. K., Janus Membranes: Exploring Duality for Advanced Separation. *Angew. Chem. Int. Ed. Engl.* **2016,** *55* (43), 13398-13407.
40. Zhang, H.; Hou, X.; Zeng, L.; Yang, F.; Li, L.; Yan, D.; Tian, Y.; Jiang, L., Bioinspired artificial single ion pump. *J. Am. Chem. Soc.* **2013,** *135* (43), 16102-10.
41. Cao, M.; Ju, J.; Li, K.; Dou, S.; Liu, K.; Jiang, L., Facile and Large-Scale Fabrication of a Cactus-Inspired Continuous Fog Collector. *Adv. Funct. Mater.* **2014,** *24* (21), 3235-3240.
42. Tian, X.; Jin, H.; Sainio, J.; Ras, R. H. A.; Ikkala, O., Droplet and Fluid Gating by Biomimetic Janus Membranes. *Adv. Funct. Mater.* **2014,** *24* (38), 6023-6028.
43. Zhang, M.; Wang, L.; Hou, Y.; Shi, W.; Feng, S.; Zheng, Y., Controlled Smart Anisotropic Unidirectional Spreading of Droplet on a Fibrous Surface. *Adv. Mater.* **2015,** *27* (34), 5057-62.
44. Zhang, Z.; Kong, X. Y.; Xiao, K.; Liu, Q.; Xie, G.; Li, P.; Ma, J.; Tian, Y.; Wen, L.; Jiang, L., Engineered Asymmetric Heterogeneous Membrane: A Concentration-Gradient-Driven Energy Harvesting Device. *J. Am. Chem. Soc.* **2015,** *137* (46), 14765-72.
45. Yang, H.-C.; Hou, J.; Wan, L.-S.; Chen, V.; Xu, Z.-K., Janus Membranes with Asymmetric Wettability for Fine Bubble Aeration. *Adv. Mater. Interfaces* **2016,** *3* (9).
46. Yang, H. C.; Xie, Y.; Hou, J.; Cheetham, A. K.; Chen, V.; Darling, S. B., Janus Membranes: Creating Asymmetry for Energy Efficiency. *Adv. Mater.* **2018,** *30* (43), e1801495.
47. Stahl, T.; Mattern, D.; Brunn, H. J. E. S. E., Toxicology of perfluorinated compounds. **2011,** *23* (1), 38.
48. Deng, Y.; Wei, J.; Sun, Z.; Zhao, D., Large-pore ordered mesoporous materials templated from non-Pluronic amphiphilic block copolymers. *Chem. Soc. Rev.* **2013,** *42* (9), 4054-70.
49. Innocenzi, P.; Malfatti, L., Mesoporous thin films: properties and applications. *Chem. Soc. Rev.* **2013,** *42* (9), 4198-216.
50. Calvo, A.; Angelomé, P. C.; Sanchez, C.; Scherlis, D. A.; Williams, F. J.; Soler-Illia, G. J. A. A., Mesoporous Aminopropyl-Functionalized Hybrid Thin Films with Modulable Surface and Environment-Responsive Behavior. *Chem. Mater.* **2008,** *20*, 4661-4668.
51. Sing, K. S. W.; Everett, D. H.; Haul, R. A. W.; Moscou, L.; Pieroti, R. A.; Rouquerol, J.; Siemieniewska, T., IUPAC Recommendations, Reporting physisorption data for gas/solid systems. *Pure Appl. Chem.* **1985,** *57* (4), 603-619.
52. Kresge, C. T.; Leonowicz, M. E.; Roth, W. J.; Vartuli, J. C.; Beck, J. S., Ordered mesoporous molecular sieves synthesized by a liquidcrystal template mechanism. *Nature* **1992,** *359*, 710-712.
53. Beck, J. S.; Vartuli, J. C.; Roth, W. J.; Leonowicz, M. E.; Kresge, C. T.; Schmitt, K. D.; Chu, C. T.-W.; Olson, D. H.; Sheppard, E. W.; McCullen, S. B.; Higgins, J. B.; Schlenker, J. L., A new Family of Mesoporous Molecular Sieves Prepared with Liquid Crystal Templates. *J. Am. Chem. Soc.* **1992,** *114*, 10834-10843.
54. Boissiere, C.; Larbot, A.; Bourgaux, C.; Prouzet, E.; Bunton, C. A., A Study of the Assembly Mechanism of the Mesoporous MSU-X Silica Two-Step Synthesis. *Chem. Mater.* **2001,** *13*, 3580-3586.
55. Grosso, D.; Cagnol, F.; Soler-Illia, G. J. A. A.; Crepaldi, E. L.; Amenitsch, H.; Brunet Bruneau, A.; Bourgeois, A.; Sanchez, C., Fundamentals of Mesostructuring Through Evaporation-Induced Self-Assembly. *Adv. Funct. Mater.* **2004,** *14* (4), 309-322.
56. Nicole, L.; Boissiere, C.; Grosso, D.; Quach, A.; Sanchez, C., Mesostructured hybrid organic–inorganic thin films. *J. Mater. Chem.* **2005,** *15*, 3598-3627.
57. Cagnol, F.; Grosso, D.; Soler-Illia, G. J. d. A. A.; Crepaldi, E. L.; Babonneau, F.; Amenitsch, H.; Sanchez, C. m., Humidity-controlled mesostructuration in CTAB-templated silica thin film processing. The existence of a modulable steady state. *Journal of Materials Chemistry* **2003,** *13* (1), 61-66.
58. Hua, Z.-L.; Shi, J.-L.; Wang, L.; Zhang, W.-H., Preparation of mesoporous silica films on a glass slide: surfactant template removal by solvent extraction. *Journal of Non-Crystlline Solids* **2001,** *292*, 177-183.

59. Fan, H.; Reed, S.; Baer, T.; Schunk, R.; Lopez, G. P.; Brinker, C. J., Hierarchically structured functional porous silica and composite produced by evaporation-induced self-assembly. *Microporous and Mesoporous Materials* **2001,** *44-45*, 625-637.
60. Yuan, L.; Guliants, V. V., Mesoporous niobium oxides with tailored pore structures. *Journal of Materials Science* **2008,** *43* (18), 6278-6284.
61. Das, S. K.; Bhunia, M. K.; Sinha, A. K.; Bhaumik, A., Self-Assembled Mesoporous Zirconia and Sulfated Zirconia Nanoparticles Synthesized by Triblock Copolymer as Template. *The Journal of Physical Chemistry C* **2009,** *113* (20), 8918-8923.
62. Crepaldi, E. L.; Soler-Illia, G. J. A. A.; Grosso, D.; Cagnol, F.; Ribot, F.; Sanchez, C., Controlled Formation of Highly Organized Mesoporous Titania Thin Films: From Mesostructured Hybrids to Mesoporous Nanoanatase TiO2. *J. Am. Chem. Soc.* **2003,** *125*, 9770-9786.
63. Brezesinski, T.; Groenewolt, M.; Gibaud, A.; Pinna, N.; Antonietti, M.; Smarsly, B., Evaporation-Induced Self-Assembly (EISA) at Its Limit: Ultrathin, Crystalline Patterns by Templating of Micellar Monolayers. *Advanced Materials* **2006,** *18* (17), 2260-2263.
64. Shimojima, A.; Kuroda, K., Controlled synthesis of nanostructured silica-based materials from designed alkoxysilanes. *Journal of Sol-Gel Science and Technology* **2008,** *46* (3), 307-311.
65. Kobayashi, M.; Susuki, K.; Otani, T.; Enomoto, S.; Otsuji, H.; Kuroda, Y.; Wada, H.; Shimojima, A.; Homma, T.; Kuroda, K., Thickness control of 3-dimensional mesoporous silica ultrathin films by wet-etching. *Nanoscale* **2017,** *9* (24), 8321-8329.
66. Wei, J.; Sun, Z.; Luo, W.; Li, Y.; Elzatahry, A. A.; Al-Enizi, A. M.; Deng, Y.; Zhao, D., New Insight into the Synthesis of Large-Pore Ordered Mesoporous Materials. *Journal of the American Chemical Society* **2017,** *139* (5), 1706-1713.
67. Hoheisel, T. N.; Hur, K.; Wiesner, U. B., Block copolymer-nanoparticle hybrid self-assembly. *Progress in Polymer Science* **2015,** *40*, 3-32.
68. Stefik, M.; Guldin, S.; Vignolini, S.; Wiesner, U.; Steiner, U., Block copolymer self-assembly for nanophotonics. *Chem Soc Rev* **2015,** *44* (15), 5076-91.
69. Simon, P. F. W.; Ulrich, R.; Spiess, H. W.; Wiesner, U., Block Copolymer-Ceramic Hybrid Materials from Organically Modified Ceramic Precursors. *Chem. Mater.* **2001,** *13*, 3464-3486.
70. Soler-Illia, G. J. d. A. A.; Crepaldi, E. L.; Grosso, D.; Sanchez, C., Block copolymer-templated mesoporous oxides. *Current Opinion in Colloid & Interface Science* **2003,** *8* (1), 109-126.
71. Templin, M.; Franck, A.; Du Chesne, A.; Leist, H.; Zhang, Y.; Ulrich, R.; Schädler, V.; Wiesner, U., Organically Modified Aluminosilicate Mesostructures from Block Copolymer Phases. *Science* **1997,** *278* (5344), 1795-1798.
72. Boissiere, C.; Grosso, D.; Lepoutre, S.; Nicole, L.; Brunet Bruneau, A.; Sanchez, C., Porosity and Mechanical Properties of Mesoporous Thin Films Assessed by Environmental Ellipsometric Porosimetry. *Langmuir* **2005,** *21*, 12362-12371.
73. Faustini, M.; Louis, B.; Albouy, P. A.; Kuemmel, M.; Grosso, D., Preparation of Sol−Gel Films by Dip-Coating in Extreme Conditions. *The Journal of Physical Chemistry C* **2010,** *114* (17), 7637-7645.
74. Faustini, M.; Nicole, L.; Ruiz-Hitzky, E.; Sanchez, C., History of Organic-Inorganic Hybrid Materials: Prehistory, Art, Science, and Advanced Applications. *Advanced Functional Materials* **2018**, 1704158.
75. Ceratti, D. R.; Faustini, M.; Sinturel, C.; Vayer, M.; Dahirel, V.; Jardat, M.; Grosso, D., Critical effect of pore characteristics on capillary infiltration in mesoporous films. *Nanoscale* **2015,** *7* (12), 5371-82.
76. Boudot, M.; Ceratti, D. R.; Faustini, M.; Boissière, C.; Grosso, D., Alcohol-Assisted Water Condensation and Stabilization into Hydrophobic Mesoporosity. *The Journal of Physical Chemistry C* **2014,** *118* (41), 23907-23917.
77. Grosso, D., How to exploit the full potential of the dip-coating process to better control film formation. *Journal of Materials Chemistry* **2011,** *21* (43), 17033.

78. Faustini, M.; Ceratti, D. R.; Louis, B.; Boudot, M.; Albouy, P. A.; Boissiere, C.; Grosso, D., Engineering functionality gradients by dip coating process in acceleration mode. *ACS Appl Mater Interfaces* **2014,** *6* (19), 17102-10.
79. Hwang, J.; Shoji, N.; Endo, A.; Daiguji, H., Effect of withdrawal speed on film thickness and hexagonal pore-array dimensions of SBA-15 mesoporous silica thin film. *Langmuir* **2014,** *30* (51), 15550-9.
80. Bindini, E.; Naudin, G.; Faustini, M.; Grosso, D.; Boissière, C., The Critical Role of the Atmosphere in Dip-Coating Process. *The Journal of Physical Chemistry C* **2017,** *121* (27), 14572-14580.
81. Fuertes, M. C.; Colodrero, S.; Lozano, G.; Gonzalez-Elipe, A. R.; Grosso, D.; Boissiere, C.; Sanchez, C.; Soler-Illia, G. J. A. A.; Miguez, H., Sorption Properties of Mesoporous Multilayer Thin Films. *J. Phys. Chem. C* **2008,** *112*, 3157-3163.
82. Bonifacio, L. D.; Lotsch, B. V.; Puzzo, D. P.; Scotognella, F.; Ozin, G. A., Stacking the Nanochemistry Deck: Structural and Compositional Diversity in One-Dimensional Photonic Crystals. *Advanced Materials* **2009,** *21* (16), 1641-1646.
83. Tom, J. C.; Appel, C.; Andrieu-Brunsen, A., Fabrication and in situ functionalisation of mesoporous silica films by the physical entrapment of functional and responsive block copolymer structuring agents. *Soft Matter* **2019,** *15* (40), 8077-8083.
84. Angelomé, P. C.; Fuertes, M. C.; Soler-Illia, G. J. A. A., Multifunctional, Multilayer, Multiscale: Integrative Synthesis of Complex Macroporous and Mesoporous Thin Films with Spatial Separation of Porosity and Function. *Advanced Materials* **2006,** *18* (18), 2397-2402.
85. Soler-Illia, G. J.; Innocenzi, P., Mesoporous hybrid thin films: the physics and chemistry beneath. *Chemistry* **2006,** *12* (17), 4478-94.
86. Fuertes, M. C.; López-Alcaraz, F. J.; Marchi, M. C.; Troiani, H. E.; Luca, V.; Míguez, H.; Soler-Illia, G. J. A. A., Photonic Crystals from Ordered Mesoporous Thin-Film Functional Building Blocks. *Advanced Functional Materials* **2007,** *17* (8), 1247-1254.
87. Mahoney, L.; Koodali, R. T., Versatility of Evaporation-Induced Self-Assembly (EISA) Method for Preparation of Mesoporous TiO2 for Energy and Environmental Applications. *Materials* **2014,** *7* (4), 2697-2746.
88. De Paz-Simon, H.; Chemtob, A.; Croutxé-Barghorn, C.; Rigolet, S.; Michelin, L.; Vidal, L.; Lebeau, B., Surfactant-directed synthesis of mesoporous films made single-step by a tandem photosol-gel/photocalcination route. *APL Materials* **2014,** *2* (11), 113306.
89. Walcarius, A., Mesoporous materials and electrochemistry. *Chem Soc Rev* **2013,** *42* (9), 4098-140.
90. Fan, H.; Lu, Y.; Stump, A.; Reed, S. T.; Baer, T.; Schunk, R.; Perez-Luna, V.; López, G. P.; Brinker, C. J., Rapid prototyping of patterned functional nanostructures. *Nature* **2000,** *405*.
91. Senlis, G.; Dubarry, M.; Lejeune, M.; Chartier, T., 3D Piezoelectric Structures Made by Ink-Jet Printing. *Ferroelectrics* **2002,** *273* (1), 279-284.
92. Noguera, R.; Dossou-Yovo, C.; Lejeune, M.; Chartier, T., 3D fine scale PZT skeletons of 1-3 ceramic polymer composites formed by ink-jet prototyping process. **2005,** *126*, 133-137.
93. Noguera, R.; Lejeune, M.; Chartier, T., 3D fine scale ceramic components formed by ink-jet prototyping process. *Journal of the European Ceramic Society* **2005,** *25*, 2055-2059.
94. Mougenot, M.; Lejeune, M.; Baumard, J. F.; Boissiere, C.; Ribot, F.; Grosso, D.; Sanchez, C.; Noguera, R., Ink Jet Printing of Microdot Arrays of Mesostructured Silica. *Journal of the American Ceramic Society* **2006,** *89* (6), 1876-1882.
95. Fousseret, B.; Mougenot, M.; Rossignol, F.; Baumard, J.-F. o.; Soulestin, B.; Boissière, C. d.; Ribot, F. o.; Jalabert, D.; Carrion, C.; Sanchez, C. m.; Lejeune, M., Inkjet-Printing-Engineered Functional Microdot Arrays Made of Mesoporous Hybrid Organosilicas. *Chemistry of Materials* **2010,** *22* (13), 3875-3883.
96. De Los Cobos, O.; Fousseret, B.; Lejeune, M.; Rossignol, F.; Dutreilh-Colas, M.; Carrion, C.; Boissière, C.; Ribot, F.; Sanchez, C.; Cattoën, X.; Wong Chi Man, M.; Durand,

J.-O., Tunable Multifunctional Mesoporous Silica Microdots Arrays by Combination of Inkjet Printing, EISA, and Click Chemistry. *Chemistry of Materials* **2012,** *24* (22), 4337-4342.
97. Putz, F.; Scherer, S.; Ober, M.; Morak, R.; Paris, O.; Hüsing, N., 3D Printing of Hierarchical Porous Silica and α-Quartz. *Advanced Materials Technologies* **2018**, 1800060.
98. Duoss, E. B.; Twardowski, M.; Lewis, J. A., Sol-Gel Inks for Direct-Write Assembly of Functional Oxides. *Advanced Materials* **2007,** *19* (21), 3485-3489.
99. Kotz, F.; Arnold, K.; Bauer, W.; Schild, D.; Keller, N.; Sachsenheimer, K.; Nargang, T. M.; Richter, C.; Helmer, D.; Rapp, B. E., Three-dimensional printing of transparent fused silica glass. *Nature* **2017,** *544* (7650), 337-339.
100. Sico, G.; Montanino, M.; Prontera, C. T.; De Girolamo Del Mauro, A.; Minarini, C., Gravure printing for thin film ceramics manufacturing from nanoparticles. *Ceramics International* **2018,** *44* (16), 19526-19534.
101. Shi, S.; Allonas, X.; Croutxé-Barghorn, C.; Chemtob, A., Activation of the sol–gel process by visible light-emitting diodes (LEDs) for the synthesis of inorganic films. *New J. Chem.* **2015,** *39* (7), 5686-5693.
102. Sibeaud, M.; De Paz-Simon, H.; Croutxé-Barghorn, C.; Rigolet, S.; Michelin, L.; Lebeau, B.; Vidal, L.; Albouy, P. A.; Chemtob, A., Scaling-up of mesoporous silica films via an eco-efficient UV processing method. Part 1: Photoinduced mesostructuration. *Microporous and Mesoporous Materials* **2018,** *257*, 42-50.
103. Hoffmann, F.; Cornelius, M.; Morell, J.; Froba, M., Silica-based mesoporous organic-inorganic hybrid materials. *Angew. Chem. Int. Ed. Engl.* **2006,** *45* (20), 3216-51.
104. Cagnol, F.; Grosso, D.; Sanchez, C., A general one-pot process leading to highly functionalised ordered mesoporous silica films. *Chem. Commun.* **2004,** (15), 1742-3.
105. Nie, Z.; Kumacheva, E., Patterning surfaces with functional polymers. *Nat Mater* **2008,** *7* (4), 277-90.
106. Cheng, J. Y.; Ross, C. A.; Smith, H. I.; Thomas, E. L., Templated Self-Assembly of Block Copolymers: Top-Down Helps Bottom-Up. *Advanced Materials* **2006,** *18* (19), 2505-2521.
107. Park, C.; Yoon, J.; Thomas, E. L., Enabling nanotechnology with self assembled block copolymer patterns. *Polymer* **2003,** *44* (22), 6725-6760.
108. Lazzari, M.; Liu, G.; Lecommandoux, S., *Block Copolymers in Nanoscience*. Wiley VCH Verlag GmbH: 2006.
109. Liu, G.; Petrosko, S. H.; Zheng, Z.; Mirkin, C. A., Evolution of Dip-Pen Nanolithography (DPN): From Molecular Patterning to Materials Discovery. *Chemical Reviews* **2020**.
110. Chen, Y., Nanofabrication by electron beam lithography and its applications: A review. *Microelectronic Engineering* **2015,** *135*, 57-72.
111. Hu, W.; Sarveswaran, K.; Lieberman, M.; Bernstein, G. H., Sub-10 nm electron beam lithography using cold development of poly(methylmethacrylate). *Journal of Vacuum Science & Technology B: Microelectronics and Nanometer Structures Processing, Measurement, and Phenomena* **2004,** *22* (4), 1711-1716.
112. Liu, G.; Hirtz, M.; Fuchs, H.; Zheng, Z., Development of Dip-Pen Nanolithography (DPN) and Its Derivatives. *Small* **2019,** *15* (21), 1900564.
113. Brunsen, A.; Diaz, C.; Pietrasanta, L. I.; Yameen, B.; Ceolin, M.; Soler-Illia, G. J. A. A.; Azzaroni, O., Proton and Calcium-Gated Ionic Mesochannels: Phosphate-Bearing Polymer Brushes Hosted in Mesoporous Thin Films As Biomimetic Interfacial Architectures. *Langmuir* **2012,** *28* (7), 3583-3592.
114. Gilles, F. M.; Tagliazucchi, M.; Azzaroni, O.; Szleifer, I., Ionic Conductance of Polyelectrolyte-Modified Nanochannels: Nanoconfinement Effects on the Coupled Protonation Equilibria of Polyprotic Brushes. *The Journal of Physical Chemistry C* **2016,** *120* (9), 4789-4798.
115. Pérez-Mitta, G.; Marmisollé, W. A.; Albesa, A. G.; Toimil-Molares, M. E.; Trautmann, C.; Azzaroni, O., Phosphate-Responsive Biomimetic Nanofluidic Diodes Regulated by Polyamine–Phosphate Interactions: Insights into Their Functional Behavior from Theory and Experiment. *Small* **2018,** *14* (18), 1702131.

116. Brilmayer, R.; Förster, C.; Zhao, L.; Andrieu-Brunsen, A., Recent trends in nanopore polymer functionalization. *Current Opinion in Biotechnology* **2020,** *63*, 200-209.
117. Levinson, H. J., *Principles of Lithography. Third Edition*. SPIE Press: Washington, 2011.
118. Hilleringmann, U., *Silizium-Halbleitertechnologie*. Vieweg+Teubner Verlag: Suttgart

Leipzig, 2002.
119. Rothschild, M.; Bloomstein, T.; Efremow, N.; Fedynyshyn, T.; Fritze, M.; Pottebaum, I.; Switkes, M., Nanopatterning with UV Optical Lithography. *MRS Bulletin* **2005,** *30* (12), 942-946.
120. Stamm, U.; Schwoerer, H.; Lebert, R., Strahlungsquellen für die EUV-Lithographie. *Physik Journal 1* **2002,** *12*, 33-39.
121. Li, M.; Cushing, S. K.; Wu, N., Plasmon-enhanced optical sensors: a review. *The Analyst* **2015,** *140* (2), 386-406.
122. Knoll, W.; Kasry, A.; Yu, F.; Wang, Y.; Brunsen, A.; Dostálek, J., New concepts with surface plasmons and nano-biointerfaces. *Journal of Nonlinear Optical Physics & Materials* **2008,** *17* (2).
123. Kabatc, J.; Pączkowski, J., Monomeric asymmetric two- and three-cationic monomethine cyanine dyes as novel photoinitiators for free-radical polymerization. *Dyes and Pigments* **2010,** *86* (2), 133-142.
124. Valdes-Aguiler, O.; Pathak, C. P.; Shi, J.; Watson, D.; Neckers, D. C., Photopolymerization Studies Using Visible Light Photoinitiators. *Macromolecules* **1992,** *25*, 541-547.
125. Chegel, V.; Whitcombe, M. J.; Turner, N. W.; Piletsky, S. A., Deposition of functionalized polymer layers in surface plasmon resonance immunosensors by in-situ polymerization in the evanescent wave field. *Biosens Bioelectron* **2009,** *24* (5), 1270-5.
126. Ibn-El-Ahrach, H.; Bachelot, R.; Lérondel, G.; Vial, A.; Grimault, A.-S.; Plain, J.; Royer, P.; Soppera, O., Controlling the plasmon resonance of single metal nanoparticles by near-field anisotropic nanoscale photopolymerization. *Journal of Microscopy* **2008,** *229*, 421-427.
127. Dostert, K. H.; Alvarez, M.; Koynov, K.; del Campo, A.; Butt, H. J.; Kreiter, M., Near field guided chemical nanopatterning. *Langmuir* **2012,** *28* (8), 3699-703.
128. Fischer, J.; Vogel, N.; Mohammadi, R.; Butt, H. J.; Landfester, K.; Weiss, C. K.; Kreiter, M., Plasmon hybridization and strong near-field enhancements in opposing nanocrescent dimers with tunable resonances. *Nanoscale* **2011,** *3* (11), 4788-97.
129. Deeb, C.; Bachelot, R.; Plain, J.; Baudrion, A.-L.; Jradi, S.; Bouhelier, A.; Soppera, O.; Jain, P. K.; Huang, L.; Ecoffet, C.; Balan, L.; Royer, P., Quantitative Analysis of Localized Surface Plasmons Based on Molecular Probing. *ACS Nano* **2010,** *4* (8), 4579-4586.
130. Nguyen, M.; Lamouri, A.; Salameh, C.; Levi, G.; Grand, J.; Boubekeur-Lecaque, L.; Mangeney, C.; Felidj, N., Plasmon-mediated chemical surface functionalization at the nanoscale. *Nanoscale* **2016,** *8* (16), 8633-40.
131. Nguyen, M.; Kherbouche, I.; Gam-Derouich, S.; Ragheb, I.; Lau-Truong, S.; Lamouri, A.; Levi, G.; Aubard, J.; Decorse, P.; Felidj, N.; Mangeney, C., Regioselective surface functionalization of lithographically designed gold nanorods by plasmon-mediated reduction of aryl diazonium salts. *Chem Commun (Camb)* **2017,** *53* (82), 11364-11367.
132. Nguyen, V.-Q.; Ai, Y.; Martin, P.; Lacroix, J.-C., Plasmon-Induced Nanolocalized Reduction of Diazonium Salts. *ACS Omega* **2017,** *2* (5), 1947-1955.
133. Erzina, M.; Guselnikova, O.; Postnikov, P.; Elashnikov, R.; Kolska, Z.; Miliutina, E.; Švorčík, V.; Lyutakov, O., Plasmon-Polariton Induced, "from Surface" RAFT Polymerization, as a Way toward Creation of Grafted Polymer Films with Thickness Precisely Controlled by Self-Limiting Mechanism. *Advanced Materials Interfaces* **2018,** *5* (22), 1801042.
134. Silies, L.; Didzoleit, H.; Hess, C.; Stühn, B.; Andrieu-Brunsen, A., Mesoporous Thin Films, Zwitterionic Monomers, and Iniferter-Initiated Polymerization: Polymerization in a Confined Space. *Chemistry of Materials* **2015,** *27* (6), 1971-1981.

135. Tom, J.; Brilmayer, R.; Schmidt, J.; Andrieu-Brunsen, A., Optimisation of Surface-Initiated Photoiniferter-Mediated Polymerisation under Confinement, and the Formation of Block Copolymers in Mesoporous Films. *Polymers* **2017,** *9* (10), 539.
136. Herzog, N.; Kind, J.; Hess, C.; Andrieu-Brunsen, A., Surface plasmon & visible light for polymer functionalization of mesopores and manipulation of ionic permselectivity. *Chem. Commun.* **2015,** *51* (58), 11697-700.
137. V., V. D. P. e. *Papier Kompass 2017/2016*; Verband Deutscher Papierfabriken e. V.: Bonn, 2017.
138. *EUWID Papier und Zellstoff* **2016,** *41*.
139. Blechschmidt, J., *Taschenbuch der Papiertechnik*. Carl Hanser Verlag: München, 2013.
140. Martinez, A. W.; Phillips, S. T.; Butte, M. J.; Whitesides, G. M., Patterned paper as a platform for inexpensive, low-volume, portable bioassays. *Angew Chem Int Ed Engl* **2007,** *46* (8), 1318-20.
141. Pelton, R., Bioactive paper provides a low-cost platform for diagnostics. *TrAC Trends in Analytical Chemistry* **2009,** *28* (8), 925-942.
142. Yetisen, A. K.; Akram, M. S.; Lowe, C. R., Paper-based microfluidic point-of-care diagnostic devices. *Lab Chip* **2013,** *13* (12), 2210-51.
143. Xia, Y.; Si, J.; Li, Z., Fabrication techniques for microfluidic paper-based analytical devices and their applications for biological testing: A review. *Biosens Bioelectron* **2016,** *77*, 774-89.
144. Credou, J.; Berthelot, T., Cellulose: from biocompatible to bioactive material. *J. Mater. Chem. B* **2014,** *2* (30), 4767-4788.
145. Chen, Y. H.; Kuo, Z. K.; Cheng, C. M., Paper - a potential platform in pharmaceutical development. *Trends Biotechnol* **2015,** *33* (1), 4-9.
146. Ng, K.; Gao, B.; Yong, K. W.; Li, Y.; Shi, M.; Zhao, X.; Li, Z.; Zhang, X.; Pingguan-Murphy, B.; Yang, H.; Xu, F., Paper-based cell culture platform and its emerging biomedical applications. *Materials Today* **2017,** *20* (1), 32-44.
147. Gutbrod, B.; Haas, D.; Travitzky, N.; Greil, P., Preceramic Paper Derived Alumina/Zirconia Ceramics. *Advanced Engineering Materials* **2011,** *13* (6), 494-501.
148. Kos, P.; Plenio, H., A Fluorescent Molecular Probe for the Detection of Hydrogen Based on Oxidative Addition Reactions with Crabtree-Type Hydrogenation Catalysts. *Angew Chem Int Ed Engl* **2015,** *54* (45), 13293-6.
149. Lovikka, V. A.; Khanjani, P.; Väisänen, S.; Vuorinen, T.; Maloney, T. C., Porosity of wood pulp fibers in the wet and highly open dry state. *Microporous and Mesoporous Materials* **2016,** *234*, 326-335.
150. Schöttner, S.; Schaffrath, H.-J.; Gallei, M., Poly(2-hydroxyethyl methacrylate)-Based Amphiphilic Block Copolymers for High Water Flux Membranes and Ceramic Templates. *Macromolecules* **2016,** *49* (19), 7286-7295.
151. Dubois, C.; Herzog, N.; Rüttiger, C.; Geissler, A.; Grange, E.; Kunz, U.; Kleebe, H. J.; Biesalski, M.; Meckel, T.; Gutmann, T.; Gallei, M.; Andrieu-Brunsen, A., Fluid Flow Programming in Paper-Derived Silica-Polymer Hybrids. *Langmuir* **2017,** *33* (1), 332-339.
152. Noh, H.; Phillips, S. T., Metering the Capillary-Driven Flow of Fluids in Paper-Based Microfluidic Devices. *Anal. Chem.* **2010,** *82*, 4181-4187.
153. Whitesides, G. M., The origins and the future of microfluidics. *Nature* **2006,** *442*, 368.
154. Berthier, E.; Young, E. W. K.; Beebe, D., Engineers are from PDMS-land, Biologists are from Polystyrenia. *Lab on a Chip* **2012,** *12* (7), 1224-1237.
155. Osborn, J. L.; Lutz, B.; Fu, E.; Kauffman, P.; Stevens, D. Y.; Yager, P., Microfluidics without pumps: reinventing the T-sensor and H-filter in paper networks. *Lab on a Chip* **2010,** *10* (20), 2659-2665.
156. Böhm, A.; Carstens, F.; Trieb, C.; Schabel, S.; Biesalski, M., Engineering microfluidic papers: effect of fiber source and paper sheet properties on capillary-driven fluid flow. *Microfluid Nanofluid* **2014,** *16*, 789-799.

157. Bump, S.; Böhm, A.; Babel, L.; Wendenburg, S.; Carstens, F.; Schabel, S.; Biesalski, M.; Meckel, T., Spatial, spectral, radiometric, and temporal analysis of polymer-modified paper substrates using fluorescence microscopy. *Cellulose* **2015,** *22*, 73-88.
158. Carrilho, E.; Martinez, A. W.; Whitesides, G. M., Understanding Wax Printing: A Simple Micropatterning Process for Paper-Based Microfluidics. *Anal. Chem.* **2009,** *81*, 7091-7095.
159. Postulka, N.; Striegel, A.; Krausse, M.; Mager, D.; Spiehl, D.; Meckel, T.; Worgull, M.; Biesalski, M., Combining Wax Printing with Hot Embossing for the Design of Geometrically Well-Defined Microfluidic Papers. *ACS Appl Mater Interfaces* **2019,** *11* (4), 4578-4587.
160. Giokas, D. L.; Tsogas, G. Z.; Vlessidis, A. G., Programming fluid transport in paper-based microfluidic devices using razor-crafted open channels. *Anal Chem* **2014,** *86* (13), 6202-7.
161. Yamada, K.; Henares, T. G.; Suzuki, K.; Citterio, D., Papierbasierte tintenstrahlgedruckte Mikrofluidiksysteme für die Analytik. *Angew. Chem.* **2015,** *127*, 5384-5401.
162. Soler-Illia, G. J. A. A.; Azzaroni, O., Multifunctional hybrids by combining ordered mesoporous materials and macromolecular building blocks. *Chem. Soc. Rev.* **2011,** *40* (2), 1107-1150.
163. Tagliazucchi, M.; Szleifer, I., Transport mechanisms in nanopores and nanochannels: can we mimic nature? *Mat. Today* **2015,** *18*, 131-142.
164. Alberti, S.; Soler-Illia, G. J. A. A.; Azzaroni, O., Gated supramolecular chemistry in hybrid mesoporous silica nanoarchitectures: controlled delivery and molecular transport in response to chemical, physical and biological stimuli. *Chem. Commun.* **2015,** *51*, 6050-6075.
165. Yameen, B.; Ali, M.; Neumann, R.; Ensinger, W.; Knoll, W.; Azzaroni, O., Ionic Transport Through Single Solid-State Nanopores Controlled with Thermally Nanoactuated Macromolecular Gates. *Small* **2009,** *5* (11), 1287-1291.
166. Ma, Y.; Xue, S.; Hsu, S. C.; Yeh, L. H.; Qian, S.; Tan, H., *Phys. Chem. Chem. Phys.* **2014,** *16*, 20138-20146.
167. Calvo, A.; Yameen, B.; Williams, F. J.; Soler-Illia, G. J. A. A.; Azzaroni, O., Mesoporous Films and Polymer Brushes Helping Each Other To Modulate Ionic Transport in Nanoconfined Environments. An Interesting Example of Synergism in Functional Hybrid Assemblies. *J. Am. Chem. Soc.* **2009,** *131* (31), 10866-10868.
168. Shang, Y. L.; Zhang, Y.; P., L.; Kong, X.-Y.; Liu, W.; Xiao, K.; Xie, G.; Tian, Y.; Wen, L.; Jiang, L., DNAzyme tunable lead(II) gating based on ion-track etched conical nanochannels. *Chem. Commun.* **2015,** *51*, 5979-5981.
169. Siwy, Z. S.; Howorka, S., Engineered voltage-responsive nanopores. *Chem. Soc. Rev.* **2010,** *39* (3), 1115-1132.
170. Seifert, A.; Gopfrich, K.; Burns, J. R.; Fertig, N.; Keyser, U. F., Bilayer-Spanning DNA Nanopores with Voltage-Switching between Open and Closed State. *ACS Nano* **2015,** *9*, 1117-1126.
171. Powell, M. R.; Cleary, L.; Davenport, M.; Shea, K. J.; Siwy, Z., Electric-field-induced wetting and dewetting in single hydrophobic nanopores. *Nat. Nanotechnol.* **2011,** *6*, 798-802.
172. Brunsen, A.; Cui, J.; Ceolín, M.; Campo, A. d.; Soler-Illia, G. J. J. A.; Azzaroni, O., Light-activated gating and permselectivity in interfacial architectures combining “caged” polymer brushes and mesoporous thin films. *Chem. Commun.* **2012,** *48*, 1422-1424.
173. Vlassiouk, I.; Park, C. D.; Vail, S. A.; Gust, D.; Smirnov, S., Control of nanopore wetting by a photochromic spiropyran: A light-controlled valve and electrical switch. *Nano Letters* **2006,** *6* (5), 1013-1017.
174. Wang, G.; Bohaty, A. K.; Zharov, I.; White, H. S., Photon Gated Transport at the Glass Nanopore Electrode. *J. Am. Chem. Soc.* **2006,** *128*, 13553-13558.
175. Rosenholm, J. B., Liquid spreading on solid surfaces and penetration into porous matrices: Coated and uncoated papers. *Advances in Colloid and Interface Science* **2015,** *220*, 8-53.

176. Masoodi, R.; Pillai, K. M., Darcy's law-based model for wicking in paper-like swelling porous media. *AIChE Journal* **2010,** *56* (9), 2257-2267.
177. Elbert, J.; Krohm, F.; Rüttiger, C.; Kienle, S.; Didzoleit, H.; Balzer, B. N.; Hugel, T.; Stühn, B.; Gallei, M.; Brunsen, A., Polymer-Modified Mesoporous Silica Thin Films for Redox-Mediated Selective Membrane Gating. *Advanced Functional Materials* **2014,** *24* (11), 1591-1601.
178. Elbert, J.; Gallei, M.; Rüttiger, C.; Brunsen, A.; Didzoleit, H.; Stühn, B.; Rehahn, M., Ferrocene Polymers for Switchable Surface Wettability. *Organometallics* **2013,** *32* (20), 5873-5878.
179. Sun, W.; Zhou, S.; You, B.; Wu, L., A facile method for the fabrication of superhydrophobic films with multiresponsive and reversibly tunable wettability. *Journal of Materials Chemistry A* **2013,** *1* (9), 3146.
180. Shi, F.; Song, Y.; Niu, J.; Xia, X.; Wang, Z.; Zhang, X., Facile Method To Fabricate a Large-Scale Superhydrophobic Surface by Galvanic Cell Reaction. *18* **2006**, 1365-1368.
181. Feng, C. L.; Zhang, Y. J.; Jin, J.; Song, Y. L.; Xie, L. Y.; Qu, G. R.; Jiang, L.; Zhu, D. B., Reversible Wettability of Photoresponsive Fluorine-Containing Azobenzene Polymer in Langmuir-Blodgett Films. *Langmuir* **2001,** *17*, 4593-4597.
182. Pei, Y.; Travas-Sejdic, J.; Williams, D. E., Reversible electrochemical switching of polymer brushes grafted onto conducting polymer films. *Langmuir* **2012,** *28* (21), 8072-83.
183. Xin, B.; Hao, J., Reversibly switchable wettability. *Chem Soc Rev* **2010,** *39* (2), 769-82.
184. Drelich, J.; Chibowski, E.; Meng, D. D.; Terpilowski, K., Hydrophilic and superhydrophilic surfaces and materials. *Soft Matter* **2011,** *7* (21), 9804.
185. Alexander, S.; Eastoe, J.; Lord, A. M.; Guittard, F.; Barron, A. R., Branched Hydrocarbon Low Surface Energy Materials for Superhydrophobic Nanoparticle Derived Surfaces. *ACS Appl Mater Interfaces* **2016,** *8* (1), 660-6.
186. Rüttiger, C.; Mehlhase, S.; Vowinkel, S.; Cherkashinin, G.; Liu, N.; Dietz, C.; Stark, R. W.; Biesalski, M.; Gallei, M., Redox-mediated flux control in functional paper. *Polymer* **2016,** *98*, 429-436.
187. Tagliazucchi, M.; Szleifer, I., Transport mechanisms in nanopores and nanochannels: can we mimic nature? *Materials Today* **2015,** *18* (3), 131-142.
188. Alberti, S.; Soler-Illia, G. J.; Azzaroni, O., Gated supramolecular chemistry in hybrid mesoporous silica nanoarchitectures: controlled delivery and molecular transport in response to chemical, physical and biological stimuli. *Chem Commun (Camb)* **2015,** *51* (28), 6050-75.
189. Travitzky, N.; Windsheimer, H.; Fey, T.; Greil, P., Preceramic Paper-Derived Ceramics. *J. Am. Ceram. Soc.* **2008,** *91* (11), 3477-3492.
190. Zhang, Y.; Liu, X.; Huang, J., Hierarchical Mesoporous Silica Nanotubes Derived from Natural Cellulose Substance. *ACS Applied Materials & Interfaces* **2011,** *3* (9), 3272-3275.
191. de Gennes, P.-G., Soft Matter (Nobel Lecture). *Angew. Chem. Int. Ed. Engl.* **1992,** *31*, 842-845.
192. Casagrande, C.; Fabre, P.; Raphael, E.; Veyssié, M., Janus Beads: Realization and Behaviour at Water/Oil Interfaces. *Europhys. Lett.* **1989,** *9* (3), 251-255.
193. Seddon, A. M.; Casey, D.; Law, R. V.; Gee, A.; Templer, R. H.; Ces, O., Drug interactions with lipid membranes. *Chem. Soc. Rev.* **2009,** *38* (9), 2509-2519.
194. Sugano, K.; Kansy, M.; Artursson, P.; Avdeef, A.; Bendels, S.; Di, L.; Ecker, G. F.; Faller, B.; Fischer, H.; Gerebtzoff, G.; Lennernaes, H.; Senner, F., Coexistence of passive and carrier-mediated processes in drug transport. *Nature Reviews Drug Discovery* **2010,** *9*, 597.
195. Hikita, M.; Tanaka, K.; Nakamura, T.; Kajiyama, T.; Takahara, A., Super-liquid-repellent surfaces prepared by colloidal silica nanoparticles covered with fluoroalkyl groups. *Langmuir* **2005,** *21* (16), 7299-7302.
196. Yang, H. L.; Liang, F. X.; Chen, Y.; Wang, Q.; Qu, X. Z.; Yang, Z. Z., Lotus leaf inspired robust superhydrophobic coating from strawberry-like Janus particles. *Npg Asia Mater* **2015,** *7*.

197. Xia, B.; Yan, L.; Li, Y.; Zhang, S.; He, M.; Li, H.; Yan, H.; Jiang, B., Preparation of silica coatings with continuously adjustable refractive indices and wettability properties via sol–gel method. *RSC Adv.* **2018,** *8* (11), 6091-6098.
198. Liu, D.; Wu, Q.; Andersson, R. L.; Hedenqvist, M. S.; Farris, S.; Olsson, R. T., Cellulose nanofibril core–shell silica coatings and their conversion into thermally stable nanotube aerogels. *J. Mater. Chem. A* **2015,** *3* (30), 15745-15754.
199. Xu, Q. F.; Wang, J. N.; Sanderson, K. D., A general approach for superhydrophobic coating with strong adhesion strength. *J. Mater. Chem.* **2010,** *20* (28), 5961-5966.
200. Chen, P.-H.; Hsu, C.-C.; Lee, P.-S.; Lin, C.-S., Fabrication of semi-transparent super-hydrophobic surface based on silica hierarchical structures. *J Mech Sci Technol 25*, 43-47.
201. Ke, Q. P.; Fu, W. Q.; Jin, H. L.; Zhang, L.; Tang, T. D.; Zhang, J. F., Fabrication of mechanically robust superhydrophobic surfaces based on silica micro-nanoparticles and polydimethylsiloxane. *Surf Coat Tech* **2011,** *205* (21-22), 4910-4914.
202. Soz, C. K.; Trosien, S.; Biesalski, M., Superhydrophobic Hybrid Paper Sheets with Janus-Type Wettability. *Acs Appl Mater Inter* **2018,** *10* (43), 37478-37488.
203. Kavale, M. S.; Mahadik, D. B.; Parale, V. G.; Wagh, P. B.; Gupta, S. C.; Rao, A. V.; Barshilia, H. C., Optically transparent, superhydrophobic methyltrimethoxysilane based silica coatings without silylating reagent. *Appl Surf Sci* **2011,** *258* (1), 158-162.
204. Cai, S.; Zhang, Y. L.; Zhang, H. L.; Yan, H. W.; Lv, H. B.; Jiang, B., Sol-Gel Preparation of Hydrophobic Silica Antireflective Coatings with Low Refractive Index by Base/Acid Two-Step Catalysis. *Acs Appl Mater Inter* **2014,** *6* (14), 11470-11475.
205. Ding, B.; Li, C. R.; Hotta, Y.; Kim, J. H.; Kuwaki, O.; Shiratori, S., Conversion of an electrospun nanofibrous cellulose acetate mat from a super-hydrophilic to super-hydrophobic surface. *Nanotechnology* **2006,** *17* (17), 4332-4339.
206. Vasiljevic, J.; Gorjanc, M.; Tomsic, B.; Orel, B.; Jerman, I.; Mozetic, M.; Vesel, A.; Simoncic, B., The surface modification of cellulose fibres to create super-hydrophobic, oleophobic and self-cleaning properties. *Cellulose* **2013,** *20* (1), 277-289.
207. Ferrero, F.; Periolatto, M., Application of fluorinated compounds to cotton fabrics via sol-gel. *Appl Surf Sci* **2013,** *275*, 201-207.
208. Cappelletto, E.; Callone, E.; Campostrini, R.; Girardi, F.; Maggini, S.; della Volpe, C.; Siboni, S.; Di Maggio, R., Hydrophobic siloxane paper coatings: the effect of increasing methyl substitution. *J Sol-Gel Sci Techn* **2012,** *62* (3), 441-452.
209. Fors, B. P.; Hawker, C. J., Control of a living radical polymerization of methacrylates by light. *Angew Chem Int Ed Engl* **2012,** *51* (35), 8850-3.
210. Treat, N. J.; Fors, B. P.; Kramer, J. W.; Christianson, M.; Chiu, C.-Y.; Read de Alaniz, J.; Hawker, C. J., Controlled Radical Polymerization of Acrylates Regulated by Visible Light. *ACS Macro Letters* **2014,** *3* (6), 580-584.
211. McKenzie, T. G.; Wong, E. H. H.; Fu, Q.; Sulistio, A.; Dunstan, D. E.; Qiao, G. G., Controlled Formation of Star Polymer Nanoparticles via Visible Light Photopolymerization. *ACS Macro Letters* **2015,** *4* (9), 1012-1016.
212. Chen, M.; MacLeod, M. J.; Johnson, J. A., Visible-Light-Controlled Living Radical Polymerization from a Trithiocarbonate Iniferter Mediated by an Organic Photoredox Catalyst. *ACS Macro Letters* **2015,** *4* (5), 566-569.
213. Yeow, J.; Sugita, O. R.; Boyer, C., Visible Light-Mediated Polymerization-Induced Self-Assembly in the Absence of External Catalyst or Initiator. *ACS Macro Letters* **2016,** *5* (5), 558-564.
214. Ogawa, K. A.; Goetz, A. E.; Boydston, A. J., Metal-free ring-opening metathesis polymerization. *J Am Chem Soc* **2015,** *137* (4), 1400-3.
215. Goetz, A. E.; Boydston, A. J., Metal-Free Preparation of Linear and Cross-Linked Polydicyclopentadiene. *J Am Chem Soc* **2015,** *137* (24), 7572-5.
216. Schultz, D. M.; Yoon, T. P., Solar synthesis: prospects in visible light photocatalysis. *Science* **2014,** *343* (6174), 1239176.

217. Fouassier, J. P.; Morlet-Savary, F.; Lalevee, J.; Allonas, X.; Ley, C., Dyes as Photoinitiators or Photosensitizers of Polymerization Reactions. *Materials (Basel)* **2010,** *3* (12), 5130-5142.
218. García, O.; Costela, A.; García-Moreno, I.; Sastre, R., Pyrromethene 567 Dye as Visible Light Photoinitiator for Free Radical Polymerization. *Macromolecular Chemistry and Physics* **2003,** *204* (18), 2233-2239.
219. Kim, D.; Scranton, A. B.; Stansbury, J. W., Effect of the electron donor structure on the shelf-lifetime of visible-light activated three-component initiator systems. *Journal of Applied Polymer Science* **2009,** *114* (3), 1535-1542.
220. Knoll, W., Interfaces and thin films as seen by bound electromagnetic waves. *Annu. Rev. Phys. Chem.* **1998,** *49*, 569-638.
221. Kretschmann, E.; Raether, H., Radiative Decay of Non Radiative Surface Plasmons Excited by Light. *Z. Naturforsch.* **1968,** *23a*, 2135-2136.
222. Schasfoort R. B. M.; Tudos, A. J., *Handbook of Surface Plasmon Resonance*. Royal Society of Chemistry: Cambridge, UK, 2008.
223. Malitson, I. H., Interspeciment Comparison of the Refractive Index of Fused Silica. *Journal of the Optical Society of America* **1965,** *55* (10), 1205-1209.
224. Hale, G. M.; Querry, M. R., Optical Constants of Water in the 200-nm to 200-Mm Wavelength Region. *Applied Optics* **1973,** *12* (3), 555-563.
225. Rakic, A. D.; Djurisic, A. B.; Elazar, J. M.; Majewski, M. L., Optical properties of metallic films for vertical-cavity optoelectronic devices. *Applied Optics* **1998,** *37* (22), 5271-5283.
226. Brett, C. M. A.; O., B. A. M., *Electrochemistry: principles, methods and applications*. Oxford University Press Inc.: New York, 1993.
227. Bard, A. J.; Faulkner, L. R., *Electrochemical methods fundamentals and applications*. John Wiley & sons, inc.: United States of America, 2001; Vol. 2.
228. Etienne, M.; Guillemin, Y.; Grosso, D.; Walcarius, A., Electrochemical approaches for the fabrication and/or characterization of pure and hybrid templated mesoporous oxide thin films: a review. *Anal Bioanal Chem* **2013,** *405* (5), 1497-512.
229. Spanier, J. E.; Herman, I. P., Use of hybrid phenomenological and statistical effective-medium theories of dielectric functions to model the infrared reflectance of porous SiC films. *Physical Review B* **2000,** *61* (15), 10437-10450.
230. Tompkins, H. G.; Irene, E. A., *Handbook of ellipsometry*. William Andrew, Inc: United States of America, 2005.
231. Brunsen, A.; Calvo, A.; Williams, F. J.; Soler-Illia, G. J.; Azzaroni, O., Manipulation of molecular transport into mesoporous silica thin films by the infiltration of polyelectrolytes. *Langmuir* **2011,** *27* (8), 4328-33.
232. Lenza, R. F. S.; Vasconcelos, M. L., Preparation of silica by Sol-Gel Method Using Formamide. *Materials Research* **2001,** *4* (3), 189-194.
233. Marple, D. T. F., Refractive Index of ZnSe, ZnTe, and CdTe. *Journal of Applied Physics* **1964,** *35* (3), 539-542.
234. Yang, C.-M.; Zibrowius, B.; Schmidt, W.; Schüth, F., Stepwise Removal of the Copolymer Template from Mesopores and Micropores in SBA-15. *Chemistry of Materials* **2004,** *16* (15), 2918-2925.
235. Spiehl, D.; Haming, M.; Sauer, H. M.; Bonrad, K.; Dorsam, E., Engineering of Flexo- and Gravure-Printed Indium-Zinc-Oxide Semiconductor Layers for High-Performance Thin-Film Transistors. *IEEE Transactions on Electron Devices* **2015,** *62* (9), 2871-2877.
236. Giordano, G.; Vilà, N.; Aubert, E.; Ghanbaja, J.; Walcarius, A., Multi-layered, vertically-aligned and functionalized mesoporous silica films generated by sequential electrochemically assisted self-assembly. *Electrochimica Acta* **2017,** *237*, 227-236.
237. Babu, D. J.; Yadav, S.; Heinlein, T.; Cherkashinin, G.; Schneider, J. J., Carbon Dioxide Plasma as a Versatile Medium for Purification and Functionalization of Vertically Aligned Carbon Nanotubes. *The Journal of Physical Chemistry C* **2014,** *118* (22), 12028-12034.

238. Paz-Simon, H. D.; Chemtob, A.; Crest, F.; Croutxé-Barghorn, C.; Michelin, L.; Vidal, L.; Rigolet, S.; Lebeau, B., Thick mesostructured films via light induced self-assembly. *RSC Advances* **2012,** *2* (31).
239. Sibeaud, M.; Croutxé-Barghorn, C.; Rigolet, S.; Michelin, L.; Josien, L.; Vidal, L.; Lebeau, B.; Wörner, M.; Chemtob, A., UV aerosol synthesis: a one-step route to silica, organic-silica and surfactant/silica nanostructured materials. *RSC Adv.* **2016,** *6* (69), 65047-65054.
240. Chemtob, A.; Belon, C.; Croutxé-Barghorn, C.; Brendlé, J.; Soulard, M.; Rigolet, S.; Le Houérou, V.; Gauthier, C., Bridged polysilsesquioxane films via photoinduced sol–gel chemistry. *New Journal of Chemistry* **2010,** *34* (6), 1068-1072.
241. Crivello, J. V.; Bulut, U., Curcumin: A naturally occurring long-wavelength photosensitizer for diaryliodonium salts. *Journal of Polymer Science Part A: Polymer Chemistry* **2005,** *43* (21), 5217-5231.
242. Sabnis, R. W., *Handbook of Biological Dyes and Stains: Synthesis and Industrial Applications*. John Wiley & Sons Inc.: 2010.
243. (1994-2016), A. C. D. A. L. S. V., 2016.
244. Zhang, J.; Kirkham, J.; Robinson, C.; Wallwork, M. L.; Smith, D. A.; Marsh, A.; Wong, M., Determination of the Ionization State of 11-Thioundecyl-1-phosphonic Acid in Self-Assembled Monolayers by Chemical Force Microscopy. *Anal. Chem.* **2000,** *72*, 1973-1978.
245. FA, E. S.; Siopa, F.; Figueiredo, B. F.; Goncalves, A. M.; Pereira, J. L.; Goncalves, F.; Coutinho, J. A.; Afonso, C. A.; Ventura, S. P., Sustainable design for environment-friendly mono and dicationic cholinium-based ionic liquids. *Ecotoxicol Environ Saf* **2014,** *108*, 302-10.
246. Patil, R. R.; Turgman-Cohen, S.; Srogl, J.; Kiserow, D.; Genzer, J., On-demand degrafting and the study of molecular weight and grafting density of poly(methyl methacrylate) brushes on flat silica substrates. *Langmuir* **2015,** *31* (8), 2372-81.
247. Brilmayer, R.; Kübelbeck, S.; Khalil, A.; Brodrecht, M.; Kunz, U.; Kleebe, H.-J.; Buntkowsky, G.; Baier, G.; Andrieu-Brunsen, A., Influence of Nanoconfinement on the pKa of Polyelectrolyte Functionalized Silica Mesopores. *Advanced Materials Interfaces* **2020,** *7* (7), 1901914.
248. Aguilar, M. R.; Elvira, C.; Gallardo, A.; Vázquez, B.; Román, J. S., Smart Polymers and Their Applications as Biomaterials. Eds. N Ashammakhi, R Reis & E Chiellini Topics in Tissue Engineering, 2007; Vol. 3.
249. John, D.; Mohammadi, R.; Vogel, N.; Andrieu-Brunsen, A., Surface-Plasmon- and Green-Light-Induced Polymerization in Mesoporous Thin Silica Films. *Langmuir* **2020,** *36* (7), 1671-1679.
250. Knoll, W., Polymer thin films and interfaces characterized with evanescent light. *Makromol. Chem* **1991,** *192*, 2827-2856.
251. Kooyman, R. P. H., Chapter 2 Physics of Surface Plasmon Resonance. In *Handbook of Surface Plasmon Resonance*, The Royal Society of Chemistry: 2008; pp 15-34.
252. Martinez, A. W.; Phillips, S. T.; Whitesides, G. M., Three-dimensional microfluidic devices fabricated in layered paper and tape. *Proc Natl Acad Sci U S A* **2008,** *105* (50), 19606-11.
253. Cheng, C. M.; Martinez, A. W.; Gong, J.; Mace, C. R.; Phillips, S. T.; Carrilho, E.; Mirica, K. A.; Whitesides, G. M., Paper-based ELISA. *Angew Chem Int Ed Engl* **2010,** *49* (28), 4771-4.
254. Martinez, A. W.; Phillips, S. T.; Whitesides, G. M., Diagnostics for the Developing World: Microfluidic Paper-Based Analytical Devices. *Anal. Chem.* **2010,** *82*, 3-10.
255. Li, X.; Ballerini, D. R.; Shen, W., A perspective on paper-based microfluidics: Current status and future trends. *Biomicrofluidics* **2012,** *6* (1), 11301-1130113.
256. Grünberg, A.; Yeping, X.; Breitzke, H.; Buntkowsky, G., Solid-State NMR Characterization of Wilkinson's Catalyst Immobilized in Mesoporous SBA-3 Silica. *Chem. Eur. J.* **2010,** *16*, 6993-6998.

257. Weng, X.; Bao, Z.; Xing, H.; Zhang, Z.; Yang, Q.; Su, B.; Yang, Y.; Ren, Q., Synthesis and characterization of cellulose 3,5-dimethylphenylcarbamate silica hybrid spheres forenantioseparation of chiral beta-blockers. *Journal of Chromatography A* **2013,** *1321*, 38-47.
258. Sequeira, S.; Evtuguin, D. V.; Portugal, I.; Esculcas, A. P., Synthesis and characterisation of cellulose/silica hybrids obtained by heteropoly acid catalysed sol–gel process. *Materials Science and Engineering C* **2007,** *27*, 172-179.
259. Weng, X.; Bao, Z.; Zhang, Z.; Su, B.; Xing, H.; Yang, Q.; Yang, Y.; Ren, Q., Preparation of porous cellulose 3,5-dimethylphenylcarbamate hybrid organosilica particles for chromatographic applications. *J. Mater. Chem. B* **2015,** *3* (4), 620-628.
260. Ikai, T.; Yamamoto, C.; Kamigaito, M.; Okamoto, Y., Organic-inorganic hybrid materials for efficient enantioseparation using cellulose 3,5-dimethylphenylcarbamate and tetraethyl orthosilicate. *Chem Asian J* **2008,** *3* (8-9), 1494-9.
261. Gallei, M.; Rüttiger, C., Recent Trends in Metallopolymer Design: Redox-Controlled Surfaces, Porous Membranes, and Switchable Optical Materials Using Ferrocene-Containing Polymers. *Chemistry* **2018,** *24* (40), 10006-10021.
262. Ran, C.; Ding, G.; Liu, W.; Deng, Y.; Hou, W., Wetting on Nanoporous Alumina Surface: Transition between Wenzel and Cassie States Controlled by Surface Structure. *Langmuir* **2008,** *24* (18), 9952-9955.
263. Wakelyn, P. J.; Bertoniere, N. R.; French, A. D.; Thibodeaux, D. P.; Triplett, B. A.; Rousselle, M.-A.; Goynes Jr., W. R.; Edwards, J. V.; Hunter, L.; McAlister, D. D.; Gamble, G. R., *Cotton Fiber Chemistry and Technology*. Taylor & Francis Group, LLC: United States of America, 2007.
264. Kozlowski, R. M., *Handbook of natural fibres*. Woodhead Publishing Limited: United Kingdom, 2012; Vol. Volume 1: Types, properties and factors affecting breeding and cultivation.
265. Temming, H., *Temming-Linters: technische Informationen über Baumwollcellulose*. Temming AG: Glückstadt, 1965.
266. Biermann, C. J., *Handbook of Pulping and Papermaking - second edition*. ACADEMIC PRESS an Imprint of Elsevier: United Dtates of America, 1996.
267. De, G.; Karmakar, B.; Ganguli, D., Hydrolysis–condensation reactions of TEOS in the presence of acetic acid leading to the generation of glass-like silica microspheres in solution at room temperature. *J. Mater. Chem.* **2000,** *10* (10), 2289-2293.
268. Thommes, M.; Kaneko, K.; Neimark, A. V.; Olivier, J. P.; Rodriguez-Reinoso, F.; Rouquerol, J.; Sing, K. S. W., Physisorption of gases, with special reference to the evaluation of surface area and pore size distribution (IUPAC Technical Report). *Pure and Applied Chemistry* **2015,** *87* (9-10).
269. Kruk, M.; Jaroniec, M., Gas Adsorption Characterization of Ordered Organic−Inorganic Nanocomposite Materials. *Chemistry of Materials* **2001,** *13* (10), 3169-3183.
270. Mantanis, G. I.; Young, R. A.; Rowell, R. M., Swelling of compressed cellulose fiber webs in organic liquids. *Cellulose* **1995,** *2*, 1-22.
271. Fidale, L. C.; Ruiz, N.; Heinze, T.; Seoud, O. A. E., Cellulose Swelling by Aprotic and Protic Solvents: What are the Similarities and Differences? *Macromolecular Chemistry and Physics* **2008,** *209* (12), 1240-1254.
272. Dunphy, D. R.; Sheth, P. H.; Garcia, F. L.; Brinker, C. J., Enlarged Pore Size in Mesoporous Silica Films Templated by Pluronic F127: Use of Poloxamer Mixtures and Increased Template/SiO2Ratios in Materials Synthesized by Evaporation-Induced Self-Assembly. *Chemistry of Materials* **2015,** *27* (1), 75-84.
273. Steldinger, H., Esposito, A., Brunnengräber, K., Gläsel, J., Etzold, B. J. M., Activated Carbon in the Third Dimension—3D Printing of a Tuned Porous Carbon. *Adv. Sci.* 2019, 6, 1901340.
274. Goerlitzer, E. S. A.; Speichermann, L. E.; Mirza, T. A.; Mohammadi, R.; Vogel, N., Addressing the plasmonic hotspot region by site-specific functionalization of nanostructures. *Nanoscale Adv.*, 2020, 2, 394-400.

275. Quilis, N. G.; Hageneder, S.; Fossati, S.; Auer, S. K.; Venugopalan, P.; Bozdogan, A.; Petri, C.; Moreno-Cencerrado, A.; Toca-Herrera, J. L; Jonas, U.; Dostalek, J., UV-Laser Interference Lithography for Local Functionalization of Plasmonic Nanostructures with Responsive Hydrogel. *J. Phys. Chem. C* **2020**, 124, 5, 3297-3305.

Appendix

Appendix related to chapter 6.1:

Table 8. Ellipsometry results of dip-coated mesoporous silica films with different withdrawal speeds (mm/s) for 6-8 nm pores. Values for film thickness and refractive index are obtained by fitting the obtained data to a one-box model. V_{pore} values are calculated using the Bruggeman approximation[229]. All samples printed on silicon wafer. Given errors are determined by standard deviation of minimal three measured points. Further Experimental details are given within the experimental section.

Withdrawal speed [mm s^{-1}]	Layer thickness [nm]	Refractive index	RMSE	V_{pore}* [vol%]
0.05	419.8 ± 127.6	1.210 ± 0.08	4.441	53
0.5	168.8 ± 14.4	1.235 ± 0.008	1.779	47
0.9	152.8 ± 16.3	1.252 ± 0.011	1.041	44
1	140.5 ± 6.8	1.242 ± 0.035	0.407	46
2	180.4 ± 7.5	1.250 ± 0.002	0.688	44
3	226.3 ± 5.0	1.253 ± 0.001	1.439	44
4	267.5 ± 2.9	1.259 ± 0.000	0.745	42
5	265.3 ± 2.5	1.261 ± 0.000	0.760	42
6	290.4 ± 3.4	1.273 ± 0.001	0.422	39
7	323.9 ± 16.5	1.265 ± 0.011	0.843	41
8	316.5 ± 0.7	1.278 ± 0.000	0.495	38
9	339.3 ± 11	1.299 ± 0.019	0.769	34
10	372.0 ± 13.2	1.275 ± 0.035	1.278	39
15	395.5 ± 34.2	1.245 ± 0.001	1.576	45
20	398.2 ± 46.6	1.270 ± 0.054	2.987	40
25	357.9 ± 8.4	1.282 ± 0.010	0.927	38
30	353.4 ± 4.7	1.269 ± 0.001	0.868	40

Table 9. Ellipsometry results of dip-coated mesoporous silica films with different withdrawal speeds (mm/s) for 8-16 nm pores. Values for film thickness and refractive index are obtained by fitting the obtained data to a one-box model. V_{pore} values are calculated using the Bruggeman approximation[229]. All samples printed on silicon wafer. Given errors are determined by standard deviation of minimal three measured points. Further Experimental details are given within the experimental section.

Withdrawal speed [mm s^{-1}]	Layer thickness [nm]	Refractive index	RMSE	V_{pore}^{*} [vol%]
0.25	256.9 ± 0.9	1.191 ± 0.001	0.706	57
0.5	292.0 ± 9.4	1.305 ± 0.029	2.215	33
1	318.6 ± 1.6	1.232 ± 0.004	0.377	48
1.5	530.9 ± 2.4	1.139 ± 0.002	0.937	68
2	595.5 ± 5.4	1.162 ± 0.005	2.614	63
4	906.7 ± 16	1.127 ± 0.008	3.433	70
7	856.7 ± 18	1.149 ± 0.011	3.778	66
10	1016 ± 17	1.149 ± 0.008	5.482	66

Table 10. Ellipsometry results of printed mesoporous silica films with different cylinders of different cell volumes (mL/m^2) for 6-8 nm pores (700 N). Values for film thickness and refractive index are obtained by fitting the obtained data to a one-box model. V_{pore} values are calculated using the Bruggeman approximation[229]. All samples printed on silicon wafer. Given errors are determined by standard deviation of minimal three measured points. Further Experimental details are given within the experimental section.

Printing cell volume [mL m^{-2}]	Layer thickness [nm]	Refractive index	RMSE	V_{pore}^{*} [vol%]
12.23	111.4 ± 2.1	1.319 ± 0.026	0.432	30
10.14	103.1 ± 0.9	1.249 ± 0.009	0.215	44
9.19	98.7 ± 2.3	1.287 ± 0.038	0.491	36
8.30	93.3 ± 0.8	1.253 ± 0.006	0.275	44
5.98	77.1 ± 2.0	1.255 ± 0.112	0.127	43
4.71	72.6 ± 4.7	1.271 ± 0.031	0.382	40
2.72	48.9 ± 0.8	1.406 ± 0.020	0.252	-
1.67	37.8 ± 0.2	1.459 ± 0.013	0.059	-
0.93	21.1 ± 0.6	1.500 ± 0.052	0.148	-
0.45	8.9 ± 1.6	1.872 ± 0.154	0.041	-

Table 11. Ellipsometry results of printed mesoporous silica films with different cylinders of different cell volumes (mL/m²) for 8-16 nm pores (700). Values for film thickness and refractive index are obtained by fitting the obtained data to a one-box model. V_{pore} values are calculated using the Bruggeman approximation[229]. All samples printed on silicon wafer. Given errors are determined by standard deviation of minimal three measured points. Further Experimental details are given within the experimental section.

Printing cell volume [mL m^{-2}]	Layer thickness [nm]	Refractive index	RMSE	V_{pore}* [vol%]
12.23	199.3 ± 3.3	1.220 ± 0.002	0.597	51
10.14	174.7 ± 4.1	1.222 ± 0.014	0.448	50
9.19	175.2 ± 2.8	1.217 ± 0.004	0.683	51
8.30	165.8 ± 3.4	1.215 ± 0.006	0.613	52
5.98	141.4 ± 1.4	1.214 ± 0.013	0.536	52
4.71	87.4 ± 0.6	1.212 ± 0.018	0.323	52
1.67	59.0 ± 1.2	1.239 ± 0.002	0.136	47
0.93	35.8 ± 1.8	1.346 ± 0.040	0.128	24
0.45	19.4 ± 1.0	1.378 ± 0.264	0.214	17

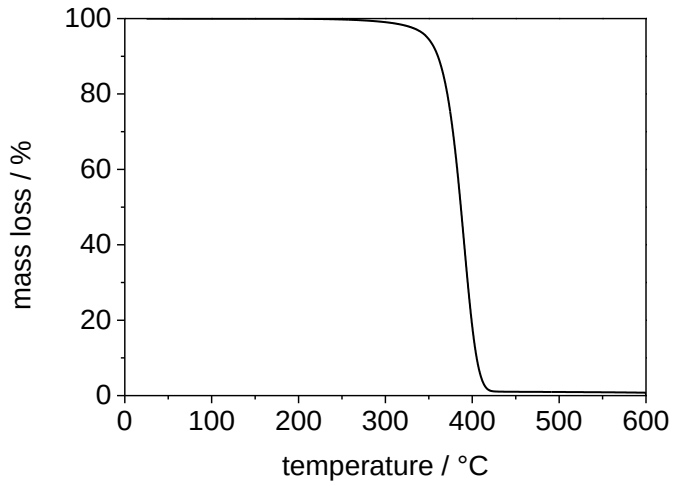

Figure 87. TGA of Pluronic® F127.

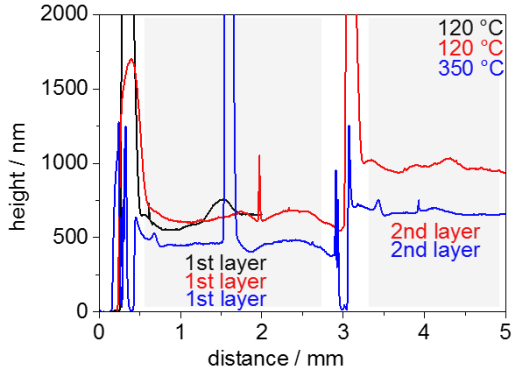

Figure 88. Profiler measurements of film thickness of first layer cured at 120 ° C (black), first and second layer cured at 120 ° C (red) and first and second layer cured at 350 ° C (blue). Complementary method to the ellipsometry measurements of **Figure 21**.

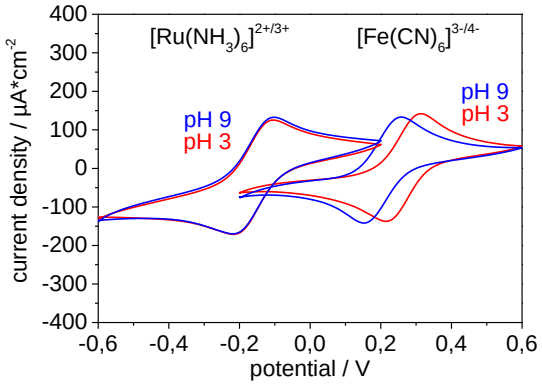

Figure 89. Cyclic voltammetry measurements of an untreated indium-tin-oxid electrode at a scanrate of 100 mV s^{-1} and a pH 3 (red) and pH 9 (blue) using $[Ru(NH_3)_6]^{2+/3+}$ and $[Fe(CN)_6]^{3-/4-}$ as an ionic redox probe molecule at a concentration of 0.01 mM in 100 mM KCl.

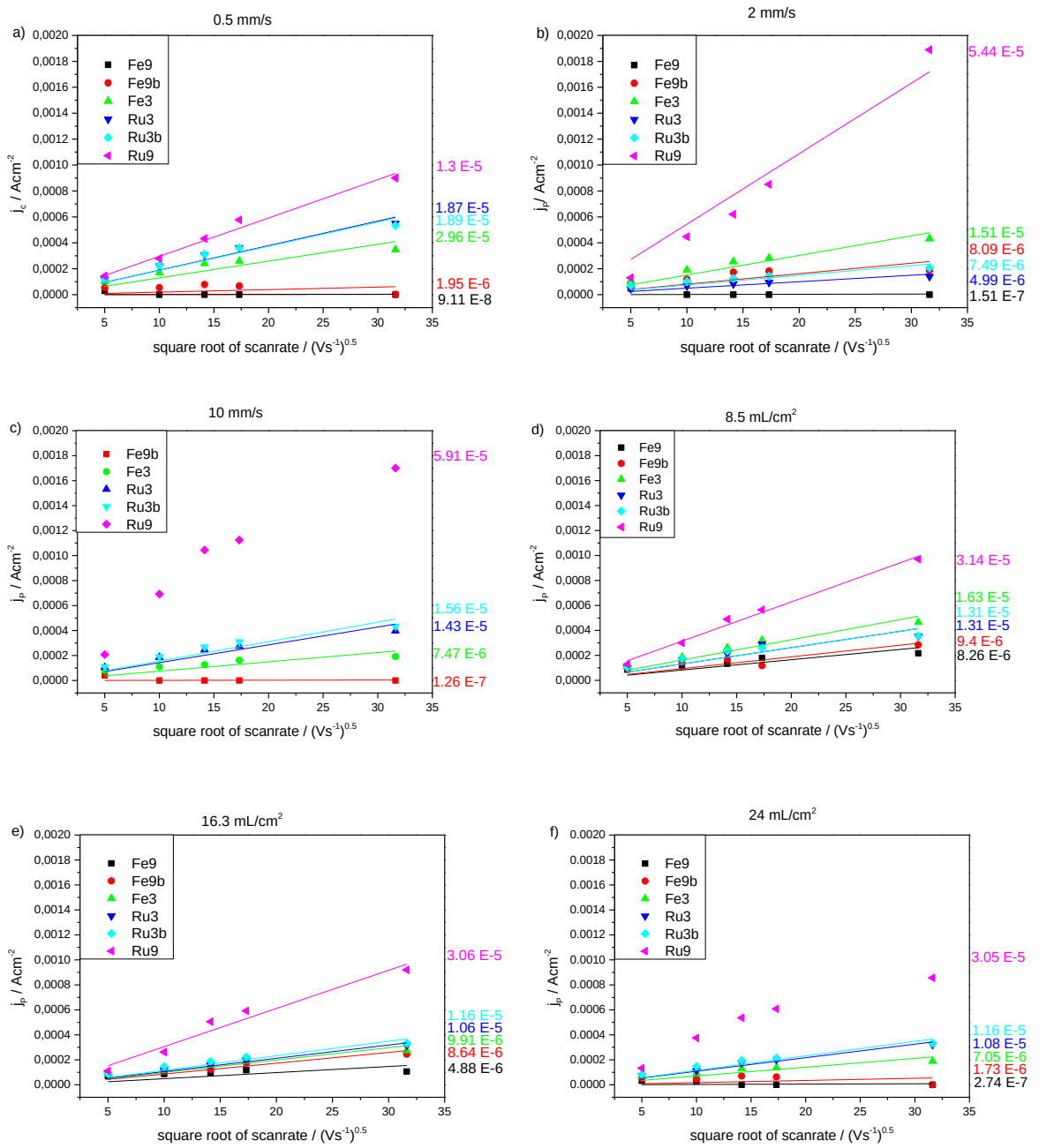

Figure 90. Randles-Sevcik relation between scan rate and Ip extracted from cyclic voltammograms of mesoporous silica thin films using $[Ru(NH_3)_6]^{2+/3+}$ (-0.6 V - + 0.2 V) (Ru) and $[Fe(CN)_6]^{3-/4-}$ (-0.2 V - +0.6 V) (Fe) as ionic redox probes at pH 3 and 9. The dip-coated mesoporous silica films are prepared with different withdrawal speeds a) 0.5 mm s^{-1} b) 2 mm s^{-1} and c) 10 mm s^{-1} resulting in film thicknesses of a) 140 nm (47 vol% porosity), b) 180 nm (44 vol% porosity), c) 300 nm (39 vol% porosity). Mesoporous silica films prepared by gravure printing are prepared using different cell volumes of d) 8.5 mL m^{-2} e) 16.3 mL m^{-2} and f) 24 mL m^{-2} resulting in film thicknesses of d) 100 nm (48 vol% porosity), e) 162 nm (40 vol% porosity), f) 250 nm (48 vol% porosity). The data sports are fitted with a linear fit and the resulting slope is written in the same color next to the graphs. For c) and f) for basic pH and the positively charged probe molecule no linear fitting is possible. The figures belongs to **Figure 24**. Figure adapted from N. Herzog *et al.* in RSC Adv. 2019, 9, 23570-23578 used by CC BY.

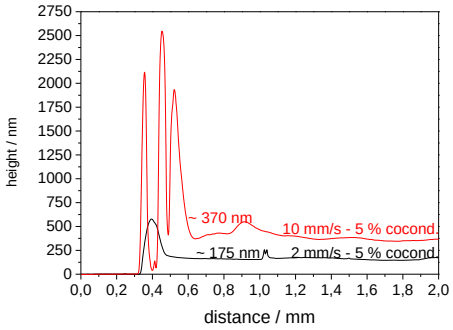

Figure 91. Profilometer measurement for 5 mol% coinitiator co-condensed mesoporous silica films dip-coated with two different withdrawal speeds.

Appendix related to chapter 6.2:

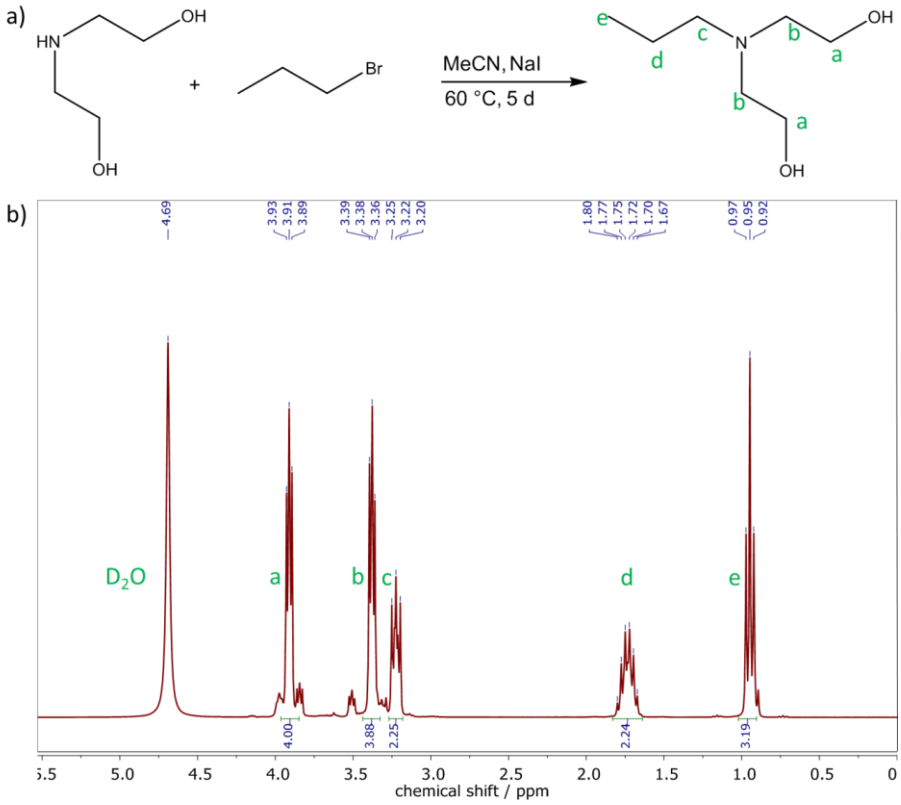

Figure 92. a) Synthesis of the coinitiator, propyldiethanolamine, without an anchor group for polymerization in solution with diethanolamine and 1- brompropan in acetonitrile and sodium iodid at 60 °C for 5 d. b) ^{1}H NMR (300 MHz, D_2O) of anchorless coinitiator with assignment of the signals with letters to the chemical structure in a).

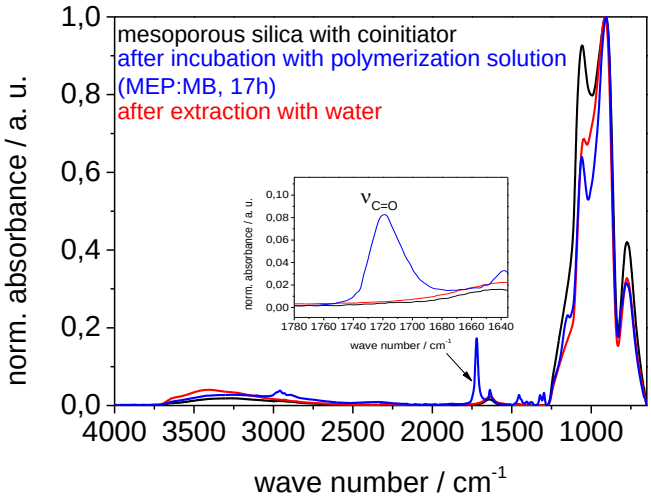

Figure 93. Extraction test. Mesoporous silica film (black, 370 nm film thickness) is incubated into polymerization solution (9:1 DMAEMA:methylenblue, 450 mg/mL MEP, 0.0052 mg/mL MB in 0.01 M $NaHCO_3$) for 17 h (overnight) without illumination with light (blue). Than the substrate is extracted with water (red). No polymer is generated.

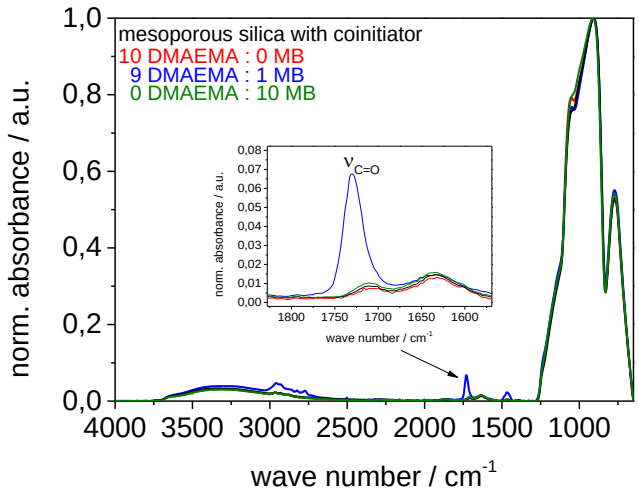

Figure 94. Test of DMAEMA polymerization in the presence (blue, green) and absence (red) of methylene blue. The polymerization time is adjusted to 10 minuted under irradiation using the Lumatec®Lamp (400-700 nm, 32 mW/cm²). The black spectrum shows mesoporous silica post-grafted with coinitiator. The red spectrum shows the polymerization in absence of methylene blue and blue spetrum the polymerization with the 9:1 ratio DMAEMA:MB (450 mg/mL DMAEMA, 0.0052 mg/mL MB in 0.01 M $NaHCO_3$). The green spectrum shows the illumination and extraction of methylene blue.

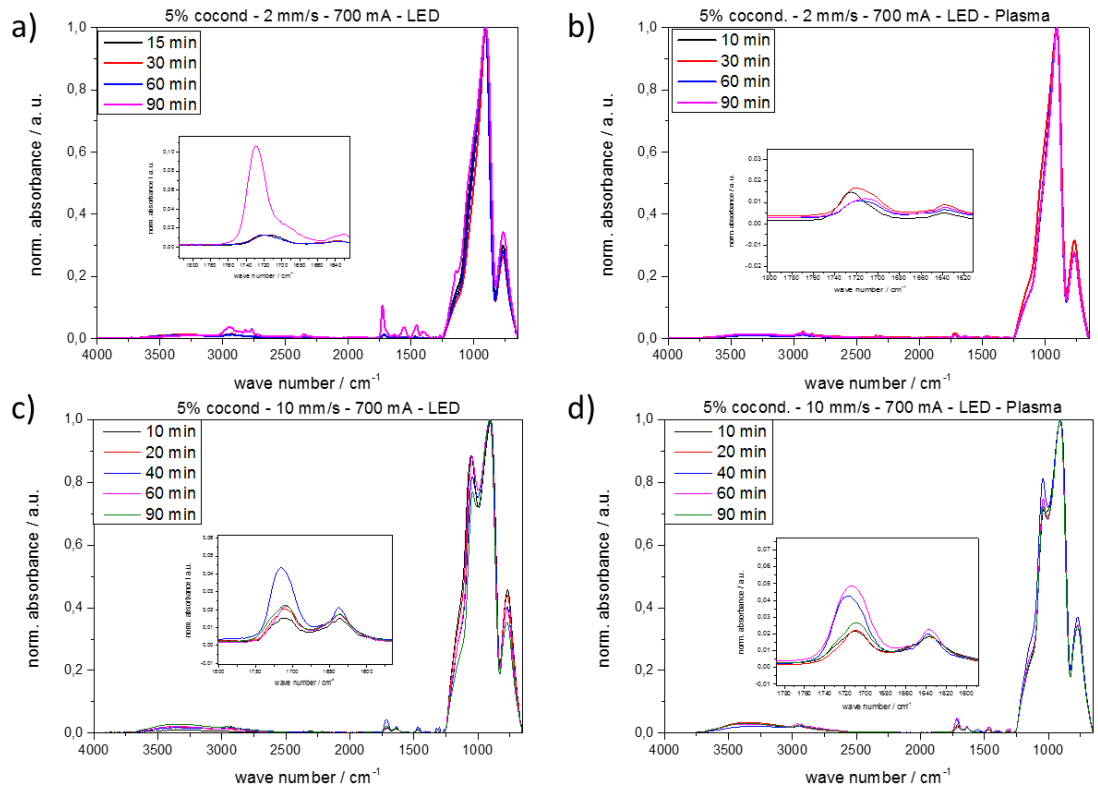

Figure 95. ATR-IR-spectra belonging to **Figure 46**a and b.

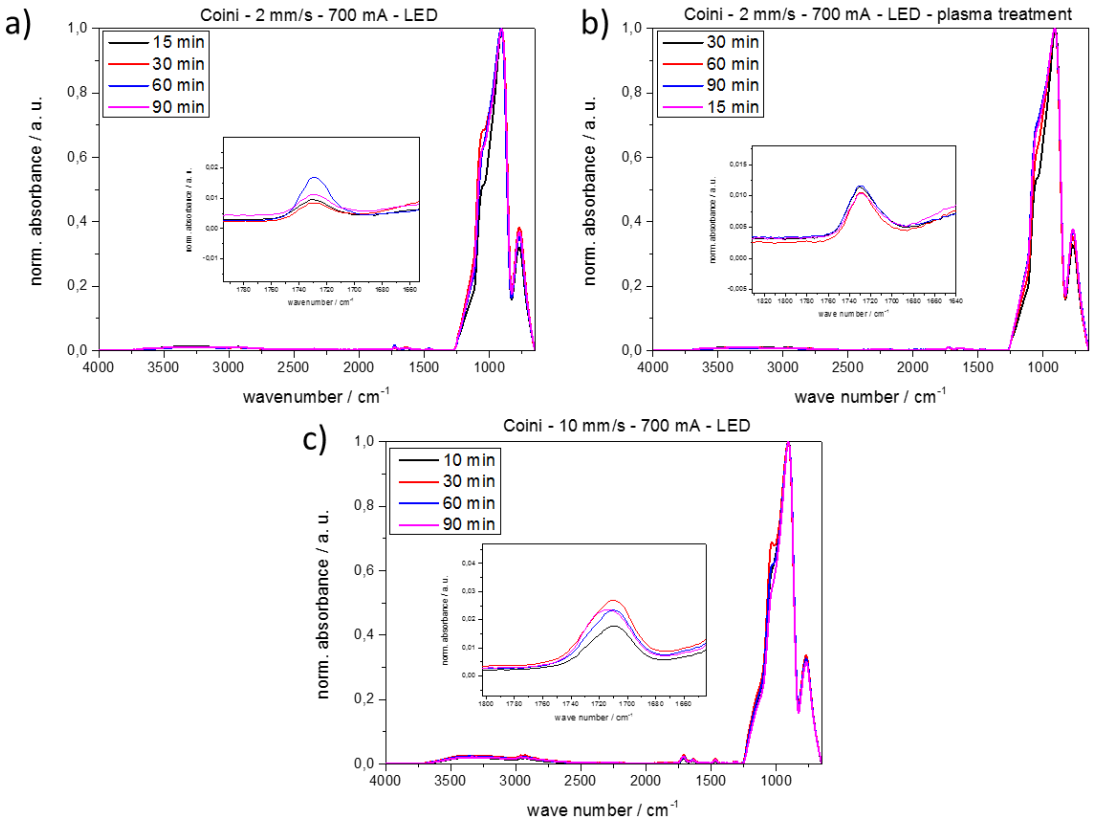

Figure 96. ATR-IR spectra belonging of **Figure 46**c.

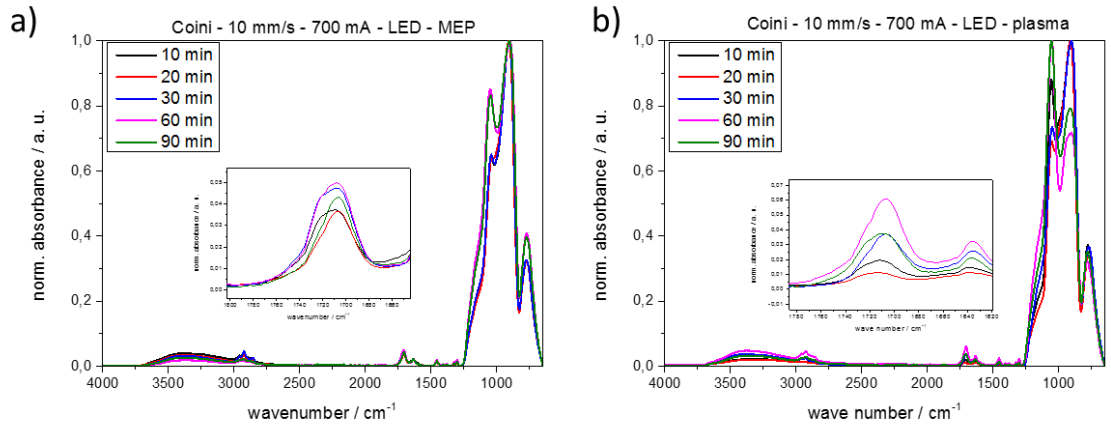

Figure 97. ATR-IR spectra belonging to **Figure 46**d.

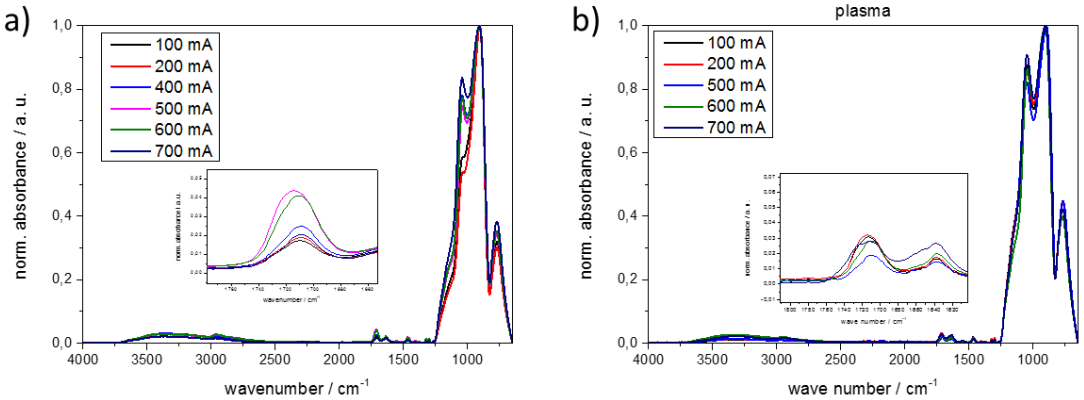

Figure 98. ATR-IR spectra belonging to **Figure 47**.

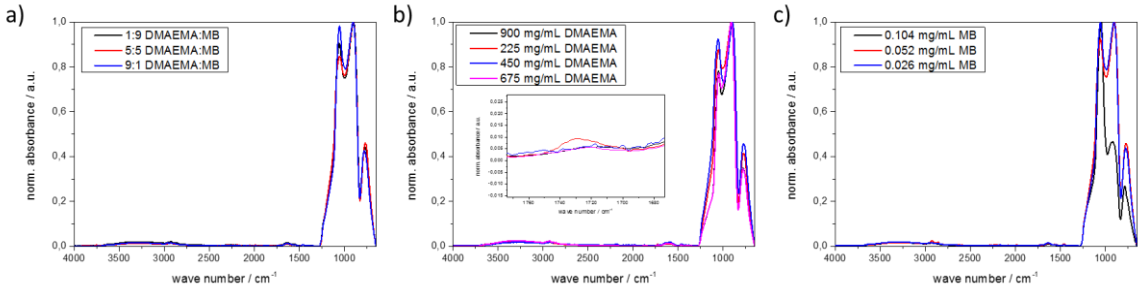

Figure 99. ATR-IR belonging to **Figure 48**.

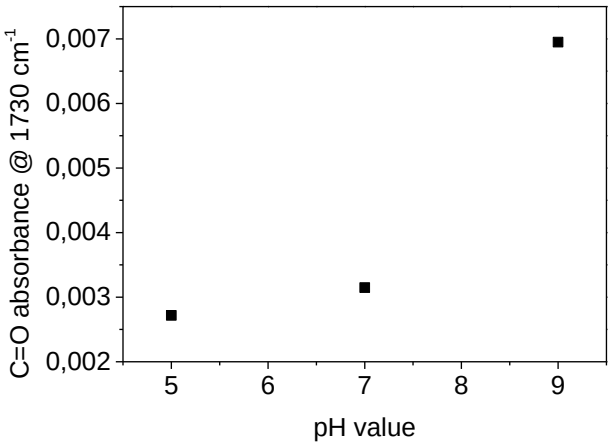

Figure 100. Results from polymerization at different pH values using DMAEMA and methylene blue in a 9:1 volume ratio (450 mg/mL DMAEMA/0.0052 mg/mL methylene blue).

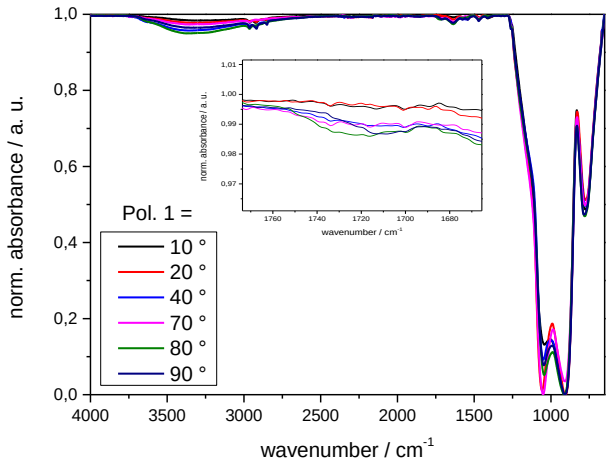

Figure 101. ATR-IR spectra belonging to **Figure 49**b.

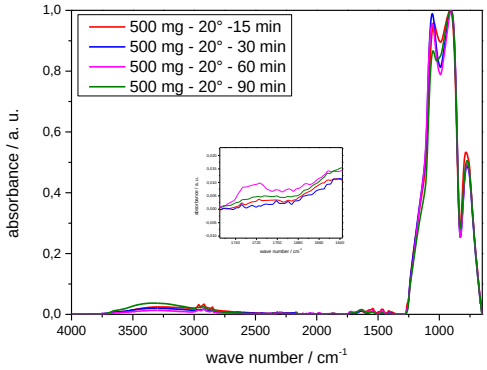

Figure 102. ATR-IR spectra belonging to **Figure 50**a.

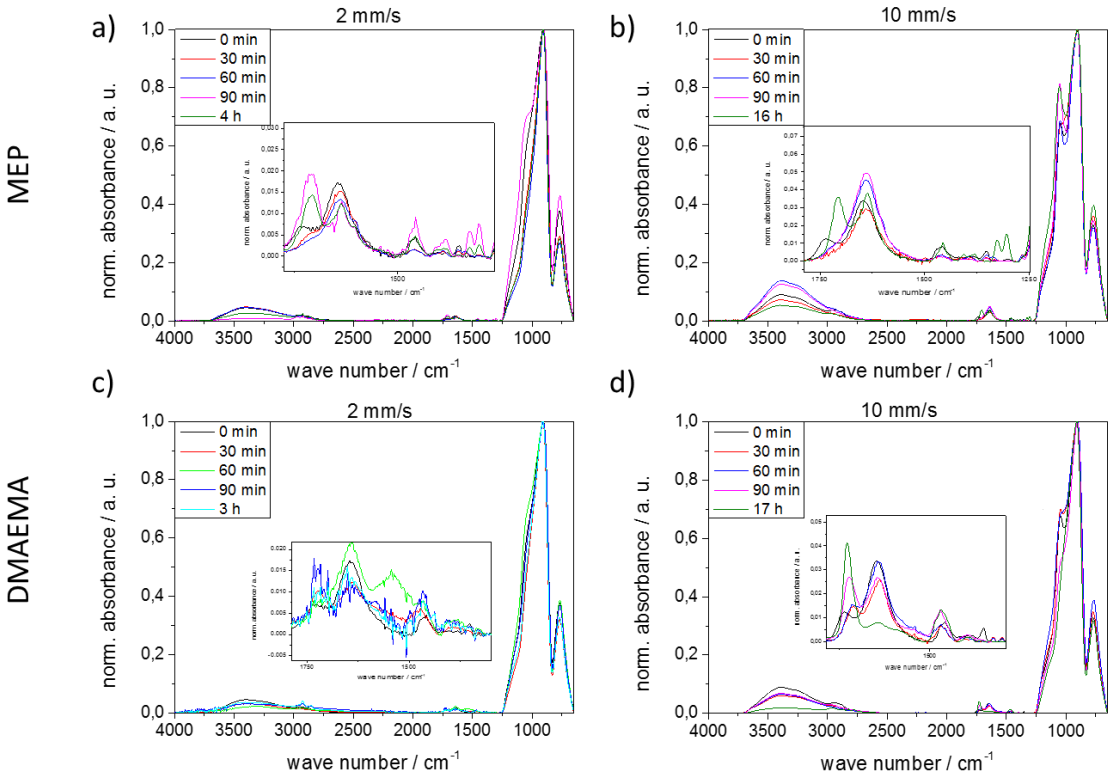

Figure 103. ATR-IR spectra belonging to **Figure 50**b.

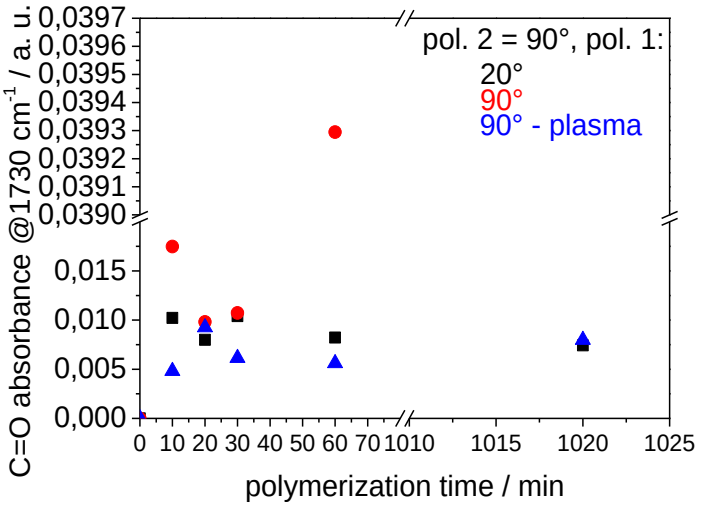

Figure 104. Time dependent polymerization of MEP with He/Ne-Laser as irradiation source. The coinitiator functionalized mesoporous silica film has a film thickness of about 300 nm. In black the polarizer 1 has 20° (0.2 mW) , in red 90° and in blue 90° (6.5 mW), here the films are plasma treated before polymerization. Polarizer 2 is constant at 90°.

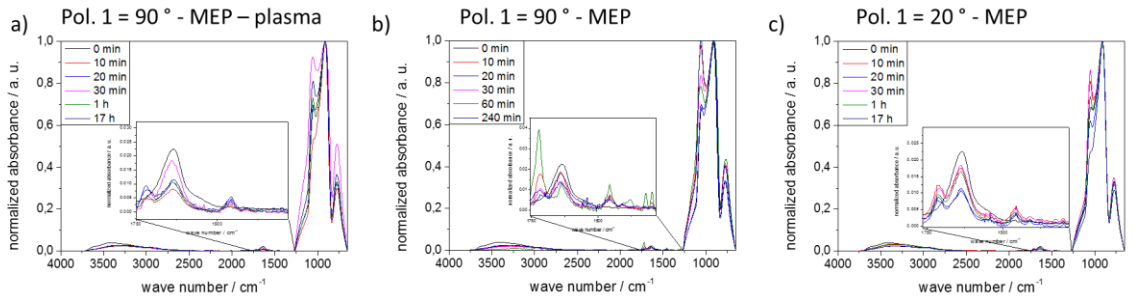

Figure 105. ATR-IR spectra belonging to **Figure 104**.

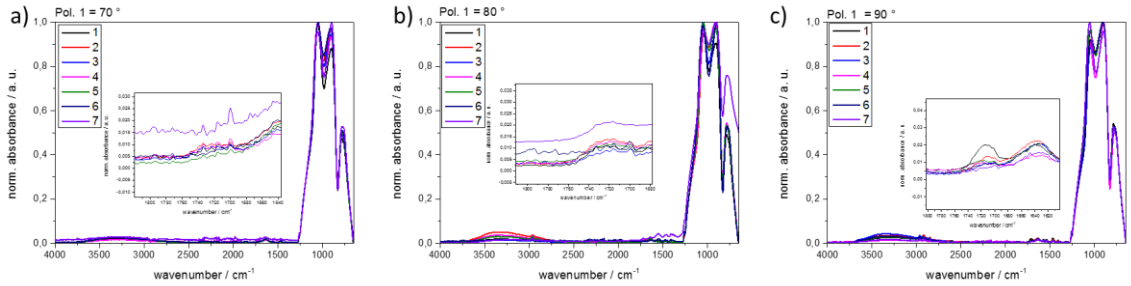

Figure 106. ATR-IR spectra belonging to **Figure 52**.

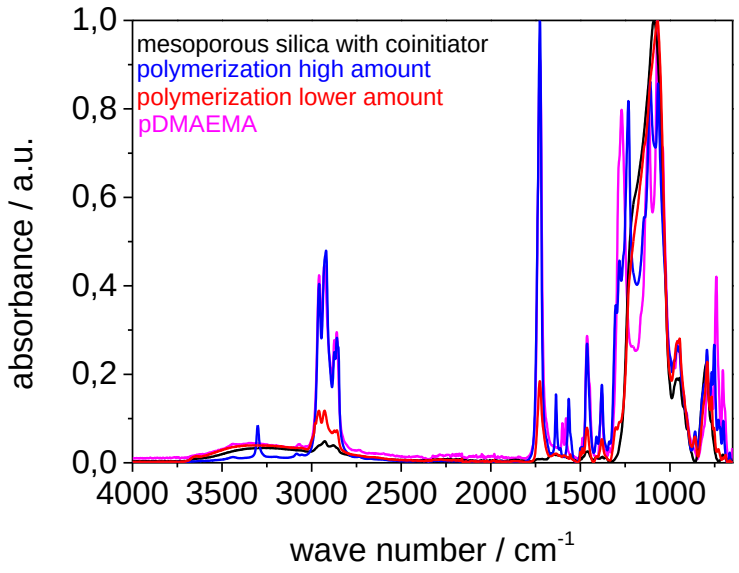

Figure 107. ATR-IR spectra of mesoporous silica functionalized with coinitiator (black), mesoporous silica functionalized with a high amount of PDMAEMA (blue) and a lower amount of PDMAEMA (red) and bulk PDMAEMA (magenta). the spectra a normalized to 1080 cm^{-1}.

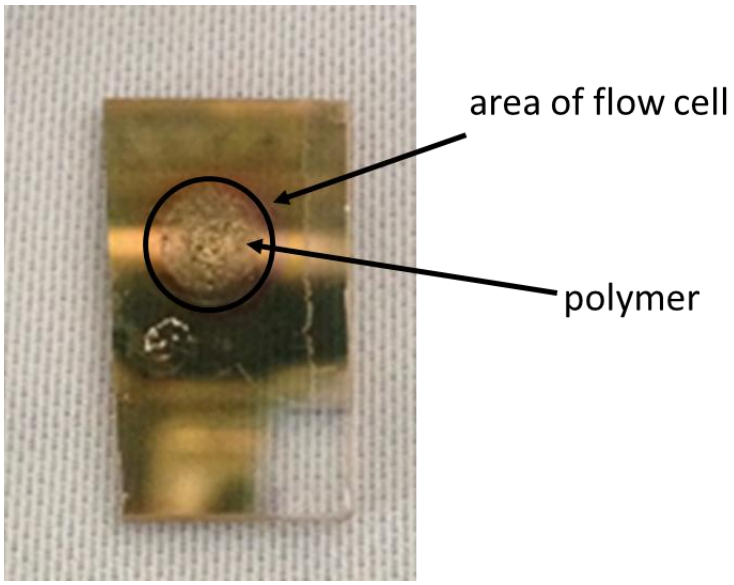

Figure 108. Image of the gold coated LaSFN9 substrate with polymer functionalized mesoporous silica film. In the area of flow cell the polymer is visible by eye. Leading to very high C=O vibrational bands in Si-O-Si_{asym} (1070 cm^{-1}). normalized ATR-IR spectra. Image belongs to polymerization for 2 h in 160 nm thick films (**Figure 55**, blue).

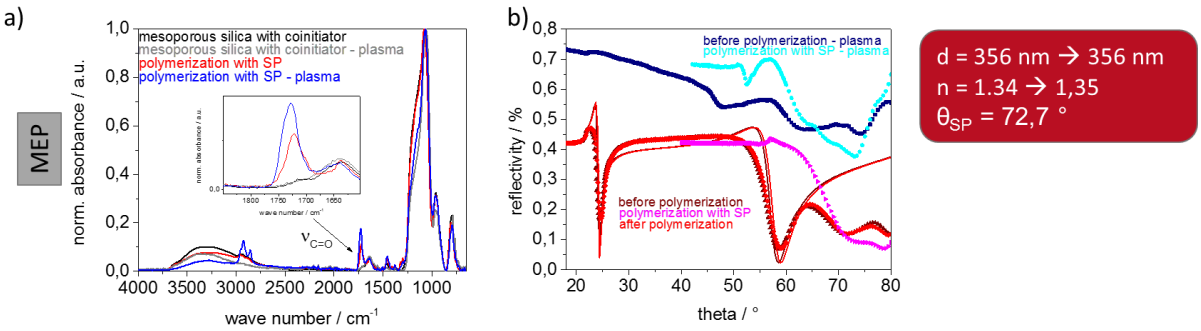

Figure 109. Polymerization of mesoporous silica films post-grafted with coinitiator with SP with and without plasma treatment after coinitiator binding. a) ATR-IR spectra, b) SPR spectra showing in red polymerization with SP and in blue polymerization with SP after Plasma treatment. MEP (450 mg/mL MEP, 0.0052 mg/mL methyleneblue in 0.1 M $NaHCO_3$ solution) is used as monomer. Polymerization is done for 2 h with a laser power of 5 mW (λ = 632.8 nm). The film thickness is around 350 nm with small pore diameter of 3-8 nm..

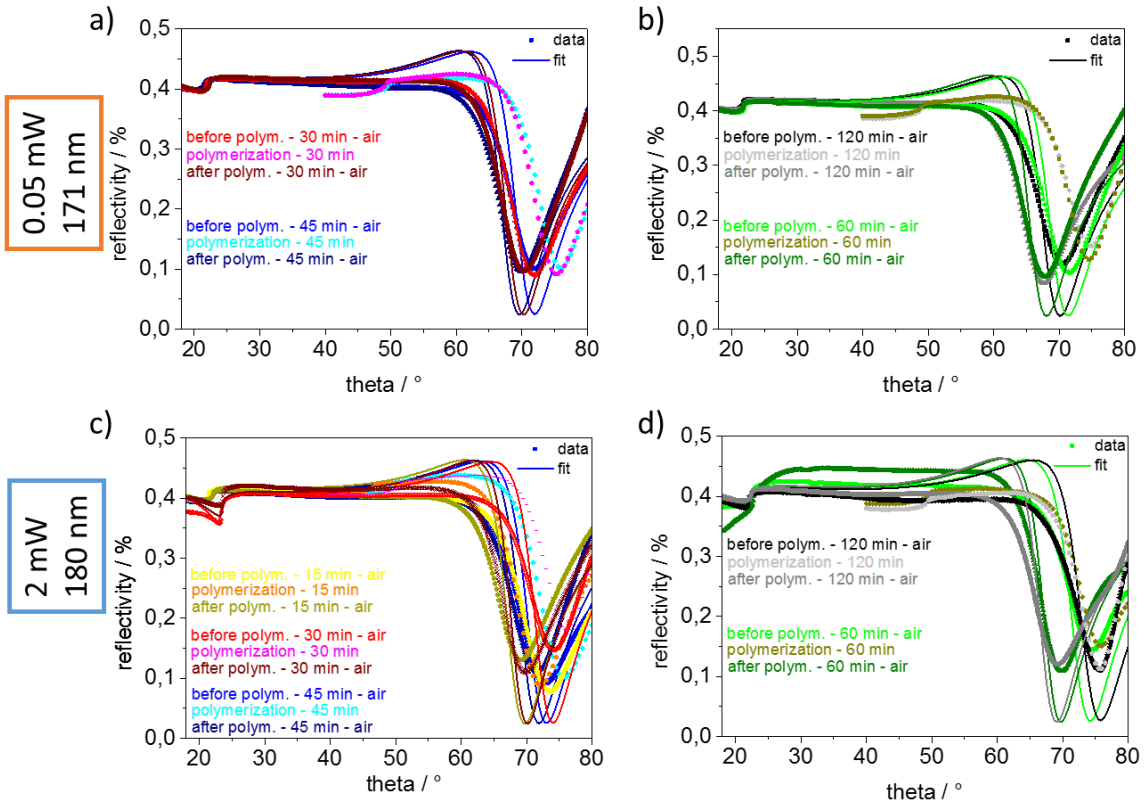

Figure 110. Time-depended polymerization with SP with two different laser powers black = 0,05 mW and red = 2 mW (λ = 632.8 nm). The mesoporous silica films post-grafted with coinitiator has a film thickness around 170 nm and a pore diameter of 3-6 nm. The used monomer is DMAEMA with 225 mg/mL (225 mg/mL DMAEMA, 0.0052 mg/mL methyleneblue in 0.1 M $NaHCO_3$ solution).

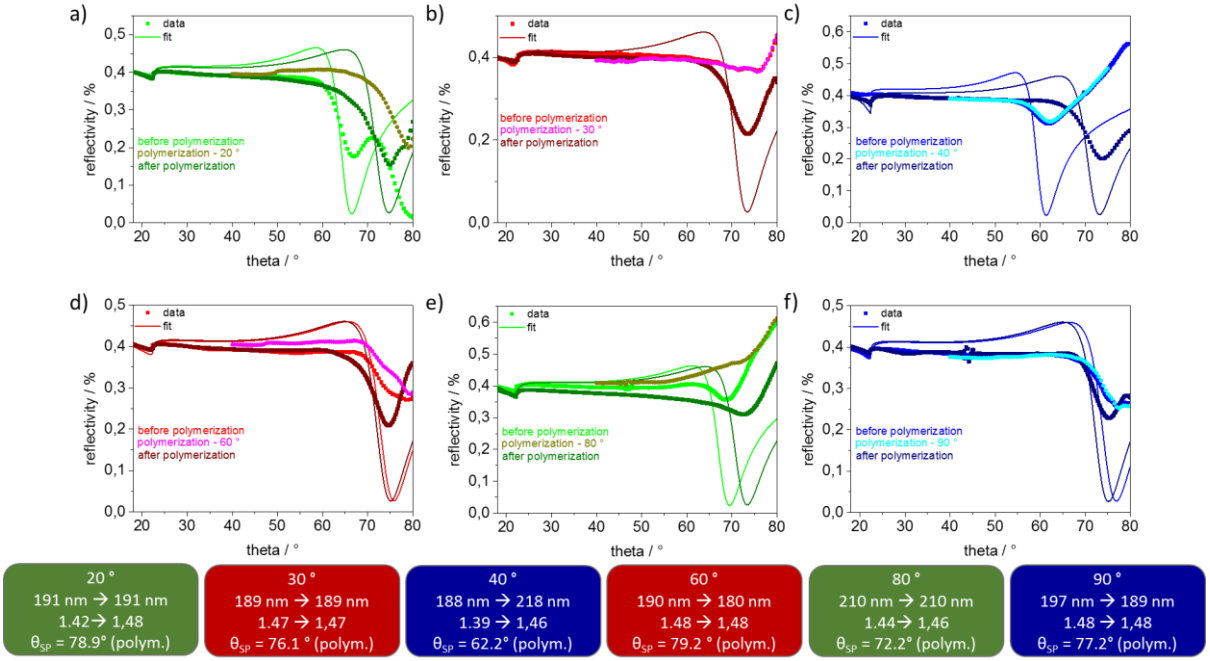

Figure 111. Energy dependent polymerization with SP. These spectra belong to **Figure 60**a, b.

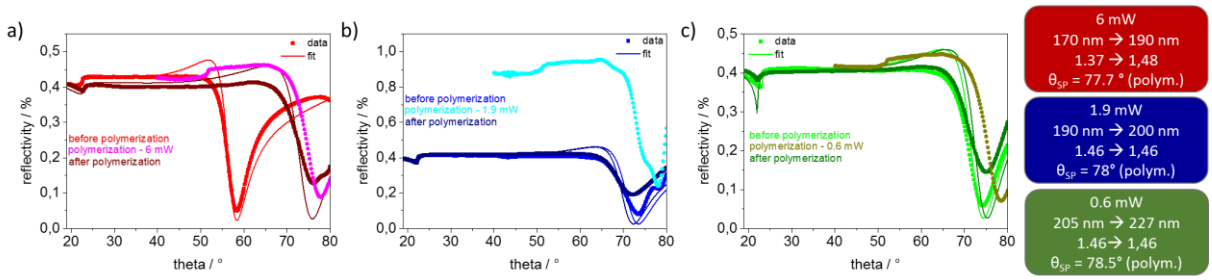

Figure 112. Energy dependent polymerization with SP. Using monomer concentration (450 mg/mL DMAEMA, 0.0052 mg/mL methylene blue in 0.1 M $NaHCO_3$ solution) and a shorter polymerization time of 10 min. The laser powers are a) 6 mW, b) 1.9 mW and c) 0.6 mW. These spectra belong to **Figure 60**c, d.

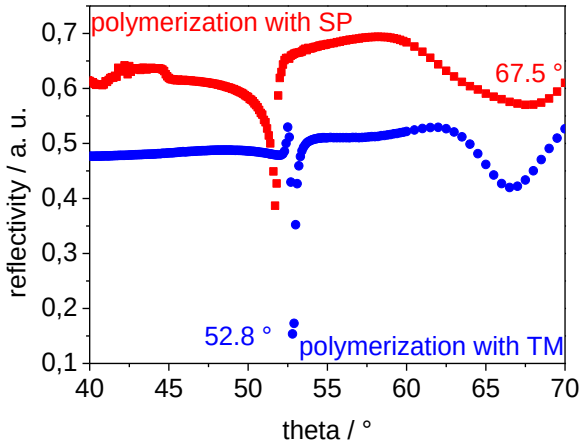

Figure 113. SPR measurements against polymerization solution for polymerization with SP and TM in **Figure 61**.

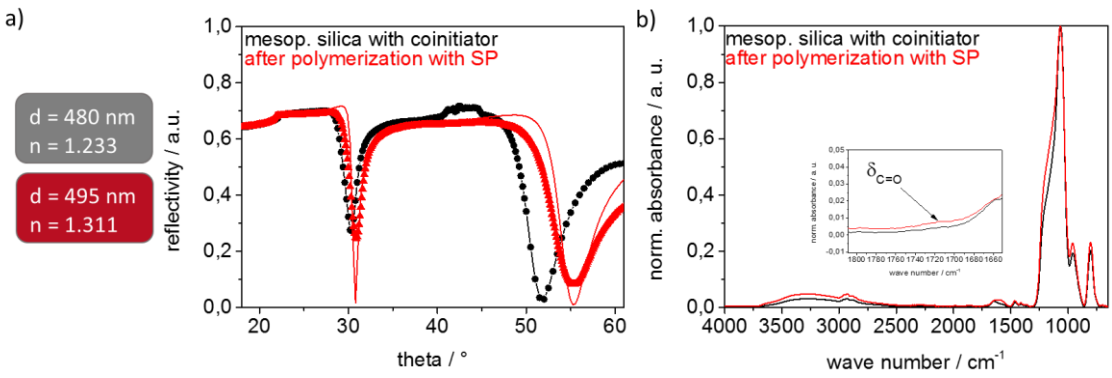

Figure 114. Polymerization of DMAEMA with SP (red) in a mesoporous silica film functionalized with coinitiator (black) with a layer thickness of 480 nm and pore diameters of 3-8 nm. The used laser power is 5 mW (λ =632.8 nm) and 1 h time with a constant flow of polymerization solution of 5µL/s a) SPR spectra measured against air (dots) before polymerization (black) and after polymerization (red). The fit curves are shown as line. b) ATR-IR spectra of mesoporous silica films before and after polymerization with SP to SPR spectra. This figure belongs to the experiment in **Figure 61**.

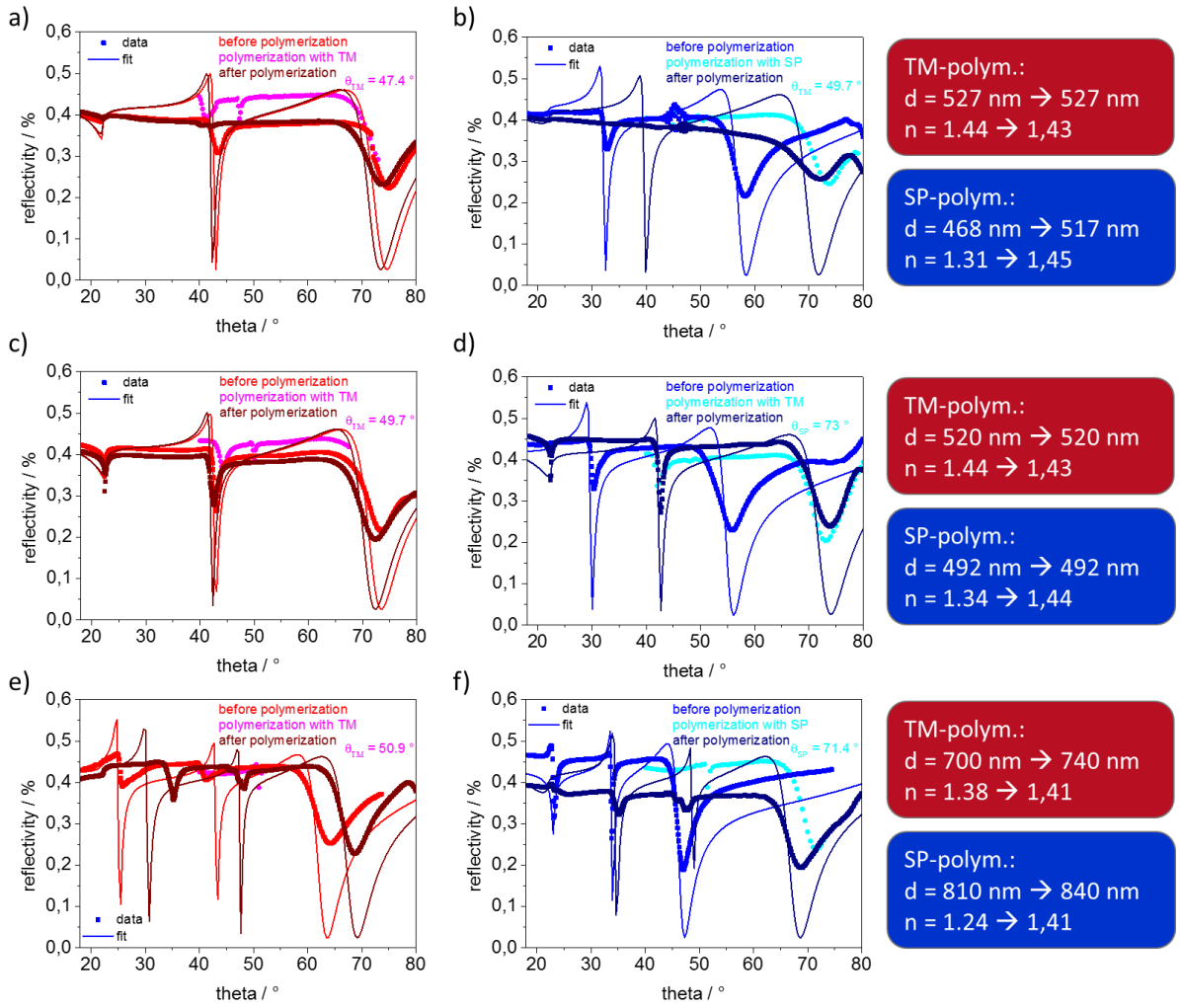

Figure 115. Polymerization of SP (blue) and TM (red) with two different monomers. Polymerization time is 30 min at a constant flow of 5 µL/min and a concentration of 225 mg/mL of monomer (laser power = 2 mW). Pore diameters of mesoporous silica films are between 8-16 nm. a + b) DMAEMA as monomer. Mesoporous silica film has a thickness of around 500 nm. c+d) MEP as monomer. Mesoporous silica film has a thickness of around 500 nm. e+f) DMAEMA as monomer. Mesoporous silica film has a thickness of around 800 nm. These spectra belong to **Figure 63**.

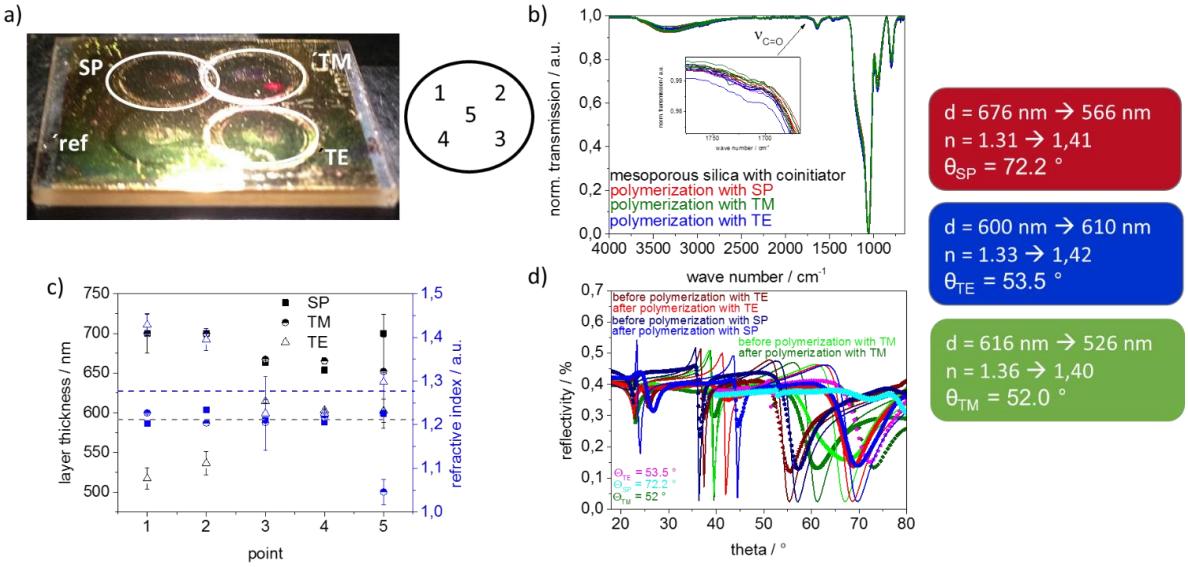

Figure 116. Polymerization with SP, TM and TE using DMAEMA (450 mg/mL DMAEMA, 0.0052 mg/mL methylene blue in 0.1 M $NaHCO_3$ solution) as monomer. The polymerization time is 30 min with a laser power of 3 mW (λ = 632.8 nm). Mesoporous silica films are post-grafted with coinitiator. The film thickness is around 600 nm and has a pore diameter of 8-16nm. a) image of the mesoporous silica film on gold coated glass after the polymerization showing the two rings of the flow cell from SPR set up with the five spots measured with ellipsometry (one-box fitting model for layer thickness and refractive index) c) and ATR-IR b). The polymerization with SP is in red, TM in green and TE in blue. d) SPR spectra before (dark colors, red = TE, blue = SP and TM = green) and after (bright colors) polymerization. Magenta (TE) and cyano (SP) and dark green (TM) shows spectra measured against polymerization solution.

Appendix related to chapter 6.3:

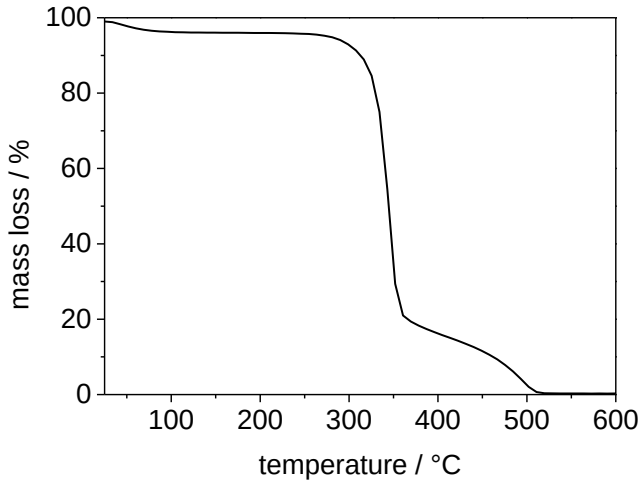

Figure 117. TGA of Cotton Linters 44 g/m².

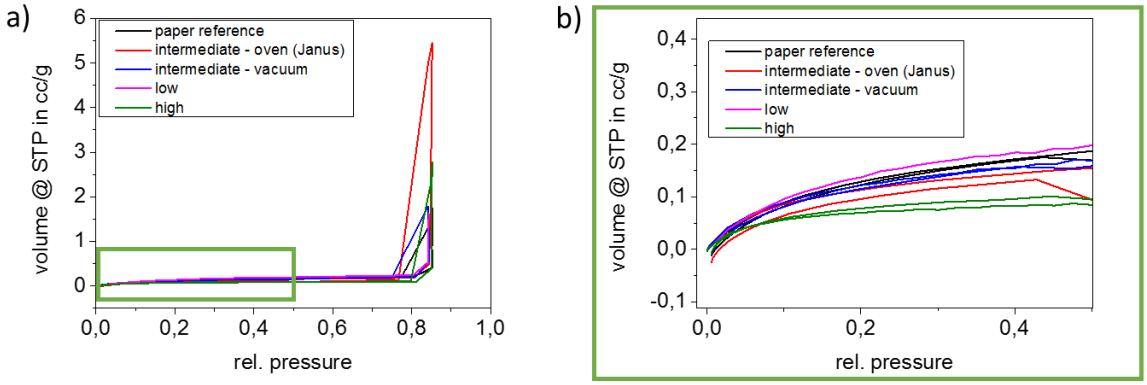

Figure 118. Kr-BET measurements of paper sheets coated with different amounts of silica.

Erklärung zur Dissertation

Nicole Herzog

Darmstadt,

Erklärung zur Dissertation

Ich erkläre hiermit, dass ich meine Dissertation selbstständig und nur mit den angegebenen Hilfsmitteln angefertigt und noch keinen Promotionsversuch unternommen habe.

_____

(Nicole Herzog)

Nicole Herzog

Darmstadt,

Erklärung der Übereinstimmung

Ich erkläre hiermit, dass die elektronische Version der Doktorarbeit mit der schriftlichen Version übereinstimmt. Die elektronische Version liegt dem Prüfungssekretariat vor.

_____

(Nicole Herzog)